Pushing the Boundaries of Endothermic Singlet Fission in Organic Semiconductors through Structure and Energetic Control

Arya Thampi

Department of Physics

University of Cambridge

This dissertation is submitted for the degree of

Doctor of Philosophy in Physics

St. John's College

August 2019

To Achan and Amma

Declaration

I hereby declare that except where specific reference is made to the work of others, the contents of this dissertation are original and have not been submitted in whole or in part for consideration for any other degree or qualification in this, or any other University. This dissertation is the result of my own work and includes nothing which is the outcome of work done in collaboration, except where specifically indicated in the text. This dissertation contains less than 60,000 words including appendices, bibliography, footnotes, tables and equations and has less than 150 figures.

Arya Thampi

August 2019

Acknowledgements

And the air was full of thoughts and things to say. But at times like these, only the small things are ever said. Big things lurk unsaid inside.

-The God of Small Things, Arundhati Roy

Doing a PhD is like running a marathon are words to live by for any graduate student and was the first piece of advice I received when I started this expedition in the Optoelectronics Group, in 2015. In the last four years, there have been many people who helped shape my academic as well as personal journey in Cambridge. First and foremost of all, I would like to thank my supervisor, Akshay, for his patience, perennial zeal and stirring scientific acumen. The many troubles of PhD life were treaded with tremendous support from him, as I reminisce our chats through some difficult times with great fondness. I thank my college, St. John's College, and the Dr. Manmohan Singh Scholarship for their prolonged financial support and other services provided during my PhD. I am grateful to have had wonderful mentors like Hannah Stern, Tom Jellicoe, Alex Cheminal and Leah Weiss, from the early days of my PhD. Hannah, thank you for taking me under your wings, for all the singlet fission chats, introducing me to the world of spectroscopy and all the good times we have had over coffee. Leah, thanks for the smiles, the unwavering enthusiasm and the spin-physics you taught me; certainly made my thesis and PhD life more wholesome. Steven, thanks for being the wonderful friend that you are, and for all the smiles and hugs. Coffee and dinners with you certainly calmed me down during times of mild insanity.

The niche that the Rao Empire (thanks Tom for naming it so aptly!) provides, with vibrancy and presence of extremely talented colleagues, was the best anybody could have asked for; thank you guys. The truly international nature of the group continues to influence all of us positively, enabling to embrace scientific and cultural openness. I am grateful to the very patient postdocs in OE and the Rao Empire, for the vigorous scientific discussions we have shared, especially Victor and Jooyoung for their insights and the time spent on this dissertation. Ture, Hope, Jesse, Raj, Limeng and Qifei- I warmheartedly remember the time

spent with you all from the beginning of my PhD. I can't thank you enough for lending your ears to me talking about science, failed experiments, sleepless nights, movies, *life, universe and everything*. Some of my fondest memories in Cambridge have you guys in it, on sunny and rainy days, over coffee or an occasional beer. *So long, and thanks for all the fish!*

Rohit, you were always around in times of happiness and hardship- you have been and continue to be one of my pillars of support and I couldn't have asked for a better friend. Saudamini, days were brighter when spent with you. Thanks for being around and for showing me the mystical city of Edinburgh. Pranav, thanks for sharing your movie enthusiasm with me- it helped sculpt my dissertation, quite literally, and continue to shape my life. Chaithra and Ghanashyam- thanks for bearing with me for the last twelve years. I love you both for (and amidst) all those bad jokes and gossip we shared. Emma, the last one and a half years were tough and you helped me sail through that. I'm forever indebted to you!

Acha and Amme, I know how difficult it must have been when your daughter decided to move five thousand miles away from home. I love you for understanding and supporting through my decisions, and for never letting me feel alone. Vichu, I am grateful for the sibling that you are, the friends that we have become and the love we share. Sangam, a smile from you made the sun shine in my world and thanks for carrying it around- it made all the difference, *Sakhave*.

Pushing the Boundaries of Endothermic Singlet Fission in Organic Semiconductors through Structure and Energetic Control

Arya Thampi

Singlet exciton fission (SF) is an exciton multiplication process in organic semiconductors in which a photoexcited singlet exciton is converted to two triplet excitons. SF based solar cells help break the Shockley-Quisser limit as high energy photons are used to generate two electron-hole pairs per photon absorbed with power conversion efficiencies (PCE) ~40%. Energetics of the states involved in SF determine the nature of driving force for SF, making it either an entropy-driven endothermic system or enthalpy-driven exothermic system. Many efforts to understand and implement SF in photovoltaics (PV) have been undertaken in the recent years. However, a fundamental understanding of triplet formation and physical parameters that govern the process is incomplete, and of paramount importance.

In this dissertation, we study how two key parameters influence endothermic SF: morphology and energetics. SF occurs via two steps in acenes: a photoexcited singlet, S_1, decays to form TT, and TT breaks into two free triplets, T_1. The role played by morphology or the local geometry of molecules in triplet generation via SF is vital, as the process depends on the placement of adjacent molecular pairs. Morphology, determined by molecular structure as well as sample preparation methods, is thus linked directly to the efficiency of SF. We first demonstrate this in a model system: endothermic SF nanoparticles. Further, we engineer these nanoparticles to suit triplet transfer into inorganics for PV applications. The effect of molecular and crystal structures on SF dynamics is further explored in a new class of photo-stable molecules, thienoanthracenes. We investigate the endothermicity of thienoanthracenes by assessing their singlet and triplet energies. Thereafter, we delve into thermodynamic and kinetic parameters that determine efficient SF in thienoanthracenes. We choose one of the thienoanthracenes as a model system to understand what drives endothermic SF efficiently in it. An entropy based model with a statistical mechanics perspective is built to predict key factors that help assess the thermodynamic feasibility of SF in endothermic systems.

Contents

List of Figures

List of Tables

Nomenclature

AO Atomic Orbitals

CCD Charge Coupled Device

CMC Critical Micellar Concentration

CT Charge Transfer

DAS Decay Associated Spectra

DET Dexter Energy Transfer

E Internal Energy

ESR Electron Spin Resonance

FCW DOS Frank-Condon Weighted Density of States

FRET Forster Resonance Energy Transfer

FROG Frequency Resolved Optical Grating

FT Fourier Transform

FWHM Full Width at Half Maximum

G Gibb's Free Energy

GA Genetic Algorithm

GSB Ground State Bleach

HOMO Highest Occupied Molecular Orbital

IC Internal Conversion

ISC Inter-System Crossing

LUMO Lowest Unoccupied Molecular Orbital

MO Molecular Orbitals

NMR Nuclear Magnetic Resonance

NPs Nanoparticles

OA Oleic Acid

OPV Organic Photo Voltaic

PbS QDs Lead Sulphide Quantum Dots

Pc Pentacene

PCE Power Conversion Efficiency

PdPc Palladium(II) octabutoxy-phthalocyanine

PdTPTBP Pd(II) meso-Tetraphenyl Tetrabenzoporphyrin

PES Potential Energy Surface

PIA Photo-Induced Absorption

PL Photoluminescence used synonymously to Emission

PLQE Photoluminescence Quantum Efficiency

S Entropy

S-Q Limit Shockley-Queisser Limit

SAED Selected Area Electron Diffraction

SDS Sodium Dodecyl Sulphate

SE Stimulated Emission

SF Singlet Exciton Fission

SVD Singular Value Decomposition

T Temperature

TA Thienoanthracene, synonymous to Anthrathiophene

Tc Tetracene

TCSPC Time Correlated Single Photon Counting

TEM Transmission Electron Microscopy

TIBS-FTA 5,10-bis(triisobutylsilylethynyl) 2-fluoro anthrathiophene

TIBS-TA 5,10-bis(triisobutylsilylethynyl) anthrathiophene

TIPS-FTA 5,10-bis(triisopropylsilylethynyl) 2-fluoro anthrathiophene

TIPS-TA 5,10-bis(triisopropylsilylethynyl) anthrathiophene

TIPS-Tc 5,12- bis(triisopropylsilylethynyl)tetracene

TRES Time-Resolved Emission Scan

$(TT)^1$ or TT Correlated Intermediate Triplet-Pair State

XRD X-Ray Diffraction

Z Atomic Number

Chapter 1

Introduction

The seemingly simple elements, carbon, hydrogen and oxygen, through a vast number of combinations in liaison with others, bring colour to the physical world. The beauty of Chemistry of organic molecules lies in the extension of molecular structures to their photophysics, altering their optical characteristics. The tuneable optical nature of these molecules can thus be applied to a plethora of real-life problems involved in drug-discovery, biomedical and chemical imaging, energy applications and so on.

In this era of increasing energy demand, the role of organic molecules to aid harvesting solar energy, which is abundant in our world, is colossal. Various avenues of solar energy research have been explored for many years now, with joint efforts from organic chemists and physicists to improve the fundamental understanding of photophysical processes in organic molecules. This interdisciplinary field of research, termed *Optoelectronics of Organics* has shed much light on quantum mechanical processes that harvest and harness light. The field of organic photovoltaics (OPVs) that work on these principles that provide low-cost, large-scale fabrication of solar cells, has seen an impressive increases in efficiencies and fabrication techniques, in the last two decades. Following this, many countries in the first and developing world have adapted to the use of solar power. The deployment of solar cells on a larger, tangible-by-the-commoner-scale calls for technology with high efficiency in converting solar energy to electric current, or the power conversion efficiency (PCE) of a solar cell. Realising inherent limitations of single-junction solar cells, a part of OPV-research has been streamlined into harnessing solar power via a class of organic materials known to

exhibit a process known as Singlet Fission. The process of singlet fission (SF) helps in overcoming certain limitations to conventional single-junction solar cells and can boost PCE by 30% when incorporated with appropriate PV-architecture. Although discovered in the 1960s, the mechanism and drive for SF remain a mystery.

The central theme of this dissertation is to explore the mechanism of endothermic SF in acene molecules. We unearth an interesting phenomenon of photo-engineering the fate of excited-states involved in SF in TIPS-Tc nanoparticles, in chapter 4. The influence of polymorphism in endothermic SF of TIPS-Tc nanoparticles is explored in chapter 5. Here we tune the morphology of TIPS-Tc nanoparticles by encapsulating them in micellar structures and observe substantial changes in SF dynamics. Further, we try to incorporate SF-nanoparticles with energy transfer to an inorganic system, PbS quantum dots, with suitable energetics. While both these chapters expand on the nature/dynamics of SF in a previously well-studied system (TIPS-Tc), we introduce a new class of endothermic SF materials known as thienoanthracenes in chapter 6. In this chapter we study four thienoanthracenes with varying endothermicities and crystal structures. We try to correlate the energetic and structural parameters of these thienoanthracenes with their SF dynamics. Chapter 7 details our investigation on what drives SF in endothermic systems, where SF is enthalpically uphill. We probe into the temperature-activated mechanism of triplet formation in a thienoanthracene model system in this chapter. We introduce a model based on entropy-driven endothermic SF facilitated by triplet diffusion, bringing crucial insights into molecular design for SF.

Chapter 2

Background and Theory

This chapter includes a brief survey of several theoretical and contextual concepts used in this dissertation. We predominantly deal with the concept of endothermic singlet fission and present fundamental perceptions that lie in the backdrop of photophysical processes in related organic materials. Principles behind photophysical and other measurements performed in this thesis including spin-sensitive techniques (ESR, NMR) are discussed in the experimental section briefly. Theoretical concepts pertaining to specific parts of this thesis are included within respective chapters (surface modification, polymorphism, thermodynamics of singlet fission etc) for better reading.

2.1 Electronic States of Organic Molecules

Organic molecules are a class of molecules based on carbon, hydrogen and oxygen. Not only do organic molecules make up a vast majority of the living world, they are also responsible for giving colour to much of the physical world. Electronic transitions in organic molecules occur such that they absorb and/or emit near the visible part of the electromagnetic spectrum[1]. These transitions are linked to the presence of electronic states composed of what are known as molecular orbitals (MOs)[2], which extend spatially over chemical bonds in a molecule. MOs are in turn composed of the atomic orbitals (AOs) that define the electronic configuration of an atom. For example, in its ground state, carbon has six electrons in the configuration $1s^2\ 2s^2\ 2p^2$, with the 2p orbitals having a degeneracy of three: $2p_x$, $2p_y$ and $2p_z$. With four electrons in the outermost 2s and 2p AOs, carbon has a valency of four, thus capable of making four covalent bonds. In organic molecules, carbon atoms are connected to other atoms such as hydrogen or oxygen by 'mixing' of these AOs. This 'mixing' or *hybridisation* is the process of generating MOs from AOs. The nature of the covalent bonds in organic molecules thus depends on these hybridised orbitals, typically, sp^3, sp^2 and sp.

2.1.1 Molecular Orbitals

When all four of the 2s, $2p_x$, $2p_y$ and $2p_z$ are degenerately involved, four sp^3 hybridised orbitals, otherwise known as σ-orbitals, are formed. The four equivalent orbitals of carbon form a tetrahedron as shown in methane, Figure 2.1. Another example for sp^3 hybridised MOs is ethane, where four sp^3 AOs of carbon bond with sp^1 AOs of four hydrogens. In another common configuration, the 2s and two of the 2p orbitals of carbon hybridise to form sp^2 orbitals. This results in three σ-orbitals oriented on the same plane, with $2p_z$ lying perpendicular to this plane, unoccupied. When two such carbons in an sp^2 hybridised state interact, the out of plane $2p_z$ orbitals form what is known as a π-orbital. Thus, in ethene, two carbons share one σ and π bond (hybridised orbitals and bonds are synonymous) each, and one σ-bond each with two hydrogens, shown in Figure

2.2. A triple bond is formed as a result of sp orbitals formed with one each of the 2s and 2p orbitals, like in ethyne where two carbons share two π-bonds and one σ-bond, and one σ-bond with one hydrogen, each.

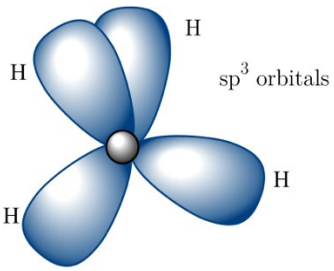

Figure 2.1- sp^3 hybridisation in methane (CH_4), with a bond angle of 109.5° between the degenerate orbitals. 2p orbitals from carbon and 1s orbital from hydrogen hybridise to from the sp^3 orbitals in methane i.e. four σ-bonds.

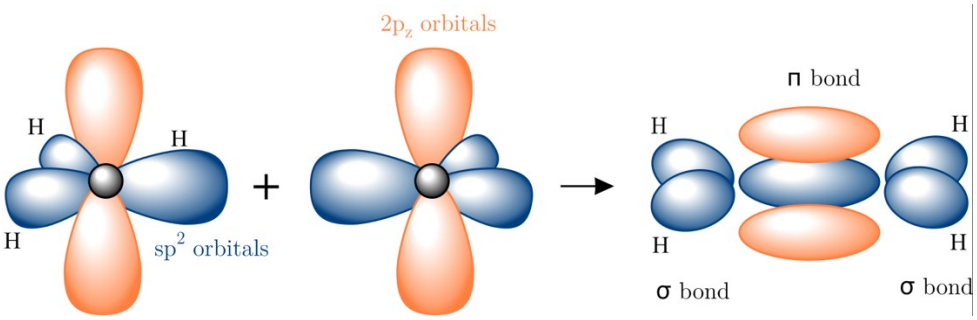

Figure 2.2- Bonding in ethene with sp^2 hybridised orbitals. The three sp^2 AOs of carbon are 120^0 with respect to each other and lie on the molecular plane (blue). The unoccupied $2p_z$ orbital (orange) lies perpendicular to the molecular plane, forming π-bond in ethene that helps in electron delocalization.

Electrons in σ-bonds are tightly bound and thus lack reactivity in optical processes. However π-bonds consist of weakly bound electrons and their orbitals lie perpendicular to the molecular plane. Thus, π-bonds are crucial for electron conjugation in organic molecules. Conjugation describes the nature of electron delocalisation over π-bonds in a molecule. In conjugated molecules, π-electrons are extensively delocalised which makes them associated lesser with individual

atoms, but more with the molecule as a whole. According to *Hückel theory*, MOs are formed as a linear combination of AOs (LCAO) given by[3],

$$\Psi_{\pm} = c_1\phi_1 \pm c_2\phi_2 \qquad 2.1$$

where $\Psi_{\pm}$ is the bonding or anti-bonding MO and ϕ_i is the AO. Thus, an MO can be observed as the result of two electron wavefunctions interfering constructively (bonding MO, Ψ_+ or Ψ) or destructively (anti-bonding MO, Ψ_- or Ψ^*). The energy levels associated with these superpositions are different from individual AOs, with the energy of Ψ_+ lower compared to Ψ_- due to enhanced stability of the former. The energies, which are generally also the second spatial derivative of the wavefunction, can be calculated from the Schrödinger equation with the Hamiltonian operator being the sum of potential and kinetic energies.

Figure 2.3 shows the nature of MOs present in benzene. The ground state of benzene consists of three bonding π-orbitals that are fully occupied, and an unoccupied anti-bonding π^*-orbital. This is because each $2p_z$ orbital has a potential occupancy of two (two spin degrees of freedom)[2], but each carbon contributes only a single electron to π-bonding. The highest occupied MO (HOMO) and the lowest unoccupied MO (LUMO) are of particular interest here. The switch of a single electron from HOMO to LUMO in organic molecules constitutes the lowest energy optical transition (optical gap) via absorption of photons. Although this destabilizes the molecule, it does not generally lead to disintegration as the equivalent photon energy does not overcome the total bonding energy of the remaining bonds. Occupation of HOMO and LUMO levels or electronic states, can also occur via processes such as thermalization.

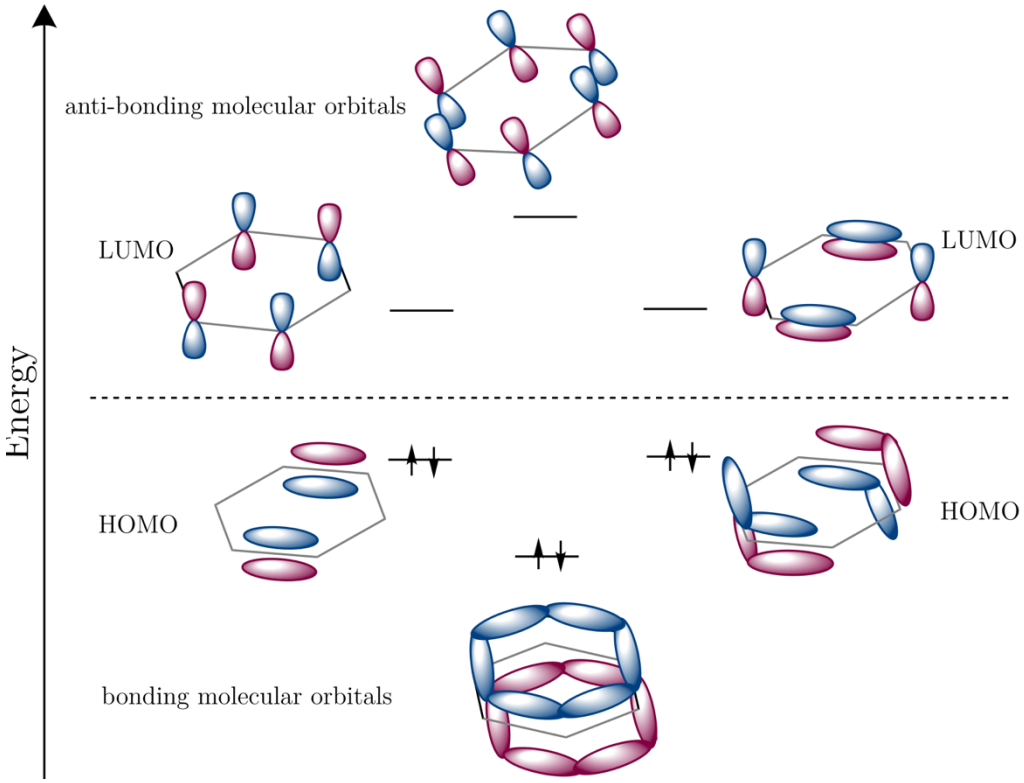

Figure 2.3- Schematic diagram of MOs in benzene. Bonding MOs are more stabilized than anti-bonding MOs in energy due to differences in their electronic configurations.

2.1.2 The Exciton

We have so far discussed the construct of HOMO-LUMO in organic molecules, within the premise of a one-body system. Introduction of orbitals and states prove to be simpler with this approach. However in reality, physical processes often deal with many-body systems and is not different for photophysical processes. In this section we introduce the more complex, yet more accurate nature of excited states and their photophysics in organic semiconductors.

Upon photoexcitation at the optical gap in an organic molecule, an electron is transferred to the LUMO, leaving a hole behind in the HOMO. These charge carriers of opposite polarities within MOs that are spatially correlated share some Coulombic attraction, resulting in the formation of an electron-hole pair. This

two-body system, or the exciton, is an electrically neutral quasi-particle first coined by Frenkel[4], to explain the transfer of energy in emissive molecules without the flow of charges[5].

Excitons in organic molecules are generalised as Frenkel excitons due to their low dielectric constants and tight localisation[6,7]. Thus, Frenkel excitons in organic molecules are not easily dissociated by external perturbations at room temperature[8]. In inorganic molecules due to their high dielectric constants, excitons are highly delocalised, known as *Mott-Wannier excitons*[9]. This makes them indistinguishable from free charges at room temperatures and are effectively delocalised spatially well above their crystal lattice parameters.

2.1.2.1 Singlet and Triplet Excitons

Molecular orbitals are represented uniquely by their corresponding electronic configurations with four electronic quantum numbers[3]:

(i) Principal quantum number (n), describes the principal electron shell
(ii) Angular momentum quantum number (l), defines the shape or angular distribution of the orbital (s,p,d,f)
(iii) Magnetic quantum number (m_l), describes the subshell
(iv) Spin quantum number (m_s), describes the spin-state of the electron

Pauli's exclusion principle states that no two electrons can exist in an atom or a molecule with same four quantum numbers. Thus, an orbital can hold two electrons with the same n,l,m_l quantum numbers ($1s^2$ has $n=1$, $l=0$, $m_l=0$) but the m_s quantum number must be unique to each of these two electrons with opposite spin, $m_s=\pm 1/2$. Quasi-particles such as electrons and excitons can be thus divided based on their spin configurations into singlets with 2 possible spins and a spin multiplicity of 0 ($m_s=\pm 1/2$), triplets with 3 possible spins and a spin multiplicity of 1 ($m_s=\pm 1,0$) etc, where spin multiplicity is given by $2S+1$ and $S=\Sigma m_s$. In an exciton, the spins of the electrons in HOMO and LUMO can be in a parallel (triplet) or an anti-parallel (singlet) configurations.

Photoexcitation leads to the formation of the anti-parallel singlet denoted by S_n, configuration and formation of a triplet state would require a spin-flip to form the parallel spin configuration. The Coulombic coupling between the two spin-1/2 electrons to form an exciton gives rise to four distinct spin configurations. Three among of these spin states have a total angular momentum of 1, thus are triplet excitons (T_1) and the remaining is a singlet (S_1). These spin states are labelled in the notation $|s\ m_s>$ where s is the eigenvalue of the total angular momentum operator acting on the state, and m_s is the spin quantum number, or the z-axis component of angular momentum.

$$\text{Triplets:} \begin{cases} |1\ 1> = |\uparrow_1 \uparrow_2> \\ |1\ 0> = \frac{1}{\sqrt{2}} \left(|\uparrow_1 \downarrow_2> + |\downarrow_1 \uparrow_2> \right) \\ |1\ -1> = |\downarrow_1 \downarrow_2> \end{cases}$$

$$\text{Singlet:} \quad |0\ 0> = \frac{1}{\sqrt{2}} \left(|\uparrow_1 \downarrow_2> - |\downarrow_1 \uparrow_2> \right)$$

While triplet spin states are symmetric in nature (rearrangement of particles/indices does not change the nature of the state), the singlet state is anti-symmetric, as seen above. The overall nature of the wavefunction of fermions is given by the product of their spatial and spin wavefunctions and will be asymmetric in nature. Thus, the spatial part of the singlet wavefunction will be symmetric and that of triplets will be anti-symmetric. The contribution of two indistinguishable fermions leads to the excitonic Hamiltonian,

$$K_{ij} = \iint \Psi_i^*(r_1)\, \Psi_j^*(r_2)\, V_{e\text{-}e}(r_1\text{-}r_2) \Psi_j(r_1) \Psi_i(r_2)\, dr_1\, dr_2 \qquad 2.2$$

where Ψ_i is the total wavefunction of the i^{th} electron, $V_{e\text{-}e}(r_1\text{-}r_2)$ is the electron-electron interaction. For fermions, K_{ij} is repulsive (positive) and correlates to the spatial overlap of HOMO and LUMO. Most of this repulsive interaction will be between charges residing on the same atomic site[10], as the probability distribution

is very high near atoms. The resulting diminished wavefunction amplitude on each atomic site decreases contributions from the large number of atomic sites around. Thus, the exchange energy does not scale strongly with the size of the delocalised π system[11]. The strength of the exchange energy instead depends critically on the spatial overlap of the HOMO and the LUMO on the same atom. As the exchange energy of the singlet is $-K$ and that of the triplet is $+K$, the energy splitting between the two is given by $\Delta 2K$. In conjugated molecules this effect is manifested as the lowering of triplet's electronic energy below that of the singlet by ~1-0.7 eV[11,12].

The spin-configuration of excited states thus play a pivotal role in the nature of excited states formed in conjugated organic molecules. When two electrons with all the same quantum numbers except for differing spin-configurations interact, their state energies vary to large extents.

2.1.2.2 Correlated TT States

Following the description of singlet and triplet excitons, we drive this section on excitons slightly towards a distinct state relevant to this dissertation on singlet fission, the correlated TT-pair state. Singlets and triplets are highly delocalised excitons while TT states are delocalized excitonic wavefunctions. Effectively, this is an excitonic state delocalised over two molecules that can carry two electrons each.

Let us take a closer look at the spin-configurations for the singlet and triplet states in a two molecular basis with molecules are A and B. The spin-basis we use now for better clarity is $|\alpha>$ for spin-up ($\uparrow$) and $|\beta>$ for spin-down ($\downarrow$) configurations.

The two spin-singlet solutions of the total spin angular momentum operator, $\hat{S}^2$, are thus given by,

$$|S_1^{(2)}> = \frac{1}{\sqrt{2}} (|\alpha\beta>_A - |\beta\alpha>_A) \frac{1}{\sqrt{2}} (|\alpha\beta>_B - |\beta\alpha>_B) \quad 2.3$$

$$|S_2^{(2)}> = -\frac{1}{\sqrt{2}}(|\alpha\alpha>_A|\beta\beta>_B+|\beta\beta>_A|\alpha\alpha>_B)+\frac{1}{2\sqrt{3}}(|\alpha\beta>_A+|\beta\alpha>_A)(|\alpha\beta>_B+|\beta\alpha>_B) \quad 2.4$$

where the superscript represents the number of electrons in the system.

While eq. 2.3 refers to two molecules both in singlet state, eq. 2.4 cannot be written as a product of singlets alone and thus is a superposition of triplet states. In the absence of a magnetic field the eigenstates that make up the zero-field Hamiltonian are,

$$|x> = \frac{1}{\sqrt{2}}(|\beta\beta> - |\alpha\alpha>)$$

$$|y> = \frac{i}{\sqrt{2}}(|\beta\beta> + |\alpha\alpha>)$$

$$|z> = \frac{1}{\sqrt{2}}(|\alpha\beta> + |\beta\alpha>) \quad 2.5$$

For four particle systems with two accessible spins each, there are 2^4 possible spin configurations in all: two spin-singlet states (*S=0*), nine spin-triplet states (*S=1*) and five spin-quintets (*S=2*)[13]. In this new basis of $|x>$,$|y>$ and $|z>$, the four-electron triplet-pair wavefunctions can be written as $|xx>$, $|xy>$, $|xz>$, $|yx>$, $|yy>$, $|yz>$, $|zx>$, $|zy>$ and $|zz>$, with $|xx>$, $|yy>$ and $|zz>$ showing singlet character[14]. Note that the solutions in eq. 2.5 are not the eigenstates of $\hat{S}^2$ and $|S_2^{(4)}>$ can be written as,

$$|S_2^{(4)}> = \frac{1}{\sqrt{3}}(|x>_A|x>_B + |y>_A|y>_B + |z>_A|z>_B) \quad 2.6$$

i.e. the second spin-singlet solution can be expressed as the superposition of the zero-field eigenstates. Thus, instead of being purely spin-singlet in nature, this state denoted by $(TT)^1$ is a superposition of the wavefunctions of the nine sub-levels originating from the interaction of two spin-triplet states with a singlet

spin[13,15]. $(TT)^1$ once formed can either decouple to form separated triplets or dissociate to form singlets. The spin nature of $(TT)^1$ is crucial during processes such as triplet annihilation to form a singlet, a transition occurs from $|S_2^{(4)}>$ to $|S_1^{(4)}>$, without necessitating a spin-flip.

2.2 Excited state Processes in Organic Molecules

The lion's share of this dissertation talks about optical processes and the nature of excited state transitions, whether radiative or non-radiative in nature. Thus, we briefly discuss the theoretical framework of what happens when organic molecules are photoexcited.

2.2.1 Optical Processes and Selection Rules

We have discussed the electronic origin of molecular orbitals and states in organic molecules thus far. Specifically, we have looked at criteria based on fundamental properties of fermions which will become relevant when discussing photophysics of excited states. In this section we focus on the origin of photophysical processes in organic molecules, in particular the absorption and emission of photons.

Probing molecules with light to extract information on their structural and dynamic properties, otherwise known as studying light-matter interactions, is the core of this dissertation. We begin from a fundamental quantum mechanical concept to understand such light-matter interactions, *Fermi's golden rule.* We then solve for transition rates from an initial state to a final continuum of states with first-order time-dependent perturbation theory[16]. In conceptual terms, the transitions rate is given by a transition probability which depends on the strength of coupling between the initial state, $|\Psi_i>$, and the final state, $|\Psi_f>$, also influenced by the final density of states. Note that the wavefunction depicted here is a product of electronic, vibrational and spin components[17].

$$\mathbf{\Psi} \text{ or } \Psi_{total} = \Psi_{el}\, \Psi_{vib}\, \Psi_{spin}$$

2.7

In the common treatment of this method[2,17–19], each energy level corresponding to the states under consideration is an eigenfunction of the unperturbed Hamiltonian, $\hat{H}_0$. The complete Hamiltonian is thus given by a sum of the unperturbed one and the time-dependent one,

$$\hat{H}(t) = \hat{H}_0 + \hat{H}_I(t)$$

2.8

The eigenfunctions of the complete Hamiltonian is therefore written as an expansion over the unperturbed states and the interaction Hamiltonian. For simple molecular systems, solving for the time-evolution for $\hat{H}(t)$ may be done with ease where changes caused by the perturbation are small.

Under the premise of first-order perturbation theory where only the first term is considered[17], transition rate from $|\Psi_i\rangle$ to $|\Psi_j\rangle$ can be written as,

$$k_{i\rightarrow f} = |M_{i\rightarrow f}|^2 \, \rho_f(E)$$

2.9

where $\rho_f(E)$ is the density of final states as a function of energy. $|M_{i\rightarrow f}|$ is the matrix element between $|\Psi_i\rangle$ and $|\Psi_j\rangle$ coupled by $\hat{H}_I(t)$ and given by,

$$|M_{i\rightarrow f}| = \langle\Psi_f| \, \hat{H}_I| \, \Psi_i\rangle$$

2.10

In the adiabatic limit the transition rate peaks at the degeneracy, $k_{i\rightarrow f} \propto \delta(E_f - E_i)$, as the strength of the perturbation grows slowly from zero at $t\rightarrow-\infty$ observing energy conservation[17,20]. In the case of a harmonic perturbation with frequency ω applied to the system adiabatically, the interaction Hamiltonian is given by,

$$\hat{H}_I(t) = \hat{H}_I(0) \, e^{\eta t} \cos(\omega t), \quad \eta \in \mathbb{R}^+$$

At timescales long after rapidly oscillating terms diminish, the transition rate becomes,

$$k_{i\rightarrow f} \propto |M_{i\rightarrow f}|^2 \left[\delta(E_f - E_i + \hbar\omega) + \delta(E_f - E_i - \hbar\omega) \right] \quad 2.11$$

From eq. 2.11 only two transitions are allowed, where the initial to final, or vice-versa, equals the photon energy, i.e. the processes of absorption and stimulated emission, respectively. While we began with the definition of transition probability based on the density of final states (eq. 2.9), at this point we see that effectively a selection of discrete states with the right energy is what these rates boil down to. The motivation behind considering a continuum of final states is to reflect the loss of quantum coherence that occurs in physical systems that have many weakly interacting states.

Now we get back to the matrix element in eq. 2.10, the spectroscopically most relevant quantity. If we assume that $\hat{H}(t)$ arises from the interaction between a molecule and a monochromatic plane wave with wavelength much larger than the dimensions of the oscillating electric dipole $|M_{i\rightarrow f}|$ becomes[17,19],

$$|M_{i\rightarrow f}| \propto |E_0| \; |\mu_{i\rightarrow f}| \equiv |E_0| \langle \Psi_f | \boldsymbol{\mu}.\boldsymbol{\epsilon} | \Psi_i \rangle \quad 2.12$$

where $\boldsymbol{\mu} = -e \sum_j \boldsymbol{r}_j$ is the dipole operator, e is the fundamental charge and $\boldsymbol{\epsilon}$ is a unit vector in the direction of polarization of the perturbing electric field. We notice two things: (i) transition rates are directly proportional to electric field strength, and (ii) both the matrix element and the rates are time-independent in the limit where the initial state population is negligibly depleted. Under these premises, the transition dipole moment thus only depends on molecular properties and characterizes the strength of the transition.

Numerical and theoretical evaluation of the above discussed parameters are possible with methods such as time-dependent density functional theory (TD-DFT) for many molecular systems. However due to the strongly electron-correlated nature of the excited states in acenes, similar calculations need not be accurate[21,22]. However, one can obtain qualitative insights by means of selection rules that govern transitions and vibronic coupling, by the following formulation.

2.2.2 The Electronic Factor: Symmetry

The matrix element $|M_{i\to f}|$ given by eq. 2.12, determines if the transition is dipole-allowed when non-zero, or otherwise, dipole-forbidden, as the dipole operator is anti-symmetric under spatial inversion (rotation about principal axis)[2,23]. The anti-symmetric nature of the operator implies that single photon transitions are only allowed between states of opposite symmetry. In point group notations, states are called *gerade* if symmetric with respect to spatial inversion, and *ungerade,* if anti-symmetric[23]. The ground state of the singlet exciton is of *gerade* nature. Hence, populating *ungerade* states from the ground state is possible only by single photon excitation, otherwise the integral in 2.12 vanishes.

When spectroscopically probing molecules in solution the orientation of molecular axes do not hold a fixed relation to the polarization of the incident electric field. Therefore, one needs to consider only inversion symmetry for transitions in such cases. However, molecular crystals may have a well-defined geometric relationship between the molecular axes and beam polarisation. Thus, one needs to be careful about counting in parity under reflection about the Cartesian axes while probing molecular crystals. In this case the transition dipole moment operator components in *x,y,z* components, can be written in the form $|\mu_{x\,i\to f}| \equiv |E_0|\langle\Psi_f|\boldsymbol{\mu}_x|\Psi_i\rangle$. The total $\boldsymbol{\mu}$ is given by its Cartesian components[21] as,

$$|\mu_{i\to f}|^2 = \sqrt{|\mu_{x\,i\to f}|^2 + |\mu_{y\,i\to f}|^2 + |\mu_{z\,i\to f}|^2} \qquad 2.13$$

The value of the integral $<\Psi_f|\ \boldsymbol{\mu}.\epsilon\ |\Psi_i>$ scales with the value of the transition dipole moment $\boldsymbol{\mu}$. Hence, the matrix element will be large if the orbitals involved are not only well-overlapped but also well-extended, as $\boldsymbol{\mu}$ acts along various axis depending on the molecular system. For instance, while the absorption-emission intensities for short conjugated molecules are well-known to increase with the oligomer length, in anthracene and longer acenes the lowest-lying singlet state is polarised along the short axis, rendering the transition intensities to decrease with oligomer length[24].

2.2.3 The Vibrational Factor: Phonon Coupling

Beginning from orbitals to states and finally symmetry considerations for excited state transitions, we have been exclusively discussing electronic factors. Let us recall that the total wavefunction is a product of electronic, vibrational and spin components[2] from eq. 2.7. While the electronic part decides the overall intensity of the transition, the product of the vibrational wavefunctions $<\Psi_{vib,f}|\Psi_{vib,i}>$ controls the spectral shape. Another factor that was taken for granted for the preceding discussion on the topic is the stationary nature of the states involved in optical processes generated by their Hamiltonian. In this section we discuss the nature of excited states in the context of coupling with vibrational modes.

Classically, the energy of a state depends on interactions between all degrees of freedom for each particle in the system. Extending this analogy to a molecule, the energy of any state depends on the degrees of freedom possessed by the electrons, nuclei etc that form the molecular structure. However, the *Born-Oppenheimer approximation* postulates that within the timescales of optical processes, nuclei (inherently heavier than electrons) are static relative to electronic motion.

Thus, $\hat{H}_0$ can be separated into the kinetic energy of the electrons (T_{el}), the potential energy experienced by the valence electrons due to screening of the nucleus's electric potential ($V_{el\text{-}nuc}$) and the potential energy due to inter-electron interactions ($V_{el\text{-}el}$) given by,

$$\hat{H}_0\,(R) = T_{el} + V_{el\text{-}nuc} + V_{el\text{-}el}$$

2.14

Solutions to this Hamiltonian are product states of an electronic state $|\phi>$ and a vibrational level $|\chi>$, giving $|\Psi>= |\phi>|\chi>$[18]. These are commonly expressed in what are known as *normal co-ordinates*, Q, where nuclear displacements are calculated relative to the ground state configuration[2]. Thus, each co-ordinate corresponds to a vibrational mode of the system. The centre of vibrational harmonic potential wells for a pair of initial and final states can differ as electronic states differ in equilibrium configurations. This results in a horizontal displacement of these potential wells along Q, shown in Figure 2.4.

Under the *Frank-Condon approximation*[17], the dipole operator acts only on the electric component of the wavefunction i.e. all optical transitions occur vertically with respect to Q. Modifying the matrix element within the premise of the *Born-Oppenheimer approximation* eq. 2.12 becomes,

$$|\mu_{i\rightarrow f}|= <\chi_f |<\phi_f| \boldsymbol{\mu}.\epsilon |\phi_i>| \chi_i>$$

2.15

With the *Frank-Condon approximation* this reduces to,

$$|\mu_{i\rightarrow f}|= |\mu_{i\rightarrow f}|^e <\chi_f \mid \chi_i>$$

2.16

where $|\mu_{i\rightarrow f}|^e$ is the electronic matrix element evaluated at Q between the two states with respect to the equilibrium position of the initial state. The inner product $<\chi_f|\chi_i>$ is the overlap integral between the vibrational wavefunctions, whose square gives the *Frank-Condon factor* for the transition. The *Frank-Condon factor* with eq. 2.9 gives the Frank-Condon Weighted Density of States (*FCW DOS*) which shall become significant when discussing intersystem crossing later (section 2.2.4).

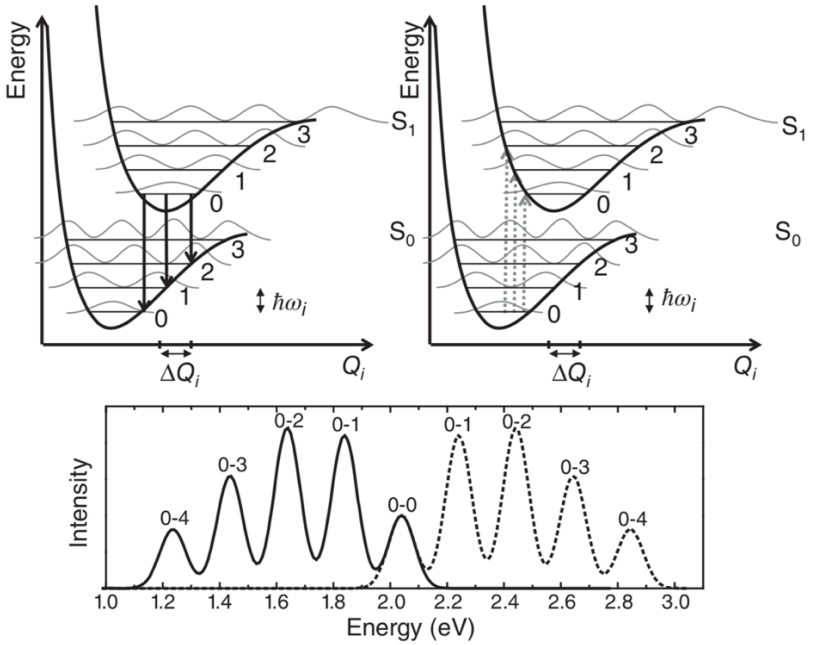

Figure 2.4- Schematic showing optical transitions between the ground and an excited state displaced by ΔQ along the normal co-ordinate. Solid lines show the transitions between the lowest vibrational level of the excited electronic state and the vibrational manifold of the ground electronic state, giving the emission spectrum. Dotted lines show the transitions between the lowest vibrational levels of the ground electronic state to the excited state vibrational manifold, giving the absorption spectrum. The relative intensities of the peaks in these spectra are given by the transition dipole moment of the respective transition as well as the strength of coupling between the electronic and vibrational levels. Figure from Anna Köhler and Heinz Bässler,'Electronic Processes in Organic Semiconductors', p 42, 2015, Copyright Wiley-VCH Verlag GmbH & Co. KGaA. Reproduced with permission.

In radiative transitions, the dependence of the transition rate on the overlap integral suggests that electronic excitation can preferentially couple to higher lying vibrational states with the largest wavefunction overlap[19]. Figure 2.4 also illustrates how vibrational transitions contribute to the absorption (dotted) and emission (solid) spectra in a system. While electronic transitions dictate the overall energy and shape of the spectra, the finer structure is determined by the transition probability between different vibrational levels[25]. The dotted arrows show the transitions from the electronic ground state to the vibrational levels of the electronic excited state (*0 to n*), emerging from the lowest vibrational level of

the ground state (*0*). The relative strengths of these transitions emerge from the electron-phonon coupling strength characterized by the *Huang-Rhys parameter,* denoted as ***S***. Experimentally speaking, ***S*** determines the peak intensity ratio between the 0-1 and 0-0 peaks in the absorption spectrum of a molecule. The transition dipole moment for a given transition is reflected in the intensity of the resulting vibrational bands in the absorption spectrum shown in the lower panel. The labels 0-n suggests the starting ground state vibrational level and the ending excited state vibrational level. In the case shown in Figure 2.4, 0-2 transition is the strongest. The emission spectrum is usually the mirror image of the absorption spectrum as the lowest vibrational level of the excited state couples to the vibrational manifold of the electronic ground state. The absorption and emission spectra are displaced by an energy difference known as the *Stokes shift*[26].

The effect of intermolecular coupling on the relative strength of the vibrational features is an important extension of this theory, performed by *Spano et. al*[27]. The intensity ratios between 0-0 and 0-1 peaks can change considerably upon changes in the local environment of the molecules due to processes such as aggregation[19]. An examples of this is when molecules are arranged in a fashion such that the excitation delocalizes over certain crystalline phases[28,29], preferentially. In such cases changes in the spectral shape can be attributed quite closely to the strength of intermolecular coupling.

2.2.4 The Spin-Factor: Intersystem Crossing

The spin of an exciton such as singlet or triplet, is crucial to the nature of the optical transitions it can undergo, as discussed before. The ground state of a molecule has singlet character. Conservation of total angular momentum suggests that the decay of triplet excitons to the ground state is quantum mechanically forbidden[7]. Therefore, the radiative decay of triplet excitons occurs only through the 'mixing' of singlet and triplet states. Spin-orbit coupling is such an interaction where the change in angular momentum due to spin is balanced by a change in the orbital angular momentum, thus partially relaxing the spin-rule. This results

in an emission termed as *phosphorescence*[11] that typically occurs at very long (µs-ms) timescales.

Spin-orbit coupling usually scales to the fourth power of the atomic number (Z) and thus is weak in organic molecules that do not contain heavy atoms[30]. In these organic molecules, spin-orbit coupling can be enhanced, however slightly, by mechanisms involving phonon-mediated symmetry breaking in planar molecules[31] or the presence of lone pairs[32]. Phosphorescence or the transition between T_1 to S_0 results in very long lifetimes for triplet excitons (< 1s), as compared to singlets (< 10 ns). Triplet states in organic molecules are not photogenerated in significant quantities as their absorption cross-sections are considerably lower than that of the singlet. Therefore, triplet states are populated by transitions between the singlet and triplet excitation manifolds, referred to as intersystem crossing (ISC). In the presence of spin-orbit coupling and formalism developed by *Beljonne et al.*[30], the ISC rate is given by,

$$k_{ISC} = \frac{2\pi}{\hbar} |<{}^1\Psi^0|\hat{H}_{spin\text{-}orbit}|{}^3\Psi^0>|^2 \left[FCW\ DOS\right] \qquad 2.17$$

where $|{}^1\Psi^0>$ and $|{}^3\Psi^0>$ are the unperturbed singlet and triplet states, respectively, and *FCW DOS* is the Frank-Condon weighted density of states[20] (see section 2.2.3).

We see that k_{ISC} is directly influenced by the vibrational and energy overlap between the singlet and triplet states. Relaxed singlet and triplet states are substantially different in terms of their energies due to exchange interactions. Thus, instead of the weak, direct conversion between the relaxed singlet (S_1) and the lowest lying triplet (T_1), ISC will be more efficient via two steps: (i) ISC to a higher-lying triplet state degenerate with S_1 and (ii) subsequent thermal relaxation to the lowest-lying T_1 state[7]. For molecules with negligible energy splitting between S_1 and T_1 such as C_{60}, and those with heavy atoms, ISC is expected to be rapid and efficient[33–35]. Such molecules are often used as sensitizers for detecting triplet energies of organic molecules, as described in the experimental

section, chapter 3. We discuss the high triplet yields of acenes such as pentacene and tetracene when isolated, due to rapid ISC, compared with the inefficiently competing radiative decay channels.

2.2.5 Internal Conversion

Radiationless decay of excited electronic states within the spin-manifold is termed as internal conversion. They are also known as multiphonon decay as these transitions involve dissipation of energy in the form of molecular vibrations[7]. In this process, a vibrationally-relaxed and electronically-excited state is converted into vibrationally-relaxed lower-lying electronic state. The process begins with the adiabatic transition from the initial electronic state to a vibrationally-excited level of the lower-lying electronic state. This is followed by rapid vibrational relaxation (~100 fs)[36,37] to the lowest-lying vibrational level along the manifold of high-energy modes via sequential emission of multiple phonons[7]. The rate of adiabatic transition[3,38,39] when vibrational coupling is weak, is given by,

$$k_{IC} \propto e^{\frac{-\gamma \Delta E}{\hbar \omega}} \tag{2.18}$$

where γ depends on molecular parameters, ΔE the energy difference between the initial and final states, and ω gives the highest-energy of the phonon coupled to π-conjugated orbitals or the electronic transitions[7]. Contributions from low-energy phonons are usually neglected as they are very low[40].

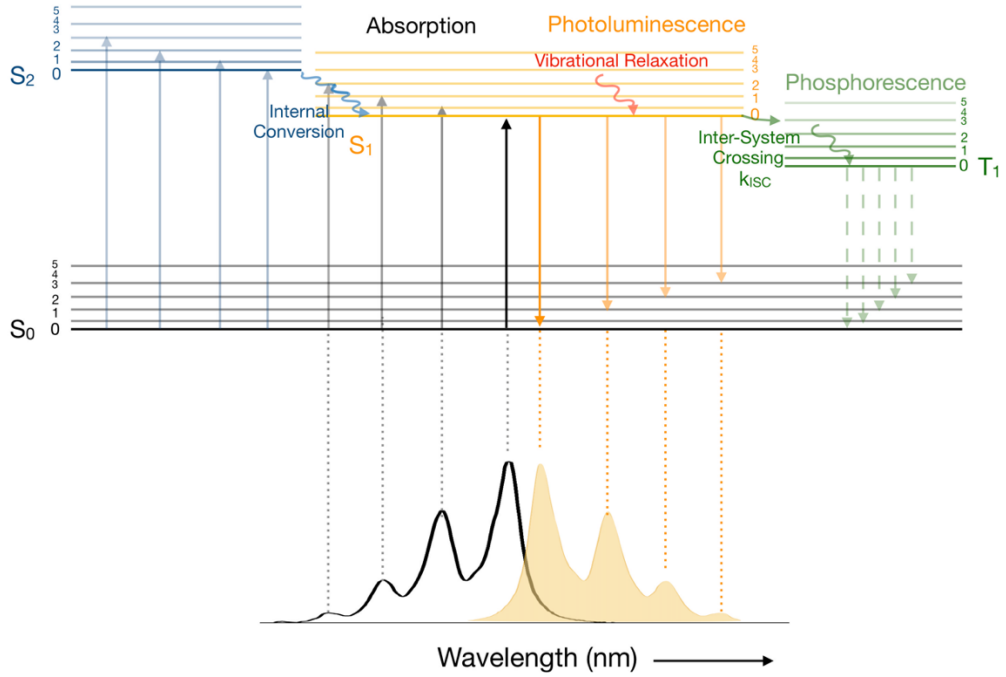

Figure 2.5- Excited states and transitions in an organic molecule. Absorption of photons occurs from the vibrational and electronic ground state S_0, to the vibronic singlet manifold S_1-S_n. Processes such as absorption (black), photoluminescence (orange) or emission, and non-spin-allowed phosphorescence (green) that occur via weak spin-orbit coupling are shown. The processes assisting them, intersystem crossing and internal conversion are also depicted.

In organic molecules, internal conversion happens rapidly[36,37] from higher excited states down to the lowest-lying excited state of the same spin multiplicity. This is rather fast compared to the rate of radiative decay in most systems[2]. Thus, the majority of emission from these materials will be generally observed from the lowest-lying excited singlet state[40] as shown in Figure 2.5. This is otherwise known as *Kasha's rule*[2].

In triplets, the adiabatic transition which is non-radiative in nature, is an example of intersystem crossing. Thus, the rate of this transition in triplets is slower compared to that in singlets, due to weak spin-orbit coupling in organic molecules[7]. Therefore, the triplet-specific internal conversion is a significant decay channel for them due to (i) the lack of a strong radiative channel in similar timescales to outcompete it and (ii) the reduced energy gap between T_1 and S_0[7].

Due to the nature of many closely-spaced electronic and vibrational excited states in conjugated organic molecules and the processes happening at varied timescales, excited state mixing occurs rather commonly in such systems. The nature of mixing of states and timescales heavily impact the fate of excited states rendering effects such as previously non-radiative states evolve to more radiative nature. This is discussed in detail in Chapter 4.

2.3 Energy Transfer in Organic Molecules

Excitons undergo coherent transport in a perfectly ordered crystal system where the neighbouring sites are almost degenerate. However, the lack of perfectly aligned crystal formations in amorphous or polycrystalline films of organic semiconductors lead to higher energetic disorder, breaking the exciton band. In such cases, excitons are relatively localised by interactions with phonon modes in the material, and move incoherently. There are two mechanisms that describe incoherent excitonic transport modelled as hopping between molecules, namely, *Förster resonance energy transfer*[41] (*FRET*) and *Dexter energy transfer*[42].

FRET is a radiationless transfer of excitation energies between states on two different molecules that are coupled by a dipole-dipole interaction, via virtual photons[3,43]. In the limit of the point dipole-dipole approximation, the spatial extent between the two wavefunctions is small relative to the hopping distance. The rate of *FRET*[44] is directly proportional to the dipole moments of the donor and acceptor and inversely to the distance between them (R) given by,

$$k_{FRET} \propto \frac{\mu_A^2 \mu_D^2}{R^6} J \qquad 2.19$$

where μ_A and μ_D are the dipole moments of the acceptor and donor, respectively, and J is the overlapping integral between donor emission and acceptor absorption spectra. Thus, through molecular design or selection of chromophores, rates of *FRET* can be tuned.

Note that k_{FRET} depends on the oscillator strengths of the donor and acceptor transitions through J. This implies that triplets that have no appreciable oscillator strengths, in the absence of large spin-orbit coupling, cannot undergo *FRET* efficiently[7]. Triplets undergo energy transfer predominantly by *Dexter transfer* which acts at distances much shorter than *FRET*[45]. This can be considered as a correlated electron transfer that does not require a spin-flip. The rate of *Dexter transfer*[42] is given by,

$$k_{DET} \propto e^{-2R/L} J \qquad 2.20$$

where L is the average radial extent of the donor-acceptor states.

Dexter transfer is thus heavily dependent orbital overlap of the wavefunctions involved, limiting distances below 1nm for efficient transfer. While *Dexter transfer* proceeds slower than *FRET*, the mean diffusion lengths ($l = \sqrt{D\tau}$) of triplet excitons can be much larger than that of singlets due to the former's longer lifetimes. These different modes of transport for singlet and triplet excitons in organic molecules are quite significant in the context of this dissertation as they have a significant role in the photophysical processes we study.

2.4 Singlet Exciton Fission

Singlet exciton fission or singlet fission (SF), in conjugated organic molecules, refers to the process of generating two triplet excitons from a single photoexcited singlet exciton[10]. The notion of simultaneous generation of non- ISC triplets was first proposed by *Dexter*[46] and then *Singh et al.* [47], in an attempt to explain the unusual temperature dependence of delayed fluorescence from anthracene crystals. Following these efforts, many experimental results supporting triplet generation by SF in crystals of anthracene[15,48–51], tetracene[22,52–60] and pentacene[61–67] were revealed since the 1960s. A crucial work by Merrifield and co-workers[60], among a few others[49,56,68,69], revealed the modulation of prompt and delayed fluorescence in tetracene by the application of an external magnetic field. This has been since established as a standard test for the occurrence of SF in organics and led to much theoretical understanding of the process[47,70]. In this section we focus on two aspects of SF: (i) photovoltaic applications of SF and (ii) the mechanism of SF.

2.4.1 Photovoltaic Applications

Although SF was chased from a mechanistic point of view as a fundamental physical process since the 1960s, it was not until 2006 that it was proposed to be used to improve the efficiency of single-junction solar cells by *Hannah and Nozik*[71]. They postulated that power conversion efficiencies (PCE) of single-junction solar cells can be improved by SF, through reduction in the loss of energy via *thermalization*. The theoretical efficiency of a single-junction solar cells is limited to ~33% due to the loss of excess energy from photons with energy above the bandgap of the active material. Photons with energy lower than this bandgap are not absorbed by the cell while excess energy by the absorption of blue photons is released as heat, accounting for a major loss channel in the cell, otherwise known as *thermalization losses*. The solar irradiance spectrum is shown in Figure 2.6. The unabsorbed low-energy part is shown as orange and thermalization losses are shown by the blue highlighted region, leaving behind 33% as the maximum limit

to the PCE of a single-junction solar cell, after extraction losses[72]. This is otherwise known as the *Shockley-Quisser limit*[73]. SF offers a way to beat this limit by harvesting some of the energy lost due to thermalization. SF materials absorb high-energy photons and down-convert them into two lower energy triplets, which can then be absorbed by the inorganic active material such as Silicon[74]. This was the concept introduced by *Hannah and Nozik* leading to a theoretical 200% yield from singlet excitons from the organic to the inorganic. An improvement in PCE up to 30% is expected in solar cells that contain SF materials with triplet energies close to the Si bandgap[74,75]. Significant efforts on material and architectural designs for efficient SF-based solar cells have been made since the proposal of this idea[76–81]. A recent, noteworthy work on a tetracene-Si PV device reports[82] 133% energy transfer between them, facilitated by SF in tetracene. The most promising SF candidates are those with triplet energy close to the bandgap of Si, high photostability and efficient triplet formation[1,10,75,83].

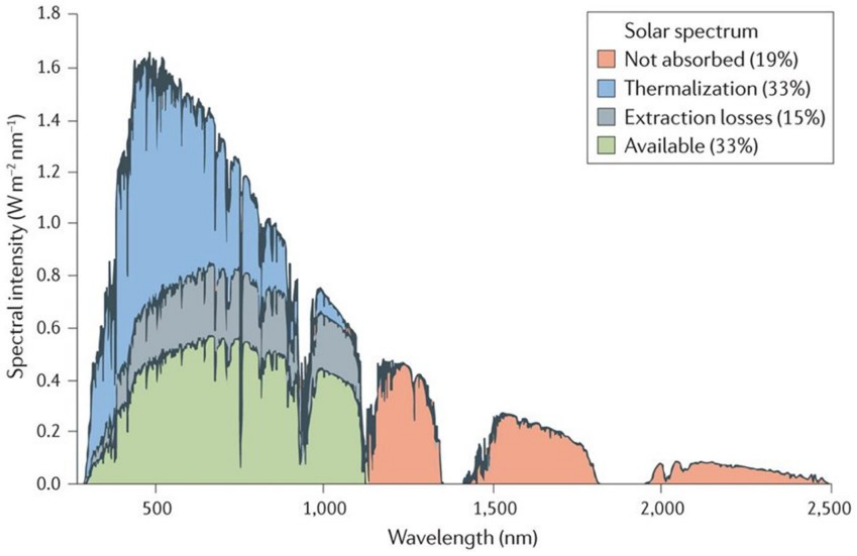

Figure 2.6- Solar irradiance spectrum and important processes to consider while energy harvesting. Figure used with permission from Springer Nature Publishing[75].

Successful harnessing of solar energy to boost PCE of solar PV devices by SF is followed by triplet transfer to inorganic materials with suitable bandgaps. We discuss triplet transfer to inorganics in detail, in Chapter 5. We explore an energetic design of a SF material and couple it with inorganic quantum dots of

suitable triplet energy to investigate transfer mechanisms. This design has been inspired by recent works of triplet energy transfer such as between PbS nanocrystals and tetracene, and PbSe nanocrystals and pentacene and PbS nanocrystals with a tetracene-derivative linked by a SF-linker molecule.

2.4.2 The Mechanism of Singlet Fission

Considerable theoretical and experimental results from as early as the 1960s draw a clear distinction between SF and ISC. When rapid triplet formation via SF and a complementary fast triplet-triplet annihilation for singlet generation were revealed, the notion that SF is not spin-forbidden emerged. Conservation of angular momentum is satisfied by the overall spin-conserved nature of triple-pair generation from a singlet, in SF. Moreover, the triplet-pair state $(TT)^1$ is created as a coupled state with singlet character, and given by,

$$S_n + S_0 \rightleftarrows (TT)^1 \rightleftarrows T_1 + T_1 \qquad 2.21$$

where S_n is the n^{th} excited state singlet, S_0 is the ground state singlet, $(TT)^1$ is the singlet-coupled correlated triplet-pair state and T_1 is the triplet in the lowest-lying excited state. The initial spin-conserving transition from a monomolecular S_1 to the bimolecular $(TT)^1$ can be very rapid. In exothermic systems this occurs within 100fs [ref] and recent works [ref] suggest that that it can be equally rapid in endothermic systems, such as those studied in this thesis. This is found to be dependent on factors such as vibrational coherence of the $(TT)^1$ state, coupling with S_1 etc. The subsequent process of free triplet formation from decoupling of the $(TT)^1$ state is slower, and its duration depends on the energetic nature of SF molecules.

Generally, there are two models for the mechanism of SF: the *direct* and the *indirect method*, differing by the nature of the intermediate state's contribution to the SF rate. The *direct method*[84] proposes that SF occurs in a single step, where the process relies on the coupling between two molecules determined by

their orbital's spatial overlap. Some theoretical work[85] proposes the idea of a dark, multiexcitonic state that mediates the conversion of S_1 to $2T_1$ in the *direct method*. The dark multiexcitonic state has been proposed to form via a conical intersection, which is a non-adiabatic coupling region where excited states can be converted into lower-energy states on vibrational timescales[86,87]. The *indirect or mediated method* of SF proposes that it occurs via an intermediate with CT character. This two-step process of SF involves electron transfer twice, distinctly. *Greyson et al.*[88] propose this model and claim that SF in certain molecules occur when the S_0, TT and CT states lie close in energy such that the system can reach low-lying CT states efficiently[89]. Some other studies compare T_1 yield by SF, via *direct* and *indirect methods*. They conclude that SF occurs by the *direct method* due to better T_1 yield and not via the *indirect method* as the energetic cost of a higher-lying CT state is detrimental to T_1 formation[90,91].

Recent studies on acenes however suggest that SF is a direct and virtually mediated process[66,92–94]. Computational methods used in these studies determine the coupling between the singlet and TT states, including CT mixing. The results paved way to the emergence of a general model for SF in acenes, with the coupling constants central to the occurrence of SF. Molecules such as tetracene and pentacene that exhibit efficient SF are in the regime of high coupling constants where SF occurs adiabatically with the rate controlled by nuclear motion. Although this model[66] is limited by the need of a temperature-dependent term to fit experimental SF rates to those calculated from the coupling constants, it still provides considerable insight into the mechanism of SF.

2.4.3 Criteria for Single Fission

Acenes such as pentacene (Pc) and tetracene (Tc) have been the canonical systems to study SF for many years now. The energetic criterion for SF is given by[75,83],

$$\Delta E \text{ or } E_{STT} = E_{S_1} - 2E_{T_1} \sim 0 \qquad 2.22$$

where E denotes the enthalpy or internal energy of the state and E_{STT} is the endothermicity of the system. Based on the energies of the singlets and triplets, SF materials can be classified into three: (i) endothermic when $E_{STT} < 0$, (ii) isoenergic when $E_{STT} = 0$ and (iii) exothermic when $E_{STT} > 0$. Pc is an exothermic SF system, while Tc is endothermic by 180 meV. Historically, SF was thought to be rapid and highly efficient in exothermic systems as the enthalpy of the final triplet state is lower than that of the singlet, and slower in endothermic systems as the enthalpy scale is reversed and therefore uphill in the latter[10]. However this notion has been challenged recently[95], driving more scrutiny of the energetic criterion in the SF mechanism. Energy conservation cannot be fiddled with, and therefore the deficit in enthalpies must be made up by other factors in endothermic systems. The most important aspect for a thermodynamically feasible process is the negative overall change in Gibb's free energy,

$$\Delta G_{i \rightarrow f} = \Delta E_{i \rightarrow f} - T\Delta S_{i \rightarrow f} \qquad 2.23$$

where $\Delta G_{i \rightarrow f}$ is the change in Gibb's free energy from the i^{th} to the f^{th} state, ΔS is the entropy change during the process and T is the temperature of the system. Consequently, entropy has been postulated to be a major factor in driving endothermic SF systems to make up for their endothermicity[87,96–98]. We explore this further in a highly endothermic SF system, in Chapter 7. In the endothermic SF under study in this chapter, triplet formation is experimentally observed to be temperature-dependent, leading to an activated mechanism. Figure 2.7 shows a general schematic of SF in exothermic and endothermic systems with respect to the enthalpies of states involved.

This dissertation provides efforts to understanding how factors of electronic and morphological nature influence the mechanism of SF in organic systems. In addition to that, the quest for new, photo-stable endothermic SF materials for improved triplet energy transfer into inorganic systems is undertaken. Finally, we attempt at explaining what drives the process of endothermic SF.

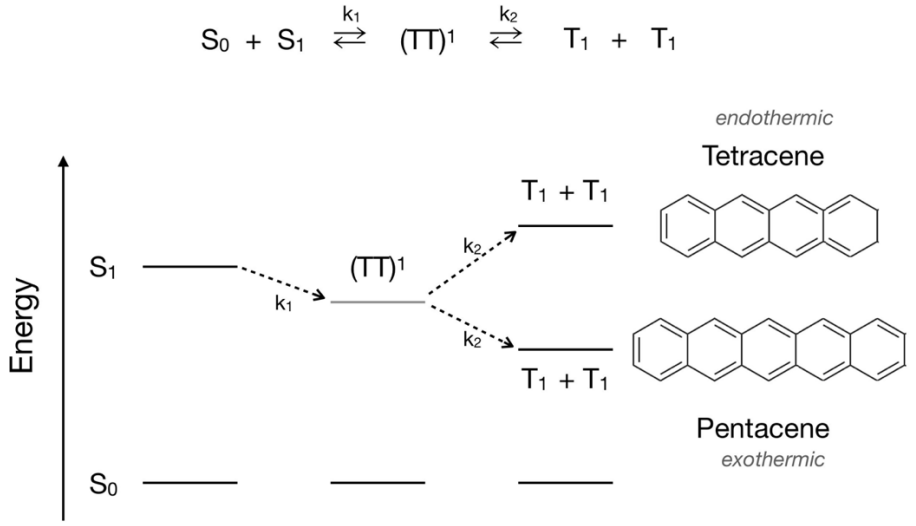

Figure 2.7- Schematic of endothermic and exothermic singlet fission in tetracene and pentacene. A photo-excited S_1 interacts with S_0 to form an intermediate (TT) state that decouples to form two free triplets (T_1) in tetracene (Tc) and pentacene (Pc). While Tc is endothermic by 180 meV, Pc is an exothermic SF system. All the energies depicted are internal energies or enthalpies of individual states. Figure adapted from the thesis of Dr. Hannah L. Stern.

Chapter 3

Experimental Section

In this chapter we discuss sample preparation methods and details of their measurements using various spectroscopic and structural characterization techniques, included in this thesis. The organic materials studied in this thesis were prepared by our collaborators at the University of Kentucky under the supervision of Prof. John E Anthony. All organic solution/film sample preparation of these molecules in this thesis were undertaken by the author herself. PbS quantum dot samples were prepared by Dr. Tom Jellicoe, used in chapter 5. Certain spectroscopic measurements such as triplet sensitisation in solution (Chapter 6) were done in liaison with Qifei Gu. Diffusion ordered 2D NMR spectroscopy (Chapter 4) was performed by Dr. Peter Grice and Duncan Howe at the Department of Chemistry, University of Cambridge. Electron microscopy (Chapters 4-5) was performed under the supervision of Jon J. Rickard at the Department of Physics, University of Cambridge. Electron Spin Resonance spectroscopy (Chapter 6) was performed with the help of Dr. Leah R Weiss (Department of Physics, University of Cambridge) and Dr. William K. Myers at the Centre for Advanced Electron Spin Resonance (CAESR), University of Oxford. All other experiments were performed by the author herself in the Optoelectronics Group, Cavendish Laboratory, University of Cambridge.

3.1 Preparation and Characterization of Organic Nanoparticles

Nanoparticles of organic molecules were prepared by the well-reported method of reprecipitation and is explained in detail in Chapters 4 and 5, with schematics. The samples were embedded in a gelatin polymer matrix for stability against aggregation and spectroscopic measurements.

3.1.1 Diffusion-Ordered NMR spectroscopy

Nuclear Magnetic Resonance (NMR) spectroscopy is a powerful technique used to identify the structure of molecules that are 'tagged' with isotopes of atoms such as H, C, S etc. The free electrons in these atomic isotopes that make them paramagnetic in nature and have a response upon application of an external magnetic field. The nature of such magnetic field responses changes with interactions between neighbouring atoms and can be tracked with the NMR spectrum obtained. Such responses otherwise known as chemical shifts can be recorded as a function of the external magnetic field applied and compose an NMR spectrum of a given molecule. The intensity and chemical shifts for individual atoms or groups of atoms mark are unique and help one in constructing the structure of molecules. NMR spectroscopy can be performed in multiple ways that reveal more information about the chemical and physical nature of molecules or molecular formations.

In this study we use one such technique known as Diffusion-Ordered NMR that maps the diffusion constants in solution of the different chemical species present in a sample. The samples used are composed of TIPS-Tetracene (TIPS-Tc) nanoparticles to see the effect of a certain solvent (THF) on surface passivation. The chemical shifts that are unique to chemical species such as the nanoparticles and the solvent molecules of interest are recorded with specific diffusion constants. If the diffusion constants of the two are close enough it is an indication that they diffuse together in solution which means that they are closely connected. We

perform a control experiment with a solution of TIPS-Tc that was used to prepare the nanoparticles from the same solvent system to see their inherent diffusion constants in solution. All the solvents used in these experiments were deuterated. Figure 3.1 shows a theoretical case of a three species-system in solution and their Diffusion-Ordered NMR spectra. The diffusion constants for each NMR peak is mapped out in the y-axis domain and are colour coded. Each chemical species is assigned to its unique chemical shift and diffusion constant in this 2D plot. The species' with closer diffusion constants (blue and light-blue in the figure) indicate their spatial closeness and thus diffusing together compared to the purple species.

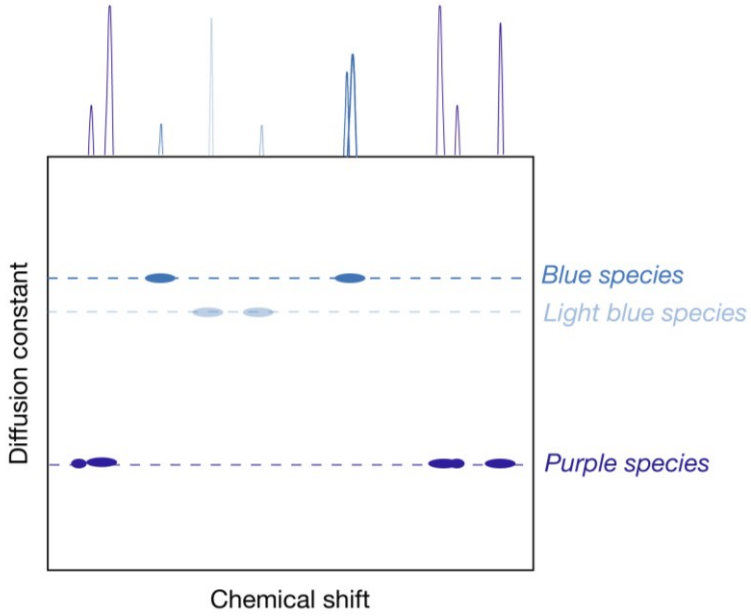

Figure 3.1- Diffusion ordered NMR theoretical demonstration. NMR chemical shifts for three different species with their respective diffusion constants. The diffusion constants of the blue and light blue species are closer when compared to the purple species indicating that the former two are physically closely attached than the purple species.

TIPS-Tc nanoparticles were prepared by the method of reprecipitation, using deuterated solvents for capturing their NMR signature. Such prepared nanoparticles (60 µg/mL) in D_2O/THF-d8 were decanted into a quartz NMR tube of 2.7 mm diameter, sealed in N_2 and sent for the measurements. ^1H NMR spectra were acquired on a Bruker Avance III HD 500 MHz spectrometer (Bruker BioSpin

GmbH, Karlsruhe, Germany) with ^{1}H cryoprobe (CP DUL500C/H, Bruker BioSpin GmbH). ^{1}H NMR spectra were acquired and processed using the TopSpin software (Bruker GmbH). ^{1}H spectra were acquired using the pulse program noesypr1d, a Diffusion-Ordered Spectroscopy (DOSY) experiment using pre-saturation to suppress the water signal.

3.1.2 Electron Microscopy and Crystal Structure

For transmission electron microscopy (TEM) studies, sample solutions were dropcast on a carbon film covered Cu TEM grid with a mesh size of 200. Transmission electron microscopy (TEM) measurements of the samples were performed on a Fei Tecnai F20 200 kV high-resolution electron microscope with a field emission electron source. Diffraction images using the same source were captured from regions of high crystallinity. The microscopy images were captured using SIS Imaging software and were analysed using ImageJ 1.50b. Crystal structures generated from single crystal X-Ray diffraction (XRD) were obtained from our collaborators at the University of Kentucky, where all the molecules studied in this thesis were synthesized. X-RD spectra from these crystal structures were simulated in Mercury 3.9 (build RC1) to compare with that obtained from TEM. In cases where diffraction images could not be captured due to sample stability, interference patterns in the electron microscopy images were Fourier-transformed to create the corresponding reciprocal lattice in ImageJ with d-spacing values, and were compared to the XRD spectra.

3.2 Steady-State Absorption Spectroscopy

Material characterisation often begins with recording steady-state absorption spectrum that reveals information about the vibronic structure of the molecule. In organic molecules, when excited with a broad-energy radiation (typically 250-900 nm) the ground state molecules instantaneously absorb suitable part of the spectrum and an excited state population (S_1-S_n) is created. The transmitted light

after the absorption process is collected at the detector. Peaks in the absorption spectrum indicate the electronic and underlying vibronic structure of molecules. UV-Vis absorption studies of the samples were recorded with a Cary 400 UV-Visible spectrometer in the wavelength range of 350-800 nm. Solution samples were measured in a cuvette with 100 μm pathlength. Encapsulated films were directly used for measurements alongside a blank substrate as controls.

3.3 Photoluminescence Spectroscopy

While absorption is a process that happens instantaneously upon photoexcitation, the excited state population in S_1 -S_n states radiatively relax to the ground electronic state S_0 in nanoseconds. This is recorded as the emission or photoluminescence (PL) of a molecule which also gives information about its underlying vibronic structure. Transitions such as those between electronic states like internal conversion or inter-system crossing to triplet states, vibrational relaxation within an electronic state etc occur upon photoexcitation. At longer timescales, in milliseconds, the non-spin-allowed process of phosphorescence emerging from triplet states to S_0 is observed as well. A schematic representation of all these processes are shown in chapter 2, with detailed discussion.

PL measurements in steady-state as well as time-resolved fashion were performed for solution and film samples. Steady-state PL spectra of the samples were recorded with a pulsed laser (PicoQuant LDH400 40 MHz) at 470 nm and collected on a 500 mm focal length spectrograph (Princeton Instruments, SpectraPro2500i) with a cooled CCD camera. Phosphorescence measurements to measure triplet energies (Chapter 6) were performed as follows. The experimental protocol for making films for triplet sensitisation is as follows. Solution mixture of the acene (3% by weight) and the sensitizer (10% by weight) in chloroform was prepared in N_2 atmosphere. On a clean glass substrate, 50 μL was dropcast and let to dry for 5 minutes. The encapsulated, sensitized film samples excited with a pulsed laser at 658 nm (Thorlabs L658P040). The emission was collected on a 500

mm focal length spectrograph (Shamrock SR-303i spectrometer) with a cooled CCD camera and spectra analyzed using Andor Solis, Oxford Instruments.

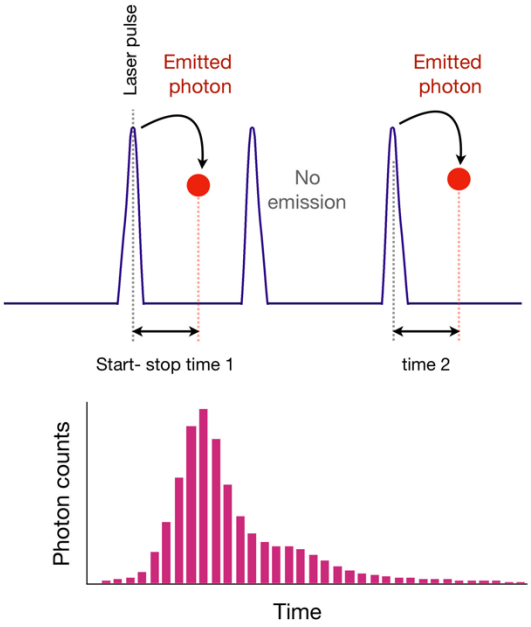

Figure 3.2- Schematic of TCSPC working principle.

Time-resolved photoluminescence measurements were performed on films using a Time Correlated Single Photon Counting setup (Figure 3.2) with a PicoQuant LDH400 40 MHz (470 nm emission) and collected using a 500 mm focal length spectrograph (Princeton Instruments, SpectraPro2500i) with a cooled CCD camera. Time-resolved emission scans were performed on the same setup with emission kinetics recorded for every 5nm step in a given experimental spectral range, typically within 200 ns after photoexcitation. The time-resolution of this setup was 300 ps.

3.4 Pump-Probe Spectroscopy

Pump-probe spectroscopy is a powerful technique that helps unravel mysteries of excited state processes that transcend from femtoseconds to milliseconds. These experiments are done in several ways defined by the probe-ranges and time

resolution used. Pump-probe experiments in this thesis may be divided into three classes: femtoseconds to picoseconds, picoseconds to nanoseconds and nanoseconds to microseconds, depending on the timescales of the phenomena one is interested in. Fundamental principles behind these experiments and the apparatus used are discussed in the following sections.

3.4.1 Principle

Pump-probe spectroscopy deals with excitation of samples using laser pulses to monitor changes in the excited states by means of observing their absorption signatures. As this technique relies on the universal process of absorption, rather than a process specific to certain molecules such as photoluminescence, comprehensive spectral information about excited states can be acquired, non-specifically. This is rather important as we try to elucidate the dynamics of both emissive and non-emissive excited states in this thesis. By this technique one can correlate relative signal strengths to excited state populations by their absorption cross-sections. This is unlike photoluminescence or scattering spectroscopy where a small fraction of the population that is more responsive (emits or scatters more) than the rest skews the results. High temporal resolutions and tuneable spectral range in pump-probe technique make it an important tool in probing excited state populations. In these experiments, the transmittance of the probe (T) through the sample after absorption is detected.

A basic understanding of several photophysical processes following absorption of the electromagnetic spectrum were discussed in section 3.2. Steady-state absorption gives information about transitions emerging from the ground state of a molecule. However, to explore the nature of higher lying states, one needs to be able to access them in a photophysical manner. In pump-probe technique, a pump pulse excites a fraction of ground state molecules to higher lying states, depending on the energy used. The time-width of the pump determines the how coherent thus generated excited state wavepackets will be. By tuning this parameter of the pump, experiments of varying time resolutions from fs to ms can be designed; faster pump (fs) helps unravel the nature of coherence in excited states while

slower pump (ps-ns) helps determine long-time dynamics. The sea of transitions accessible to the excited state population is different to that of the ground state. By careful comparison to ground state transitions (from absorption and PL spectra), one can separate transitions unique to the excited states captured by pump-probe spectroscopy. With spectral identities revealed, pump-probe spectroscopy gives us a plethora of information about dynamics of species, the chemical environment they reside in and transitions they undergo.

Once the pump generates excited state populations, we need a broadband pulse that helps us 'see' the transitions they undergo. This second pulse or the probe (typically 300-500 nm broad) can be of UV, visible or IR nature depending on the nature of the transitions one likes to study. A large number of optical and vibrational transitions happen in timescales between fs and ms, in the excited states. In order to 'see' or capture the absorptive behaviour of these processes in these timescales, the probe used must be of similar time-domain. Thus, capturing optical transitions with varying time delays of capture, a complete picture of excited states with spectra and dynamics can be constructed.

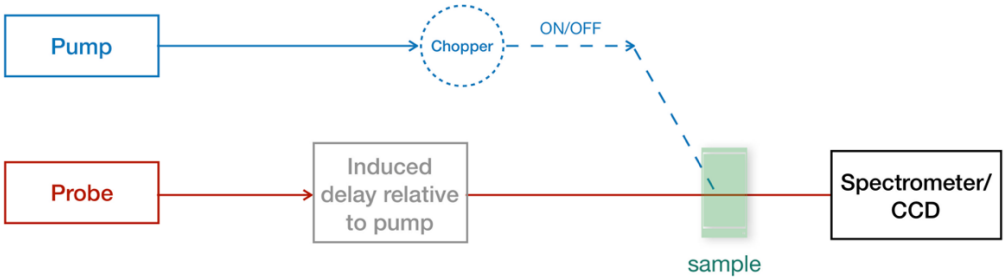

Figure 3.3- Schematic of pump-probe spectroscopy setup used in this thesis.

In pump-probe experiments used in this thesis, a mechanical/electronic chopper is used to turn the pump ON and OFF, at a frequency half of that of the probe. This is done in order to measure the differential transmission ($\Delta T/T$) of the sample with the probe, while the sample is excited and not excited. The final output of the experiment is excited state behaviour captured by differential transmission thus measured given by,

$$\frac{\Delta T}{T} = \frac{T_{pumpON} - T_{pumpOFF}}{T_{pumpOFF}}$$

where T_{pumpON} and $T_{pumpOFF}$ are transmittances through the sample when the pump is ON and OFF, respectively. After the sample is photoexcited by the pump, ΔT/T is measured upon the arrival of the probe. The time delays for measurements using the probe or the time-steps of measurements ranges between fs to μs, in this thesis. Shot-to-shot variation in the probe pulse is monitored throughout the course of the experiment and noise levels typically of the order 10^{-4} to 10^{-6} are maintained. A schematic of the apparatus used in shown in Figure 3.3 and details of the specific setup used in this thesis is discussed in the following section.

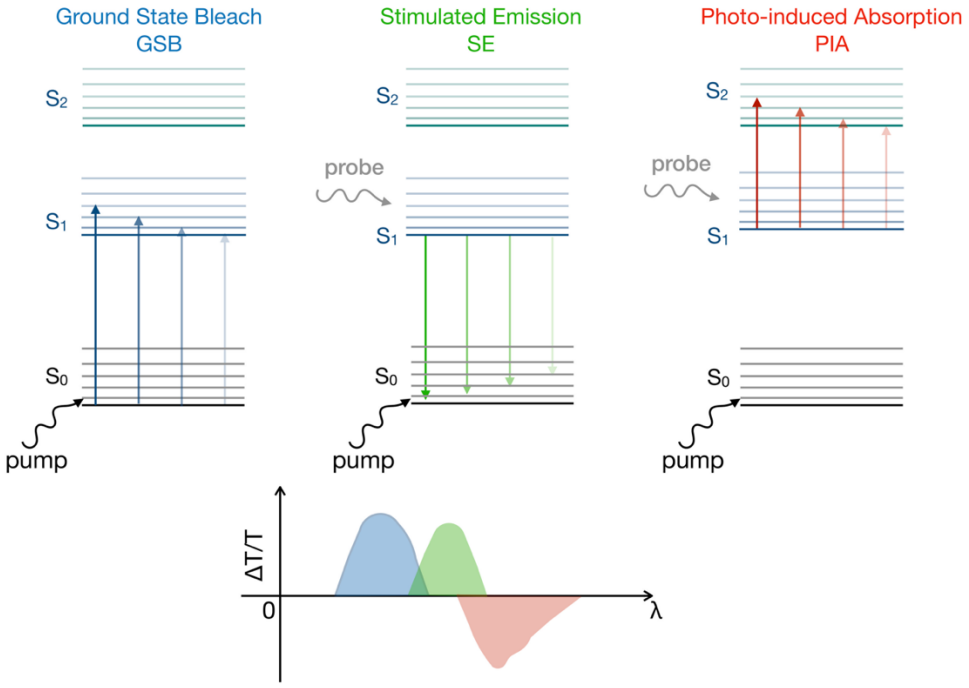

Figure 3.4- Excited state processes in a pump-probe experiment. GSB (blue) represents the depletion of the ground state population upon a fraction of it transitioning to the excited state, S_1 with a positive $\Delta T/T$. SE (green) represents the emission of photons from S_1, stimulated by the arrival of the probe pulse in the experiment, with a positive $\Delta T/T$. PIA (red) shows the absorption of the probe pulse by the excited state population, resulting in a negative $\Delta T/T$.

The nature of excited state transitions observed by pump-probe spectroscopy, within the context of this thesis can be broadly divided into three: ground state bleach (GSB), stimulated emission (SE) and photo-induced absorption (PIA). Upon initial photoexcitation by the pump, only a fraction of molecules go to the excited state, the rest left behind in the ground state. Thus, the absorption by the ground state is weakened during this process. This resulting increase in transmittance manifests as a positive $\Delta T/T$ signal, termed as the ground state bleach. GSB of a molecule should thus match its steady-state absorption. Increase in $\Delta T/T$ can also occur by the probe-induced emission from excited states that undergo radiative relaxation such as singlet excitons. This results in a positive feature known as stimulated emission (SE) and often matches the steady-state PL spectrum of a molecule. The excited states (singlets, triplet, radicals etc) can also absorb the probe pulse and go to higher lying states resulting in a negative $\Delta T/T$ signal known as photo-induced absorption (PIA). These processes are depicted in the schematic shown in Figure 3.4. All these features of various species present constitute the pump-probe spectra of a system, with overlapping signals. We use numerical methods, described in a later section, that help us decompose such overlapping signals to isolate population dynamics unique to the species.

3.4.2 Apparatus

The ultrafast fs-ps pump-probe experiments were performed using an Yb-based amplified system (PHAROS, Light Conversion) providing 14.5 W at 1025 nm and 38 kHz repetition rate. The probe beam is generated by focusing a portion of the fundamental in a 4 mm YAG substrate and spans from 520 to 900 nm. The pump beam is generated in a noncollinear optical parametric amplifiers (NOPAs; 37° cut BBO, type I, 5° external angle) pumped with the third harmonic of the source. The NOPA outputs 1mW power centred at 530 nm, with pulse durations <12 fs (upper limit determined by frequency resolved optical-gating, FROG). The white light is delayed using a computer-controlled piezoelectric translation stage, and a sequence of probe pulses with and without pump is generated using a chopper wheel on the pump beam. After the sample, the probe pulses are seeded through

a visible (550 nm blazed grating) spectrograph and imaged using an InGaAs photodiode array camera (Sensors Unlimited).

Ps-ns pump-probe spectroscopy done in chapter 4 was performed as follows. A Ti: Sapphire amplifier system (1 kHz, Spectra-Physics Solstice) was used to generate the pump and probe beams. A part of the 1 kHz pulse pumps a TOPAS optical parametric amplifier whose output is led to a delay stage that helps in producing a tuneable excitation source for short-time measurements. Another part of the output from the Ti:sapphire system is used to generate broadband probe beams in the visible and near-IR region. Excitation energy dependence (λ_{exc}= 532, 500 and 480 nm) and fluence dependence measurements were also carried out on the same sample with the above-mentioned conditions.

Ps-ns pump-probe measurements in the rest of the thesis were performed using an Yb -based amplifying system, Light Conversion PHAROS, with 400 J per pulse at 1030 nm at a repetition rate of 38 kHz. This laser output is modified using a 4 mm YAG plate to produce the probe beam from 520 to 900 nm. Using a narrow-band optical parametric oscillator system (ORPHEUS-LYRA, Light Conversion) fed by a 1030 nm seed, the pump beam is generated at 480 nm. The probe pulse is delayed using a computer-controlled piezoelectric translation stage (Newport) and the pulses are chopped by means of a mechanical chopper (Thorlabs) to create ON-OFF pulses (for calculating $\Delta T/T$) before hitting the sample. The pump and probe beams are focused with sizes 300×300 μm and 40×50 μm respectively at the sample position, giving a pump fluence of 40 μJ/cm^2. The probe pulse transmitted through the thin film sample is collected using a silicon line scan camera (AViiVA EM2/EM4) with a visible monochromator containing a grating blazed at 550 nm. For temperature dependent pump-probe measurements in chapter 7, a helium dynamic flow cryostat was mounted on the above setup and data recorded from 298 to 10 K.

Ns-μs (1 ns to 100 μs) pump-probe measurements including solution sensitisation, were performed using a Nd:YVO4 laser (AOT-YVO-25QSPX,Advanced Optical Technologies) with electronically controlled delay. The pump and probe beams

are overlapped on the sample adjacent to a reference probe beam. This reference is used to account for any shot-to-shot variation in transmission. The beams are focused into an imaging spectrometer (Andor, Shamrock SR 303i) and detected using a pair of linear image sensors (Hamamatsu, G11608) driven and read out at the full laser repetition rate by a custom-built board from Stresing Entwicklungsburo.

3.5 Electron Spin Resonance Spectroscopy

Singlet Fission (SF) is a spin allowed process of the formation of two non-correlated triplets generated from one high-energy singlet upon photo-excitation. For highly efficient SF materials this is the major pathway that produces long-lived triplets that help in tackling thermalisation losses when incorporated into PV devices. However, an alternate pathway is present for all molecules for the formation of free triplets via inter-system crossing as discussed in section 2.2.4. These ISC triplets decay as phosphorescence or non-radiatively into the ground state, not contributing to improving device efficiencies. Hence it is vital to isolate SF-triplets from ISC-triplets and we explore their spin signatures for this, using Electron Spin Resonance (ESR) spectroscopy.

Upon applying a magnetic field to a material under photoexcitation, various excited-state species such as triplets, quintets and radicals, with near-degenerate sub-levels are probed. This results in Zeeman splitting to form non-degenerate sub-levels in the same energy scale as microwaves that show characteristic absorption (A) or emission (E) features in their ESR spectra. These patterns known as polarization patterns represent various spin state transitions under magnetic field with the relative spin population as a function of molecular orientation. The spin polarization patterns as a function of applied magnetic field ($\mathbf{B}$) are observed to be unique for inter-system crossing (ISC) triplets, SF triplets, weakly bound TT pairs, quintet states, charge transfer states etc. which makes ESR a powerful diagnostic tool to study SF and its dynamics.

Time-resolved electron spin resonance (tr-ESR) experiments were conducted on a Bruker E680 spectrometer operating at X-band (~9.6 GHz) with a Bruker EN 4118X-MD4 resonator. Thin film samples (spincoated from toluene) were degassed and sealed in vacuum inside a 2.7 mm quartz tube. The samples were photoexcited at 500 nm by the output of a GW versaScan-ULD and uvScan OPO (20 Hz repetition rate, 3 mJ per pulse, 5 ns duration), fiber-coupled to the sample, leading to unpolarized light. A DG645 Stanford delay generator was used to trigger the spectrometer's SpecJet digitizer. The ESR spectra were obtained in direct detection mode using a transient recorder without a lock-in amplifier. The samples maintained at 80K by an Oxford Instruments N_2 gas flow cryostat, and raw data acquired were baseline corrected during data processing. The ESR spectra discussed in Chapter 6 are integrated up to 5 µs after photoexcitation (time res. ~ 200 ns) and are used to detect the presence of unique triplet signatures generated by SF.

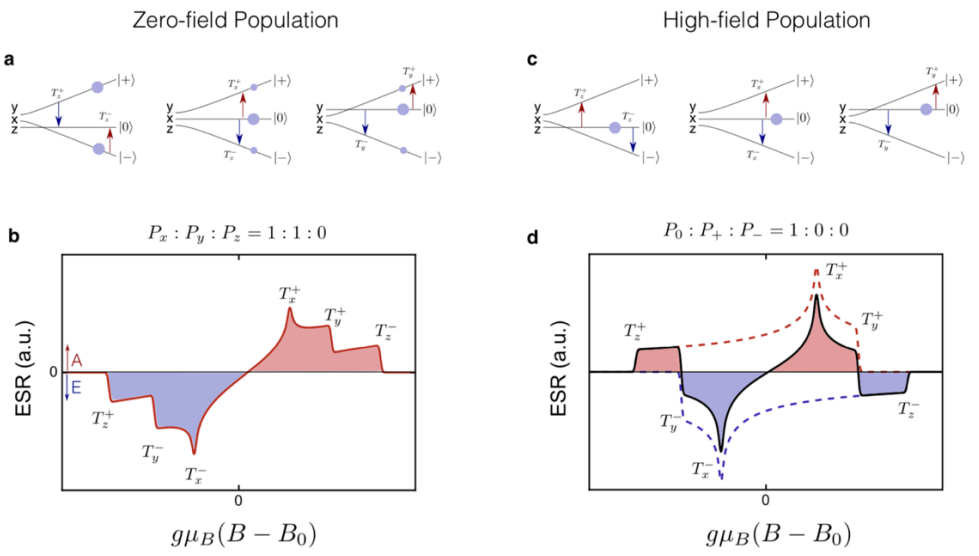

Figure 3.5- ESR polarisation patterns in zero-field and high-field triplet populations, in a disordered film. (a,c) Triplet levels ordered by energy and transitions T_+ between the |0> and |+> states (red) and T_- between |-> and |0> (blue) in zero and high-field populations. (b,d) T_+ and T_- transitions for film with a uniform orientation distribution, in zero and high-field populations. The polarisation pattern in (d) is showcased by SF-generated triplets. Figure from the thesis of Dr. Leah R. Weiss, used with permission.

3.6 Numerical Methods

Spectral deconvolution by numerical methods is crucial in this thesis as we deal with complex spectral-temporal data involving mixing of multiple species. This is performed in this thesis by two methods: decay-associated spectra led by SVD and the genetic algorithm, weighing more on the former. These methods are discussed in detail below.

3.6.1 SVD and Decay-Associated Spectra

Time-resolved data from different spectroscopic techniques in this thesis are analyzed by an algorithm based on Singular Value Decomposition (SVD) method[99]. SVD is a numerical deconvolution method that generates the data matrix into its major components. Thus, species with major spectral and kinetic contributions to a given dataset are identified using matrix formulation discussed below.

Let A be the matrix of time-resolved data with wavelength, time and intensity of the signal as the three main variables. The rank of A is defined by the number of steps of wavelength and time points used to collect the data. The method of SVD factorizes the matrix A as a product of three matrices, as shown below.

$$A = UDV^{T}$$

where the column vectors of U and V are orthonormal to each other, and D is a diagonal matrix with positive, real constants. By performing SVD on A, column vectors that represent individual species (U_i, wavelength domain) in U and their corresponding kinetics (V_i, time domain) in V are calculated. The relative strengths of each of such identified species are represented in the diagonal matrix D (D_i). The weight of elements D_i thus tells the number of major species present in the dataset. Thus, the product of the first few components (i=1,2,3..) as shown in Figure 3.6 should give rise to a very good approximation to A, at times even eliminating experimental artifacts.

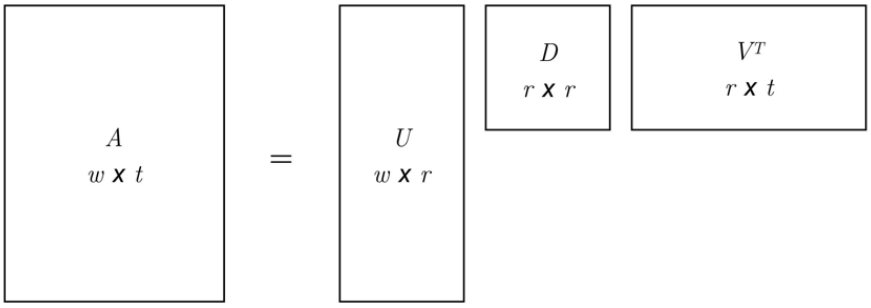

Figure 3.6- SVD-matrix formulation, where A is the data matrix along wavelength and time axes. Matrix A is deconvoluted into its principle components in matrix U (wavelength or spectra), matrix V (time or kinetics) and matrix D with weights corresponding to the components in U and V.

SVD is a powerful yet purely mathematical concept with orthogonality conditions imposed on U and V^T. Often this leads to physically inaccurate matrix formulations that make perfect mathematical sense. Thus one needs to be careful and approach the results generated by SVD with an understanding of real-world physical phenomena. To make the results of SVD more sensible physically, we resort to an additional step to estimate what is known as decay-associated spectra or DAS. The first step of DAS is performing an SVD analysis on A to generate U, V and D matrices. The next step that is to minimize the term,

$$\min_{k \in \mathbb{R}} ||A\text{-}U(k)V^T||^2$$

where k denotes the kinetic parameters such that V_i's are converted into mono-exponential decays occurring in parallel. Each V_i tied to a mono-exponential timeconstant generates $U(k)$ as the spectral contribution associated with it, or in other words the decay-associated spectrum. Thus, by forcing the kinetics of all major components to be mono-exponential in nature, we are restricting this method of global analysis within the realms of meaningful physical processes decaying mono-exponentially. The resultant spectra associated with this kinetic model can be identified as purely belonging to either a single spectral species but sometimes mixing of multiple species, depending on the timeconstants extracted.

In this thesis, we perform SVD-led DAS as described above and discuss spectra unique to species (ignoring the mixed species spectra) and timeconstants associated with them. DAS proved to give a reasonable understanding of excited state processes within the time-window of experiments performed. However, some ultrafast (fs) and long-lived (µs) processes had timeconstants 'predicted' not within the dataset by this method of global analysis. Also, one needs to be careful in defining time-zero of the experiment adequately as fitting the mono-exponential kinetics in parallel by this method is heavily dependent on that. Changes in time-zero values were proven to affect the fitting quite dramatically. Thus, although DAS is a powerful mathematical tool for global analysis, one needs to be careful to watch out the reliability of fittings, time constants generated and the nature of the associated spectra. While DAS-SVD is used predominantly in this dissertation, we perform the genetic algorithm as well for sanity-checks in some sections of the thesis.

3.6.2 The Genetic Algorithm

The genetic algorithm (GA) is an evolutionary algorithm that tries to pull out individual spectral components and their corresponding kinetics, which best reproduce the experimental data with a given set of physical constraints related to spectral shape and expected kinetics. The code that has been used in this work was initially developed by Dr. Simon Gädinas.

The idea behind GA is similar to that of population dynamics in a naturally evolving biological system. There is an initial pool of individuals, or genotypes to be more specific, that are given by various Gaussian distributions. This gene pool is let to multiply by mixing and as soon as they reach a target population, there is some amount of mutation that has crept into the system. In our GA code, this mutation rate has been set to some specific value, which controls how fast and thus how close GA can reproduce the experimental data. While the system evolves over several generations, a fitness parameter is calculated and the convergence of this is monitored. After a desired number of generations with additional physical constraints such as spectral shape and extent of kinetics imposed on, we are

expected to obtain a desired number of principal spectra that is capable of reproducing the entire dataset. GA is a more advanced search algorithm than most of the other standard search algorithms for multi-dimensional TA data since it searches for a global minimum for spectral deconvolution which is vital since TA data almost always contain overlying spectral features that could belong to multiple species. In this work, GA was mainly used to look at TA data.

Chapter 4

Endothermic Singlet Fission in Organic Nanoparticles

When you are in the middle of a story it isn't a story at all, but only a confusion; a dark roaring, a blindness, a wreckage of shattered glass and splintered wood; like a house in a whirlwind, or else a boat crushed by the icebergs or swept over the rapids, and all aboard powerless to stop it. It's only afterwards that it becomes anything like a story at all. When you are telling it, to yourself or to someone else.

-Alias Grace by Margaret Atwood

The results presented in this chapter have been published in *Thampi et.al.*[100] This chapter explores morphological factors affecting endothermic singlet fission (SF). We use TIPS-Tetracene (TIPS-Tc) nanoparticles (NPs) as the model system as TIPS-Tc is an extensively characterised endothermic SF system with high triplet yield. We introduce a fabrication method for TIPS-Tc NPs and optimizes the structure of NPs to suit spectroscopic studies and thin film based photovoltaic applications. Structural characterisation of these nanostructures of ~30nm in size is performed by electron microscopy and we analyse their crystallinity by extrapolating diffraction patterns from these microscopy images. We employ several steady-state, time-resolved spectroscopic techniques with varying spatial-temporal resolutions to identify excited states and study their dynamics.

With the high packing density of molecules in the NPs, we observe the occurrence of SF and generation of free triplets. The initially photo-excited singlet states (S_1) formed in the NPs show unique spectral features such as ground state bleach

(GSB), stimulated emission (SE) and photo-induced absorption (PIA). Under 200fs, we see ultrafast formation of intermediate, correlated triplet pair states (TT) that have some S_1 character, but yet distinguishable from its PIA in the near-IR region. While S_1 decays with a lifetime of ~12 ps, TT states are long-lived up to several hundred ps. We notice an excitation energy dependence in the formation dynamics as well as spectral features of the TT state. At high energy of excitation radiative transitions from the TT state at nanosecond timescales to S_0 state leading to TT emission are favoured. This has been observed in both pump-probe as well as time-resolved fluorescence measurements, where a low-energy TT emission centred at 650 nm grows in by 1 ns when excited at 480 nm. The decay dynamics of these differently photo-engineered TT states are also different, affecting the formation and yield of free triplets (T_1).

Comparison of TT to T_1 dynamics in the NPs and films of varying morphologies hints at spatial migration of TT states. Some preliminary evidence suggests that the TT states form in the crystalline core of the NPs, migrate to the amorphous exterior and break up there to form $2T_1$ states. This indicates that formation of $2T_1$ states is facilitated by morphology driven TT migration. Our results hint that the kinetic and structural evolution of the TT state are highly morphology dependent. We also show that the relaxation of the initially formed TT states can occur via multiple pathways, leading to very different relaxed TT states at longer times. On nanosecond timescales, we observe the dissociation of the TT state to form free triplets that live for several microseconds, even within the confined geometry of the NPs.

4.1 Background and Motivation

SF is observed in various organic materials such as acenes[55,101–103], biradicaloids[104,105], polymer aggregates such as carotenoids[106–108] etc. The process of SF is contingent on the condition that the energy of S_1 must be close to twice the energy of T_1. The difference between the energy of S_1 and twice of that of T_1, $\Delta E = 2E(T_1)-E(S_1)$, is used to classify SF materials into exothermic ($\Delta E< 0$), isoenergic ($\Delta E=0$) and endothermic ($\Delta E >0$) systems. While SF has been extensively studied in exothermic systems, endothermic systems such as tetracene are of particular interest due to their potential use in photovoltaic (PV) devices (see below) and understand the fundamental nature of the process[109].

One of the most studied endothermic system is tetracene[27,58,110–112] and, in this study, a particularly interesting tetracene derivative, 5,12-bis(triisopropylsilylethynyl) tetracene (TIPS-Tc) is chosen for the purpose of studying morphological influence on the SF dynamics in this chapter. TIPS-Tc is an endothermic SF system, like the parent molecule tetracene, with an $E(S_1)=$ 2.3 eV and $E(T_1)=$ 1.2-1.25 eV. The difference in enthalpy (internal energy of states) or the endothermicity (ΔE) of TIPS-TC is thus 200 meV. TIPS- Tc is more soluble in organic solvents, compared to tetracene, improving its processing from solution. This opens interesting device fabrication opportunities. Importantly, $E(T_1)$ of TIPS-Tc compliments the bandgap (1.1 eV) of Si in PV devices. This makes TIPS-Tc an important system to study endothermic SF. Triplet yields as high as 120% also makes this a viable candidate for energy transfer and harvesting $2T_1$ excitons to improve power conversion efficiencies in PV devices. Finally, the various excited states in the process of singlet fission and their absorption signatures have been previously characterized for solution[113] and films[109] of TIPS- Tc.

Organic NPs provide an alternate platform to study SF dynamics with the added advantage of size and morphology control of the system. Nanoparticles of acene derivatives of pentacene and tetracene have been studied[114–116] previously in nanoparticles of size above 100 nm, but the dynamics of TT states have not been

explicitly addressed. In this work, we study the formation and dynamics of TT states in NPs with tuned morphology. Further we probe the dynamics of decoupling of TT states to form free triplets ($2T_1$) and the role morphology plays in driving triplet formation.

4.2 Preparation of the Nanoparticles

NPs are synthesized using an extensively reported method of reprecipitation[59,114–117]. 0.6 mg of crystalline powder of TIPS-Tc is first dissolved in 1 mL of tetrahydrofuran (THF) solution. 100 μL of the TIPS-Tc solution is rapidly injected into 5mL of de-ionized water while stirring. This mixed solution is left for NP growth at room temperature in a dark, inert environment. After 30 minutes of stirring of the solution, steady-state absorption and photoluminescence measurements are performed to confirm NP growth.

The NP solution and spin-coated/drop-casted NP films were observed to degrade with laser exposure. To improve the stability of the NPs for spectroscopic studies, they are embedded in a polymer matrix. Among several polymers, a gelatin type A polymer was chosen due to its amphiphilic nature. When the NPs are mixed with the gelatine type A, the NPs selectively attach to the hydrophobic end of the polymer. To embed the NPs in a gelatin matrix, gelatin is dissolved in water at 55^0C, precipitated by acetone and centrifuged to remove the light molecular weight part. The heavy molecular weight part of gelatin is collected by centrifugation and re-dissolved in 10mL of water at 55^0C. 200 μL of the NP solution in water is added to the heavy molecular solution of gelatin, slowly while stirring, and maintained at 55^0C for 30 minutes. To make thin films, 150 μL of the NP-gelatin solution is drop-cast on spectrosil substrates at room temperature and let them cool down to facilitate phase transfer from liquid to gel phase. About an hour later when the phase transformation is complete, the films are encapsulated under N_2 and used for spectroscopic studies. A schematic procedure of TIPS-Tc NPs is depicted in Figure 4.1.

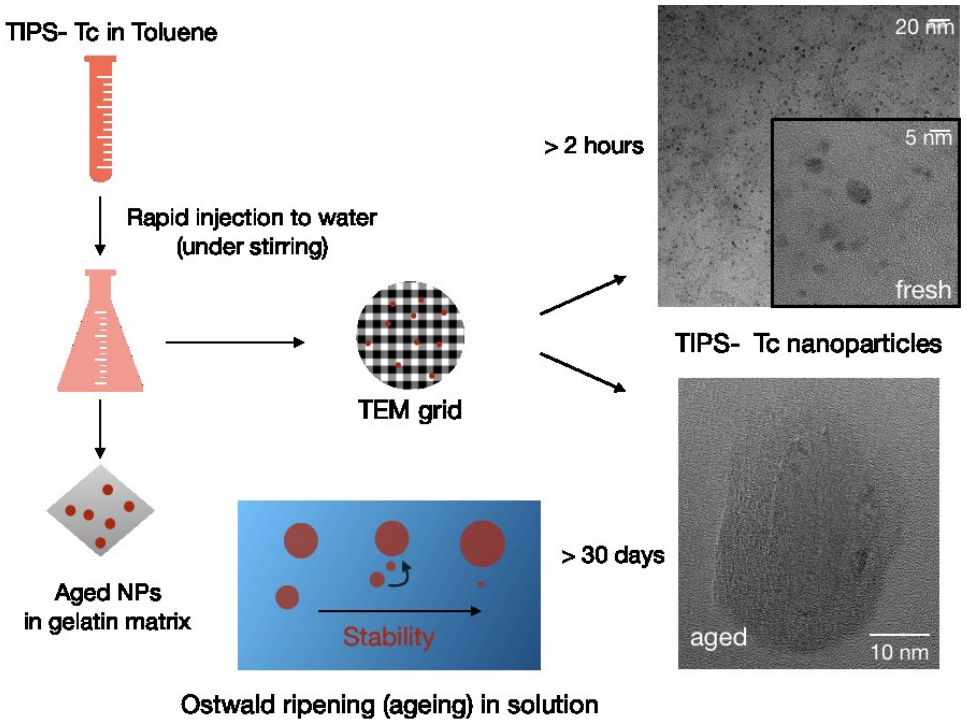

Figure 4.1-Preparation of TIPS-Tc NPs. NPs are prepared by the re-precipitation method and allowed to age in solid state to a size of ~30nm. The NPs are embedded in a gelatin matrix for spectroscopic studies.

4.3 Structural Characterisation and Morphology

TIPS-Tc packs in a slip-stacked structure with four molecules per unit cell in the monoclinic crystal system. Molecular geometry plays an important role in the formation of excited states[65,118] that decouple to form free triplets and thus facilitate SF. It is therefore crucial to understand the packing of molecules that make up the NPs used in this study. While the steady-state PL spectral differences between the molecular and NP systems shed some light on the size as well as crystallinity of the NPs (section 4.4), we resort to structural characterisation by electron microscopy and diffusion ordered NMR-studies in this section.

4.3.1 Transmission Electron Microscopy (TEM)

Transmission Electron Microscopy (TEM) is used to assess the structure and crystallinity of the NPs at two different stages post-synthesis. The aim of the experiment is to understand the evolution of size distribution and crystallinity of the NPs. Figure 4.2 shows images of NPs after 12 hours and 30 days of the synthesis. The fresher sample has ~5 nm sized particles with size distribution shown in the inset. After 30 days of synthesis we see that larger hexagonal shaped particles of size ~30 nm are formed. The larger particles are sparsely distributed on the TEM grid. Interestingly, the NPs have developed a crystalline core with clear interference fringes in the TEM image, and an amorphous exterior. This physical phenomenon can be explained by Ostwald ripening[119,120], which describes spontaneous formation of larger particles when smaller particles come together. Since formation of larger particles are energetically favoured than smaller ones, Ostwald ripening is a thermodynamically-driven process of small particles cohesively coming together, becoming larger through dissolution and reprecipitation. This results in larger, more stable particles. A schematic of this is shown in Figure 4.1. From calculations correlating molecular density and crystal structure, a 30 nm crystalline NP may contain as many as 10,000 molecules of TIPS-Tc. While the confinement of such a large number of molecules in a 30 nm hexagonal structure passes the criteria for molecular proximity to enable SF[10], apart from energetic matching, molecular geometry within these nanostructures is also crucial.

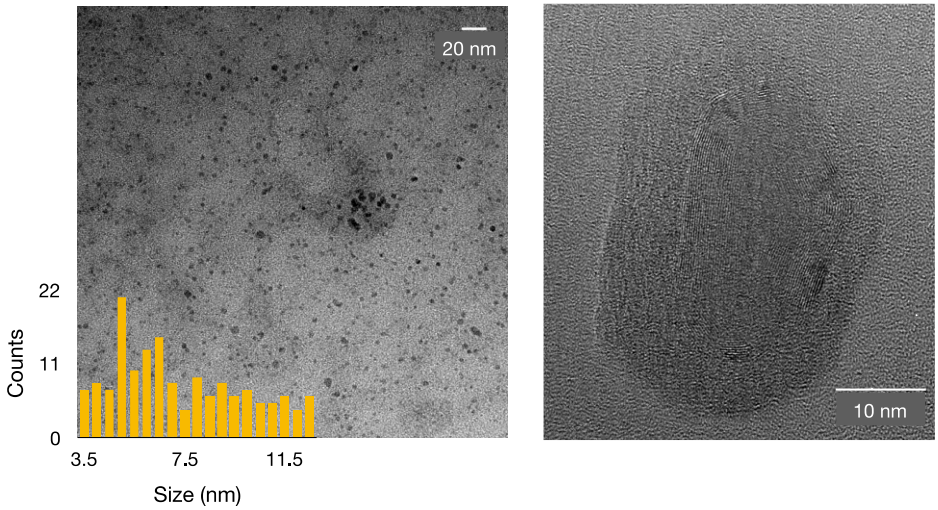

Figure 4.2-TEM images of NPs in solution 12 hours (right) and 30 days (left) after synthesis. (right) TIPS-Tc NPs upon completion of the reaction in solution, ~5 nm size and irregular shaped and (left) NPs grown to ~30 nm, hexagonal shaped showcasing a crystalline core and an amorphous exterior, 30 days after synthesis. Inset shows the size distribution histogram of NPs with an average size of ~5 nm.

In order to ascertain the crystallinity of the sample, X-ray diffraction techniques were attempted, but deemed unsuccessful due to the low concentration of the sample. Therefore we go back to the TEM images to analyse crystallinity of the NPs. Note the presence of interference fringes in the core of the 30 nm NPs, in Figure 4.2 and Figure 4.3. The electron beam used for microscopy, interacts with crystal planes of suitable order inside the NPs, giving rise to interference patterns or fringes. The Fourier-transform of these fringes creates electron diffraction images of the corresponding reciprocal lattice and the d-spacing values between molecular planes. Examples of the Fourier-transformation (FT) of interference fringes from TEM images of the NPs are shown in Figure 4.4, with the obtained d-spacing values highlighted. These d-spacing values are compared to those calculated from simulated XRD spectrum from the crystal data of TIPS-Tc, and the comparison is shown in Figure 4.4. The peaks in the XRD spectrum that match with the d-spacing values obtained from the above-described FT-TEM analysis are highlighted in black in the figure. Therefore, we confirm the presence of certain crystalline phases in the NP core. The same analysis performed on the

exterior of the NPs showed no diffraction patterns of the reciprocal lattice and confirms that the NPs are amorphous on the outside.

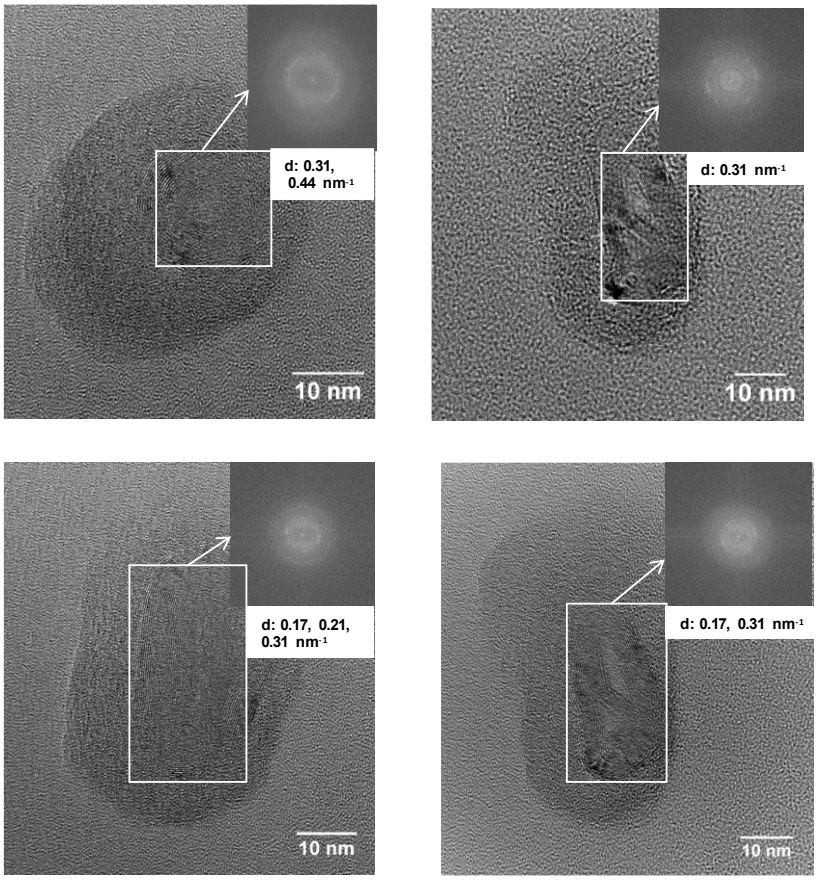

Figure 4.3-Assessing crystallinity of NPs through TEM. Images of NPs made in independent reactions. The size of all observed structures are similar (~30 nm) and have reproducible morphology of a crystalline core and an amorphous exterior. Diffraction patterns depicting reciprocal lattice of the crystalline core were obtained by Fourier transformation and have been included as insets in each individual figures. The d-spacing values associated with them are also marked on the figures.

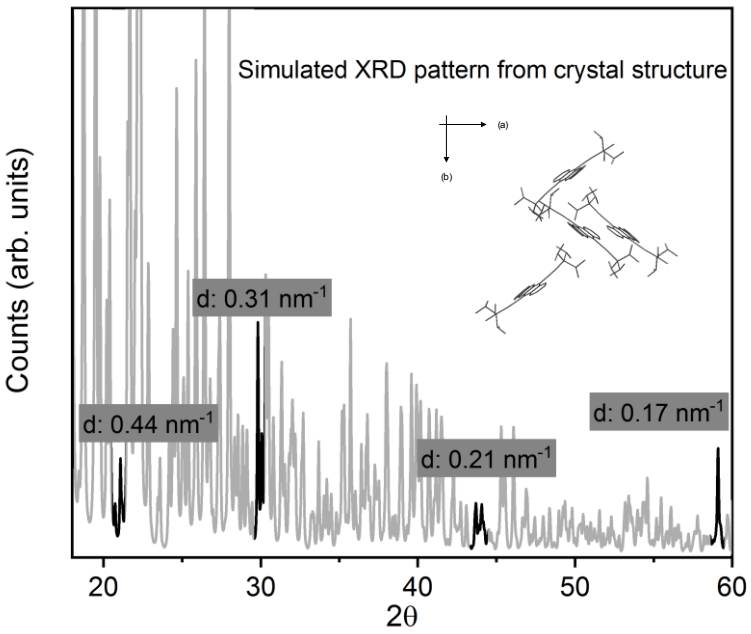

Figure 4.4-Simulated XRD pattern of TIPS-Tc from crystal structure. The highlighted peaks along 2θ axis correspond to the d-spacing values in the reciprocal lattice obtained by the Fourier transform of interference fringes in the NP core, shown in figure 4.3. The close matching of the peaks corresponding to the estimated d-values from experiments confirm the crystalline nature of the NP core. Inset shows the crystal structure of TIPS-Tc in the ab plane used for the generating the XRD pattern.

These results indicate that the NPs contain both crystalline and amorphous regions, which have been previously studied in thin films and shown to have very different TT state dynamics. In this study, the synthesis of NPs is repeated with a high degree of reproducibility in terms of stability, morphology and size control, allowing one to probe a highly reproducible nanostructure, unlike thin films, with wide sample-to-sample variation.

4.3.2 Diffusion-Ordered NMR Spectroscopy

Diffusion-ordered Nuclear Magnetic Resonance or DOSY-NMR spectroscopy is performed to elucidate the role of THF in the formation and stabilization of the NPs in solution. DOSY-NMR is performed on both the molecular (in THF) and the NP samples dispersed in water. Figure 4.5 shows the DOSY-NMR of the molecular TIPS-Tc sample in THF-d8 and Figure 4.6 shows the DOSY-NMR of

the NP sample in D_2O. A DOSY-NMR spectrum is a two-dimensional plot that gives information regarding the chemical shift of chemical species versus its diffusion constant that has been detected by indirect methods in the same setup. Thus, if two distinguishable chemical species have their chemical shifts read across a common value of diffusion constant from the DOSY-NMR data, it means that they are physically held together in the system[121]. See section 3.1.1 for more discussion on this technique. Hence if THF has a role in the growth or stabilization of the NPs, DOSY-NMR should be able to capture it based on diffusion constants.

^{1}H NMR peaks of THF previously reported[122] are 1.76ppm and 3.58ppm with diffusion constant $9.5x10^{-10}$ m^2/s marked in the DOSY-NMR spectrum in Figure 4.5. All other peaks we see have larger diffusion constants ($> 1.92x10^{-9}$ m^2/s) since they belong to TIPS-Tc, a bulky molecular system. ^{1}H NMR of TIPS-Tc has been reported elsewhere[123] and the peaks observed in this experiment match on comparison. The observed TIPS-Tc peaks are: δ1.35 ppm (s), δ7.48 ppm (dd), δ7.56 ppm (dd), δ8.04 ppm (dd), δ8.65 ppm (dd) and δ9.34 ppm (s) where 's' stands for singlet and 'dd' stands for doublet of doublet (when a doublet pair is split further into doublets with a final intensity ratio of 1:1:1:1 due to two distinct but close coupling constants). All the dd and s curves are not seen clearly in the recorded spectra as the concentration of the sample was low to avoid aggregation.

Sample preparation has been mentioned in detail in Chapter 3, with D_2O and THF-d8 replacing their non-deuterated counterparts. Handling samples with D_2O was done with caution (to avoid back-conversion to protons), but still in the NPs, while taking the NMR spectrum water peaks creep in to the region above 5 ppm leading the spectrum rendering noisy. Hence, the NPs spectrum up to 4 ppm has been plotted. The only TIPS-Tc peak found in the region is the δ1.35 ppm (s) in the NP sample, lying close to the marked THF peaks. We also see that the THF peak at δ1.76 ppm shows multiple diffusion coefficients which could be because there of the size distribution of the NPs. Note that the diffusion coefficient of THF changes to $8x10^{-10}$ m^2/s from the molecular sample to the NPs, while that of TIPS-Tc decreases by 5 times to $7.6x10^{-10}$ m^2/s from molecular sample to the

NPs. The smaller diffusion constant in the latter sample corresponding to the chemical signature of TIPS-Tc suggests the formation of NPs that can diffuse slower than single molecules. Although we need to study a larger range of NMR peaks for doing a thorough analysis, it is unambiguous to conclude that THF molecules are physically diffusing close to the NPs, maybe even attached to the defect sites on the NP-surface. However, it is less likely that THF molecules are inside the core of the particles since getting an NMR signal from the core is dubious.

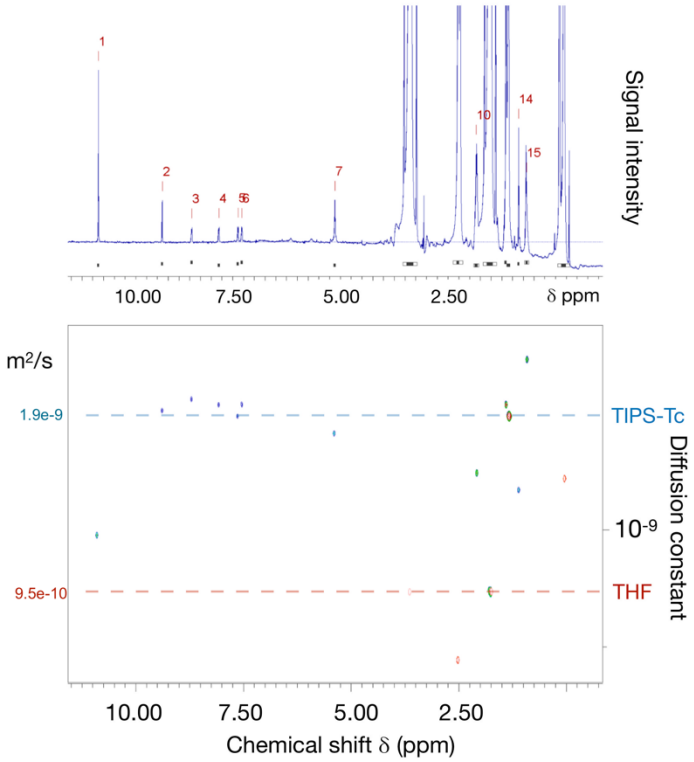

Figure 4.5-DOSY-NMR spectrum of TIPS-Tc molecules in THF-d8. The top plot shows the NMR signatures of chemical species present in the sample and the bottom one shows the corresponding DOSY-NMR spectrum. The X-axis for the DOSY-NMR plot shows the chemical shift in ppm (parts per million) and the Y-axis shows the diffusion coefficient in m^2/s. The marked red dotted line shows the THF ^1H peaks and the blue dotted line shows TIPS-Tc peaks.

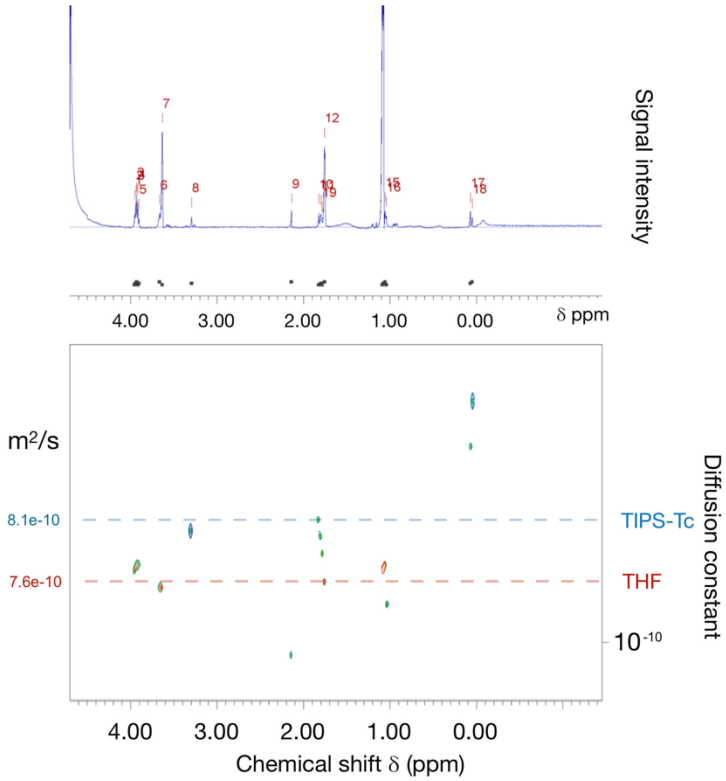

Figure 4.6-DOSY-NMR spectrum of TIPS-Tc NPs in D_2O. The top plot shows the NMR signatures of chemical species present in the sample and the bottom one shows the corresponding DOSY-NMR spectrum. The X-axis of the DOSY-NMR spectrum shows the chemical shift in ppm (parts per million) and the Y-axis shows the diffusion coefficient in m^2/s. The red dotted line shows the ^1H peaks of THF and the blue dotted line shows TIPS-Tc peaks. Certain residual chemical species picked up during the experiment are the green dots in the data and assignments are not included for clarity.

4.4 Optical properties of TIPS-Tc Nanoparticles

Vibronic structure of absorption and photoluminescence (PL) spectrum is known to be sensitive to the phase transfer of molecules, especially when they form nanostructures with increased molecular proximity and confinement in the nano-regime[124,125]. Accordingly, we performed steady-state absorption and photoluminescence measurement to detect the formation of NPs from their molecular state. We divide the study into three sections: (i) dilute molecular

solutions of TIPS-Tc where individual molecules are far apart thus impeding SF, (ii) NPs suspended in solution immediately after the reaction has ended and (iii) NPs embedded in polymer matrix to stabilise and arrest their growth.

4.4.1 TIPS-Tc Molecules in Dilute Solution

TIPS-Tc is a well characterised endothermic SF system, with SF in various phases such as solutions[113] and films[95] have been explored before. Following the report of *Stern et. al.*[113] dilute solutions of TIPS-Tc (<10 mg/mL) do not exhibit SF as molecules are far apart, hindering SF as it is a diffusion limited process in solution-state. The steady-state absorption and PL spectra of dilute TIPS-Tc solution at 1 mg/mL are shown in Figure 4.7. The major peaks in the absorption and PL spectra show the 0-0, 0-1 and 0-2 vibronic transitions of the singlet state in the molecule, with an absorption maximum at 540 nm.

4.4.2 Nanoparticles in Solution

NPs of TIPS-Tc are synthesised by re-precipitation method as described in chapter 4.2. The absorption and PL spectra of TIPS-Tc NPS in solution are recorded and shown in Figure 4.7. We notice no significant difference in the absorption spectrum with respect to the molecular solution, except the peaks in the NP solution seem to have red-shifted by a small amount (c.a., 4 nm). This may give an insight about differences in structural regularity between the molecular and the NP phases. Note that the PL spectrum of the NPs upon excitation at 470 nm shows an additional broad emission in above 650 nm with similar PL feature of TIPS-Tc molecules. This broad emission centred at 640 nm alters the peak height ratios of S_1 vibronic transitions. The presence of this broad, red emission in the solution of NPs could be because of an effective increase in conjugation and coupling between molecules when confined inside the NPs versus free in solution.

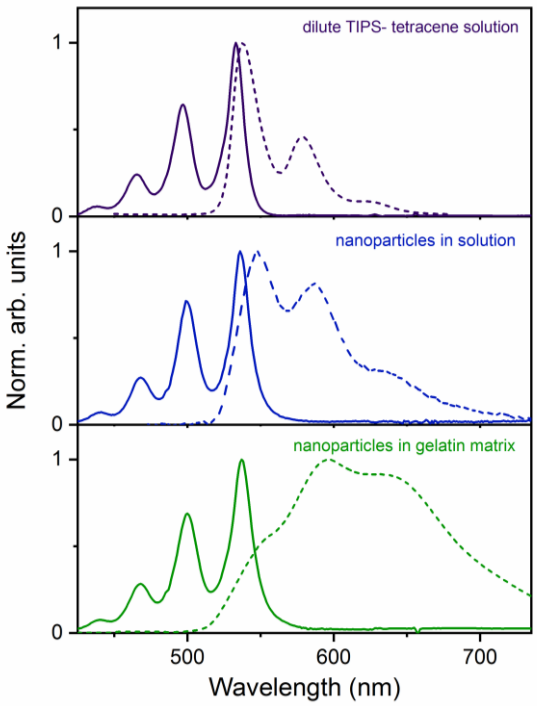

Figure 4.7-Steady state absorption and photoluminescence spectra of NPs. Steady-state absorption and PL of (top, purple) dilute molecular TIPS-Tc solution, (middle, blue) NPs in solution and (bottom, green) NPs in gelatin matrix. λ_{exc}: 470 nm for all PL spectra.

4.4.3 Nanoparticles in Gelatin Matrix

The NPs are purified and transferred to a gelatin matrix for stability and arresting their growth in order to study their photophysics in a consistent, controlled manner. We note that absorption spectrum of the NPs in the gelatin matrix is blue-shifted by 7 nm from that of the solutions discussed above. The NPs in gelatin matrix also show a prominent broad emission from a low-energy species whose transient and physical behaviour shall be discussed later. This low-energy emission, also present in NPs in solution, indicates their more-disordered-than-crystalline molecular arrangement. Further analysis on the SF photophysics of these structures are discussed in the following sections. The photoluminescence quantum efficiency (PLQE) measured for NPs in gelatin matrix is 1.5% while

dilute TIPS-Tc solutions show a high PLQE of 76%. This is consistent with the presence of a new non-radiative decay pathway for the S_1 exciton in the NPs.

4.5 Photophysics of Excited States in the NPs

So far we have built a basic understanding of the S_1 vibronic structure of the NPs in solution and in films (gelatin). We have also seen the presence of a broad, low-energy emission from the NP films. From structural characterisation we have developed a good understanding of size variation as well as the morphology of the NPs. Henceforth we focus on the photophysics of films made of NPs embedded in gelatin matrix.

4.5.1 Identifying the Intermediate TT state

A previous study on SF in solutions of TIPS-Tc discusses the presence of an intermediate triplet pair (TT state) based on the observation of a broad, low-energy emission beyond 610nm in its steady-state PL spectrum. The TT state was further identified by correlating transient kinetics obtained from time-resolved emission scan (TRES) and pump-probe spectroscopy. In a recent study, *Stern et al.*[95] reports the influence of crystallinity on TT dynamics by comparing several different films of TIPS-Tc with varying crystallinity: polycrystalline and disordered films. Kinetics of TT states vary with crystallinity of films greatly and they break apart to form free triplets (in nanosecond timescales), in disordered films. We note here that the disordered films in the report has a weakly emissive TT state with a broad emission centred at 610 nm, similar to that of the aged NPs in the present chapter. This work will thus serve as basis for the identification of spectral signatures in the current study on TIPS-Tc NPs. We start by investigating the presence of the broad, low-energy emission from the NPs that is absent in solution and explore its transient behaviour by time-correlated single photon counting (TCSPC) measurements.

PL spectra obtained at different timedelays (1-20 ns) from TRES are normalized by area for better visual clarity of various spectral components involved (see Figure 4.8). Each spectrum in this 2D TRES represents the PL spectrum of the system at the given timedelay. Note that the figure shows the presence of an isoemissive point. The presence of an isoemissive point in an area-normalized TRES plot indicates a precursor and successor process, suggesting one evolving from the other, temporally[126]. The temporal evolution between the two emissive species is manifested as change in absolute concentrations, manifesting as changes in their relative PL. The initial-time spectra resemble that of S_1 PL in dilute molecular solutions, whereas spectra after 5 ns show a distinct red-shifted, broad emission centred around 620 nm. Spectral deconvolution by singular value decomposition (SVD) mediated global analysis of the TRES data further confirms the presence of two distinct emissive species: (i) a fast decaying S_1-like species with structured emission, and (ii) a species formed at later times with broad, low-energy emission. The low-energy species looks akin to the triplet-pair state (TT) in TIPS-Tc aggregates in solutions, reported before. Comparing the PL spectrum of the solution with that of the NPs in the present study, the broadening of the spectrum at lower energies in the latter suggests the formation of a comparable TT state. The TRES spectrum at 1 ns in the NPs is thus assigned to S_1, similar to the molecular S_1 state in solutions of TIPS-Tc. At 5 ns and beyond, the broad emission centered on 610 nm is assigned to the TT state, like that observed in disordered films before. The unusually long-lived nature of the S_1 is attributed to triplet-triplet annihilation and the re-formation of S_1 or the presence of an equilibrium between singlets and TT states.

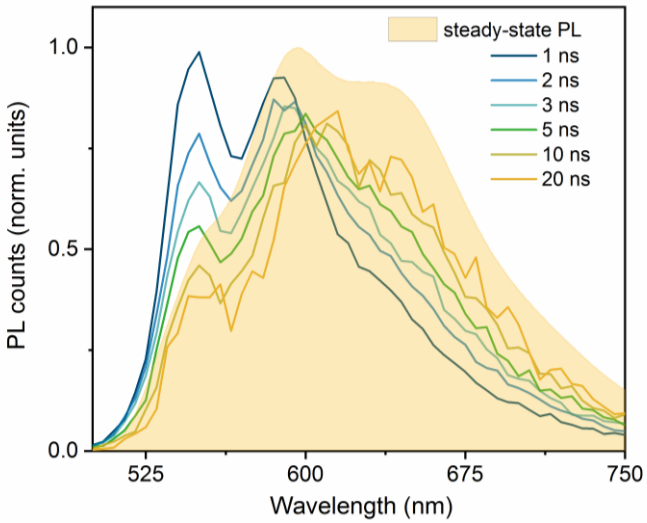

Figure 4.8-Time-resolved emission scan (TRES) of NPs at 470nm excitation. TRES data recorded from 1 ns to 20 ns, area-integrated and normalized to maximum counts. The early-time spectra remains close to that of the S_1 state, while the later forming (>5ns) low-energy emission centred at 610nm resembles TT emission reported in disordered films of TIPS-Tc. The steady-state PL from Figure 4.7 is overlaid on the timeslices to show its origin and temporal break-up of various spectral regions. The sample was excited at 470 nm to capture the PL profiles.

The kinetics of PL in the range of 540 nm to 700 nm indicate the presence of more than one emissive species when excited at 470 nm. Figure 4.9 shows the emission kinetics at 545 nm, 580 nm, 610 nm and 660 nm, normalized to highest peak count. Notice that while the decay of 545 nm and 580 nm emissions show a significant fast-decaying species (faster than instrument response ~300 ps) as well as a slow-decaying species (ns-lived), decays of the 620 nm and 660 nm emissions show only a slower decaying (ns-lived) species. Also, we note the delayed rise time of about 1ns in the emission kinetics at 620 nm and 660 nm, which we shall return to later.

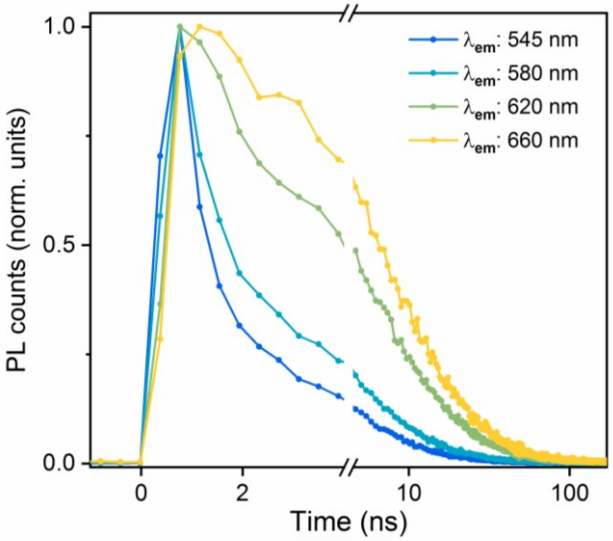

Figure 4.9-PL kinetics of various S_1 and TT spectral regions. Early-time species resemble S_1 and later (>5 ns) species resemble emissive TT states reported in TIPS-Tc films before. The low-energy TT emission rises within 2 ns and has a lifetime of 50 ns.

At this stage of investigating the emissive TT state we are left with the following questions.

(i) The normally non-radiative, dark TT states decouple to form free triplets during SF. Despite the emissive nature of TT states in TIPS-Tc NPs, does SF still occur with high efficiency?
(ii) What is the role of this emissive TT state in SF of TIPS-Tc NPs?
(iii) How does morphology influence photophysics of SF in TIPS-Tc NPs?

We try to answer these questions in the following sections.

4.5.2 Singlet Fission Mechanism in Nanoparticles

Analysis of time-resolved PL of various spectral components in section 4.5.1 unravel the ns-dynamics of the emissive S_1 and TT states. However, processes such as S_1 decay and formation of $2T_1$ due to SF must be looked at more carefully at faster timescales, in ps or fs. This section discusses fs and ps-dynamics of processes involved in SF, in TIPS-Tc NPs.

The femtosecond pump-probe spectra of the NPs when pumped with a broadband pulse centred at 530 nm (< 12 fs pulse duration, 505-555 nm), is shown in Figure 4.10. Spectra for time delays from 40 fs to 100 ps show typical spectral features expected from TIPS-Tc, as reported elsewhere. These features include ground state bleach (GSB) at 545 nm (assigned from 0-0 absorption peak), stimulated emission (SE) at 580 nm (assigned from PL) and photo-induced absorption (PIA) at higher wavelengths (assigned to multiple species). The existence of an isosbestic point at 590-600 nm in the pump-probe data from early times is of particular interest here. An isosbestic point denotes the presence of multiple spectral components that contribute to absorption at certain wavelengths to remain constant during the course of evolution between these components[127]. The negative nature of the isosbestic point here and its early appearance (< 200 fs) suggest the presence of a second species with significant absorption (PIA) in this region (590-600 nm) from as early as 200 fs. Also, note that during the experimental time window (>100 ps), this negative isosbestic point remains, though subtly blue-shifting by ~8 nm. Shifting of the isosbestic point suggests the variation in spectral populations in this region or in simpler words, rapidly evolving S_1 and TT population kinetics. Therefore, the kinetics of S_1 obtained from the decay of $\Delta T/T$ at 580 nm (S_1 SE) will contain contributions from the second species. Kinetics of the 580 nm S_1 SE band gives a time constant of 18 ps, which is not the S_1 lifetime but that of the *mixed* species, a rather ineffectual numerical quantity. Hence, we resort to an SVD-based numerical method to deconvolute multiple physical components from similar spectral regions that are *mixed* in nature.

We have now established that the presence of a negative isosbestic point indicates a secondary PIA that is generated near-instantaneously (< 200 fs in this case) which then does not undergo considerable population decay. However, one may not confuse this with the early-emergence of negative isosbestic points in recent literature on SF in solutions of TIPS-Tc. Such effects may creep in by changes in refractive index due to local sample heating, presence of hot ground states, sample

degradation in solution etc. The evidence we see in films of TIPS-Tc NPs however is due to a negative PIA growing in, attributed to TT states, clarified kinetically.

An important detail to remember is the differences in measured timeconstants by means of various experiments performed, especially while comparing transient data from absorption and emission measurements. For instance, the reader may notice that the PL lifetimes for S_1 decays do not match with the stimulated emission decays measured using pump-probe experiments. This variation is not indicative of the physical phenomenon under observation, but rather limited by the time resolution of the experiments, for example, geminate and bimolecular triplet-triplet annihilation to form S_1, resulting in an apparent longer lived S_1.

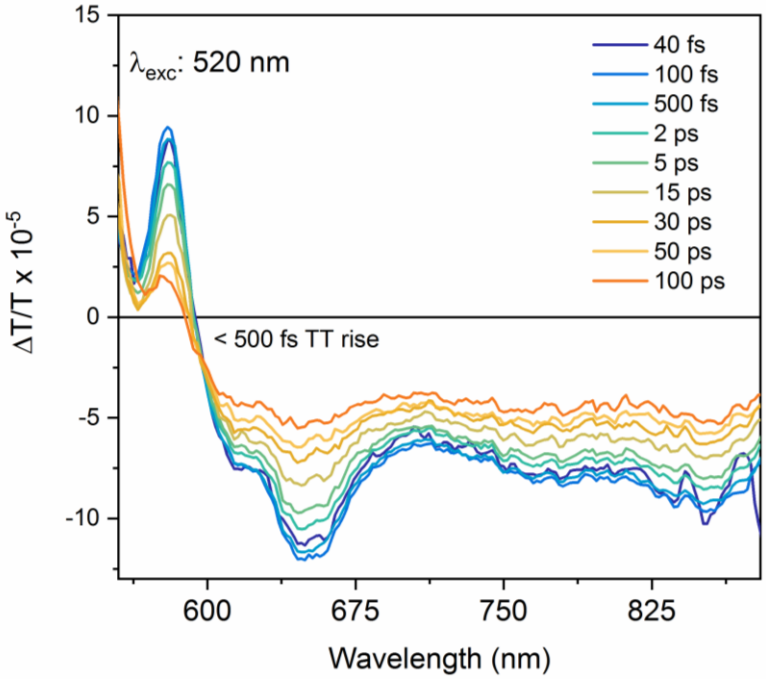

Figure 4.10-Ultrafast (fs) pump-probe data of NPs excited at 520 nm. Spectra at time delays from 40 fs to 180 ps. (a) SE and PIA of S_1 decay with a lifetime of 18 ps. The presence of a negative isosbestic point suggests two species and DAS confirms the same.

Singular Value Decomposition (SVD) sheds light of distinct species from the data above and individual decay components for these species are identified. Further, we used Decay Associated Spectral (DAS) analysis to fit the spectral data with

weighted kinetics obtained from SVD. See chapter 3 for further details on DAS and SVD. Two major, kinetically distinct components are identified using this method from the data shown in Figure 4.10. The short-lived component is identified as the S_1 state and the long-lived component is spectrally similar to the TT state observed in reports of disordered films of TIPS-Tc, with a distinctive PIA peak around 620 nm. The two major populations with associated kinetics calculated by this method are shown in Figure 4.11. The DAS-resolved S_1 state with a lifetime of 10 ps and TT state with a lifetime of 150 ps are shown in this figure. The S_1-dominating spectrum at 1 ps and TT dominating spectrum at 100 ps are overlaid in the figure to draw a comparison between the DAS components and the raw data. S_1 has peaks at 580 nm, 650 nm and a near-IR peak at 835 nm, while the 620 nm peak and a broadened 835 nm peak are assigned to the TT state. While the raw spectrum at 10 ps largely resembles S_1, the spectrum at later times (100 ps) looks like S_1 that has been *pulled* down by a large PIA below 650 nm. The DAS component we assigned as the TT state has a PIA signature in this region and a major peak at 620 nm. This *pulled negative* effect is attributed to the large population of TT states and a quickly diminishing S_1 population, in these timescales.

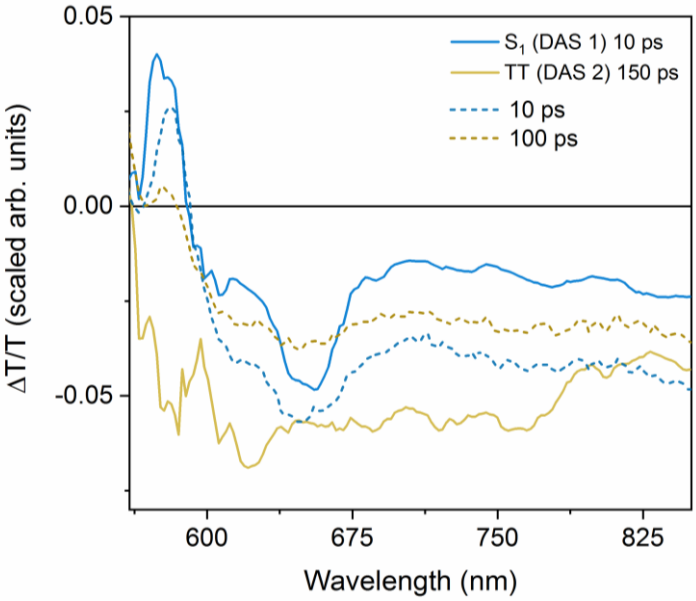

Figure 4.11-Spectral deconvolution by DAS/SVD of fs pump-probe data. Two distinct components were obtained from numerical analysis (DAS) assigned to S_1 and TT state with associated time constants, 10 ps and 150 ps, respectively.

4.5.3 Ultrafast TT Formation

Spectral deconvolution of S_1 and TT states from fs pump-probe data as discussed above confirms the ultrafast formation of TT states in TIPS-Tc NPS, similar to that reported by *Stern et. al.* in TIPS-Tc films[95]. The kinetics associated with S_1 and TT populations are fit to the pump-probe data by numerical methods, as shown in Figure 4.12. S_1 kinetics estimated from DAS gives a lifetime of 10ps, however a faster S_1 decay which diminishes 20% of its initial population occurs within 200fs, correlated to the rise of the TT state in the same timescale, carefully dug out by the algorithm. This also compliments the presence of a negative isosbestic point from, as early as < 200 fs, in the Figure 4.10. The TT state lives beyond the experimental time window, and longer time-range experiments are discussed in the following sections to investigate the fate of the TT states.

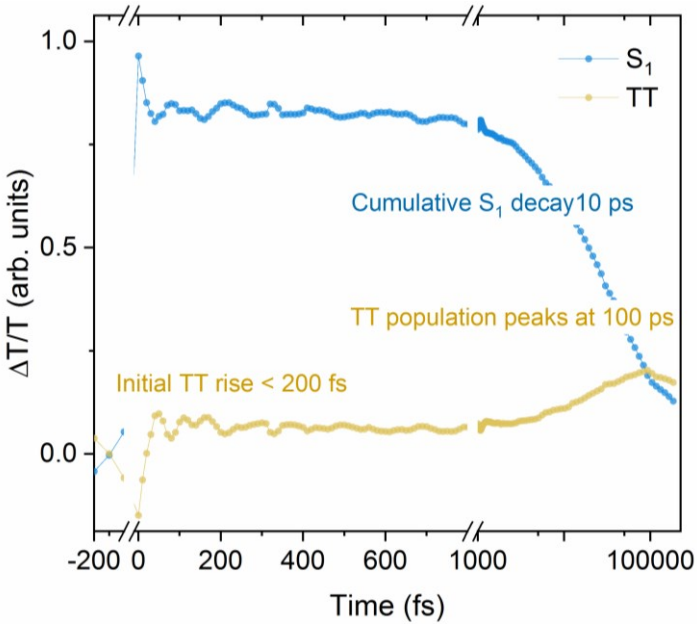

Figure 4.12-Kinetics of S_1 and TT populations obtained by global analysis of fs pump-probe data by DAS. A rapid initial decay of S_1 is correlated with the prompt-rise of the TT population within 200 fs. S_1 has a lifetime of 10 ps and TT decays with a ns-lifetime.

4.6 Photo-Engineering TT Formation Pathways

Things don't always go as planned, Mr. Angier. That's the beauty of science.
-Nikola Tesla, The Prestige

The ultrafast formation of TT states and their nanosecond lifetimes invite key questions to their physical nature as the rate limiting step in the formation of free triplets by SF. While investigating the ps to ns-photophysics of TT states in the NPs, we came across an interesting excitation energy-dependent behaviour of the SF pathway, discussed below.

4.6.1 Ultrafast Dynamics Influenced by Excitation Energy

For pump-probe experiments with longer timedelays (ps-ns), the films were excited with a 100 fs narrowband (FWHM: 15 nm) pulse at 532 nm, 500 nm and

480 nm. Pump-probe spectra with timedelays between 1ps to 1.2ns from these experiments are shown in Figure 4.13. Decay kinetics of the SE band at 580 nm gives a lifetime of ~12 ps when excited at 532 nm, 17 ps when excited at 500 nm and 28 ps at 480 nm excitation. This is different from the decay time of 18 ps of the same SE band obtained from broadband excitation. The difference in SE lifetimes may be due to the nature of excitation used. The fs-broadband pump (12 fs, FWHM:50 nm) excites a broad ensemble of states, giving rise to *mixed*, long-lifetimes. However, the narrowband pump (100 fs, FWHM:15 nm) for the ps-ns experiments excites specific sub-ensembles of electronic states, giving rise to variant, distinct lifetimes depending on the *mixed* nature of states probed, depending on the excitation energy used.

Importantly, upon excitation at 500 nm and 480 nm (narrow-band excitation) we observe the emergence of a spectrally different secondary species with increasing positive $\Delta T/T$ around 650 nm beyond 1ns. We return to this feature later in section 4.6.2. Other notable changes on exciting with higher energy excitations include: (i) the near-IR peak at 835 nm becomes sharper and more structured (S_1 peak) and (ii) the presence of sharper peaks at 900 nm and 964 nm, which are absent when excited at 532 nm. The 964 nm (1.29 eV) peak has been previously linked with the formation of TT species in a previous report on TIPS-Tc films[95]. In this study, we see the 964 nm peak at times as early as <1 ps, indicating its link with prompt TT formation.

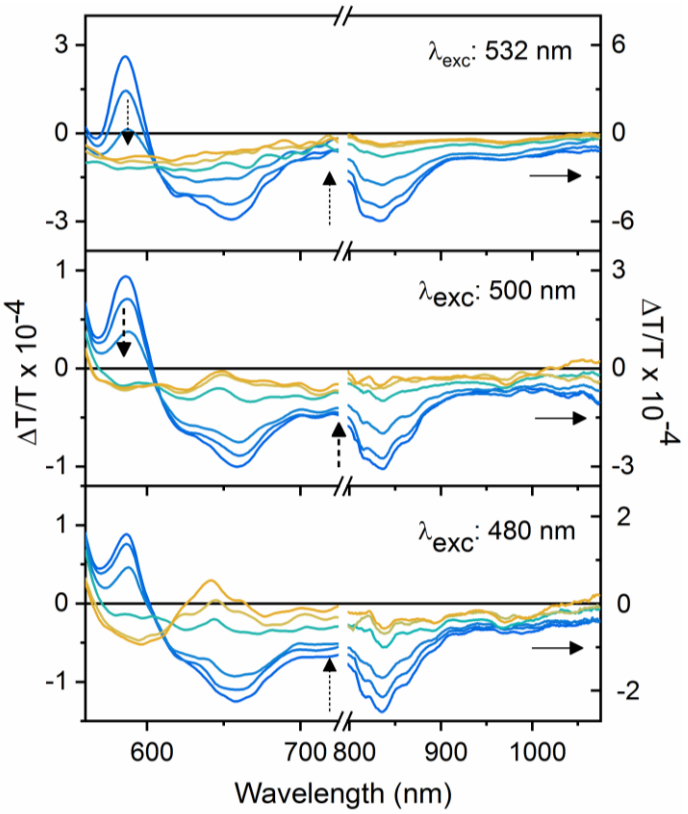

Figure 4.13-Narrowband pump-probe (ps-ns) spectra of NPs vs excitation energy. Spectra from time delays between 1 ps (blue) to 1.2 ns (orange) when excited at 532 nm, 500 nm and 480 nm, top-down. The spectral nature of S_1 state remains similar at all three λ_{exc}, but that of the intermediate TT state varies greatly. While at lower λ_{exc} bands at 900 nm and 970 nm become sharper, at higher λ_{exc}:480 nm TT states exhibit ns-emission at 620 nm.

Global analysis of the data by DAS identifies two distinct species when excited at each of these three energies, as shown in Figure 4.14. Based on previous reports and the fs pump-probe data presented in Figure 4.10 we assign these two species as S_1 and correlated TT states.

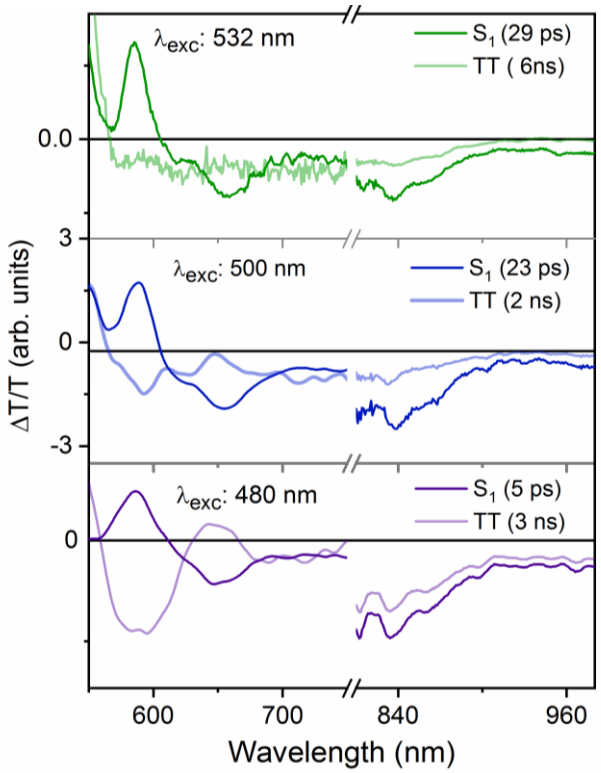

Figure 4.14-DAS components fitted through SVD of the (ps-ns) pump-probe data when excited at 532 nm, 500 nm and 480 nm (top-down). Decay constants associated with S_1 decreases with λ_{exc}, while the TT time constants fall out of the experimental time window and thus show the limiting value or beyond (2 ns).

The kinetic constants associated with S_1 and TT populations by DAS are shown in the figure above. To corroborate these results from DAS, we performed another method of spectral deconvolution by the genetic algorithm (GA, see section 3.6.2 for details on the method). Kinetics of spectral components identified as S_1 and TT states obtained by GA are shown in Figure 4.15, as a function of excitation energy. The corresponding spectra are shown in *Thampi et.al*[100]. The significant differences observed in kinetics by both methods with respect to λ_{exc} are as follows.

(i) S_1 lifetime increases from 9 ps to 28 ps when λ_{exc} decreases from 532 nm to 480 nm.

(ii) The ultrafast formation of TT states with the broadband pulse at 520 nm (see section 4.5.3) is absent when exciting the sample with narrowband, 100 fs pulses at λ_{exc}: 532 nm, 500 nm and 480 nm. Instead, ps-scale rise of

the TT state are observed. The rise-time of the TT population, deconvoluted via GA, are 2 ps when excited at 532 nm, 4 ps at 500 nm and 7 ps at 480 nm excitation. The absence of an ultrafast rise of the TT states with narrowband excitations may be due to the loss of vibrational coherence of the TT state or lack of suitably high time resolution.

(iii) TT kinetics from GA in Figure 4.15 are normalized with respect to the S_1 maximum and this gives us an estimate of the TT yield with respect to S_1. Within the limits of these estimates, TT yield is the highest (<0.8) when excited at 532 nm (i.e. 0.8^{th} of a TT state generated for every S_1 state) and the lowest (<0.4) when excited at 480 nm. Since a quantitative estimation of the TT extinction coefficient is not possible with a two-pulse pump-probe experiment, this is the closest we get to estimating TT yield in this study. Comparison of PIA intensities of TT (600 nm band) with respect to S_1 (650 nm band) in the pump-probe experiments shows the same trend as explained in the Table 4.1.

In order to verify this trend obtained from GA kinetics, we perform a similar TT yield calculation directly from DAS of the raw data, which gives similar results. DAS analysis on narrowband pump-probe data deconvolutes the processes of S_1 decay, S_1 to TT conversion and TT decay. The spectra corresponding to the DAS components are shown in Figure 4.14, with their respective timeconstants. SF is a bimolecular process, where a molecule in S_0 state interacts with the S_1 state, to give rise to a mixed S_1-TT state, which then decays into the TT state, followed by decoupling of TT into free triplets. Thus, the lifetime of the initial state $[A]_0$, $t_{0.5}$, is given by,

$$t_{0.5} = \frac{1}{k\,[A]_0}$$

where k is the rate constant associated with the decay of species A. Assuming that the initial concentration of A is constant, we extend this to S_1 and TT states. The lifetimes of S_1, TT or the mixed intermediate (S_1-TT) states are therefore inversely proportional to their respective rate constants. Thus, the trend in TT yield with respect to S_1 with varying excitation energies may be derived from the

ratio between the timeconstants of S_1-TT conversion (B) and that of overall TT decay (A) as given in Table 4.1. To compare the TT yield obtained from normalized GA kinetics with that calculated from DAS time constants, the value obtained by the latter are normalized by 0.7, the highest yield of TT estimated from GA at 532nm excitation. The normalized values of TT yield from DAS time constants show that the yield of TT is higher when excited at lower energies. Interestingly, the normalized estimated TT yields obtained from GA and DAS are strikingly close, enhancing the reliability of these numbers.

We note that the changes in photophysics of excited states by a difference of 150-200 meV in excitation energy are rather dramatic. So far our understanding of SF in the NPs goes as follows. Upon photoexcitation, S_1 decays to form coherent TT states under 200fs depending on the nature of excitation. When excited with energies higher than the HOMO-LUMO gap corresponding to the lowest S_1 transition (2.3 eV or 530 nm), the TT states generated have a rise-time typically in ps. However, the rise time of TT state in ps-timescale does not complement the S_1 decay lifetimes in all of these experiments. This could be due to the following reasons.

(i) The initial S_1 population follows different pathways, with a fraction of them forming TT states while the rest relaxing to S_0. This supports the varying TT yield with respect to the S_1 population, estimated at different λ_{exc}.

(ii) The equilibrium between S_1 and TT states is governed by the nature of the excited states, in particular, the extent of *mixing* of these states. This explains why the time constants associated with the S_1 and TT states vary with λ_{exc}.

(iii) As the result of energetic and entropic factors influenced by the geometry of the molecules in the NPs (discussed further in Chapter 7), the S_1-TT equilibrium may be pushed to favour the reverse mechanism, triplet-triplet annihilation (TTA). TTA leads to longer-than-expected S_1 lifetimes that do not complement the prompt TT rise time of 200 fs. The push in S_1-TT equilibrium backwards depends on their respective populations, which are experimentally observed to be excitation energy dependent. Kinetic

analysis in this section fits decay pathways with mono-exponential timeconstants. Since S_1 decay and subsequent TT rise are not necessarily mono-exponential processes as we see from the excitation-energy dependence data.

Table 4.1-Estimating TT yield from DAS and GA kinetics.

	$\tau_{\text{TT decay}}$ (A)	$\tau_{\text{S1 to TT}}$ (B)	B/A	B/A norm. to 0.7	TT/S_1 from GA kinetics
532 nm	24 ps	2 ps	0.083	0.7	0.7
500 nm	57 ps	4 ps	0.070	0.59	0.48
480 nm	290 ps	14 ps	0.049	0.41	0.4

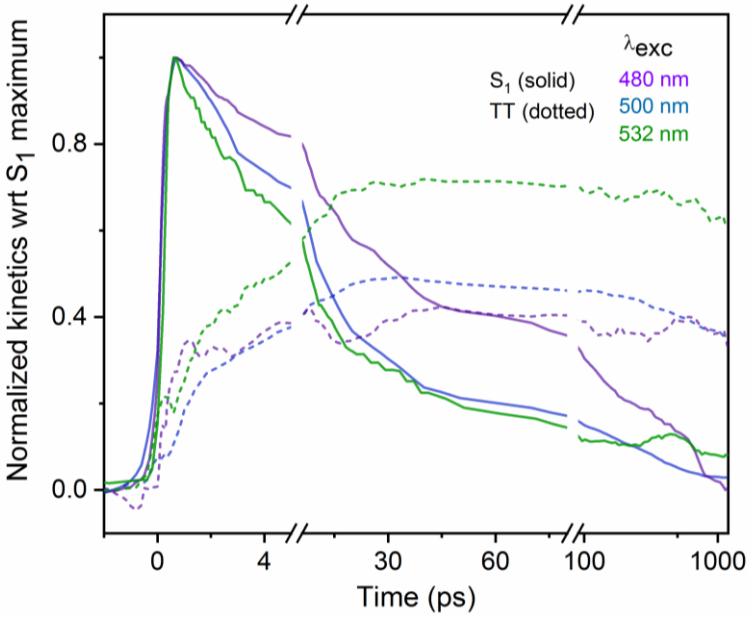

Figure 4.15- λ_{exc} dependent kinetics of S_1 and TT populations from GA. Kinetics of S_1 (solid) and TT (dotted) states at respective excitation energies fitted by GA upon spectral deconvolution of pump-probe narrowband pump-probe data. All kinetics have been normalized with respect to their corresponding S_1 maximum.

4.6.2 The Emissive TT state

We now move to how altering the excitation energy influences excited state populations involved in SF. Earlier we briefly mentioned the difference in spectral features of TT states at different excitation energies while that of S_1 remained fairly constant. The effect is most prominent when excited at 480 nm, where TT states rise >5 ps and a positive $\Delta T/T$ feature centred at 650 nm emerges by 1 ns. The delayed, low-energy 650 nm feature though absent when excited at 532 nm, shows a mild presence at similar timescales when excited at 500 nm, and strongly at 480 nm. The ns-delayed rise of this positive feature from ps-ns pump-probe data matches the delayed rise (>1 ns) of a similar low-energy emission at 620 nm in TRES data shown in Figure 4.9 (λ_{exc}: 470 nm). The delayed PL at 620 nm in the TRES data was assigned to an emissive TT state in section 4.5.1. Spectral deconvolution of the λ_{exc}-dependent pump-probe data shows that this later forming intermediate can be assigned to the TT state due to spectral similarity to the long-time PL spectrum, and the kinetics it follows. With experimental support from ps-dynamics alongside a ns-rise time of TT emission, we assign this nanosecond positive feature to be arising from the TT state as its SE. This suggests direct, radiative relaxation of TT to S_0. Another interesting aspect of this study is the inability to directly access the emissive TT state from exciting the ground state geometry of the molecule, S_0. This is not entirely surprising due to the following reasoning. Following initial excitation, the excited state wavepacket moves away from the Frank-Condon point, inducing changes in molecular geometry that may enable previously forbidden transitions to become allowed.

Acenes have been recently proven to show emission from intermediate TT states previously. Two-photon photoemission studies on tetracene suggest that TT-S_1 states have some multiphoton character, which follows that the TT state has finite S_1 character. A Herzberg-Teller type mechanism[128,129] has been raised by several studies to explain direct emission from TT states of acenes[130]. This requires breaking the degeneracy between S_1 and quintets (strongly bound TT pairs) by

suitable interchromophore exchange coupling, considering a four orbital basis of the pair excitation states. A recent study based on low temperature ESR of TIPS-Tc films[112], places an upper bound of 4.2 meV on this exchange energy for TT states that form in ns. TT states in TIPS-Tc NPs are formed in ps, much shorter than the TIPS-Tc films in the ESR-based study. We will soon discuss the process of TT states decoupling to form free triplets in ns in the following section. The multiexcitonic TT states influenced by λ_{exc} in the NPs are unlikely to be of quintet character due to the vast difference in timescales.

So far we have compared TT states produced by TRES data excited at 47 0nm and pump-probe data excited at 480 nm. For better credibility of our explanation for induced emissive nature of TT by excitation energy, we perform TRES studies complementing the λ_{exc} dependent pump-probe experiments at 530 nm, 500 nm and 480 nm in Figure 4.16. The broad emission assigned to the TT state at 620 nm is present when excited at 480 nm and 500 nm. However, at 532 nm excitation the emission spectrum is dominated by S_1 emission, which also differs in kinetics from the former. The kinetics of S_1-like and TT-like regions from these measurements confirm the presence of multiple spectral species. This validates the λ_{exc} dependent pump-probe dynamics of TT state beyond 1ns.

To summarise, when TIPS-Tc NPs are excited with varying λ_{exc} the initial Frank-Condon point varies, altering the relaxation pathway for excited states. Our results show that conditional to where the initial wavepacket forms on the excited state potential energy surface, the evolution from S_1 to TT can be longer as demonstrated by changes in decay rates of S_1. Following this, TT states of different spectral and temporal features are formed with varying λ_{exc}, leading to different TT yields. The results from TRES together with pump-probe spectroscopy prove that formation pathways of various radiative and non-radiative SF intermediates such as TT states can be photo-engineered, or manipulated by λ_{exc}. The consequence of this is rather relevant when SF systems are incorporated in PV devices. For PV designs based on SF materials, the input source of excitation is broadband solar spectrum that can give rise to various

excited state populations through different pathways depending on photon flux per energy band, based on our findings. This means that the process of SF can be driven forward or backward, depending on the population of various states and associated equilibria.

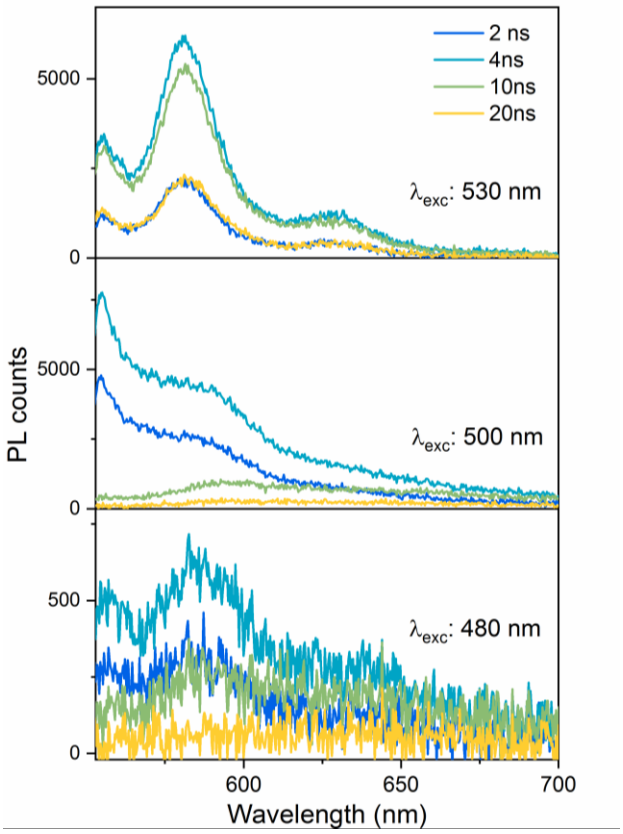

Figure 4.16-Time-resolved emission spectra (TRES) with excitations at 530 nm, 500 nm and 480 nm. Spectra at time delays from 2-20 ns show that when excited at 532 nm emission is dominated by the singlet and at higher energies is dominated by a red-shifted broad emission. As the TT is more emissive at higher energies, the kinetics of this component clearly deviates from that of the singlet, unlike that at 532nm excitation.

4.6.3 Excitation Dependent TT Formation: Nanoparticles vs Films

From structural characterisation of the NPs in our work, we have concluded that the NPs have a crystalline core and an amorphous exterior. The role of

morphology in facilitating SF has been studied in polymorphic phases of various acenes, as well as films with varying crystallinity. Thus, it is important to compare the λ_{exc}-dependent formation pathways for multiexcitonic states such as TT. To pursue morphology dependence in SF dynamics, we conducted ps-ns pump-probe experiments on disordered films of TIPS-Tc that have been previously reported to show efficient SF in similar experimental conditions. Narrowband pulses (~100 fs) at 532 nm and 480 nm were used to excite the samples and the pump-probe data recorded with a visible probe (560-750 nm) are shown in Figure 4.17.

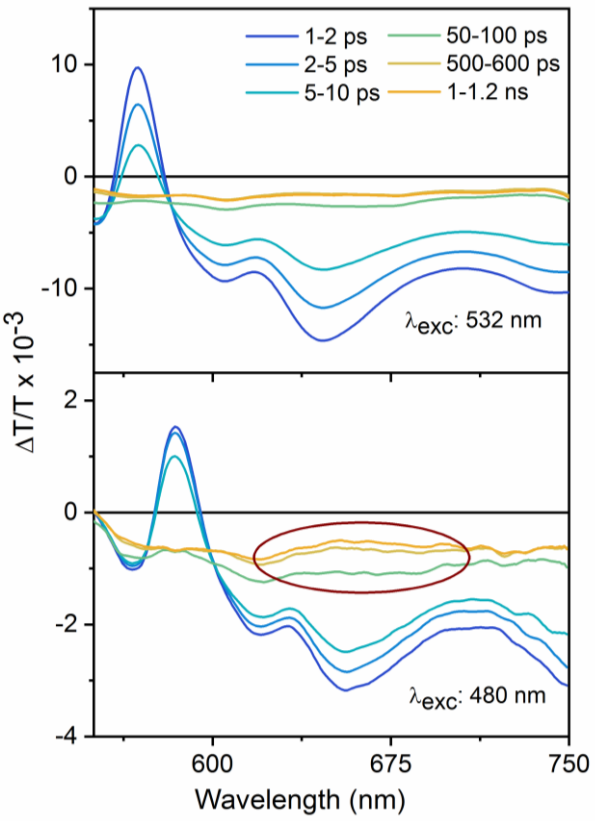

Figure 4.17-λ_{exc} dependent pump-probe data of disordered TIPS-Tc films. Pump-probe data with time delays 1 ps to 1.2 ns when disordered films of TIPS-Tc were excited with narrowband excitations at 532 nm and 480 nm and recorded with a visible probe. The initial forming S_1 decays into TT state at both excitation energies. Notice a positive $\Delta T/T$ feature at 650 nm growing in at λ_{exc}: 480 nm, but not at 532 nm.

At both excitation energies the initially formed S_1 decays into an intermediate TT state as reported elsewhere. The TT state formed at 532 nm has PIA peaks at 620 nm, 670 nm and 750 nm, similar to that in the NPs. The higher energy excitation at 480 nm induces the formation of a positive $\Delta T/T$ feature at 650 nm (red circled area in the figure above), the emissive TT state, that grows in by 1 ns. Though this growing species in TT feature in disordered films does not becomes a positive and does not show emissive feature like in the NPs, the trend observed upon higher excitation energies, encouraging the system to access multiple formation pathways for TT states, is consistent. We presume that the mixed crystalline core-amorphous exterior morphology of the NPs assists in geometry relaxation of excited states to favour TT emission to S_0 (through Herzberg-Teller mechanism explained before) at higher excitation energies. The fact that we see a similar effect in disordered films is quite encouraging to the generality of this phenomenon, one that has not been deemed important in SF studies before. The formation of different TT states and their varying kinetics shed light on multiple TT formation pathways, even leading to bright TT states that are accessible vibrationally via change in excitation energy, in different morphologies of this endothermic SF system.

4.7 TT to Free Triplets

TIPS-Tc films and other tetracene based systems[59,95,102] report very high triplet formation efficiencies (>120%), which is a vital marker for efficient SF. In this section we focus on the formation of free triplets (T_1) due to SF in TIPS-Tc NPs. To monitor triplet formation kinetics, we use pump-probe spectroscopy in the ns-μs time regimes as SF-generated triplets have been previously reported to live for longer than ns-timescales in TIPS-Tc films.

Pump-probe spectra at time delays from 1 ns to 5 μs when the NPs are excited at 532 nm and probed in the 580-1050 nm region are shown in Figure 4.18. The early time (1 ns) spectrum compares to that of the TT state with features such

as a strong PIA peak at 620 nm and broad PIA peaks at 835 nm, 968 nm and 1000 nm. This compares well with the TT state observed in ps-ns pump-probe data discussed before. The early-time spectrum (<5 ns) evolves into another spectrally distinct state within 10 ns with sharper peaks at 835 nm and 1000 nm, red-shifted peak at 972 nm (from the <5 ns TT peak at 968 nm), and a set of twin peaks at 890 nm and 925 nm. This later-forming (10 ns) state matches the sensitised T_1 spectrum of TIPS-Tc in solution and therefore confirm to be long-lived (~µs) triplets ($2T_1$) generated via SF. The rise of the new bands at 890 nm, 925 nm and sharpening of TT peaks indicate the decoupling of TT states to form free triplets localised on spatially separate molecules in the ensemble. Such long lifetimes of triplet states is beneficial for device-based applications of SF using NPs[72,74–77,80,92]. DAS analysis performed on this data gives rise to two distinct components that resemble the TT and $2T_1$ states as described above, shown in Figure 4.19. While DAS predicts a lifetime of 1 ns for the TT state, the triplets are µs-lived, essentially to the end of the experimental time window.

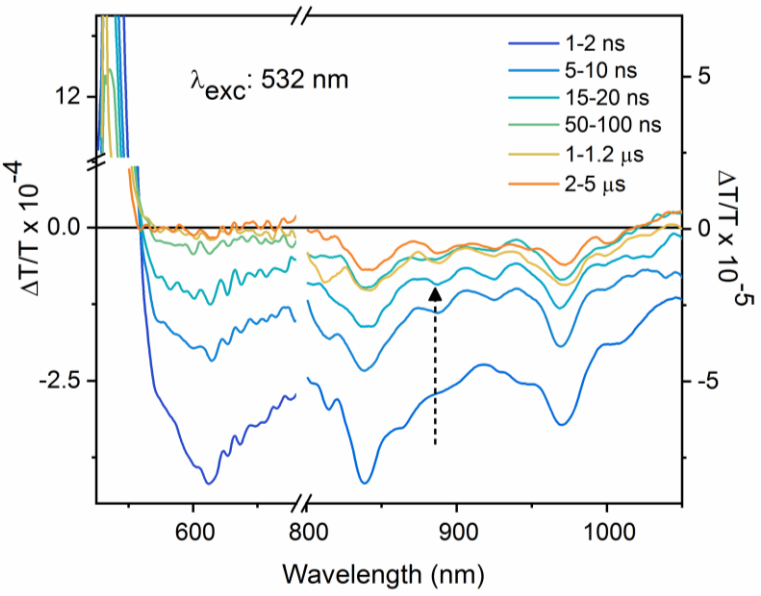

Figure 4.18-Nanosecond pump-probe spectra of NPs showing T_1 formation. Spectra when excited at 532 nm with time delays 1 ns to 5 µs. Formation of free triplets by decoupling of TT states is marked by the rise of new bands at 890 nm and 925 nm, and spectral shift from 964 nm to 972 nm, by 100 ns.

We now take a quick turn to the TRES data discussed before (Figure 4.8), where the 540 nm peak is tied to S_1 and that at 620-650 nm to the TT state. In order to correlate the ns TRES and pump-probe data together, we overlay the kinetics of these two emission bands from TRES, with the decay of the 965-970 nm $2T_1$ PIA band. Figure 4.21 shows kinetics of S_1 emission (blue), TT emission (orange) and the triplet state kinetics from pump-probe data (green).

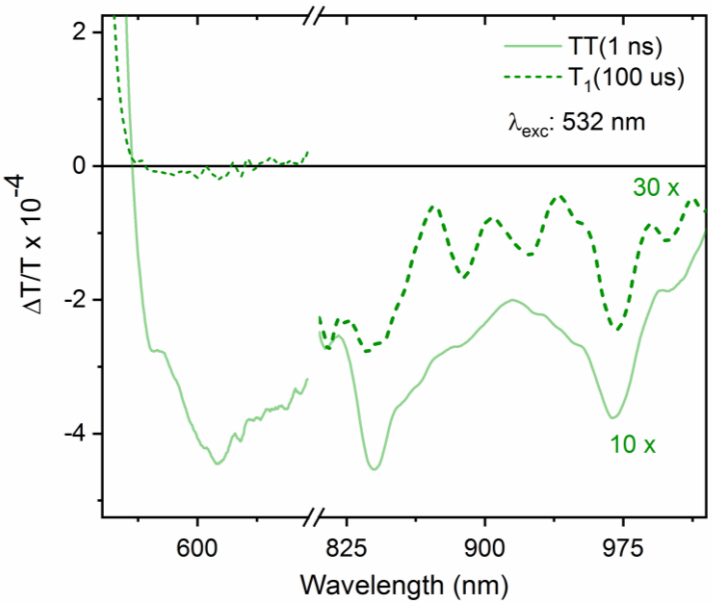

Figure 4.19-Nanosecond pump-probe spectral deconvolution of NPs. DAS spectral components after spectral deconvolution with clear spectral assignments to TT state and T_1 states.

Table 4.2-Time constants and spectral assignments for excited states.

λ_{exc}	fs-ps broadband 530 nm	ps-ns 532 nm	ps-ns 500 nm	ps-ns 480 nm	ns-µs 532 nm
S_1 decay	18 ps	12 ps	17 ps	28 ps	
TT rise-time	>200 fs	2 ps	4 ps	7 ps	
TT to T_1					3 ns
T_1 lifetime					>2 µs

From Figure 4.20 note that the TT emission kinetics at 660 nm (orange) matches the pump-probe ΔT/T kinetics at 965-970 nm (green) from early times up to 10ns. Beyond 10 ns, the latter diverges from the emission kinetics due to the formation of non-radiative triplets, only detected in the pump-probe experiment. This divergence is consistent with the timescale of $2T_1$ formation from TT states and confirms the spectral assignments for the states involved.

Table 4.2 summarises all spectral assignments and time constants associated with various species, along with the experimental conditions for them.

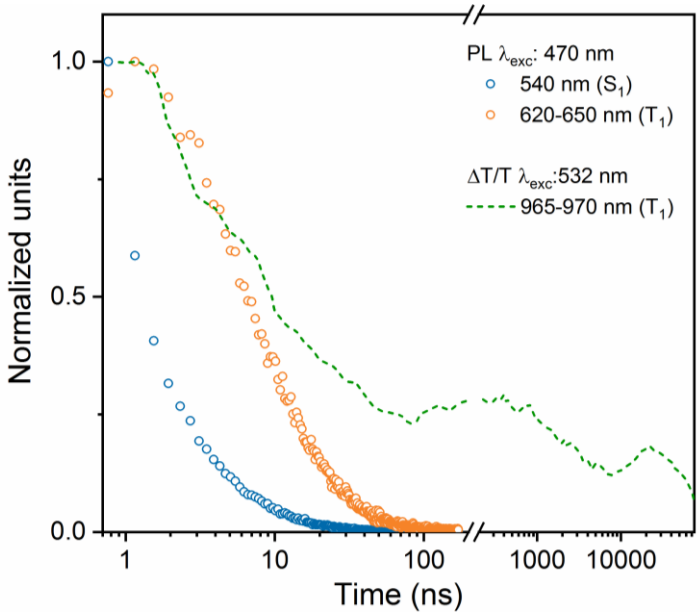

Figure 4.20- Comparison of long-time triplet kinetics from emission and pump-probe experiments. S_1 PL (blue) decays within 10 ns, TT PL (orange) and triplet PIA (green) decay along a common trace until ~10 ns after which they diverge, as free triplets form in these timescales. Triplets decay independently to TT emission beyond 10 ns.

The small details of life often hide a great significance.

-Alias Grace, Margaret Atwood

4.7.1 Shift in peak position and $2T_1$ formation

We note that in spite of distinguishable kinetic evolution of states with triplet character, shifts in peak positions of relevant marker bands shed light to this process as well. The kinetics of the mixed TT-$2T_1$ region in 965-972 nm (green) is overlaid on the change in the position of this triplet band (black circles) in Figure 4.21, which exhibits a similar bi-phasic behaviour as the triplet kinetics.

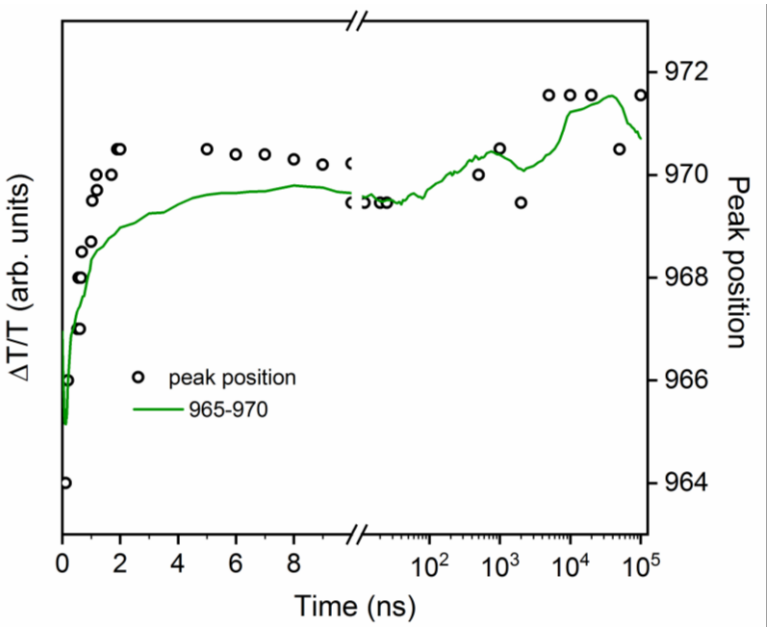

Figure 4.21-Kinetics of $2T_1$ formation and peak shifting of triplet band. Kinetics of the TT-$2T_1$ peak at 965-970 nm plotted against the peak shift observed during the same process.

TT dominated kinetics at early times (< 1ns) match the change in triplet peak position greatly. The longer second phase beginning from 100ns aligns with the formation of $2T_1$ states that are long-lived. Thus, the energetic evolution of the 964-972nm peak is a simple, yet reasonable marker for the break-up of TT to form free triplets in this system.

4.7.2 Influence of morphology in decoupling of TT to $2T_1$

The NPs prepared in this study have a very unique morphology as discussed before that governs the fate of excited states: a crystalline core and an amorphous exterior. In this section we try to find out the role of this peculiar morphology in the breakup of the TT states to form free triplets. For this, we compare our results to some published report[95] of TT and $2T_1$ dynamics influenced by film morphologies in TIPS-Tc.

TT states are known to form in a coherent and rapid (< 200 fs) fashion in both polycrystalline and amorphous films of TIPS-Tc[95]. While they decouple to form free triplets (~ns) in disordered films, they were observed to remain bound to μs timescales in polycrystalline films. The reason for such hinderance in $2T_1$ formation in polycrystalline films could be due to morphological restrictions and the inaccessibility of vibrational states that enable the break-up of the TT states. Owing to the mixed morphology of the NPs under study, we expect S_1 excitons to form in both the amorphous (disordered) and crystalline parts upon photoexcitation in sub-ps and ps timescales. Unlike polycrystalline films, we do not see the TT states living forever but rather they break-up to form free triplets. This leads to the possibility of TT states formed within the crystalline core diffusing to the amorphous exterior of the NPs, allowing them to relax into geometries that enable breaking up to form $2T_1$ states. This is suggestive of morphology driven diffusion of TT states and our results hint the possibility of TT migration, which is crucial to access morphologies that enable formation of free triplets.

We identify several potential spectral markers in pump-probe (ns-μs) data to clarify this. Figure 4.22 shows the pump-probe TT spectrum of disordered and amorphous films, and NPs, T_1 spectra of disordered film and NPs, and sensitised T_1 spectrum in solution. While the major PIA peaks at either ends of the spectral range (835 nm and 968 nm) remain similar (except for varying FWHM indicating TT to T_1 conversion)[113], there are significant differences in the 880-950 nm region. The TT spectrum of polycrystalline film show a broad peak at 910 nm, but with

no free triplets are reported to form in them. The broad 910 nm TT feature is absent in the TT spectra of disordered films and NPs, indicating the origin of this band in polycrystalline nature of the films. The presence of the twin bands at 890 nm and 925 nm in the NP T_1 spectrum is also shared with the sensitised T_1 spectrum in solution, however not with polycrystalline films. Thus, the twin peaks is clearly a marker of T_1 states. The energetic difference between these two bands is 460 cm^{-1}, which concurs with the ground state Raman mode at 470 cm^{-1}, assigned to C-C deformation vibration, observed in TIPS-Tc films. This analysis points out at the possible formation of TT states in the crystalline core of the NPs, their migration to the amorphous exterior where free triplets are formed from decoupling of TT states driven by morphology. We summarise these results of TT migration driven by morphology-gradient in the model system of TIPS-Tc NPs in Figure 4.23.

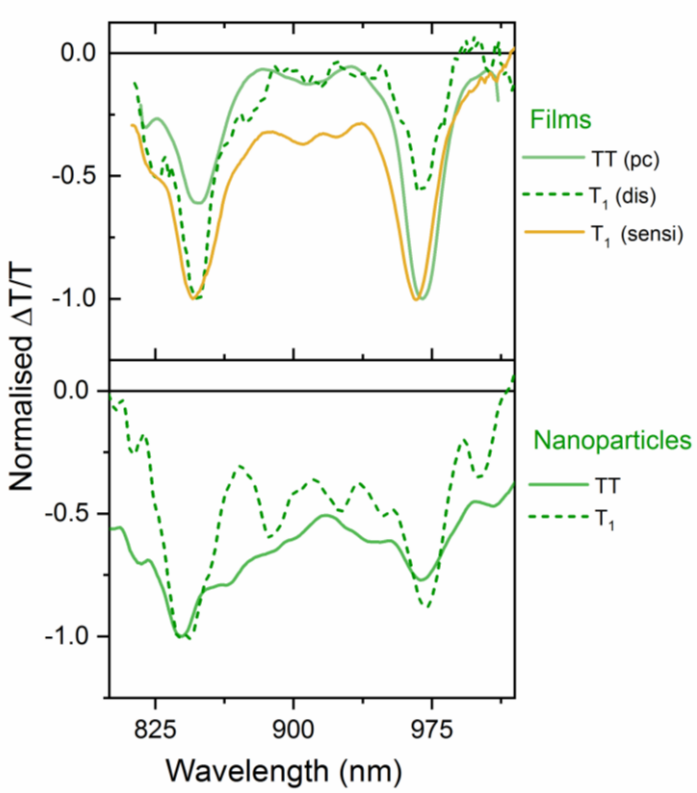

Figure 4.22-TT and T_1 spectral signatures influenced by morphology. TT spectrum of polycrystalline films (pc), T_1 spectrum of disordered films (dis) and solution sensitised T_1 spectrum (sensi) are shown in the upper panel. The broad TT peak at 910 nm splits into twin peaks at 905 and 930 nm in disordered films and the twin peaks (shifted due to phase difference) in solution. The presence of the twin peaks in the region might be originating from the lack of crystallinity. The TT spectrum of NPs in the lower panel does not have the twin peaks, indicating possibly higher crystallinity compared to T_1 spectrum with the twin peaks in the NPs, indicating that T_1 states are formed in the amorphous region on the exterior of the NPs. This suggests TT migration from the crystalline core to the amorphous exterior, that enables the breaking up of TT to form free triplets.

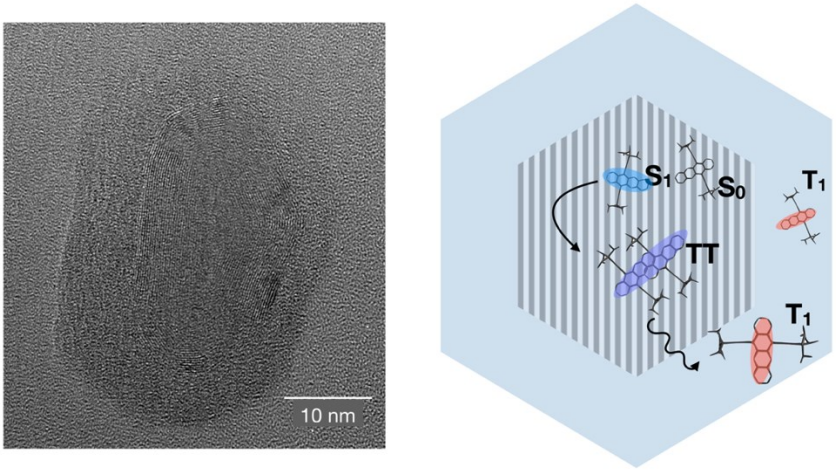

Figure 4.23-Mechanism of SF in NPs mediated by TT migration. Figure on the left shows the TEM of TIPS-Tc used in this study and cartoon on the right illustrates the mechanism of SF undergoing in the mixed morphology of the NP with a crystalline interior and an amorphous exterior. Photoexcited S_1 triggers (blue) the ultrafast formation of TT states (violet) in the crystalline core, which then migrate to the amorphous exterior facilitating the breaking up into free triplets, T_1 (red).

4.8 Conclusions and Outlook

In this chapter, we focussed on the role of morphology and nano-confinement of endothermic SF molecules, TIPS-Tc. We make a peculiar mixed morphology with a crystalline core and an amorphous exterior, characterised and assessed for crystallinity by electron microscopy. Time-resolved emission kinetics of the NPs show the emergence of an emissive TT state with a rise time of 1ns, when excited at 470nm. The emissive TT state complements the ns-emerging SE from the TT state in ps-ns pump-probe spectroscopy at similar excitation energy (480nm). We identify distinct S_1, TT and T_1 spectral and kinetic profiles from pump-probe spectroscopy.

Findings on SF in TIPS-Tc NPs developed in this chapter may be summarised as follows. The initially formed photo-excited S_1 decays into TT states that form in a coherent and rapid (<200 fs) fashion. Controlled by excitation energy incident upon the system or via 'photo-engineering' as we call it in this chapter, TT formation pathways vary largely in terms of spectral profiles and kinetics. Large differences in spectra and kinetics of excited states induced by changes in excitation energy imply that the initial relaxation away from the Frank-Condon point controls the choice of pathway for SF, with multiple distinct intermediates within the TT manifold formed in the process. These results have important implications for the mechanistic understanding of SF where the TT state is conventionally thought of as a single species. Despite being an endothermic SF system, TIPS-Tc NPs have the ability to access multiple TT states[131] on ultrafast timescales that allows SF to outcompete radiative recombination. The vital role vibrational dynamics play in mediating SF is brought forward by these results as well. Reasonable parallels can be drawn with the photophysics of molecular systems such as rhodopsin where the yield and reaction pathways are strongly dependent on the shape of the potential energy surface (PES) of excited states. Excited state reactions involving state crossing have been shown to be influenced by their PES beyond simple energetics and couplings between states in the ground state geometry of such systems. Future theoretical work will need to explicitly

consider the possibility of multiple trajectories along different potential energy surfaces, in order to provide a more accurate description of SF.

Further, we see decoupling of TT states to form free triplets in the NPs of mixed morphology. We find indicators of TT migration from the crystalline core to the amorphous exterior, where TT can access vibrational states and geometries that facilitate breaking up to form free triplets. Comparing this hypothesis with experimental data to that of polycrystalline and amorphous films reported before, we argue for a case of TT migration driven by a morphology-gradient. In the future, careful control of morphology, could result in well-optimized nanostructures where the directed flow and dissociation of TT states is achieved to maximize the generation of free triples for device applications.

Chapter 5

Singlet Fission Nanoparticles for Energy Transfer

In this chapter we modify the surface of TIPS-Tc NPs prepared in the previous chapter to make them suitable for triplet transfer to an energetically suitable inorganic system, PbS quantum dots. In Chapter 4 we discussed in detail about efficient SF in TIPS-Tc NPs. We see excellent triplet characteristics such as kinetics suggestive of long diffusion lengths, crucial to triplet transfer to inorganics. Inorganic systems such as PbS quantum dots have been explored and proven to be effective bridges from SF-generated triplets in the organics to Si in photovoltaics (PV) recently. Harvesting triplets by means of such organic-inorganic device architectures can boost PCEs in a PV device. Successful surface modification by means of encapsulating the NPs within micellar structures is performed in this work. Encapsulation within dynamic structures such as micelles induces crystallisation of the NPs within, making them closer to a decisive SF geometry that we define for endothermic SF systems. The morphology explored in this chapter showcases the fastest SF characteristics among thus far reported morphologies of TIPS-Tc. The NPs formed within micelles exhibit faster TT decay and free triplet formation by a factor of 3 compared to other morphologies of TIPS-Tc. These are indicators of attaining energetically stable, SF favouring crystal structure driven by micellar dynamics in solution. With triplet formation as fast as 100 ps within these new NPs of the order of ~300 nm, we attempt to couple PbS quantum dots and study triplet transfer between them.

5.1 Background and Motivation

The pursuit for structural schemes for highly efficient non-conventional PV cells have been a key focus of PV-design for many years now[72,74,75,78,81,101]. Recent efforts demonstrate ways to couple organics that down-convert blue photons to two near-IR photons, to inorganics for efficient triplet transfer and engineer them on to PV-device architecture[67,79,132–135]. These rather seminal works discuss the importance of energy-matching and introduce novelty in device architecture by coupling SF-organics with inorganic systems such as quantum dots (nanocrystals). Upon efficient SF and subsequent triplet transfer to the dots, one enhances the dot emission by effectively *brightening* the triplets, and improving device quantum efficiencies. Thus, the *Shockley-Queisser* (*S-Q*) *limit* for single-junction solar cells is overcome by harnessing high-energy photons and power conversion efficiencies (PCE) are improved by 30%[75].

Several structural designs such as thin films of pentacene with PbSe dots[133], or tetracene with PbS dots[67] have proven to be highly efficient for PV applications as shown in Figure 5.1. The device architecture contains a top layer of the SF material that absorbs high-energy photons and generates two triplets that are transferred to the inorganic (quantum dots+Si) layer beneath it. Meanwhile, the inorganic layer absorbs low-energy photons. The combination of these processes minimises *thermalization losses* in the device, overcoming the S-Q limit of single-junction solar cells. The triplets then undergo dissociation into charges at the interface between the layers, as depicted in the figure. Harvesting thus generated charge carriers improves PCE in this design compared to conventional single-junction PV devices[75]. PbS dots have been recently shown to couple with SF ligands with structural similarity to TIPS-Tc linked to the surface of the dots, that mediate triplet transfer from TIPS-Tc molecules in solution to the dots[79]. The effective strategy involving inorganic quantum dots and SF organics have been made possible due to long triplet lifetimes, and efficient energetic coupling between the two systems.

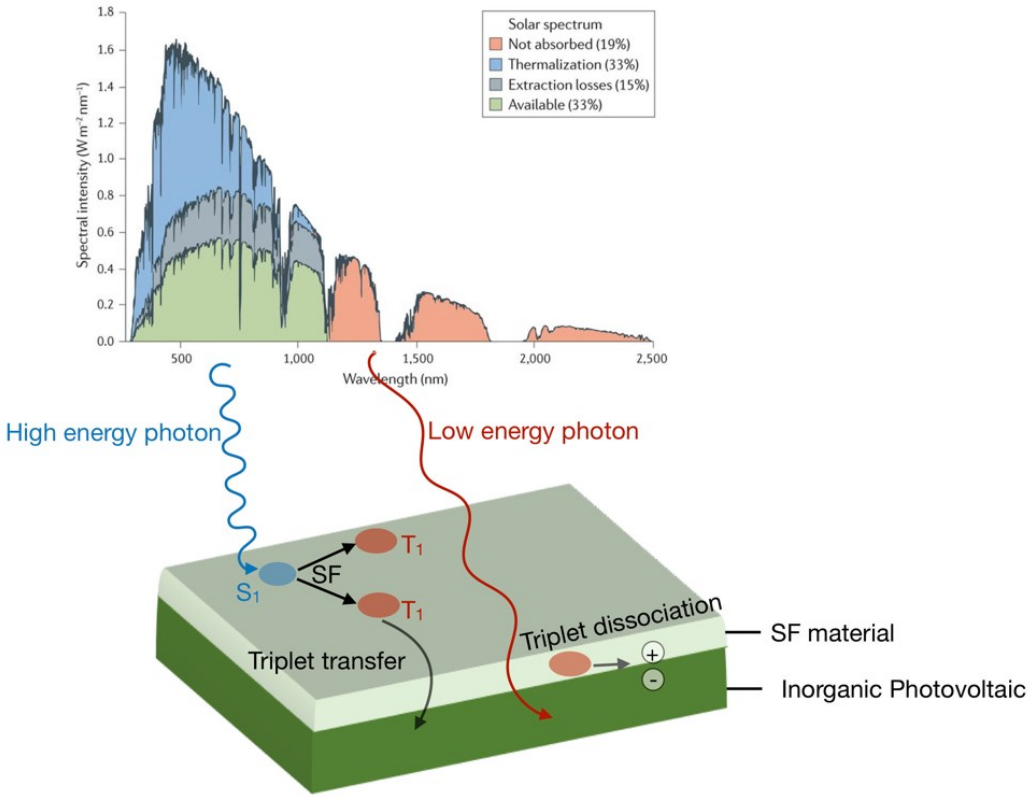

Figure 5.1-PV device design (adapted[15]) with coupled SF and inorganic layers. High-energy photons absorbed by the top layer (SF material) generates two triplets that are efficiently transferred to the inorganic-photovoltaic layer beneath it. Low-energy photons are absorbed efficiently by the lower inorganic layer. Triplet dissociation at the interface of the organic/inorganic layers gives rise to charge carriers and are manifested as a photocurrent output. Addition of a SF layer increases the PCE by 30% compared to a conventional single-junction PV cell.

This chapter can be broadly divided into two sections: (i) a highly efficient SF system, TIPS-Tc NPs[100] (introduced in chapter 4), is prepared for coupling with oleic acid (OA)-coated PbS quantum dots, (ii) to study triplet transfer between them. The major challenge and yet advantage of this system is designing these structures in the nano-regime. The organic NPs are about 30 nm in size, and we expect the coupling between these and 10 nm-sized PbS dots to be more effective due to increased surface interactions (higher surface-volume ratio). However, controlling morphologies and chemical affinities in these length scales is rather

complex and we touch upon a few key design parameters that will help us understand this better.

5.2 Tuning Morphology for Efficient Singlet Fission

The TIPS-Tc NPs in chapter 4 were prepared by means of a simple, well-reported method of re-precipitation[116]. The initially formed NPs in solution were 5 nm in size and the absence of surfactants led to their growth to ~30 nm. The process of ageing was arrested by embedding the NPs in a polymer matrix. While this strategy worked well for spectral measurements, it may not suffice for triplet transfer to the quantum dots. The reason for this is two-fold, as discussed below.

5.2.1 Polymorphism and Singlet Fission

The originally prepared bare NPs in Chapter 4 have mixed morphology with a crystalline core and an amorphous exterior that lead to some evidence of morphology-driven TT migration. This spatial migration of the coupled TT states to the amorphous exterior was followed by formation of free triplets. From structural analysis and differences in spectral features, the TT states formed in a more ordered (or polycrystalline) region and free triplets in the amorphous region were differentiated. This has been hypothesised in different film morphologies of TIPS-Tc by *Stern et. al*[95]. In this work that compared SF within film morphologies of TIPS-Tc, films of polycrystalline nature '*are composed of large (~100 μm) domains of aligned crystallites (100 nm diameter)*', as the growth of these films were by non-directed, solution deposition. X-Ray scattering analysis of these films '*predicts domains on the order of 90 nm*'. Thus, while crystallites of ~100 nm were present in these films, their geometry was not controlled resulting in its polycrystalline nature. In the same work, disordered films were formed by spincoating from solution. While this ensured uniformity in layer thickness across the film, molecules were randomly oriented. Experimentally it was shown that while TT states decoupled to form free triplets in disordered films, they lived long

enough in polycrystalline films to non-radiatively relax back to S_0. The reason for such morphology driven breaking up of TT states to free triplets could occur due to a few reasons. Solutions of TIPS-Tc show diffusion-limited SF above a concentration of 100 mg/mL[113] with the internal energies of S_1 and $2T_1$ making it endothermic by ~200 meV. Thus, energetics along with experimental evidence suggest that free triplet formation by SF is thermodynamically feasible in TIPS-Tc. However, unsuccessful triplet formation in polycrystalline films of TIPS-Tc can be ascribed to the lack of an appropriate SF geometry of neighbouring molecules that share the TT state. This brings us to the relevance of morphology and the phenomenon of polymorphism in SF materials.

Polymorphism is the existence of distinct ways of crystal formation of a molecule, mediated by difference in preparation methods by factors such as temperature, pressure and concentration of solutions used[136]. For SF systems such as pentacene[114,116,137], anthracene[50], tetracene[57,138,139] and others[140,141], multiple polymorphs exist depending on the method of preparation. These polymorphs are the most energetically stable structures at given conditions of macroscopic variables of the system. Depending on the polymorph one is dealing with, processes involving bond formation and breaking, migration of wavepackets and other excited state processes vary[142,143], especially for processes dictated by vibrational mechanisms.

SF in TIPS-Tc films[95] and NPs[100] involve the formation of photo-excited singlets (S_1) and the ultrafast (< 200 fs) formation of intermediate TT states that decouple in several nanoseconds to form free triplets ($2T_1$), as discussed in chapter 4. We have explored the effect of excitation energy in Chapter 4, where certain vibrational modes are activated which allows for emission from the otherwise dark TT states. The TT states are delocalised over two neighbouring molecules and decouple to form two localised triplets, with time. Decoupling of the TT state occurs by means of vibrational motion allowed within the molecular arrangement or the crystal structure of the system. *Stern et al.* effectively isolated Raman modes that are involved with the vibrational motion of S_1 and TT states, in a discernible manner. This is suggestive of the vital role vibrational modes hold, in

the process of SF. It is critical to note that molecular geometry influences how different vibrational modes propagate and relax from their respective excited state geometries. Therefore, molecular arrangement or film morphology plays a crucial role in allowing or forbidding vibrational degrees of freedom for SF chromophores which determine the fate of these excited states. In other words, the role of vibrational modes in decoupling correlated TT states is critical for breaking them up and form free triplets. We term the molecular geometry with the highest probability of allowing these set of SF-favourable vibrational modes that help in free triplet formation, as *the decisive SF geometry*.

The concept of *the decisive SF geometry* may be invoked to explain the difference in the nature of TT states in polycrystalline and amorphous films of TIPS-Tc. In polycrystalline films, as reported by *Stern et al.*[95], large crystalline islands of varying crystallinity and the lack of long-range order (~100 nm sized crystallites) are perhaps reasons that make TT-break up unfavourable. Therefore, the polycrystalline films are clearly not *the decisive SF geometry*. On the other hand, due to its spatially random nature, the statistical probability of two neighbouring molecules having the *decisive SF geometry* is much higher in an amorphous film than the polycrystalline film. Thus, TT states in amorphous films find it easier to break apart as they have access to the vibrational modes that aid in free triplet formation.

We therefore conclude that neither the polycrystalline nor the amorphous films maybe ideal for SF in TIPS-Tc. The same goes for TIPS-Tc NPS discussed in Chapter 4. Although they showcase SF, timescales of free triplet formation are rather long (~1 ns) and maybe attributed to the peculiar, mixed-morphology. It may even be termed as a 'stroke of luck' in terms of achieving the mixed-morphology for the NPs that did not impede SF after all. However, the same peculiar morphology has led us to chase the *decisive SF geometry* for TIPS-Tc, reading together with SF dynamics in polycrystalline and amorphous films. Exploring *the decisive SF geometry* is therefore imperative to design systems with efficient SF.

5.2.2 Chemical Functionalisation of Nanoparticles

Besides the influence of morphology, we impose the need to restrict molecules in the nano-regime to facilitate efficient triplet transfer to similarly sized quantum dots. The quest for the right morphology that aids SF while remaining in the nano-regime is a major goal of this study. While bare NPs grow to be ~30 nm (comparable to exciton diffusion lengths) by Ostwald ripening[119] (discussed in detail in section 4.3), we devise methods to maintain the size of the newly functionalized NPs to the same order of magnitude. The next challenge is to make the organic NPs *likeable* by (i) improving chemical affinity of the NPs to the quantum dots by surface chemistry modifications, or (ii) forcing the organic-inorganic phases to mix. Though we tried both approaches, the latter was found to be ineffective as it resulted in immediate aggregation at the phase boundary. Thus, we focus on surface chemistry modifications of the organic NPs that were prepared in Chapter 4, with no surfactants.

Organic NPs and their surface functionalisation is an exciting research theme for chemists with varying applications from imaging applications to designing solar cells[144–149]. We start by considering a few surfactants based on their surface charges (anionic, cationic etc) with desirable chain lengths. Surface passivation by the use of surfactants involves various chemical or physical mechanisms of encapsulation. Encapsulation, as the name suggests, is the process of enclosing particles/molecules inside hollow structures (such as cavities) in order to passivate them. Encapsulation of particles improves their chemical stability by preventing aggregation, and maintaining their chemical character. The chemical mechanism involves differences in electronegativity between the particle and an active group in the surfactant. An example of this is silver NPs coated with thiol-based surfactants, as silver has a high affinity towards thiol (-SH) groups[150]. However in the case of organic NPs, similar chemical modifications may change their electronic structure, disintegrating the inherent photophysical behaviour they possess. Thus, the physically passivating mechanism of encapsulation is be used here, by trapping NPs inside vesicular or micellar structures[151–154].

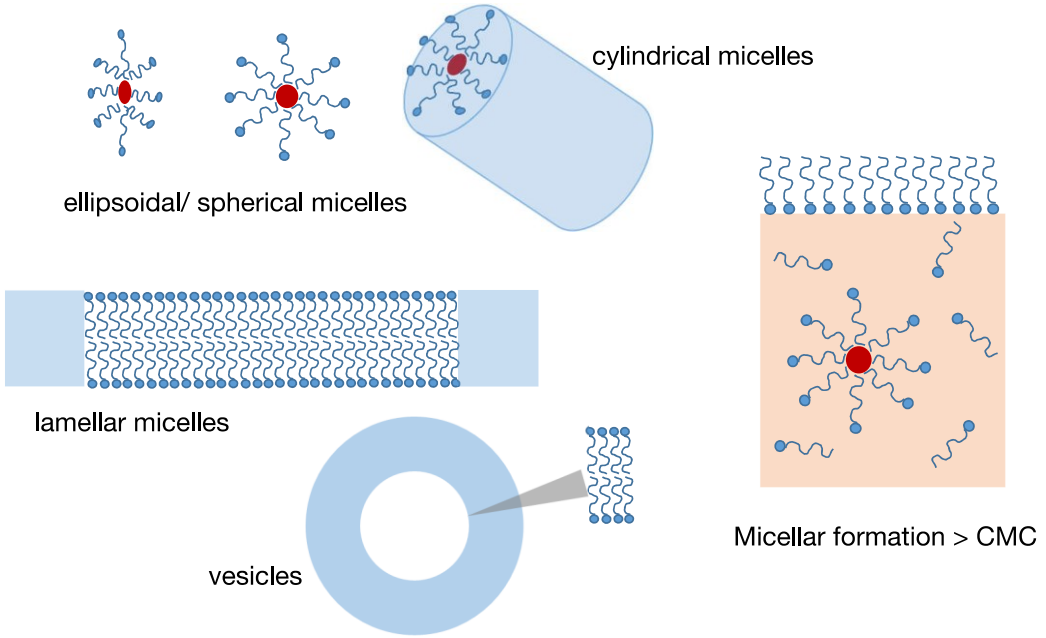

Figure 5.2-Various types of micellar formation by surfactants in solution. Micellar formation occurs in solutions above the critical micellar concentration at given conditions. The ratio between the tail-length and the head-size determines the shape of the micellar structure formed. Figure adapted [155].

Surfactants comprise of a hydrophobic tail and a hydrophilic head[156]. Depending on the ratio between tail-length to head-radius, surfactants form interesting equilibrium structures[155,157–159] such as vesicles or micelles, shown in Figure 5.2. An example of this is molecules of sodium dodecyl sulphate (SDS) forming thermodynamically stable configurations of micelles above certain concentrations in solution[160]. Micelles are formed with hydrophobic tails in the core and hydrophilic heads on the exterior, facing the solvent molecules. Thus, the core of micellar structures are hydrophobic with no solvent within. These structures that form above a minimum concentration, known as the critical micellar concentration[161] (CMC), are composed of molecules which are in dynamic equilibrium with those in the bulk. Hence, the molecules in the bulk and those forming micellar structures diffuse across these phases, within thermal fluctuations[162]. When organic molecules are introduced to a micellar solution, they move to the micellar core due to the affinity towards the hydrophobic tails of the

surfactants. The continuous motion of surfactants driven by thermal equilibrium pushes the organic molecules around in the micellar core, abetting the formation of crystalline phases. This is a well-studied phenomenon of crystallisation enabled by micellar and reverse-micellar structures[163,164]. Note that this process is very similar to crystal formation by solvent annealing, which forms the most thermodynamically stable crystal structure for molecules within constraints of accessible microstates (entropy) and thermal motion. Therefore by trapping organic molecules within micellar structures, formation of stable crystal structures can be facilitated in the nano-regime. Alongside surface chemistry modification of organic NPs, this micelle-strategy is ideal for making crystal polymorphs of the most stable and inherent form of organic molecules. Thus, one can develop a good understanding of morphology modification by changing crystallisation conditions and get closer to achieving *the decisive SF geometry*. In this work, we focus on the aspect of seeking *the decisive SF geometry* as well as surface modifications that make the NPs chemically likeable by PbS quantum dots.

5.3 The Wizardry

The secret impresses no one. The trick you use it for is everything.

-Alfred Borden, The Prestige

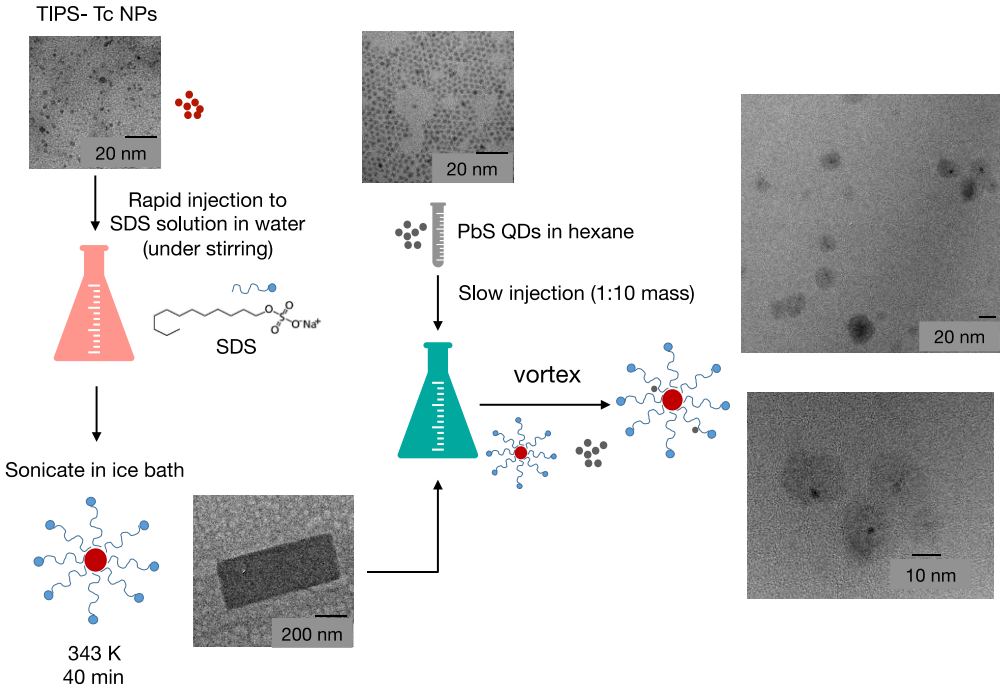

Figure 5.3-Scheme of SDS coating and coupling of TIPS-Tc NPs with PbS quantum dots.Bare NPs are injected into an SDS solution in water above its CMC, leading to the formation of crystalline NPs of sizes < 300 nm. Addition of PbS quantum dots of ~5 nm in size with a triplet energy of 1.1 eV results in the final structures which are composed of disintegrated organic cloud with a dense PbS quantum dot within it.

Bare NPs as made in section 4.2 are injected rapidly to an SDS solution in water, above its CMC. To compensate for the thermal energy released during reorganisation of solvent molecules and surfactants, the system is sonicated in an ice bath for a few minutes. The temperature of the resulting system is set at 70°C for 40 minutes, while maintaining the pH of the solution to ensure its stability. The final solution is dropcast onto a TEM grid for structural analysis and embedded in a film of gelatin matrix for photophysical studies. We will examine

these structures in the following sections. The NPs at this stage are expected to be coated by SDS micelles. PbS quantum dots in hexane are injected slowly to the micellar-NPs solution (60 μL of dots to 100 μL of NPs), under stirring and N_2 atmosphere. The resultant mixture is dropcast onto TEM grids for structural characterisation. The solution is further stabilized for photophysical characterization by embedding in a gelatin matrix. Figure 5.3 shows the schematic of the process.

5.4 Structural Characterisation of Nanostructures

The NPs are characterised at different stages of the process explained in section 5.3 by electron microscopy and the corresponding images are shown in Figure 5.5. To ascertain the crystallinity of these structures, we perform electron diffraction alongside TEM, and calculate the reciprocal lattice parameters corresponding to the crystal structure. We start the experimental process with ~30 nm sized bare NPs of TIPS-Tc and encapsulate them with SDS micelles. Upon completing this process, we observe that rectangular nanostructures in the order of 200-300 nm with very defined, sharp edges are formed, as shown below. Following the discussion from section 5.2.2 we rationalize the formation of these highly crystalline nanomotifs of TIPS-Tc as the effect of micellar dynamic equilibrium in solution. The movement of SDS molecules in the micelles and the bulk (solution) initiates the crystallisation process of TIPS-Tc inside the micellar core. These dynamics of the SDS molecules lead to the formation of highly ordered, energetically stable NPs of TIPS-Tc. The question that remains unanswered is whether this is close to *the decisive SF geometry* of TIPS-Tc, which we shall discuss in the following sections.

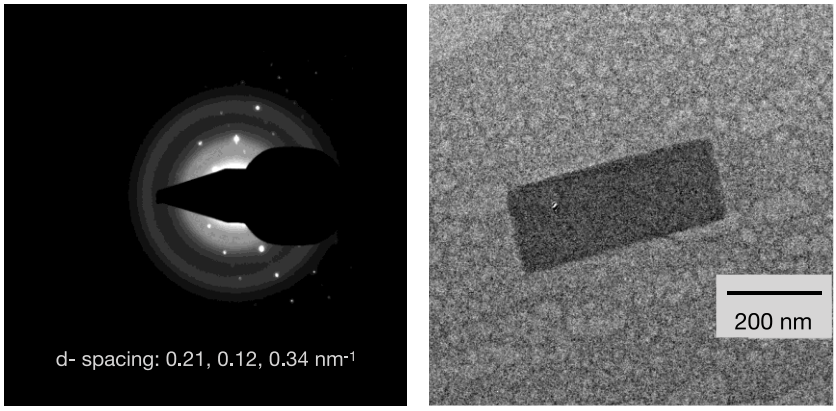

Figure 5.4-SAED pattern and corresponding microscopy image of SDS-NPs. Estimated d-spacing values in the reciprocal lattice are shown in the diffraction image on the left. The diffraction pattern suggests high degree of crystallization in the nanostructure.

Electron diffraction (Selected Area Electron Diffraction-SAED) on these structures gives rise to the images shown in Figure 5.4 with reciprocal lattice parameters listed. These values compare reasonably well to the reported single crystal data on TIPS-Tc. Changes in molecular arrangement and size of the NPs in the presence of SDS validate the changes in the PL spectrum, before and after the micellar treatment. This shall become more relevant as we discuss excited state dynamics. The highly crystalline SDS-NPs are then coupled with PbS dots, evidence for which will be discussed later. Changes in the solution environment due to addition of PbS dots in hexane is expected to disrupt the equilibrium structures of the micelles and therefore of the SDS-NPs. Although we control conditions such as temperature and pH of the system, one can assume that the micellar structures will not be in a favourable environment upon introducing an inorganic phase, leading to the distinct possibility of disintegration of the crystalline nanostructures.

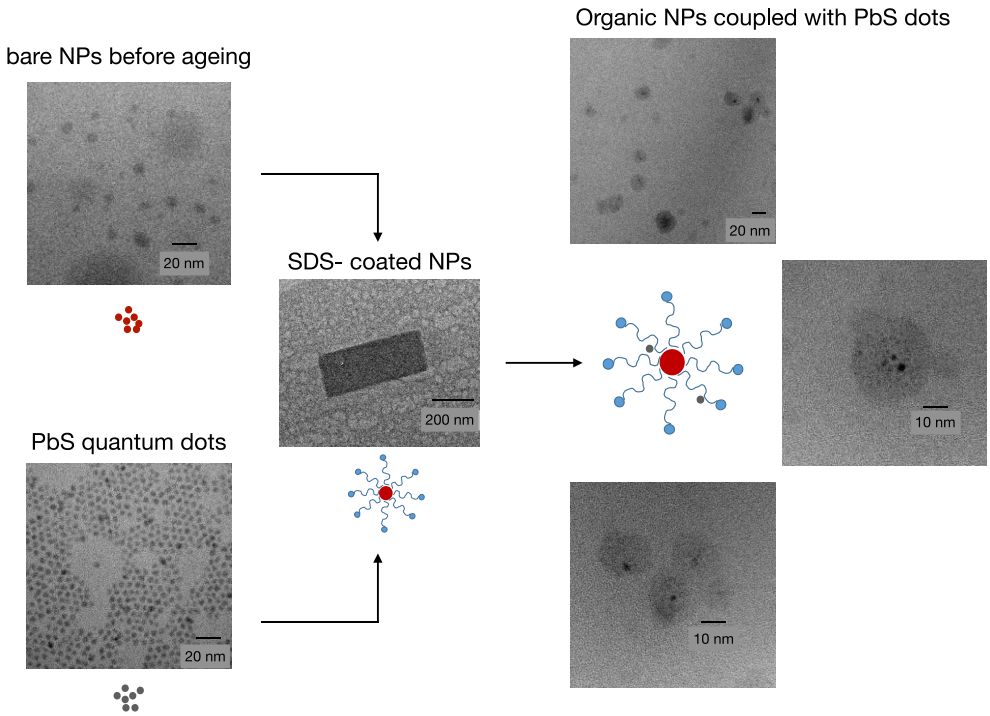

Figure 5.5-TEM images taken at various steps of preparing the NPs for coupling with PbS dots. Bare NPs of TIPS-Tc become crystalline, 300 nm-long structures once coated by SDS micelles, by attaining a thermodynamically stable crystal packing. Introducing an inorganic phase (PbS quantum dots) disrupt the equilibrium of the micellar structures, resulting in their disintegration. The inorganic-organic nanostructures formed have the dots trapped inside the organic cloud consisting of TIPS-Tc and SDS around.

Steady-state spectral data (discussed in the following section) shows that the three components: TIPS-Tc, PbS and SDS molecules are present in solution at this point. Therefore, there is reason to believe that the NPs may have evolved in structure and ordering (resulting in the shift in absorption of TIPS-Tc), while still being stabilised by SDS in the new configuration. We dropcast the ternary-solution (TIPS-Tc, SDS, PbS) onto TEM grids for structural characterization. Figure 5.5 shows some electron micrograms of SDS-NP-QDs. From differences in image contrast (organics- lighter and inorganics- darker), we assume that PbS dots are stuck inside clouds formed of TIPS-Tc and SDS. We were unable to quantitatively analyse the nanostructures for element specific information by X-ray diffraction, due to low product yield. However, by upscaling the production

process one should be able to reproduce these results and ascertain our findings with more credibility.

5.5 Optical Properties and Morphology

In this section, we analyse the steady-state absorption and photoluminescence (PL) of the NPs at every step of the process shown in the schematic above. Figure 5.6 shows the spectra of bare NPs (previously discussed in section 4.2), SDS-coated NPs (SDS-NPs) and SDS-coated NPs coupled with PbS quantum dots (SDS-NP-QDs). The absorption peak in the SDS-NPs at ~300 nm is a well-characterised SDS spectral feature[165]. The 0-0, 0-1 and 0-2 electronic transitions in SDS-NPs (>450 nm) are blue-shifted compared to that of the bare NPs. This shift in absorption along with the presence of the SDS peak at 300 nm indicate that the newly formed NPs are surface-modified by SDS with the likelihood of their crystallinity affected. The effect of crystallinity is even more apparent in PL spectra with and without SDS. The bare NPs show emission peaks at 520 nm, 580 nm and a broad feature at 640 nm, the latter assigned to emission from the TT state in section 4.6.2. However, in SDS-NPs the ratio of the PL peaks is different due to the absence of the bare NP-emission at 620 nm. While bare NPs showcased mixed morphology with crystalline and amorphous regions, narrower steady-state spectral features in SDS-NPs is indicative of a more crystalline morphology.

Introducing the PbS quantum dots to SDS-NPs results in an absorption spectrum with combined features of SDS at 300 nm, the 0-0, 0-1 and 0-2 transitions of the S_1 in TIPS-Tc, and a large absorption feature that extends in the UV region (< 400 nm) from the PbS dots, reported elsehwre[79]. Excess solvents and surfactants from the SDS-NP-QD solutions were washed off before performing spectral measurements on them. Thus, we have reasonable proof to believe that the final structures formed have a combination of TIPS-Tc, PbS as well as SDS in them. The PL spectrum of these structures is slightly more blue-shifted compared to

the SDS-NPs, possibly due to further surface modification in the presence of the quantum dots.

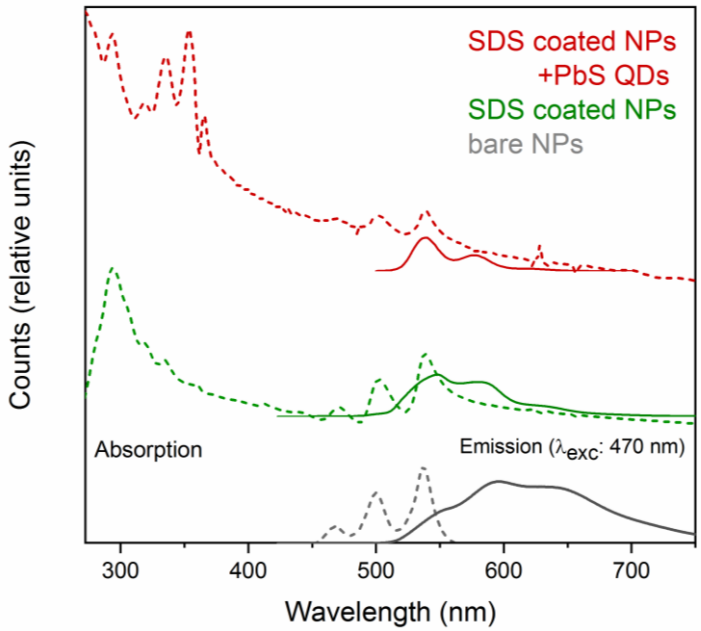

Figure 5.6-Steady-state Ab/PL spectra of bare NPs, SDS-NPs and SD coated NPs with PbS QDs.
PL peak-shifts to the blue and lowered peak-width hint at improved crystallinity of SDS-NPs compared to bare NPs. The presence of SDS is characterised by the peak at 300 nm in NPs and NPs coupled with PbS dots.

5.6 The Effect of Morphology on Excited State Dynamics

From steady-state experiments and structural characterisation, we see an interesting evolution of the NPs, in terms of molecular ordering and size discussed in previous sections. Such drastic structural changes are prone to influencing the fate of excited state processes involved in SF and are expected to be more prevalent when molecules are confined spatially in the nano-regime. For instance, the broad emission from TT at 640 nm is quenched when the NPs are coated by SDS micelles. To establish the influence of morphology on spectral and dynamic profiles of excited states, we perform a series of time-resolved emission and pump-

probe spectroscopy measurements to compare the excitonic dynamics between bare NPs and SDS-NPs.

5.6.1 Investigating the Emissive TT State in Nanoparticles

Figure 5.7 shows the time-resolved emission spectra (TRES) of SDS-NPs from 1 ns to 60 ns after photo-excitation of the films at 470 nm. The 0-0, 0-1 and 0-2 S_1 transitions of TIPS-Tc (as observed from steady-state PL spectrum) decay with >10 ns time constant. The rather long lifetime of S_1 is attributed to excited state recombination. PL spectra recorded from 1 to 200 ns in bare (bottom) and SDS-NPs (top) are shown in Figure 5.8. All spectra are area-normalized so that identification of multiple emissive species, if any, is easier to spot. While bare NPs showed a late-rising, red-emission at 640 nm, this low-energy feature is absent in SDS-NPs. In fact, there are no emissive species other than S_1 in SDS-NPs. As discussed in chapter 4, what makes TT states emissive is a Herzberg-Teller type mechanism[129] that involves accessing certain vibrational states by the excited-state geometry of TT. The absence of emissive TT states in SDS-NPs thus indicates the lack of these vibrational modes in SDS-NPs. The absence of *bright* TT states may be correlated to the improved crystallinity in SDS-NPs compared to bare NPs. While bare NPs[100] (and disordered films[95]) showcased morphologies rendering TT emission, the degree of crystallinity in SDS-NPs is much higher, disabling vibrational modes that allow TT to relax radiatively.

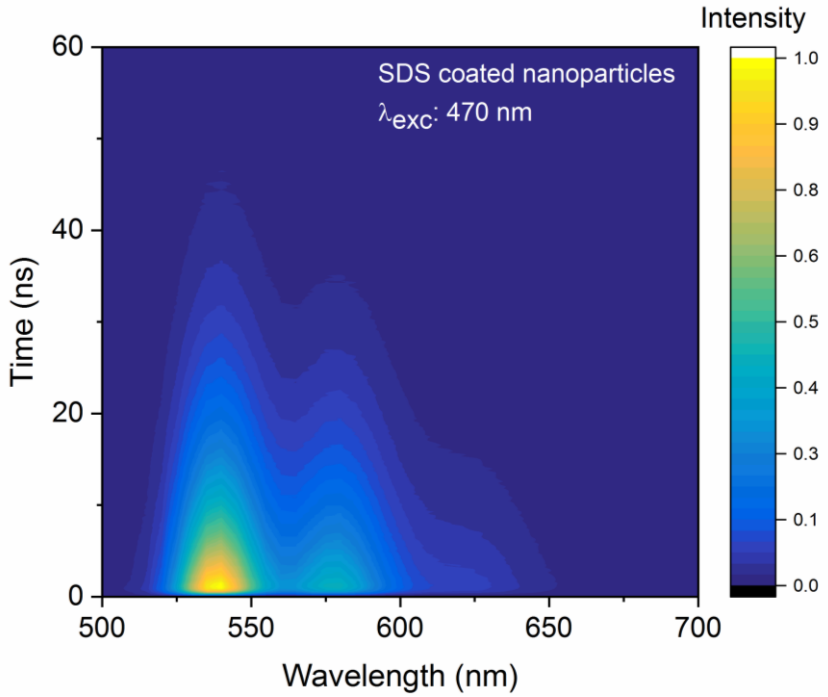

Figure 5.7-Time-resolved photoluminescence of SDS-NPs. The S_1 peaks corresponding to 0-0, 0-1 and 0-2 transitions decay with ns-long timeconstants. We do not see the emergence of multiple emissive species as in bare NPs. This means that a different polymorph of TIPS-Tc is attained in the SDS-NPs compared to bare NPs, with a distinct emissive profile.

Some reports suggest that emission from the TT state in endothermic SF systems may be seen as an alternative pathway to SF[166]. The argument in these studies is that TT states which normally decouple to form free triplets are now emissive, reducing triplet yield or SF efficiency. The accuracy of this interpretation is debatable given the nature of analysis, but may not be entirely dismissed. Regardless of the credibility of this hypothesis, the fraction of TT states that are emissive in the bare NPs is very small, thus not hampering free triplet formation with high yield in the system. If one were to consider TT emission as a loss channel for SF, then the lack of it in SDS-NPs indicates that the morphology of this system is closer to the *decisive SF geometry* than bare NPs or disordered films.

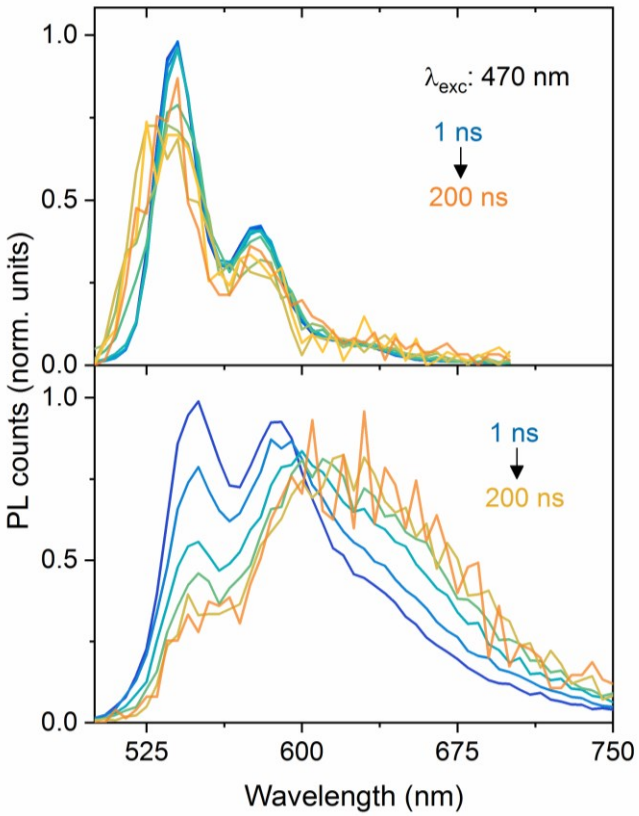

Figure 5.8-PL timeslices from SDS-coated (top) and bare nanoparticles (bottom). Samples were excited at 470 nm and spectra recorded (area-normalized) between 1 to 200 ns are shown above. While a low-energy (640 nm) emission rises at 2 ns and lives for >100 ns in bare NPs, S_1 is the only emissive species observed in SDS-NPs. The slightly blue-shifted emission spectrum and the lack of a secondary emission in SDS-NPs compared to bare NPs is attributed to the high degree of crystallinity in the former and lack of certain vibrational modes that allow radiative relaxation of TT state.

For a more comprehensive analysis of different excited states and their SF dynamics, we resort to pump-probe experiments in faster timescales on SDS-NPs, and compare them with bare NPs.

5.6.2 Ultrafast Kinetics of Singlet Fission in Nanoparticles

Bare NPs are excited at 532 nm and SDS-NPs at 520 nm, both with narrowband pulses (~200 fs, FWHM: 10 nm) and pump-probe spectra with time delays

between 500 fs to 1.2 ns using a visible probe (550-770 nm) are recorded. The pump-probe data for the bare NPs shown in Figure 5.9 is the same as in chapter 4, but in a slightly different presentation.

To summarise the relevant results from Chapter 4: photo-excited S_1 decays with a lifetime of 12 ps, marked by the GSB at 540 nm, SE at 580 nm and PIA at 610 nm and 650 nm. TT states are formed under 200 fs and have a distinct, flat PIA (except for the small 620 nm peak) with the population maximum attained beyond 100 ps. These correlated TT states decouple to form free triplets by 1 ns with PIA features at 620 nm, 685 nm, 720 nm and 760 nm in the visible region, as marked in the figure with dotted lines. Kinetics of these states are discussed in detail in Chapter 4, with expected TT and $2T_1$ yield to be the highest when excited at 532 nm. The lower panel in Figure 5.9 shows the three distinct DAS components pulled out by SVD analysis and their respective timeconstants. Though TT states form under 200 fs, they live for as long as 900 ps after which they break up to form free triplets. The initially formed TT state is heavily mixed with S_1 as we see spectral similarities between them at early-times. Molecular disorder in the amorphous exterior of the NPs lets TT states access vibrational degrees of freedom that enable them to break apart into free triplets. However, the extent of this process is understandably down to the statistics of finding molecular geometries close to *the decisive SF geometry* among neighbouring molecules in the amorphous region. Moreover, triplet formation is influenced by the strength of coupling within TT states as well. Therefore, the experimentally recorded TT dynamics is expected to be an average of time constants associated with all possible TT states formed in a system, which may or may not lead to triplet formation. This leads to a skewed understanding of TT dynamics while also stretching apparent lifetimes of these states.

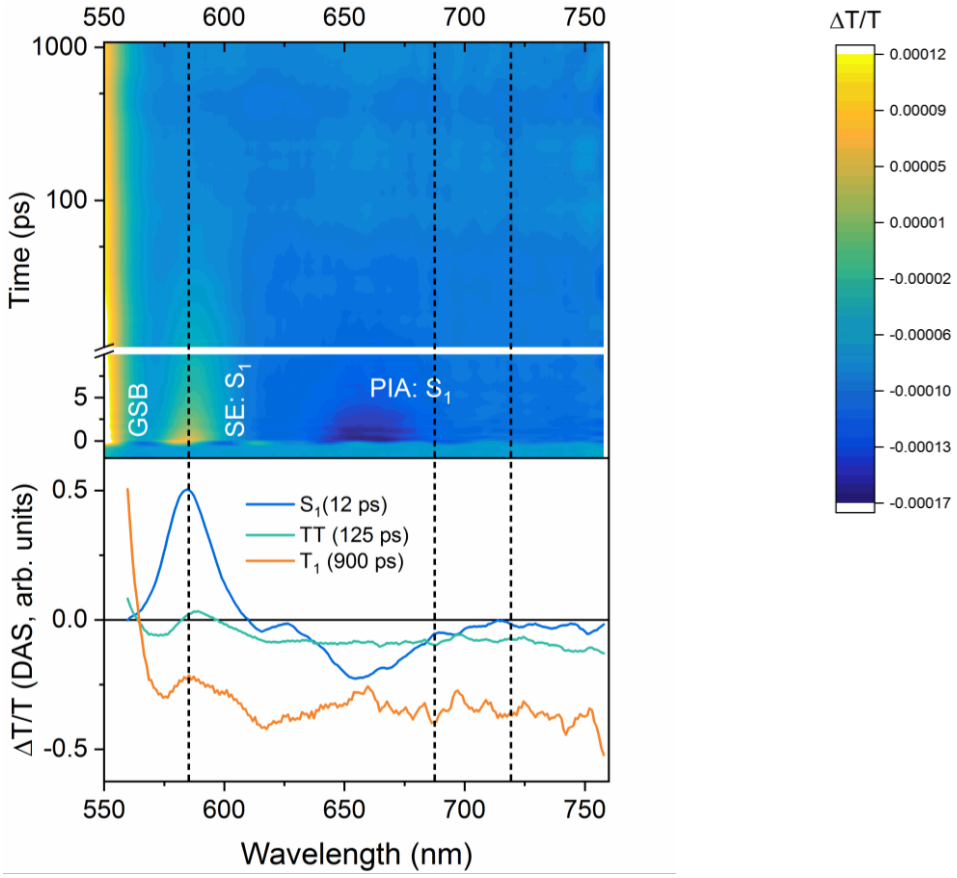

Figure 5.9-Pump-probe spectra and dynamics of bare nanoparticles excited at 532 nm and their DAS components.
S_1 decays with a lifetime of 12 ps, TT forms under 200 fs and peaks beyond 100 ps before breaking up into free triplets by 1 ns.

The pump-probe spectra of SDS-NPs are shown in Figure 5.10. S_1 features such as GSB at 540 nm, SE at 580 nm and PIA beyond 600 nm are within comparable limits to that of bare NPs, with slight spectral shifts we discussed with steady-state data. S_1 lives for slightly shorter with a lifetime of 9 ps when compared to bare NPs (12 ps). We see that TT states are formed within the instrumental response time of 200 fs and they live for a short period of < 200 ps before forming free triplets by 300-500 ps, which is twice as fast when compared to triplet formation (~1 ns) in bare NPs.

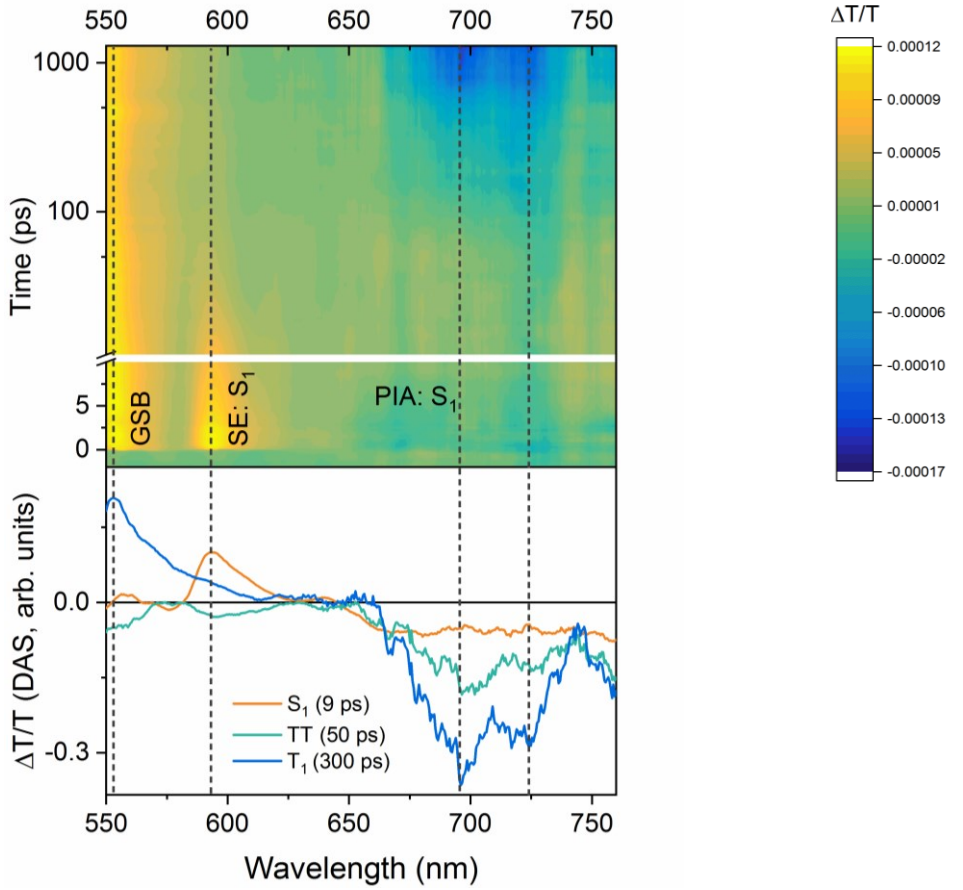

Figure 5.10-Pump-probe dynamics of SDS-coated nanoparticles excited at 520 nm and their DAS components.
S_1 decays with a lifetime of 9 ps, TT state forms under 200 fs and begins to decay under 200 ps to form free triplets. Triplet formation is 3 times faster in SDS-NPs compared to bare NPs in Chapter 4.

The triplet features in SDS-NPs are sharper and more pronounced at 685 nm and 720 nm, unlike the flat PIA in bare NPs. Although pump-probe spectra at longer time delays (1 ns to 1 μs) show very clear features for the free triplets in bare NPs (Chapter 4), the sharp PIA features in SDS-NPs at much shorter times make population decomposition easier, with clear kinetics. Thus, SDS-NP is a better system to study experimentally due to clear spectral changes and discernible kinetics. If one is interested in a more detailed analysis of morphology and excited-state dynamics as a function of anisotropy or temperature, it may be done by a single experimental window in terms of spectral and temporal ranges in this system.

The role of morphology in SF dynamics and the possibility of making nanostructures of TIPS-Tc within SDS micelles that are close to *the decisive SF geometry* has been discussed already in section 5.2.1. With inspiration from comparing crystallisation within micellar structures and that by solvent annealing, one expects to see crystals of highly energetically stable configurations, in these SDS-NPs. From pump-probe data we see that in these more crystalline (than bare NPs) system, TT states decouple rather easily and form free triplets within 300 ps. This is rather remarkable in comparison to the other three known morphologies of TIPS-Tc. In bare NPs, a small TT population is emissive at certain excitation energies and the majority of TT states decouple to form $2T_1$ states by 1 ns. In polycrystalline films, TT states live for very long times (>10 ns) and do not decouple to form $2T_1$ states. In disordered films, some TT states are emissive when excited at 470 nm, and the TT states decouple to form $2T_1$ states by 1ns or so. Hence by comparison, the SDS-NPs by far exhibit the most efficient SF with fast forming $2T_1$ states within 300-500 ps. While the bare NPs exhibited mixed morphology, polycrystalline films consisted of varied crystalline phases spread out spatially and disordered films were with random short-range order, SDS-NPs have a well-defined crystalline phase allowing for easier break-up of TT states. We believe this occurs as the excited state geometries in this crystalline morphology allow for the vibrational modes that aid this process. Thus, it is evident that the SDS-NPs prepared in this work are rather close to *the decisive SF geometry* compared to all the other morphologies of TIPS-Tc reported before. The absence of emission from the TT states in TRES measurements may also indicate that the TT to $2T_1$ efficiency is higher for this system compared to bare NPs or disordered films. This would result in a higher SF efficiency as a greater number of triplets-per-photo-excited S_1 state can be generated if one were to consider TT emission a loss channel for SF.

5.7 Coupling Nanoparticles to Quantum Dots

After a detailed analysis on the structural aspects and SF dynamics of SDS-NPs, we attempt to couple them to PbS quantum dots, for triplet transfer. By encapsulating the NPs with SDS micelles and adding PbS dots to them, the micellar equilibrium is altered leading to disruption of the NP-micelle system in solution. However, upon structural analysis by TEM, we see what looks like PbS dots within a cloudy layer of the organics. Upon addition of the inorganic phase to the SDS-NPs system, the NP-micelle system falls apart in solution. The OA-coated dots with an affinity to the hydrophobic environment of the organic NPs are drawn towards the organics. Thus, the dots end up being inside an organic cloud consisting of TIPS-Tc/SDS. Absorption and PL spectra show the presence of all three components: TIPS-Tc, PbS dots and SDS, in the final system whose TEM images were discussed before.

One of the ways to confirm the coupling between the organic and inorganic phases is to look for triplet transfer between the two, allowed by the energetics of the system. Although unsuccessful in performing time-resolved experiments to establish triplet transfer mechanism between the two phases appropriately, we show some preliminary evidence for the same. We recorded the PL spectrum for PbS dots with and without the NPs, as shown in Figure 5.11. The dots show a PL peak at 890 nm, when excited non-resonantly at 500 nm. When SDS-NP-QDs are excited at 500 nm at the same fluence (selective excitation of TIPS-Tc), we see the PL signatures of TIPS-Tc at 540 nm, 580 nm and 640 nm. We also see the selective enhancement of the dot emission at 890 nm, by a factor of ~3 (estimated by concentration of dots used and PL counts). Thus, when TIPS-Tc part of the SDS-NP-QDs is excited, excitons are transferred from the organics to the dots. The transfer of excitons is manifested as the enhanced PL response from the dots. One may consider this an exciting piece of preliminary evidence for successful coupling between TIPS-Tc NPs and PbS quantum dots within SDS-NP-QDs. However, we realise the many shortcomings of this result as one cannot distinguish between singlet transfer and triplet transfer using this method.

Considering the high energy of the dots at 1.39 eV (890 nm), it is unlikely for TIPS-Tc triplets of 1.2-1.25 eV to undergo transfer to the dots. Thus, the dot emission enhancement when exciting TIPS-Tc selectively, is likely to be caused by singlet transfer.

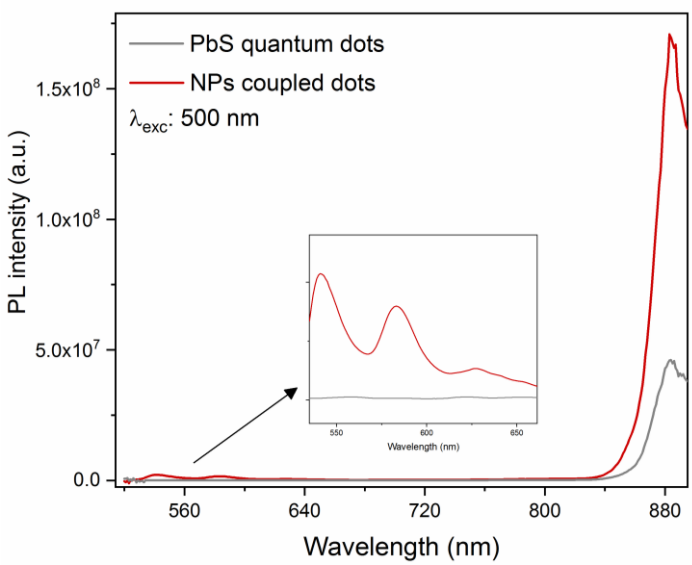

Figure 5.11-PL spectra of PbS quantum dots with and without organic NPs, excited at 500nm. When TIPS-Tc NPs are excited at 500 nm, excitons from the organics are transferred to the dots, and we see the enhancement in dot PL by a factor of ~3.

5.7.1 Experimental Challenges Faced

Without a snake or two, the main part of a story would be missing.
-Grace Marks, Alias Grace by Margaret Atwood

One of the major challenges in this work has been the stability of mixed phases of organics and inorganics, as we deal with a multi-phase solution-based system (TIPS-Tc, SDS, PbS, water and hexane). Although SDS-NPs exhibit excellent SF dynamics and long-lived triplets, structural distortion occurs upon introducing the inorganic phase to the system. Formation of rather translucent, turbid emulsions at this stage of the process proved quite hard to do any meaningful spectroscopy on them. Moreover, the stability of these nano-emulsions was poor,

leading to large particulate matter precipitating out of solution. Many experimental attempts with varying parameters such as concentration, temperature, pH, rate of addition of the dots to the system etc were performed. However, this led to little more than acknowledging the complexity of the system we were dealing with. A thorough and systematic approach with a good understanding of phase diagrams of this rather complex system is essential to achieve this and is beyond the scope of this thesis.

5.8 Conclusions and Outlook

Organic NPs of TIPS-Tc were successfully modified to a more crystalline phase, closer to the *decisive SF geometry* of TIPS-Tc. Bare NPs of ~ 30 nm were confined within SDS micelles, in solution, that led to the formation of crystalline ~300 nm nanostructures which show efficient SF. We demonstrated the process where molecules access crystal structures in a thermodynamically feasible manner, hitting the lowest point in its potential energy surface of all available crystal configurations. Comparing SF dynamics across various morphologies of TIPS-Tc studied in this thesis and elsewhere including films and bare NPs, we find that SDS-NPs were the most efficient with the fastest rate of triplet formation (300 ps). The dark nature of TT states and spectral shifts in SDS-NPs point at a higher degree of crystallinity along with differences in the nature of accessible vibrational modes for excited states. The nature of vibrational states is rather vital given how they dictate the fate of excited state processes such as decoupling of TT states. Structural characterisation by electron microscopy and electron diffraction support the claims of improved crystallinity in SDS-NPs from bare NPs. A detailed analysis of excited-state dynamics in these structures by TRES and pump-probe spectroscopy proves that triplet formation is ~3 times faster than in other morphologies of TIPS-Tc reported so far.

We attempted to couple SDS-NPs with PbS quantum dots of matching triplet energy (~1.4 eV) and saw preliminary pieces of evidence for triplet transfer between the organic and inorganic structures. Structural evolution of the organics from a highly crystalline phase to a rather disordered cloud that wraps around the dots is not surprising, given the complexity of the system and disruption of micellar equilibrium. While we see enhanced emission from the dots when exciting TIPS-Tc in these coupled SDS-NP-QDs structures, we only consider this as a preliminary, but definitive, proof for exciton transfer. A more intricate control of the nanostructures and the coupling between them, along with improved stability are key to exploring these interesting systems further for potential device applications.

Chapter 6

Thienoanthracenes: A New Class of Singlet Fission Materials

TIPS-Tetracene (TIPS-Tc) is a well reported and efficient endothermic singlet fission (SF) system, and so far in this thesis we have looked at morphological influence of SF in nanoparticles of TIPS-Tc and engineering them with inorganic quantum dots for energy transfer. Despite being a highly efficient system, the triplet energy of TIPS-Tc lies at around 1.2 eV which is lower than most inorganic systems which shall be incorporated in a PV device for triplet transfer from the organics. Anthracene, an endothermic SF system with a high triplet energy of 1.5 eV is well reported and was in fact the first system in which SF was first experimentally observed. However, due to the high endothermicity of anthracene [1,49,51,83] (0.5 eV), SF is not an efficient, viable process. This led us to study the effect of chemical modifications on anthracene, like the addition of a thiophene ring. These modifications have resulted in a new class of SF materials, thienoanthracenes, with an endothermicity expected to be higher than of Tc (0.2 eV)[54,55,57,58,60,74,167], but lower than anthracene, such that is does not impede efficient SF. We introduce thienoanthracenes as a new class of endothermic SF materials in this chapter and proceed to use them to study the role of entropy in driving SF in the following chapter.

6.1 Molecular Design of Thienoanthracenes

A computational project designed to generate a class of hypothetical molecules that satisfy high triplet energy and endothermicity was undertaken by a team at the University of Mons lead by Prof. David Beljonne. This study included in Appendix A identifies thienoanthracenes as suitable candidates. The synthesis of these molecules named as thienoanthracenes was then carried out by Prof. John Anthony's lab at the University of Kentucky.

As the name suggests, thienoanthracenes have the skeletal structure of a thiophene ring attached to an anthracene moiety with energy levels expected to be placed between anthracene and tetracene (Tc). In this study, we include four different thienoanthracenes with 5,10-bis(triisobutylsilylethynyl) 2-fluoro anthrathiophene (with substitutions for underlined species: butyl/propyl and with/without 2-fluoro) with acronyms TIBS-TA, TIBS-FTA, TIPS-TA and TIPS-FTA that vary in energetics as well as crystal packing, molecular structures shown in Figure 6.1

Thiophene rings though being aromatic (six π electrons that contributes to conjugation and planar structure) have reduced aromatic character compared to benzene, thus destabilizing the HOMO-LUMO gap when substituting the latter[168,169]. Thus, the thiophene substitution for benzene in Tc to form thienoanthracenes is expected to result in a larger HOMO-LUMO gap compared to Tc. On the other hand, adding a thiophene to anthracene is expected to decrease the HOMO-LUMO gap compared to that of anthracene. We can therefore explore the extent of endothermicity in SF better than Tc, while still exhibiting a higher triplet yield than anthracene, as demonstrated later in this work.

Differentiating factors in these four molecules are the side chains that change the molecular packing in solid state and diffusion-limited behavior in solution-state[170,171]. The fluorine substitution on the TIPS and TIBS thienoanthracenes improve the photostability of the molecules as well as changes the crystal

structure due to an electron-withdrawing effect. The fluorine substitution alters the conjugation strength in the molecule as well, making the energy gap between the singlet and triplet states larger than the non-fluorinated thienoanthracene counterparts[3]. Thus, the platform created by these four thioanthracenes offers a few advantages; (i) to understand the extent of endothermicity in SF, (ii) provides insight into the structure-function correlation in SF rates and efficiency, and (iii) the possibility of uncovering efficient SF materials that generate higher energy triplets than Tc which is key when coupling organics with Si in solar cells.

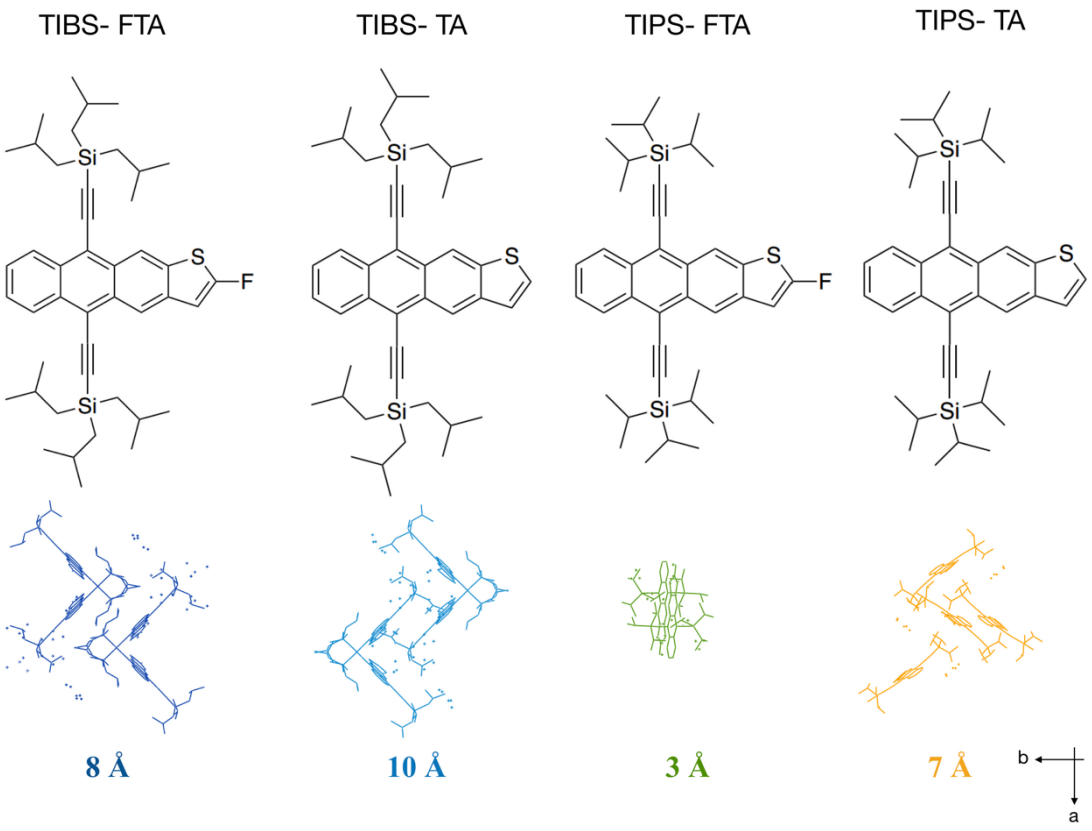

Figure 6.1-Molecular and crystal structures of thienoanthracenes in the ab plane. TIBS-TA has the lowest packing density with a nearest neighbour distance of 10 Å in the ab plane, TIPS-FTA the lowest with 3 Å, TIPS-TA with 7 Å and TIBS-FTA with 8 Å.

The crystal structures of the four thioanthracenes in this study are shown in the figure above. While they vary only slightly in molecular design, their crystal

packing varies significantly. TIBS-FTA packs in a twisted slip-stacked crystal structure in the monoclinic system with four molecules per unit cell, with the neighboring molecules separated by 8 Å in the *ab* plane where SF is expected to occur[96,172]. TIBS-TA packs in a twinned plate crystal structure in the monoclinic system with four molecules per unit cell and a distance of 10 Å in the *ab* plane between neighboring molecules, the most loosely packed TA with the highest inter-neighbor distance in this study. TIPS-FTA packs in the triclinic crystal system with two molecules per unit cell, with the highest molecular packing density among all molecules in this study with a 3 Å inter-neighbor distance in the *ab* plane. TIPS-TA packs with orthorhombic crystal structure with four molecules per unit cell and a distance of 8 Å between neighboring molecules. TIPS-TA and TIPS-FTA have shorter side chain lengths compared to TIBS-TA and TIBS-FTA. The range of molecular packing density in this study gives us an opportunity to study correlations between SF dynamics, triplet yield and structural characteristics.

Rates involved in the process of SF include S_1 decay, formation of intermediates and free triplet formation, as discussed in the chapters before. Many studies have been done in the past exploring the role of crystal packing on triplet transfer and diffusion rates[14,67,79,102,173–175], which is relevant while probing the process of harvesting triplets in devices, but not their mechanism of generation itself. Solid-state geometry, overlap of excited-state molecular orbital wavefunctions and thus inter-neighbor distances are crucial to determining the rates in SF and also efficiency of triplet formation as discussed in Chapter 2. Therefore, with variation in distances of separation between neighboring chromophores and molecular packing densities, we expect to see a distinct influence on SF rates and triplet yields.

6.2 Optical Characterization

Steady-state absorption (line), photoluminescence (filled) spectra (λ_{exc}: 470 nm) and phosphorescence (λ_{exc}: 658 nm) of the thienoanthracene films are used to characterise optical processes in thienoanthracenes, shown in Figure 6.2.

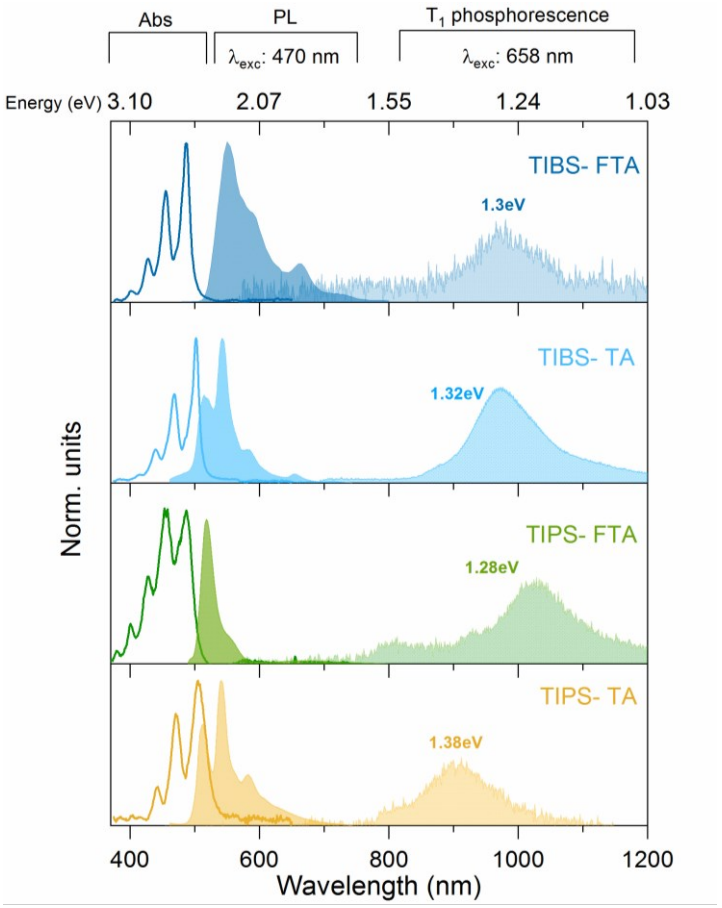

Figure 6.2-Steady-state absorption, PL and T_1 emission of the thienoanthracenes. All PL spectra recorded with films excited at 470 nm. For phosphorescent measurements, a triplet sensitizer (PdTPTBP) was used and films were excited at 658 nm. The measured T_1 energies are highlighted in the figure. The emission peak in some of the spectra at 800 nm is from the sensitizer. All films were compared with their respective solutions for self-absorption and aggregation effects for accuracy in determining S_1 energies.

We divide the four molecules into two groups for simplicity of discussion, into propyl–TA for TIPS-TA, TIPS-FTA and butyl-TA for TIBS-TA, TIBS-FTA on

the basis of side group bulkiness. The butyl molecules with a lower packing density absorb bluer than the tighter packing propyl molecules. The absorption spectra of all molecules show very structured 0-0, 0-1 and 0-2 electronic transitions, with S_1 energies between 2.3-2.45 eV. With the fluorine substitution, the HOMO-LUMO energy gap is increased and pushes the absorption spectra to bluer wavelengths in TIBS-FTA and TIPS-FTA, compared to the non-fluorinated counterparts. Note that the *Stokes shift* is higher for the molecules with fluorine substitutions. A reasonable theory that explains larger *Stokes shift* is by symmetry breaking substitutions on conjugated molecules[176]. Addition of a fluorine to the thienoanthracene backbone reduces molecular symmetry about the long axis, weakening the vibrational sub-levels. This results in reduced internal conversion to lower-lying vibrational states by excited- state molecules, resulting in a larger *Stokes shift*. Although shorter chain lengths in propyl-TA compared to butyl-TA do not result in significant changes in their absorption spectra, the latter group has emission bands above 600 nm while the PL spectra of the former group tail off significantly beyond 600-620 nm. Several factors such as molecular ordering as a function of side group bulkiness, varying conjugation lengths and changes in the vibronic structures may be attributed to the presence of low-energy emissions like this. Previous studies on Tc derivatives have shown that the presence of red emission (>650 nm) is due to multiple emissive species that are longer lived compared to the S_1 state. We discuss this further with time-resolved emission data later.

6.2.1 Identifying Triplet Energies

In order to locate the energy levels of the triplets in these molecules, we sensitise the triplets by a heavy metal based complex, Pd(II) meso-Tetraphenyl Tetrabenzoporphyrin (PdTPTBP), which readily generates triplets via efficient inter-system crossing (ISC) due to the large spin-orbital coupling of Palladium[177]. Solutions of thioanthracenes (3% by weight) and PdTPTBP (10% by weight) were dropcast on a substrate, and allowed to dry in an inert atmosphere. These solid-state samples were encapsulated and excited at 658 nm, exciting the

sensitizer. The highly efficient ISC (96%) in the sensitizer gives rise to triplets of ~1.5 eV[177] in solution. Upon successful transfer of these triplets to the thienoanthracene molecules one should be able to see a *brightened* phosphorescence from the respective triplet emission.

Figure 6.2 shows the phosphorescent spectra measured for all four thienoanthracenes, sensitized as described above. The triplet energies of the fluorinated TIBS-FTA and TIPS-FTA are lower than that of their non-fluorinated derivatives. The highest triplet energy belongs to TIPS-TA at ~1.38 eV placing its endothermicity at 340 meV, and the lowest for TIPS-FTA with a triplet energy at ~1.28 eV and an endothermicity of 166 meV. TIBS-TA has a triplet energy at 1.32 eV and TIBS-FTA at 1.3 eV. Such a large range of endothermicities is unprecedented in SF studies and allows to study the effects of endothermicity on SF dynamics, as detailed below.

6.3 Evidence for Singlet Fission

Little events, ordinary things, smashed and reconstituted. Imbued with new meaning. Suddenly, they become the bleached bones of a story.

-Arundhati Roy, The God of Small Things

The thienoanthracenes in this work has been designed to be endothermic systems with an energy gap (E_{STT}) between 170-340 meV. Thus, we expect SF to occur in these molecules and present the evidence for the same, in this section. To begin with, we perform time-resolved emission spectroscopy to analyse the nature of low-energy features as seen in the steady-state emission spectra of the molecules (Figure 6.2). Electron Spin Resonance (ESR) spectroscopy is another key experiment done to ascertain the presence of fission generated triplets, that are distinguishable from inter-system crossing (ISC) triplets due to differences in their

respective spin polarisation patterns. We look at each of them in detail in the following sub-sections.

6.3.1 Multiple Emissive Species

The presence of low energy features in butyl-TAs and the absence of the same in propyl-TAs calls for further analysis about the origin of these transitions. We perform time-resolved emission spectroscopy (TRES) on films of all four molecules in an identical fashion, exciting them at 470 nm. Area integrated TRES recorded up to 100 ns upon photoexcitation are shown in Figure 6.3. We discuss the data on each of the thioanthracenes below.

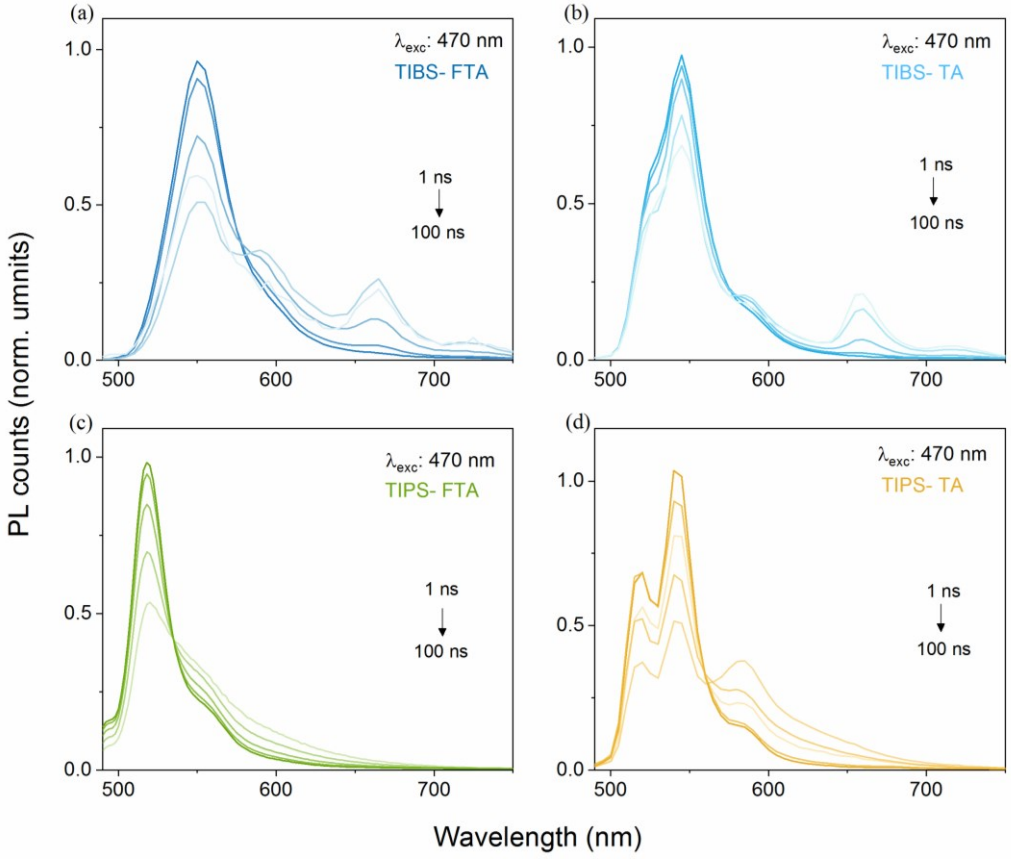

Figure 6.3-Time-resolved photoluminescence of films of thienoanthracenes when excited at 470 nm, between 1 ns to 100 ns.
Butyl-TAs show multiple emissive species: a prompt S_1 emission and a longer, low-energy emission that lives longer. Propyl-TAs show only S_1 emission. The presence of the low-energy emission in butyl-TAs are attributed to the TT states that become radiative by a Herzberg-Teller mechanism.

6.3.1.1 TIBS-FTA

S_1 emission of TIBS-FTA dominates in early-time (1-5 ns) spectra shown in Figure 6.3(a) and has a lifetime of 3 ns. With a rise time of 2 ns, we see a low-energy feature between 640-670 nm growing in which has a longer decay time of 10 ns. Following reports of a secondary, low-energy emission from TT states in other endothermic systems such as Tc and TIPS-Tc (also discussed chapters 4-6), we therefore assign this to the TT state in TIBS-FTA as well. Figure 6.4 shows the kinetics of the S_1 and TT regions obtained from these experiments. All kinetic

plots have been normalized to their respective maxima. The secondary red emission in TIBS-FTA represents a substantially smaller population compared to the initial singlets as only an area integrated PL map makes it noticeable beyond the noise levels of this experiment. As has been discussed previously in the literature for other endothermic SF, the presence of multiple emissive species may be related to the presence of an emissive (TT) state by pathways alternative/parallel to SF.

6.3.1.2 TIBS-TA

TIBS-TA has the lowest packing density of all molecules in this chapter, and also exhibits a low-energy emission. Early-time spectra is dominated by the S_1 state with peaks at 525 nm and 545 nm, with a lifetime of ~5 ns, Figure 6.3(b). The system then evolves to the slow rise (2 ns) of a low-energy emission around 660 nm- very similar to that of TIBS-FTA. S_1 emission lives for ~10 ns and the low-energy emission from possibly a very small TT population grows in by 2 ns and lives for >50 ns. The low energy emission feature in both TIBS-FTA and TIBS-TA may be due to a Herzberg-Teller type mechanism[129] as discussed previously in TIPS-Tc nanoparticles, in Chapter 4. An emissive TT state is argued to be an alternate pathway for SF, by some reports[166], as TT relaxes to the ground state rather than following the SF mechanism to break up to form free triplets. However, the signal strength of the low energy TT emission peaks and kinetics when compared to that of S_1 shows that the fraction of TT states undergoing the radiative relaxation is rather minor. Furthermore, the extremely low PLQE (< 5%) of both TIBS-FTA and TIBS-TA films indicate the presence of a major non-radiative pathway such as SF.

6.3.1.3 TIPS-FTA

TIPS-FTA has the highest molecular packing density in this chapter. S_1 emission dominates at early-times as expected with peaks at 520 nm and 550 nm. With time we see broadening of the S_1 emission as the 550 nm peak grows with respect to the 0-0 peak at 520 nm, over tens of nanoseconds. This could be due to the

presence of multiple S_1 populations in the disordered morphology of the films. Kinetics of the S_1 peak emission at 500-530 nm is compared with integrated counts between 590-610 nm for carefully inspecting the presence of a weaker red species if any, shown in Figure 6.4(c). In view of the fact that there is little difference between the two regions we conclude the absence of any secondary, TT-like emission in films of TIPS-FTA. This implies an increased number of TT states (only, marginally higher than the butyl-TA) following down the pathway of SF to form free triplets, improving the triplet yield of the system.

6.3.1.4 TIPS-TA

TIPS-TA, with the highest endothermicity in this study has S_1 emission peaks at 515 nm, 540 nm and 580 nm decay with a lifetime of 3 ns and like TIPS-FTA, we see the ratio between peak maxima of the S_1 peaks evolving over time. The most noticeable change is the strengthening of the 580 nm S_1 peak by 20 ns or so, after which the system revert to the early-time S_1 emission. This could be due to the presence of trap states at energies close to the respective vibronic transition or due to the disordered morphology of the film.

The most noticeable difference between the butyl and propyl-TA is the low energy emission that rises within 2 ns, which is present in small fraction in butyl TA, while being absent in propyl TA. Since we invoke a Herzberg-Teller mechanism that involves vibrational relaxation of excited states such as TT to a molecular geometry that allows for the radiative transition to the ground state, morphology or molecular ordering is vital[128]. As there is a distinguishable difference between propyl and butyl-TA structurally, pertaining to their side chain lengths, the molecular packing in solid state is quite diverse and might be instigating differences such as the low energy emission feature in nanoseconds.

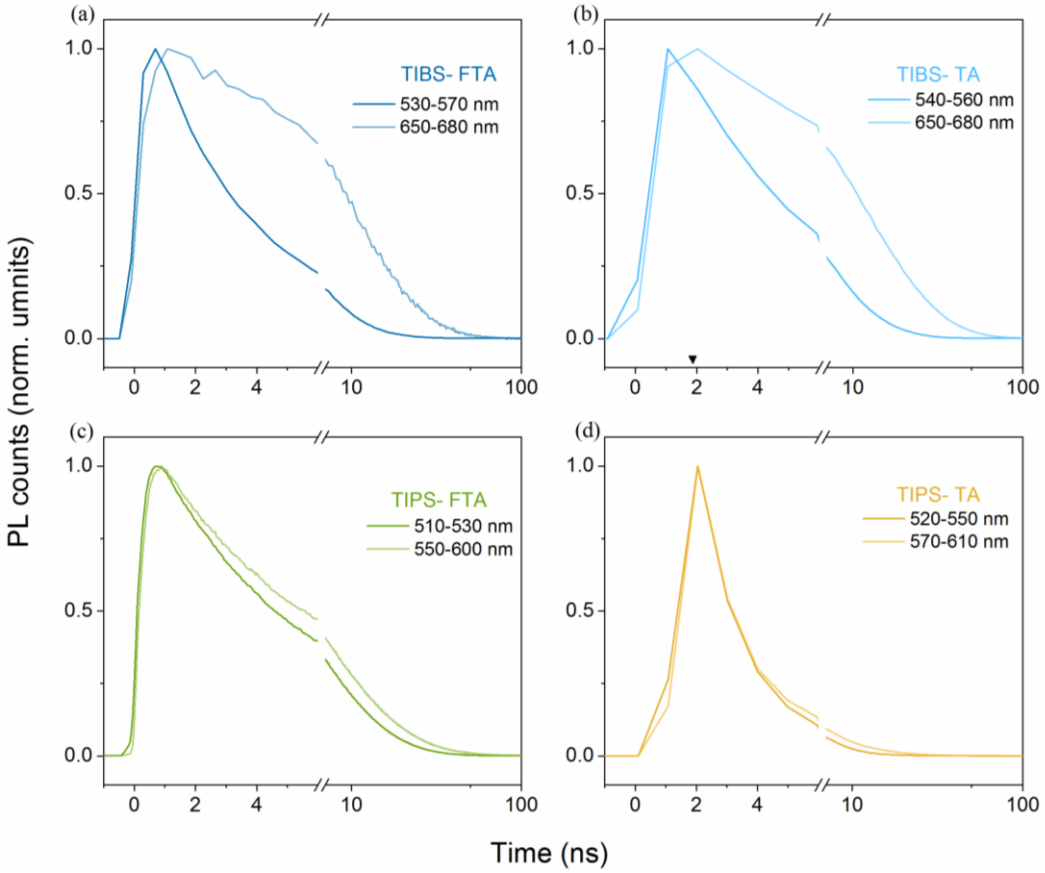

Figure 6.4-Kinetics of excited states from time-resolved photoluminescence spectroscopy of thienoanthracene films excited at 470 nm. The darker line plots show emission kinetics of S_1 and the lighter plots show the secondary emissive species, if any. While butyl-TAs show slow-rising, low-energy emission with longer lifetimes than S_1 emission, propyl-TAs exhibit only S_1 emission.

The time resolution for TRES experiments conducted here is roughly 300 ps. Hence, if we have very fast forming SF intermediates, capturing their spectral signatures in the photoluminescence configuration might prove difficult due to the dark nature of triplet states involved. A photoluminescence quantum efficiency (PLQE) of less than 5% measured for all four thin films indicate a major non-radiative pathway for excited singlet states.

6.3.2 Spin Signatures of SF-generated Triplets

Electron spin resonance (ESR) spectroscopy is used to investigate if triplets form via SF in thienoanthracenes. The experiment is performed with a time resolution of 200 ns and the film samples are excited in N_2 atmosphere between 470-485 nm. We present the ESR spectrum obtained from thin films of thioanthracenes at 70 K integrated between 200 ns to 5 μs upon photoexcitation in Figure 6.5. ESR gives rise to unique absorption (A-*positive*)- emission (E-*negative*) polarization patterns that represent various spin state transitions under magnetic field[112,178–180]. The polarization pattern as a function of magnetic field position (**B**) gives the relative spin population as a function of molecular orientation. These patterns are observed to be unique for triplets formed via inter-system crossing (ISC) and SF, as well as for the spin-states in weakly bound TT pairs, quintets, charge transfer states etc. ESR is therefore a powerful diagnostic tool to study SF and its dynamics[179,181]. Upon photoexcitation and splitting of triplet levels at different **B** values, transitions from the high-field eigenstates depend on the relative contribution of the populated zero-field states and on the angle of the molecule with respect to the external field. This is explained in detail, in Chapter 3. The characteristic emission-absorption pattern of *AEEAAE* observed in our samples is unique to triplets formed by SF, reported elsewhere[112,178]. The polarization pattern due to SF-generated triplets is distinct from the polarization pattern shown by ISC-generated triplets that emerge from the zero-field population[182,183]. We note that the large positive peak at 0.35 T is due to a free radical formation due to trapped oxygen in the sample which does not interact with the transitions under discussion. Similar polarization patterns that correspond to SF-generated triplets are observed in the case of TIBS-TA and TIPS-FTA as well, however the large positive feature at 0.35 T overshadows the much smaller ESR signal from TIPS-TA film. Therefore the identification of SF-generated triplets in the ESR spectrum of TIPS-TA becomes rather difficult. Thus, unless a reliable optical signature is observed, we will not be able to determine the occurrence of SF in TIPS-TA.

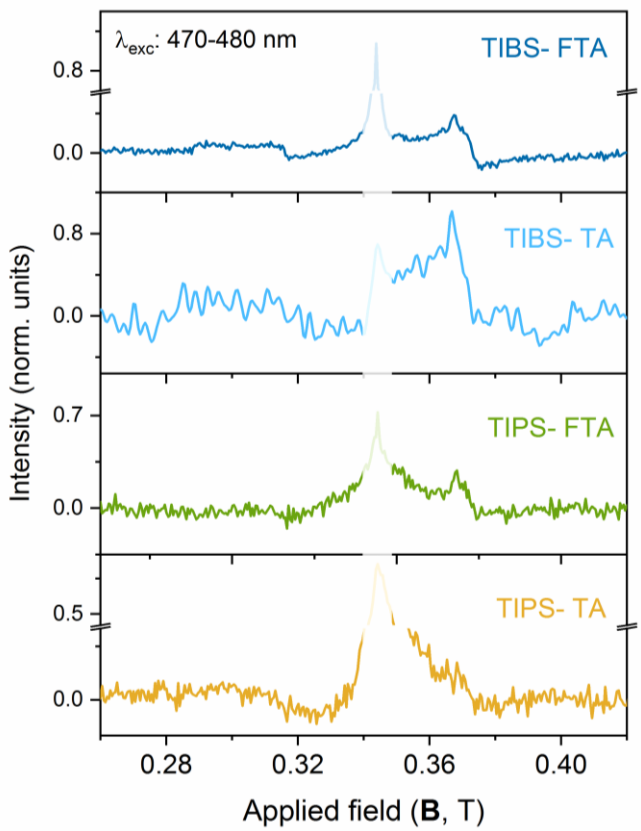

Figure 6.5-ESR spectra of the thienoanthracenes excited at 470-480 nm, integrated between 200 ns and 2 µs. AEEAAE spin polarisation pattern is seen clearly in integrated ESR spectra of TIBS-FTA, TIBS-TA and TIPS-FTA films, but not so clearly in TIPS-TA. This indicates the formation of triplets via SF that carry this distinct ESR spectrum against ISC triplets.

Therefore, the analysis of spin polarization patterns of ESR spectra confirms that TIBS-FTA, TIBS-TA and TIPS-FTA undergo SF to generate free triplet excitons, though timescales of triplet formation is still unclear due to slow time resolution of the ESR experiment (>200 ns). We shall look for further evidence from optical spectroscopy for SF in the case of TIPS-TA before ruling out SF in it, all together.

6.4 Mechanism of Singlet Fission

Solid-state ordering is one the major factors that influences rates of various processes associated with SF[184]. For instance, the right geometry of energetically favourable chromophores can facilitate the formation of free triplets[50,57,185]. We present to the excited-state dynamics of all four thienoanthracenes in this section and analyse them in the light of variation in crystal packing. Ultrafast pump-probe spectroscopy is used to study excited-state dynamics and spectral features arising from thienoanthracene films upon photoexcitation. Films are excited at 480 nm and spectra recorded from 500 fs to 2 ns for all thienoanthracenes. Identification of various spectral species has been performed by comparison of the pump-probe data with the respective steady state absorption and photoluminescence in Figure 6.2. We expect the ground state bleach (GSB) of all the molecules to lie outside our experimental spectral range (540-970 nm). Spectral assignments for the individual TA are as follows.

6.4.1 TIBS-FTA

Pump-probe dynamics of TIBS-FTA films are shown in Figure 6.7. From the steady state absorption and PL spectra of TIBS-FTA (Figure 6.2), the ground state bleach (GSB) lies outside the probe spectral window (540-900 nm). Thus, the tail of the 540nm peak is assigned to the GSB and the peak at 550 nm to the stimulated emission (SE) from S_1. The S_1 SE decays with a lifetime of 10 ps, indicating a major non-radiative channel, consistent with the low PLQE measured for films. The S_1 SE is associated with a large PIA peak at 800 nm, both decaying in the same timescale of 10 ps, which shows that this PIA emerges from the S_1 state. At 2 ns, a spectrum with distinct spectral profile and sharp features in the near-IR region remains which does not evolve further and decays in several hundreds of nanoseconds, *vide infra*.

In order to identify various excited state populations that contribute to the recorded pump-probe spectra, we compare it with the pump-probe spectrum of

TIBS-FTA solution in dilute concentrations for cleaner spectral deconvolution in Figure 6.6. The initial S_1 spectrum at 1 ps does not decay within the experimental limit of 2 ns, and the absence of any other photoexcited species indicates the absence of SF in solution. The lack of SF in solution is attributed to the large steric hinderance due to TIBS side groups on the molecules as well as its dilute concentration. Comparing the early time spectrum in films with that in solution, the films show an additional PIA beyond 700 nm, distinct to that from the solution. This suggests that at early times, the S_1 from films is mixed with some intermediate state, which does not form at low concentrations in solutions. Similar mixing of S_1 with an intermediate multiexcitonic state has been observed in other endothermic SF systems such as TIPS-Tc. These observations hint at the PIA beyond 700 nm in TIBS-FTA films arising from the mixing of S_1 with a multiexcitonic TT-like state, at very early times <200 fs.

The early forming TT state loses its S_1 character under 20 ps, and under 100 ps we see the emergence of sharp peaks at 550 nm, 820 nm, 860 nm and 890 nm. These peaks are assigned to the free triplet, T_1, from comparison to sensitization measurements, as discussed later. We validate the identification of these excited states with the help of an SVD-based spectral deconvolution (discussed in section 3.6.1).

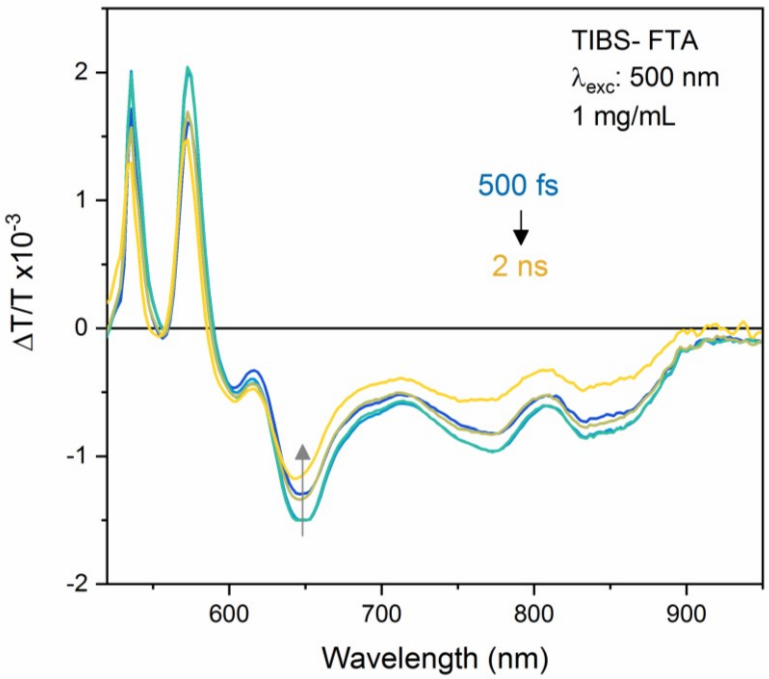

Figure 6.6-Pump-probe dynamics of a dilute TIBS-FTA solution (1 mg/mL) from 500 fs to 2 ns, excited at 500 nm. GSB (550 nm) and SE (580 nm) and PIA (650 nm, 770 nm and 850 nm) belong to the photo-excited S_1 state formed in solution. Due to the lack of molecular proximity at low dilutions, SF does not occur leading to the S_1 state's long lifetime.

Spectral deconvolution of the entire dataset gives us more insight into the total number of spectral species and their kinetics and we do this by the method of decay associated spectra (DAS). In this method, the DAS algorithm identifies major kinetic components in the given dataset and assigns a weight to every component depending on the strength of their presence across the wavelength-time regime. The first few major kinetic components are retrieved, and their spectral counterparts are matched out. The combination of these first few major spectral and kinetic components shall ideally recreate the entire data map, eliminating poor signal to noise issues, and if done correctly, spectral artefacts. This method of data deconvolution when applied to our data revealed the presence of at least three distinct species shown in the bottom panel of Figure 6.7, which after matching with raw data (top panel) are assigned to S_1, TT and T_1 species. Through the process of DAS, assigning of various PIA features

distinctive to each species in the raw data and thus attaining its unique kinetics have been made simple and reliable.

To summarize the pump-probe data shown above, we find that at early times (< 10 ps) films of TIBS-FTA show spectral signatures of S_1 mixed with an intermediate species of multiexcitonic character that rises within 200 fs, which we assign to the TT state. At intermediate times the TT state dominates the spectra and at longer timescales (>100 ps) the TT state decays to give free triplets. The triplet yield with respect to the singlets upon photoexcitation will be discussed later.

Pump-probe data for the rest of the thienoanthracenes discussed below were analyzed by spectral deconvolution techniques detailed above, and their triplet characteristics and yields will be discussed in section 6.4.5.

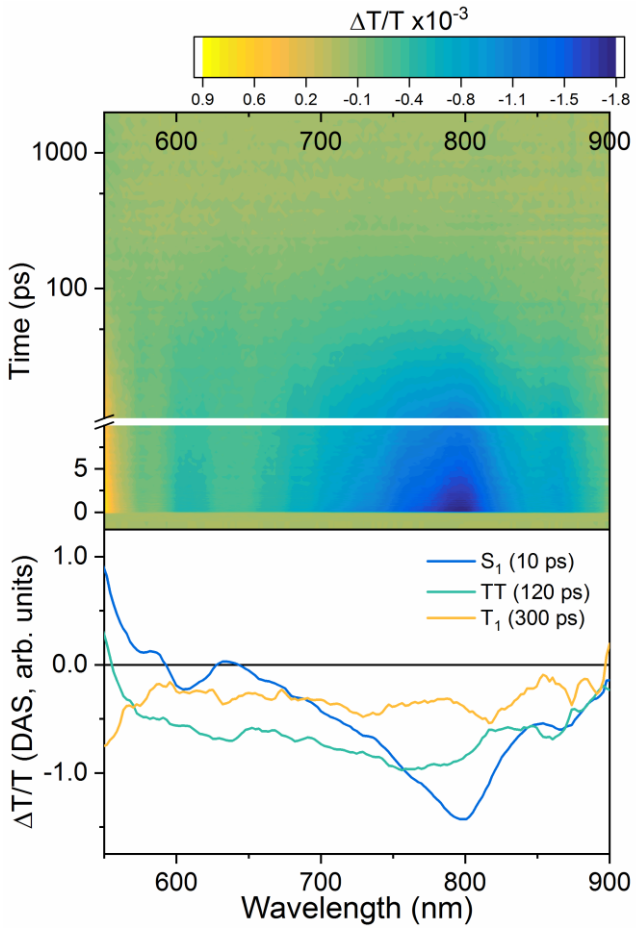

Figure 6.7-Pump-probe dynamics of SF in TIBS-FTA films excited at 480 nm, from 500 fs to 2 ns. S_1 features of SE (580 nm) and PIA (650 nm, 780-800 nm and 850 nm) are comparable to that from solution data. S_1 state and a rapidly forming TT state (<200 fs) co-exist within the S_1 lifetime of 10 ps. TT population peaks by 100 ps followed by decoupling to form free triplets as quickly as 200-300 ps with distinct PIA features(550 nm, 730 nm, 820 nm,870 nm).

6.4.2 TIBS-TA

The pump-probe dynamics of TIBS-TA thin films excited at 480 nm are shown in the top panel of Figure 6.8 between time delays of 500 fs and 2 ns. The peaks at 550 nm and 580 nm are assigned to the GSB and SE of the singlet exciton, respectively. The SE decays with a lifetime of 20 ps, however is pulled down to a more negative ΔT/T from 10 ps due to a PIA growing in at 590 nm. The S_1 SE

is associated with a large PIA peak at 800 nm, both decaying in similar timescales, thus we assign the PIA at 800 nm to the S_1 state. Sharper peaks growing in by 25 ps at 570 nm and 590 nm indicates an intermediate species that lacks S_1 character. We assign this to the TT state in TIBS-TA, which decays in several nanoseconds to form free triplets eventually. The free triplet, T_1, spectrum consists of sharp peaks at 560 nm, 840 nm and 930 nm, with remarkable similarity with the spectrum recorded at a delay of 50 ns in a separate experiment. The T_1 spectrum in films is compared with the sensitized T_1 spectrum in solution, and will be discussed later, in detail. An SVD lead DAS analysis discussed in section 6.4.1 done on the pump-probe data of TIBS-TA gives further evidence to the spectral and kinetic discussion above. The deconvoluted spectral components are shown in the bottom panel of Figure 6.8 where S_1, TT and T_1 are clearly distinct and distinguishable in the raw data. The S_1 state decays with a time constant of 14 ps, TT forms by 20 ps and evolves into T_1 by several nanoseconds. This implies that SF in TIBS-TA is slower when compared to its fluorinated derivative, TIBS-FTA. The triplet yield with respect to the singlets upon photoexcitation is calculated section 6.4.5.

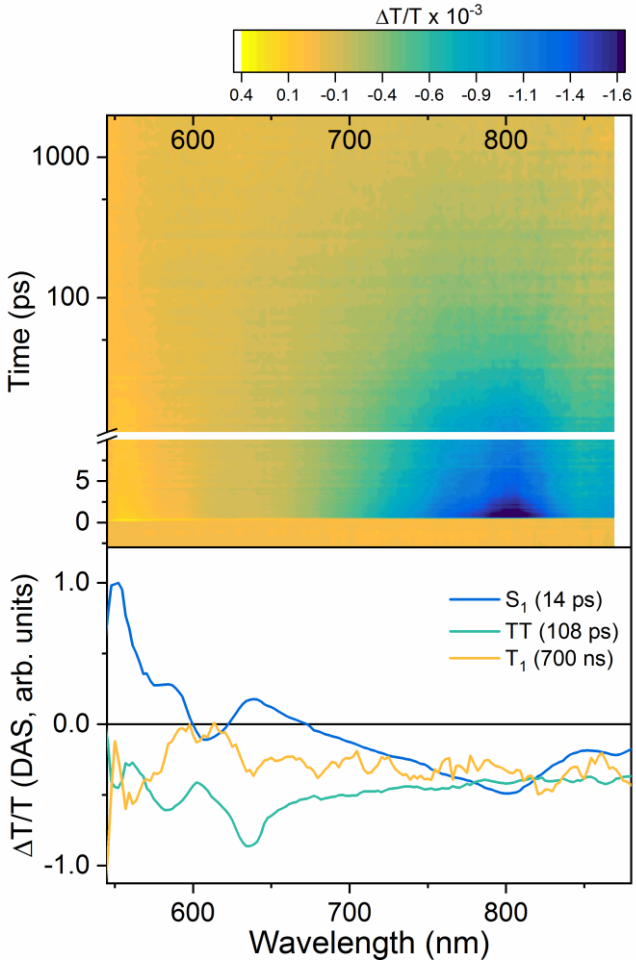

Figure 6.8-Pump-probe dynamics of SF in TIBS-TA excited film at 480 nm from 500 fs to 2 ns.
S_1 state with features of SE (590 nm) and PIA (610 nm, 770-800 nm) form TT states rather slowly, by 20 ps. TT population peaks by 500 ps followed by decoupling to form free triplets as quickly as 900 ps with distinct PIA features comparable to sensitized spectrum.

6.4.3 TIPS-FTA

Pump-probe dynamics of the thienoanthracene with the bluest absorption-emission spectra in this study, TIPS-FTA, are shown in Figure 6.9. As seen from steady state absorption-PL spectra from Figure 6.2, the GSB and SE of S_1 in this system is expected to lie outside the experimental range (540-900 nm). A broad PIA with features at 580 nm, 720-780 nm and 860 nm decay with time constants

< 100 ps, however there are considerable spectral shifts and spectral ratio differences taking place within this timescale. The peak at 580 nm is red-shifted by 8 nm within 2 ps after photo-excitation, the broad PIA at 720-780 nm flattens within 50 ps, along with the 860 nm peak disappearing by 100 ps. This shows the co-existence of multiple spectral species such as the S_1 and an intermediate state that is mixed with the S_1 from as early as 100-200 fs, the experimental time-resolution. While the characteristic PIA features of S_1 decay within 10 ps, by careful examination we assign the spectrum dominating at 50-100 ps delay to the intermediate TT state. This TT state with the distinct 720-780 nm PIA region decays with a lifetime of 100 ps distinct from the much shorter lived (< 20 ps) S_1 state. In hundreds of picoseconds, a third distinct population grows in, identified as the T_1 state, which lives for longer than 50 ns. The T_1 state was assigned after comparing the pump-probe spectrum at 1 ns to the sensitized T_1 spectrum (discussed later).

By means of SVD led DAS, we spectrally deconvolute the pump-probe data to three distinct components shown in the bottom panel of Figure 6.9. The S_1 state is characterized by its distinct broad PIA at 650 nm and 760 nm. The TT state with peaks at 600 nm and 800 nm reaches its population maximum by about 50 ps and decays into T_1 with distinct peaks at 580 nm, 700 nm and 800 nm. The S_1 population is tied to a time constant of 5 ps, with ultrafast formation of TT states (< 200 fs) and T_1 formation by 70 ps. This is by far the fastest SF dynamics we have seen in all thienoanthracenes in this study. Additionally, the third independent DAS component in orange with a nanosecond decay constant compares very closely to the sensitized triplet spectrum confirming the formation of free triplets upon decay of the TT and S_1 states.

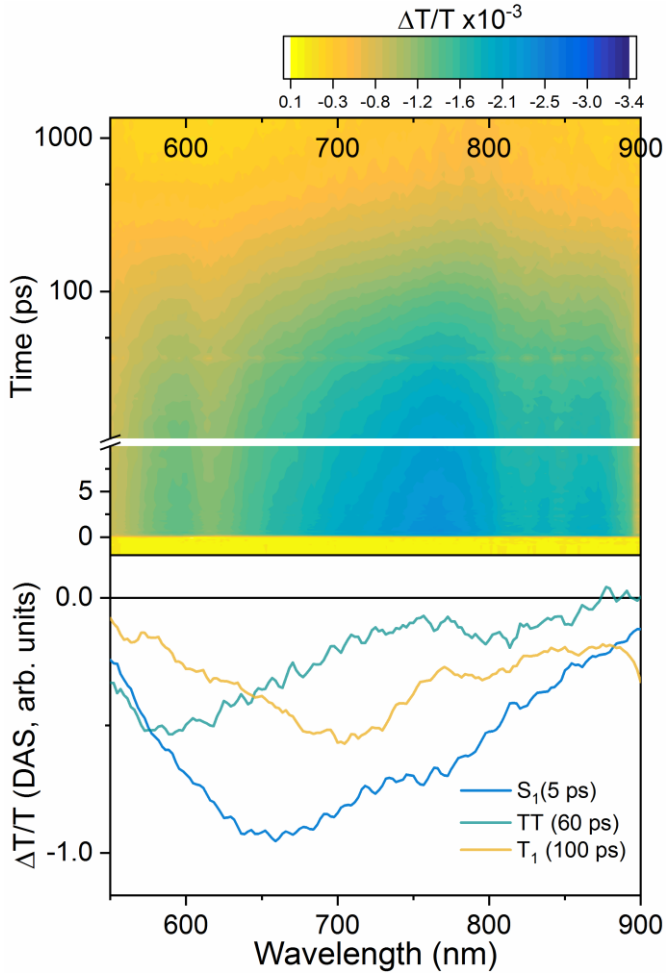

Figure 6.9-Pump-probe dynamics of SF in TIPS-FTA film excited at 480 nm, from 500 fs to 2 ns. S_1 features of GSB and SE are outside the experimental window. S_1 PIA has a broad peak at 650 nm. TT states form rapidly within the experimental time resolution (<200 fs) and co-exist within the S_1 lifetime of 5 ps. TT population peaks by 50-60 ps followed by decoupling to form free triplets as quickly as 100 ps with distinct PIA features(570 nm, 700 nm, 800 nm and 900 nm) matching the sensitized spectrum.

6.4.4 TIPS-TA

The pump-probe spectra of TIPS-TA thin films are shown in Figure 6.10 between time delays of 500 fs and 2 ns. The steady-state absorption and emission spectra from Figure 6.2 places the GSB ~500 nm which lies outside the probe spectral window in our experiment.

The SE peak at 540 nm and PIA features such as the peak at 600 nm and the broad feature between 650-820 nm are assigned to the S_1 state, which decays with a lifetime of 15 ps. Within a 100 ps we see a flatter PIA succeeding the S_1 PIA in the near-IR region (>700 nm) with a distinguishable peak at 640 nm evolving from the previous S_1 peak at 600nm. We note that this second population has been present from earlier times along with the S_1 state, and have been assigned to a multiexcitonic TT state. Population deconvolution by DAS (bottom panel) shows the S_1 and multiexcitonic TT states being distinct but still sharing some features, which also makes the S_1-TT mixing at TT state evident, as we have observed in TIBS-FTA and TIPS-FTA before. By 100 ps, the S_1 character from this multiexcitonic state vanishes entirely and the TT population reaches its population maximum. This is followed by the rise of a new population by 200-500 ps. This new state has PIA peaks at 650 nm, 720 nm and 870 nm, and complements the third DAS component in Figure 6.10. However, on comparison with sensitization measurements, this third state does not resemble free triplets. We discuss this further in the following section.

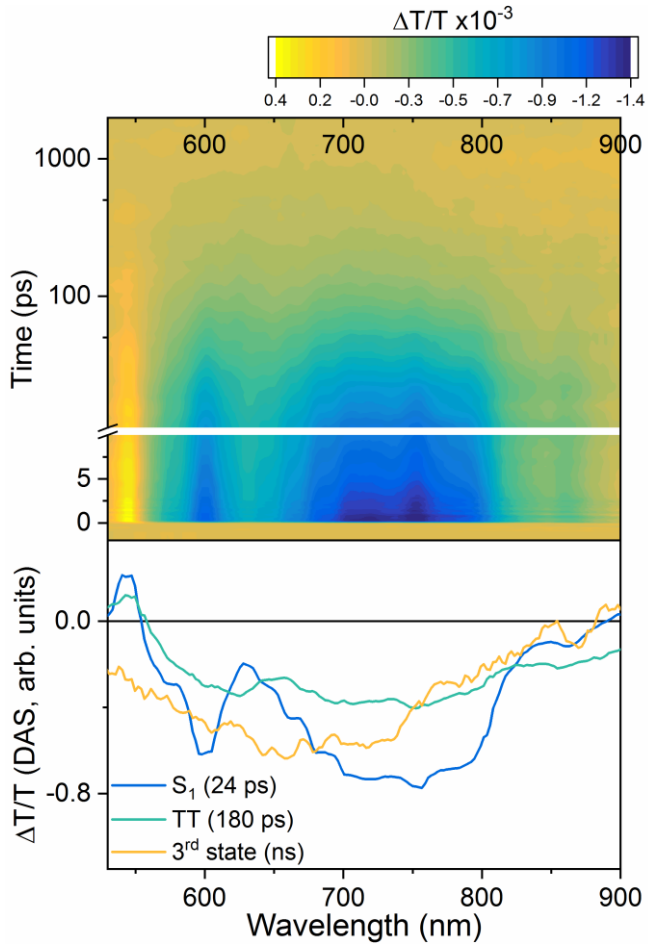

Figure 6.10-Pump-probe dynamics of SF in TIPS-TA film excited at 480 nm, from 500 fs to 2 ns. S_1 states with features of SE (550 nm) and PIA (600 nm, 700-800 nm and 850 nm) decay to TT state (<200 fs). TT population peaks by 200 ps followed by formation of a new unidentified species with broader PIA features between 600-780 nm. In the absence of formation of free triplets, SF has not occurred in TIPS-TA.

6.4.5 Triplet Formation and Yield

Triplet formation by SF is spectrally confirmed by means of comparison of inherent pump-probe spectra in films at long time delays with T_1 sensitised spectrum in solution. Triplet sensitization measurements in solutions of thienoanthracenes are done using a fullerene based sensitizer, N-methylfulleropyrrolidine, which injects triplets into thienoanthracene molecules in solution. As the triplet energy of the sensitizer (1.4 eV) is expected to be higher

than that of the thienoanthracenes (~1.3 eV), T_1 injection to the latter occurs by *Dexter transfer* in solution state (see section 2.3). Figure 6.11 shows the fullerene-sensitised T_1 pump-probe spectrum of all four thienoanthracenes in solution overlaid on the pump-probe spectrum at long-time delays where triplets are expected, when excited at 480 nm. These sensitised spectra serves as our basis to ascertain if SF occurs in these molecules and their expected T_1 spectrum.

While the respective T_1 spectra for TIBS-FTA (810, 920 nm), TIBS-TA (860-870 nm) and TIPS-FTA (900 nm) match to their sensitised spectra in solution, in TIPS-TA it is rather ambiguous. The nanosecond pump-probe spectrum in films of TIPS-TA does not in fact resemble the sensitised T_1 spectrum and this complements the lack of the SF T_1 spin polarisation pattern in ESR spectrum as well (see 6.3.2). From phosphorescent measurements discussed in section 6.2.1 we see that TIPS-TA has the highest triplet energy, making it the most endothermic thienoanthracene at 340 meV. As we do not see T_1 signature in the ESR data and pump-probe dynamics, we conclude that the system is too endothermic for SF to occur. In Chapter 7, we shall discuss factors that drives SF in the second most endothermic thienoanthracene discussed here, TIBS-FTA (endothermic by 300 meV). A combination of molecular spacing in solid-state, endothermicity and triplet diffusion lengths shall be explored in TIBS-FTA, to understand the mechanism of SF further.

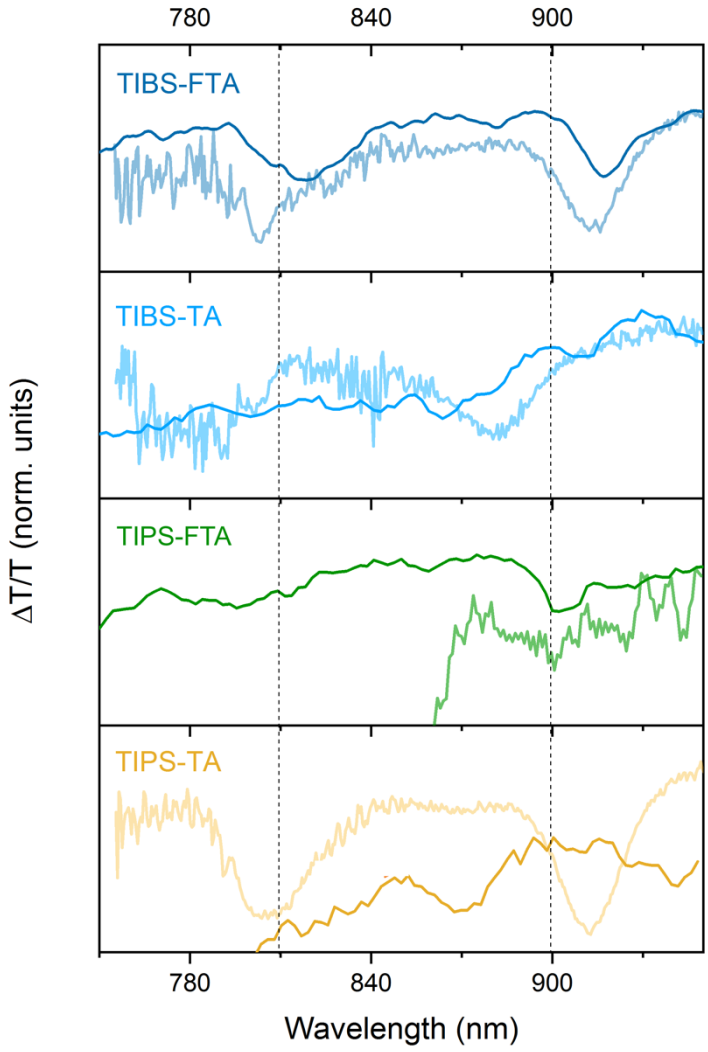

Figure 6.11-Sensitised T_1 spectra in solution (light) and inherent T_1 (dark) spectra via SF from films of TIBS-FTA, TIBS-TA, TIPS-FTA and TIPS-TA films. Sensitisation performed in solutions with a 3:10 weight percentage of the molecule:sensitiser in $CHCl_3$. While TIBS-FTA, TIBS-TA and TIPS-FTA form free triplets via SF, the final state formed in TIPS-TA does not match with that of the sensitized T_1 spectrum. The arrow shows the difference in peaks for TIPS-TA.

The unravelling of SF dynamics in films of TIBS-FTA, TIBS-TA and TIPS-FTA in the previous section shows that the triplet formation through SF varies significant between them. However, one needs to estimate triplet yields due to SF to establish the efficiency of these molecules as endothermic SF systems. We do this as follows for TIBS-FTA and similarly for the other thienoanthracenes.

The yield of T_1 formation is calculated from extinction coefficients obtained from the sensitization data shown in Figure 6.11. Molar absorptivity of TIBS-FTA is obtained from the steady-state absorption spectrum of a 1 mg/mL solution in a cuvette of path length 100 μm.

Molecular mass of TIBS-FTA= 697.1895 $gmol^{-1}$
Concentration of TIBS-FTA in solution for absorption= 1 mg/mL = 1.43 mM

Molar absorptivity of TIBS-FTA at 480nm,

$$e_{TIBSF,480}=\frac{Abs.\ at\ 480nm}{[TIBS\text{-}FTA]\ l}=\frac{0.04}{1.43*10^{-3}M*100*\ 10^{-6}m}=2.79*10^{5}\ M^{-1}m^{-1}$$

For TA measurements for the 1 mg/mL solution sample in a 100 μm cuvette , the ratio between transmitted intensity of light through the sample and that incident on the sample,

$$\frac{I}{I_0}=1\text{-}10^{-e_{TIBSF,480}[TIBSF]d}=1\text{-}10^{-0.039897}=0.087$$

For calculating the number of molecules in the S_1 state, $[S_1]^*$, the number of photons per pulse is recorded to be, power/(rep rate*energy of photon in J)

Energy of 480nm photon = $4.14*10^{-19}$ J
Repetition rate of the laser = 19000 sec^{-1}
Power = $150*10^{-6}$ W
Spot size, $\pi r^2 = 50*50\ \mu m^2$

$$Photons\ per\ pulse = \frac{power}{rep\ rate*energy\ of\ photon}=\frac{150\ \mu W}{19000*4.14*10^{-19}}$$

$$= 1.19*10^{10}\ \text{per pulse}$$

Volume excited inside the cuvette, $V= \pi r^2 d= 0.0025*10^{-6}*100*10^{-6}\ m^3$

$$= 2.5*10^{-13}\ m^3 \text{ or } 2.5*10^{-10}\ L$$

Avogadro number, $N_A = 6.023*10^{23}$

Concentration of number of molecules in excited S_1 state,

$$[S_1^*] = \frac{photons\ per\ pulse * {}^{I}/_{I_0}}{N_A * V} = 0.2588 * 10^{-3}\ \text{mol L}^{-1}$$

From the pump-probe spectrum at 1ps, $\Delta T/T$ at the SE peak of $S_1 = 20 * 10^{-4}$

Extinction coefficient of S_1,

$$e_{S_1} = \frac{\Delta A_{S_1}}{[S_1^*]d} = \frac{-log_{10}(\Delta T/T + 1)}{[S_1^*]d} = 3.36 * 10^4\ \text{M}^{-1}\text{m}^{-1}$$

From the sensitization data in Figure 6.11,

$\Delta T/T$ due to T_1 at PIA peak, 870nm$= 4.414 * 10^{-4}$
$l = 100\ \mu m$

$[T_1]$, or the concentration of the sensitizer with 96% ISC = 1.8 mg/mL= 2.6 mM

Extinction coefficient of T_1,

$$e_{T_1} = \frac{\Delta A_{T_1}}{[T_1]l} = \frac{-\log_{10}({}^{\Delta T}/_{T} + 1)}{C_{T_1} l} = 688.5\ \text{M}^{-1}\text{m}^{-1}$$

In the pump-probe data (Figure 6.7), the T_1 PIA peak (870nm) has $\Delta T/T$ at 2ns (red spectrum)$= 1.36 * 10^{-5}$

Hence, number of moles of T_1 in the 500nm thick film $= \frac{1.36 * 10^{-5}}{688.5 * 5 * 10^{-7}} = 0.0395$ mol

Number of moles of $[S_1^*]$ in the same sample$= \frac{4 * 10^{-4}}{3.36 * 10^4 * 5 * 10^{-7}} = 0.024$ mol

$$T_1 \text{ yield or SF yield} = \frac{\text{number of moles of } T_1}{\text{number of moles of } S_1} = 1.646 \sim 165 \pm 0\ \%$$

Triplet yield for TIBS-TA and TIPS-FTA were calculated by the same method as shown above as 120±0% and 170±0%, respectively.

6.5 Molecular Packing and Singlet Fission Dynamics

In section 6.3.1 we briefly touched upon the influence of molecular ordering in the solid state on the behavior of excited states. We have also discussed in detail, that by accessing electronic and vibrational degrees of freedom, previously forbidden transitions can become radiative in nature. Molecular arrangement plays a vital role in deciding the fate of excited states and the processes they undergo[186,187] and often the fate of excited states are determined by excited-state modes accessible to them. It is therefore not surprising that there is a considerable number of reports on the role of molecular structure on excited-state dynamics, which is decisive in the solid-state[188–192]. As we saw earlier in this chapter, crystal structures vary significantly with molecular structures. Thus, the molecular structure has a direct effect on the morphology and hence SF dynamics.

Apart from solid-state packing, other parameters of significance for SF such as energy levels of S_1 and T_1 states[75,83], and triplet diffusion rates that are closely linked to the entropy of endothermic SF (see Chapter 7). These parameters are controlled, directly or indirectly, by the design of the molecular structure. In this chapter, we have so far discussed the photophysics of four endothermic SF systems based on thienoanthracenes, with varying side chains and atomic substitution on the aromatic ring. In this section, we rationalize to the differences in excited state dynamics to the differences in the molecular structures.

The crystal packing of all four thienoanthracenes vary greatly as discussed in section 6.1. The highest density of molecular packing is for TIPS-FTA and the lowest for TIBS-TA as rationalized before by the difference in steric side groups. Important distinctions with respect to structure-photophysics correlations observed are as follows.

(i) Wider packed butyl-TAs (TIBS-TA and TIBS-FTA) have a low-energy emission that is secondary to that from S_1 emission and lives for tens of nanoseconds. This low-energy emission that rises in ~ 2 ns is labelled as TT emission, similar to what is reported in other endothermic SF systems

such as Tc and TIPS-Tc[95,130]. The low energy emission from the TT state in butyl-thienoanthracenes around 680-700 nm (1.77-1.82 eV) lacks vibrionic structure and may even be attributed to extremely small populations of *trap states* considering their long-lived decay and aggregate-like nature.

(ii) The absence of secondary emission from propyl-TAs, and broadening of S_1 emission in under 10 ns. Tighter packing of molecules in propyl TAs results in hampering vibrational modes accessible to TT states in the excited state-geometry. Consequently, this withholds TT states from radiatively relaxing to the ground state.

(iii) TIPS-FTA exhibits the fastest rates for S_1 decay (5 ps) and T_1 formation (70 ps), whereas TIBS-TA exhibits the slowest S_1 decay close to 20 ps and T_1 formation by 1 ns. The intermediate case of TIBS-FTA has an S_1 decay lifetime of 12 ps and T_1 formation by 300 ps. From a molecular ordering perspective, TIPS-FTA has molecules apart by 3 Å, TIBS-FTA by 8 Å and TIBS-TA by 10 Å. Thus, overcoming the energetic barrier for triplet formation with the help of entropy is easier for tightly packed TIPS-FTA and intermediate for TIBS-FTA (see Chapter 7 for a detailed discussion on TIBS-FTA), it can be expected to be less efficient for the loosely packed TIBS-TA.

(iv) Despite the intermediate packing density in TIPS-TA (7 Å), we do not see evidence for triplet formation from ESR or pump-probe spectroscopy. However, TIBS-FTA packs with a similar density to that of TIPS-TA and exhibits very efficient SF with a triplet yield of 165%. In other words, despite the seemingly favorable molecular structure design with leaner propyl side chains compared to their butyl counterparts, energetic matching and local morphology are absolutely crucial in efficient endothermic SF.

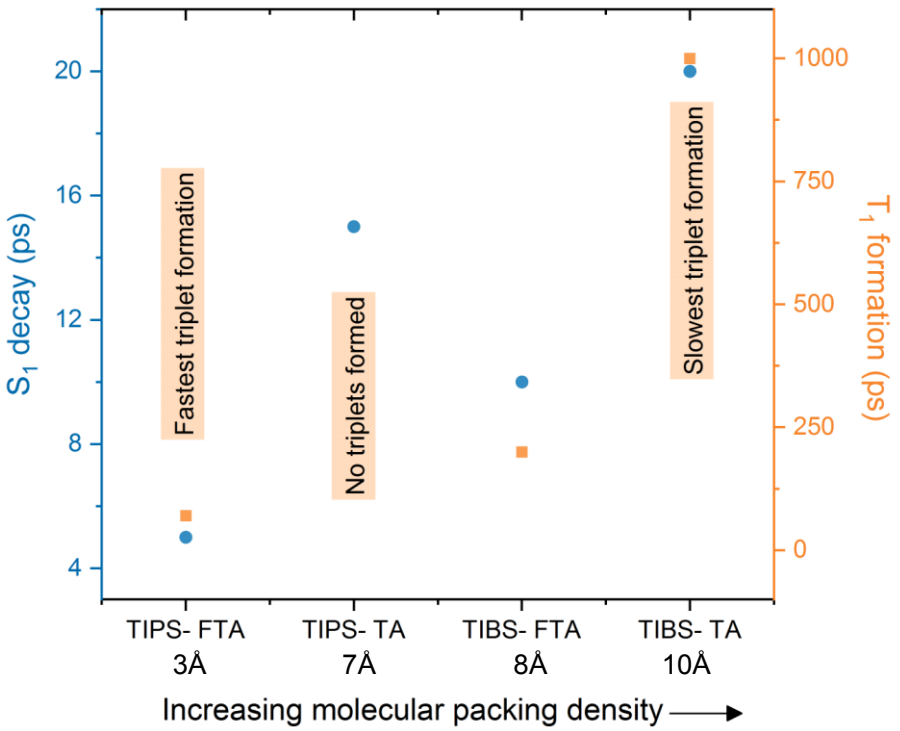

Figure 6.12-Singlet Fission timescales as a function of molecular packing densities of thienoanthracenes. TIPS-FTA with the highest packing density and lowest E_{STT} (endothermicity) shows the fastest SF. TIBS-TA with the lowest packing density and higher E_{STT} than TIPS-FTA shows the slowest SF. TIBS-FTA with intermediate packing density and higher E_{STT} compared to TIBS-TA shows faster SF than TIBS-TA, but slower than TIPS-FTA. The highest endothermic system, TIPS-TA shows no triplet formation via SF.

To emphasize the importance of side group bulkiness in endothermic SF, we demonstrate the excited state photophysics of TIBS-FTA in solution by pump-probe spectroscopy. Recent reports on endothermic SF systems such as TIPS-Tc show diffusion limited SF in concentrated solutions, activated above 100 mg/mL[113]. Here we investigate excited state photophysics of TIBS-FTA in a solution above the concentration of 300 mg/mL, shown in Figure 6.13 with time delays from 1 ns to 100 ns when excited at 500 nm. Longer time delays has been chosen for this experiment as films show free triplets by ~300 ps, with long lifetimes (ns-µs) expected. Hence we do not see S_1 state in this dataset at all. The earliest timeslice (1 ns, blue) in the data shows a large PIA between 700-800 nm.

This decays with a time constant of 2 ns to a second state with PIA peaks at 670 nm and 870 nm. TT and T_1 spectra obtained via DAS analysis of pump-probe dynamics in films are overlaid on the solution dynamics in the figure as the filled regions.

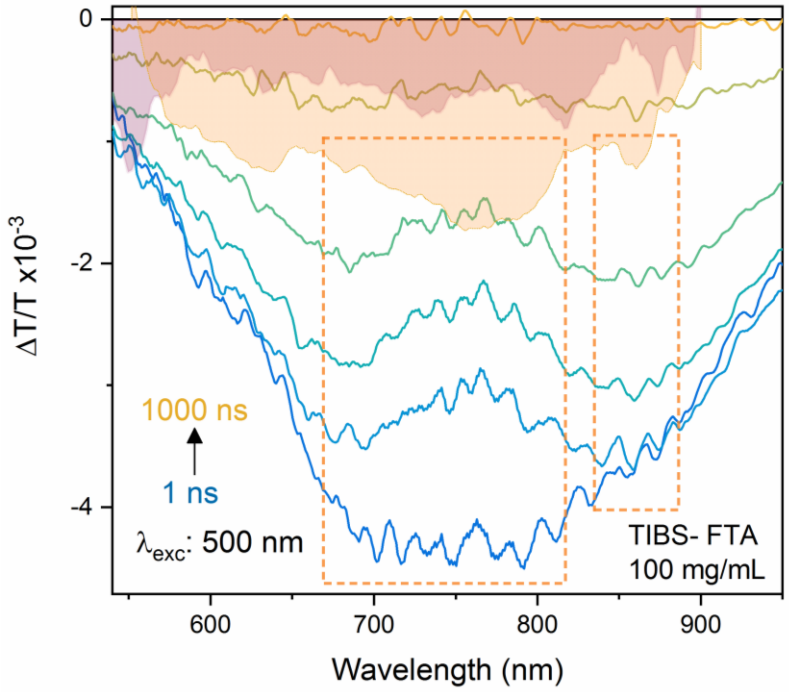

Figure 6.13-Pump-probe dynamics of TIBS-FTA in solution (100 mg/mL) with time delays between 1 ns and 1000 ns. Dynamics of concentrated solution of TIBS-FTA shows a S_1 PIA at 750 nm that decays to twin peaks at 700 nm and 850 nm (marked in squares). The latter species is spectrally similar to the TT state isolated in solid-state (yellow filled spectrum) however does not evolve further to form free triplets (red filled spectrum).

We see a remarkable similarity between the both species in the solution spectra and the TT-film spectrum (yellow filled), with no sign of free triplet formation in solution even by 1 μs. This confirms that SF does not take place in solutions of TIBS-FTA even at high concentrations and may be attributed to the bulky side chains that do not allow molecules to come close enough to facilitate SF. The final state observed to form in solution may have some TT character but does not break up to form free triplets, instead decays in several hundreds of nanoseconds non-radiatively to the ground S_0 state. We demonstrate molecular

crowding of TIBS-FTA molecules in solution schematically in Figure 6.14. The bulky butyl side chains do not let neighboring molecules in close distances that facilitate SF[193].

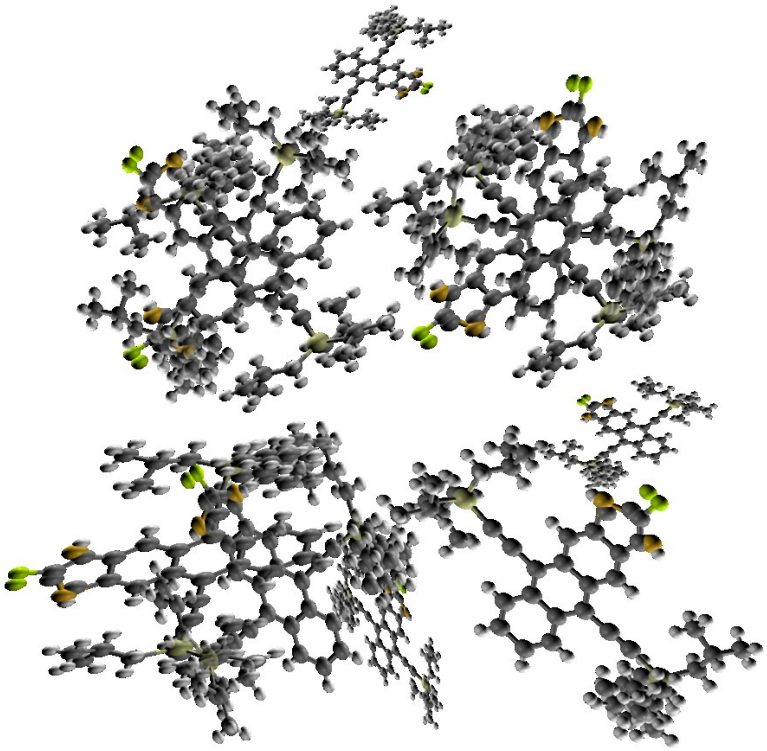

Figure 6.14-Schematic rendition of TIBS-FTA in solution.
Endothermic SF systems have shown diffusion limited SF in solution, where bulkiness of side chain on molecules is crucial. In TIBS-FTA the bulky butyl groups restrict how close the neighboring molecules can get, hampering singlet fission from happening, which is diffusion-limited in solution. Green: F, yellow: S, dark grey: C and light grey: H.

6.6 Conclusions and Outlook

In this chapter we introduced a new class of endothermic SF materials, thienoanthracenes with bluer absorption and endothermicities higher than that of Tc derivatives. The skeletal structure of thienoanthracenes constitute of an anthracene fused to a thiophene ring (five-carbon ring with sulphur substitution), essentially making it three quarter of a Tc. The thienoanthracenes are made solvent processible by means of two different side groups: butyl and propyl. To extend the range of endothermicities for the purpose of this study and to use them as efficient SF materials for device applications, a fluorine substitution on the aromatic backbone was done on TIBS-TA and TIPS-TA, making TIBS-FTA and TIPS-FTA. The use of two different side chains and the fluorine substitution resulted in significant differences in crystal packing, with inter-neighboring distances ranging between 3 Å to 10 Å; shorter for the propyl and longer for the butyl thienoanthracenes. We have studied the excited state dynamics of these four thienoanthracenes and attempted to map out structure-function correlations in terms of SF dynamics and efficiencies.

Triplet sensitization measurements in solution show that the triplet energies of all four thienoanthracenes are less than 1.4 eV. Phosphorescence measurements in films place the triplet energies between 1.2-1.4 eV as well. Using ESR spectroscopy we show that TIBS-FTA, TIBS-TA and TIPS-FTA generate free triplets through SF by analyzing their respective spin polarization pattern, unique to fission generated triplets (versus ISC-generated triplets). Time-resolved photoluminescence studies show that while a secondary, low energy emission with a rise time of ~2 ns form in the butyl-TAs, only a broadened S_1 emission feature lives at similar timescales in propyl-TAs. This low energy, late emission was explained by evoking a Herzberg-Teller type of mechanism where excited states access certain vibrational modes that let them attain certain TT configurations (molecular geometry) that allow them to radiatively relax to the ground state. The influence of local morphology is thus evident for this mechanism. Thus, while

this mechanism manifested as a long lived-low energy emission in butyl-TAs, the effect is entirely absent in propyl-TAs.

Pump-probe spectroscopy was used to build a clearer picture of the excited state dynamics of SF in thienoanthracenes, with time delays varying between fs to ns. In TIPS-FTA and TIBS-FTA we see the initially formed photoexcited S_1 state mixing with TT states as early as 200 fs, followed by S_1 decay under 10ps. Previous studies on films of TIPS-Tc have shown vibrationally coherent formation of TT states at early times (<200 fs), co-existing with S_1 due to the large excitonic coupling between them. We observed a similar rise of TT states within 200 fs alongside its mixing with S_1, in TIPS-FTA and TIBS-FTA. The coherence of TT states is lost with time and the population reaches a maximum before breaking apart to form free triplets. T_1 formation happens by 70 ps and 300 ps in TIPS-FTA and TIBS-FTA, respectively. In the system with the lowest packing density, TIBS-TA, TT formation does not happen until 20 ps after photoexcitation and S_1 decays along the same timescale indicating slower SF. The evolution of the TT states to decouple into free triplets is rather slow and happens by 1 ns in TIBS-TA.

By comparison to other thienoanthracenes, TIBS-TA exhibits the slowest case of SF. However, triplets generated by all three systems are rather long-lived, up to hundreds of ns. To emphasize the importance of less bulky side chains of SF molecules, we studied the excited state dynamics of TIBS-FTA in a concentrated solution, as SF turns on beyond a threshold concentration in solution. However, we see the emergence of a TT-like species that lives for >200 ns, does not form free triplets and decay non-radiatively to the ground state. Hence, the bulkiness of side groups and local morphology are certainly imperative for SF molecules although films of TIBS-FTA and TIBS-TA show SF, at timescales longer compared to TIPS-FTA films. Thus, tighter molecular packing leads to faster is the formation of free triplets by SF. However, the basic energy-matching criterion still needs to hold.

TIPS-TA, the highest endothermic system in this study does not show SF as it is energetically not favourable. Although we see the formation of TT states in these films, evidence for free triplet formation is obtained neither from ESR nor pump-probe spectroscopy on comparing with sensitised T_1 spectrum. While the molecular structure of TIPS-TA and side chain design was not expected to hinder SF, the high endothermicity of 340 meV was found to be detrimental to the process.

Through this rather comprehensive study of SF dynamics in thienoanthracenes with varying molecular structures and packing densities, we conclude that the following are the key parameters to ensure efficient SF and high triplet yield.

(i) Matching energetics for SF with not too high endothermicity (up to 300 meV allows SF in this study)
(ii) Molecular structures with lean side chains aid SF, resulting in faster triplet formation.

Now that we have explored the mechanism of SF in thienoanthracenes to some detail, we move on to finding what is driving SF is systems with such high endothermicity (E_{STT}= 300 meV). We take TIBS-FTA as our model system for this and hope to add to our understanding of what determines if SF should happen in endothermic systems.

Chapter 7

What Drives Endothermic Singlet Fission?

In this chapter we try to answer the long- standing question of what drives singlet fission (SF) in spite of the energetic uphill due to the endothermicity of a system. With the help of our synthetic chemistry collaborators, we presented a new class of endothermic SF materials known as thienoanthracenes in the last chapter. For the scope of this chapter, we focus on the role of entropy and endothermicity in TIBS-FTA, one of the previously introduced thienoanthracene. Major findings include experimental validation to the activation energy required for breaking up of the intermediate TT states and how it compares to the entropic energy change that facilitates SF. We characterize the excitonic dynamics using a combination of steady- state optical spectroscopy, transient electron-spin resonance (ESR) spectroscopy, time resolved emission spectroscopy (TRES) and ultrafast pump-probe spectroscopy. By analysing the temperature dependence of the rate of free triplet formation we find the activation energy of 60 meV, an order of magnitude less than the endothermicity of 300 meV. We present a model based on crystal structure and temperature dependent excitonic dynamics to estimate the entropic change of TIBS-FTA during SF, whose SF dynamics were discussed in the previous chapter. We show that both the activation energy and triplet kinetics can be predicted by the model if triplet diffusion lengths reach values of 10nm at room temperature. Our results highlight the critical role of entropy in driving endothermic SF.

7.1 Background and Motivation

Energy level ordering, molecular and excitonic coupling are important factors to consider while rationalizing free triplet formation via SF[92,96,194]. Depending on the difference between the internal energy of S_1 and that of $2T_1$, $E_{STT} = E_{S_1} - 2E_{T_1}$, SF can be classified as either endothermic or exothermic, as discussed before. For endothermic systems the process is enthalpically uphill. In endothermic SF systems however, we also need to include the role played by entropy, as suggested by *Zhu et al*[87]. We therefore choose to consider the free energy landscape of SF, including enthalpic and entropic changes, as well as excitonic coupling. Several reports on temperature dependence and the role of morphology for endothermic SF, especially tetracene and its derivatives, exist to date[20,55]. However, experimental understanding of the entropic drive in SF is lacking and often confusing, although some interesting theoretical arguments have been put forward in the past.

Schmidt and co-workers proposed[195] the treatment of SF as a statistical mechanics problem. Using this approach, they predict the limits to excited state energies (S_1 and $2T_1$) that influence energy conversion efficiencies. In the absence of triplet dissociation energy, the authors find that the entropic change in the system must always offset the endothermicity while the system attains rapid equilibrium between $|S_0>|S_1> \rightleftharpoons |T_1>|T_1>$ while the change in free energy is neutral. The optimal ratio between singlet and triplet energies are further calculated for optimal current density and open circuit voltage to attain maximum device efficiencies.

In another work, Zhu and coworkers[87] proposed ultrafast formation of a multiexcitonic state in coherent superposition with the S_1 state (with a coupling constant $||\gamma||^2$) as the first step of SF, followed by an entropic driving force facilitating the decoupling of this superposition to form $2T_1$. They linked the entropic driving force to the increased number of configurations possible for the product state ($2T_1$) compared to the initial state (S_1). The corresponding entropic contribution in tetracene was calculated, with the assumption that the number

of triplet ($2T_1$) and singlet (S_1) microstates depends on the number of molecules visited by the S_1 state alone, i.e. the singlet diffusion length. However, in systems where endothermic SF occurs within 200 fs like TIPS- Tetracene, the number of S_1 microstates should only be limited by delocalization of the singlet exciton, influenced by the electronic structure of the molecule. Also, a more accurate description of $2T_1$ microstates must depend on the mobility of triplets defined by the triplet diffusion length, which can be tuned with the molecular packing of the system. Concepts involved in the discussion on entropy such as microscopic configurations or microstates, shall be introduced in the following section.

Many studies have explored the electronic parameters involved in SF. However, understanding SF by correlating macroscopic quantities with underlying physical factors is rather inadequate. Recently, Krylov and co-workers presented a lucid analysis of experimental SF data in tetracene[96]. They use a model (henceforth referred to as the *Krylov model*) that focusses on microscopic configurations of distinct excitonic states involved in SF, accounting for the entropic change during the process. The *Krylov model* provides insight into the role of entropy in the process of SF incorporating aspects such as singlet delocalization and triplet diffusion. The *Krylov model* consists of three states, the initial S_1, TT intermediate and $2T_1$. The increase in the number of microstates from S_1 to TT to $2T_1$ is marked as increasing entropy in the system as SF proceeds. The rate of SF is determined by factors such as this thermodynamic driving force, the electronic coupling between the S_1 and TT state, $||\gamma||^2$, which are controlled by both molecular design and packing[87]. However, *Krylov et al.* reports theoretical calculations suggest that the relative coupling strength, $||\gamma||^2$, between tetracene, pentacene and hexacene being similar. Hence, they rule out the likelihood of coupling strength leading to the largely different rates of SF observed in these molecules. The study hence points out a significant, but expected influence of entropy in driving the process of SF in tetracene. For example, in pentacene which is an exothermic SF system, the thermodynamic driving force is very large resulting in very fast SF[194]. On the other hand in tetracene, an endothermic

system, an entropic driving force, along with $||\gamma||^2$, is invoked to explain the experimental SF rates.

While the *Krylov model* explains the case of systems with little temperature dependence, endothermic systems that show ultrafast SF (< 200 fs) and thermally activated, rapid $2T_1$ formation need more careful examination. Quintessential questions remain in understanding the mechanism of SF in endothermic systems. For photovoltaic device applications of SF, endothermic fission systems are required for high- efficiency energy conversion[72,74]. The enthalpically uphill process of endothermic SF ($E_{S_1} < 2E_{T_1}$) may proceed spontaneously only means of an equivalent change in entropy, according to the second law of thermodynamics. Factors that influence this change in entropy of SF are two-fold: (i) spatial parameters that influence the solid-state structure and (ii) temporal parameters that define the diffusion of excited states within SF timescales in the system. Of particular interest is the question of how endothermic SF can be whilst being efficient. SF in both tetracene and TIPS-tetracene (E_{STT}~ -0.2eV) is known to give near unity efficiency. What is the limit to how negative E_{STT} can get, for an efficient SF system? And what is the mechanism for overcoming such large gaps in enthalpy? It has long been suggested that entropy plays a role in driving the breakup of the TT state into free triplets in endothermic SF systems[87,96,98,195]. While this has been explored in a few papers from theoretical perspective, there is little experimental evidence that rigorously tests this hypothesis.

Another motivation for this work is the lack of understanding on the relative contribution of TT binding energy and activation energy to form $2T_1$ in endothermic SF. Some reports have loosely estimated this dependence to be the binding energy twice that of the activation energy, however this has not been experimentally verified. This estimate stems from theoretical observations made by *Durrant et al.*[196], in calculating the role of entropy of electron-hole separation in donor-acceptor (D-A) systems (discussed later). However, in the absence of experimental support this may not be assumed for SF, resulting in incorrectly estimated entropic driving force.

7.2 TIBS-FTA: The Model System

One of the intentions behind designing a new class of endothermic SF materials such as thienoanthracenes is to improve our understanding of the temperature dependence of SF. As the endothermicity of these molecules are higher than tetracene, it allows for better resolution for data steps experimentally undertaken, helping to model of the data become easier. From Chapter 6 we have analysed SF dynamics of four thienoanthracenes and we choose TIBS-FTA as our model system due to a few reasons.

(i) Detection of T_1 energies in SF systems have proven to be difficult as phosphorescent measurements tend to be prone to low signal- noise levels and its masking due to photoluminescence from the sample. We managed to experimentally verify the T_1 energy level of TIBS-FTA by two independent experimental techniques, by phosphorescence measurements and sensitisation pump- probe measurements, which will be discussed shortly.

(ii) Fast formation of free triplets (< 100ps), thus enabling detection of S_1, TT and $2T_1$ states and their dynamics in single shot experiments leading to consistent and reproducible results. This allowed us to systematically and reproducibly measure the temperature dependence of various processes involved in SF.

(iii) High triplet yield of ~160%.

(iv) High photostability.

7.2.1 Steady-State Characterisation

Figure 7.1 shows the molecular structure and steady-state absorption/emission spectra of TIBS-FTA, already discussed in Chapter 6.

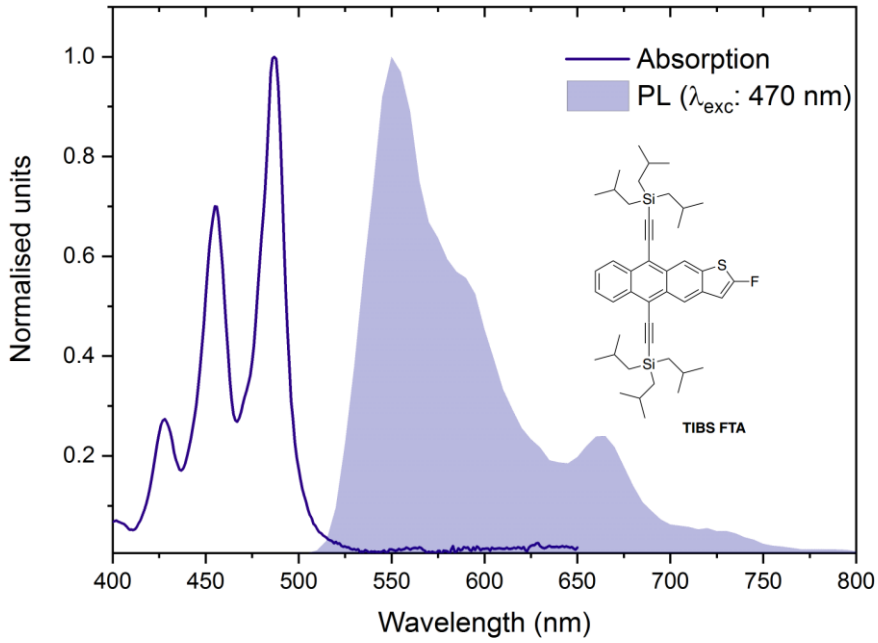

Figure 7.1- Steady- state characterisation and molecular structure of TIBS-FTA. Absorption and PL (excited at 470 nm) spectra show vibronic 0-0, 0-1 and 0-2 transitions. Inset shows the molecular structure of TIBS-FTA.

7.3 Identifying Triplet Energy in TIBS-FTA

Accurate measurements of triplet energy, E_{T_1}, of TIBS-FTA is crucial to ascertain the endothermicity of the system, as we are trying to estimate the entropic contributions that can overcome this endothermic barrier. The triplet energy has been determined from two experimental methods as well as theoretical calculations, to ensure consistency of the results. The methods were,

(i) Triplet cross-sections are much smaller than that of the singlets in organics without heavy atoms. Thus, to identify triplet energies, we sensitize the TIBS-FTA triplet state using a Palladium- based dopant (PdTPTBP). The sensitization is manifested as 'brightened' stead-state phosphorescence from TIBS-FTA triplets.

(ii) Pump-probe measurements of solutions of TIBS-FTA with two sensitizers in solution that sensitize TIBS-FTA triplets.

(iii) Time dependent density functional calculations of TIBS-FTA within the Tamm- Dancoff approximation

7.3.1 Triplet Sensitization in Solid-State

Phosphorescence from triplets or the radiative, spin-forbidden relaxation of T_1 to the ground S_0 state detected in the near- IR, is a clear marker of where the triplet energy of a molecules lies. For this, we prepared thin films of TIBS-FTA doped with Pd(II) meso-Tetraphenyl Tetrabenzoporphyrin (PdTPTBP) (see methods for details) and captured emission in the near- IR region using a cooled InGaAs camera. This sensitizer produces triplets of ~1.5eV, efficiently by ISC by spin-orbit coupling and are transferred to the lower lying triplet state of TIBS-FTA. We observe a weak emission at ~1.3eV from TIBS-FTA, as shown in Figure 7.2.

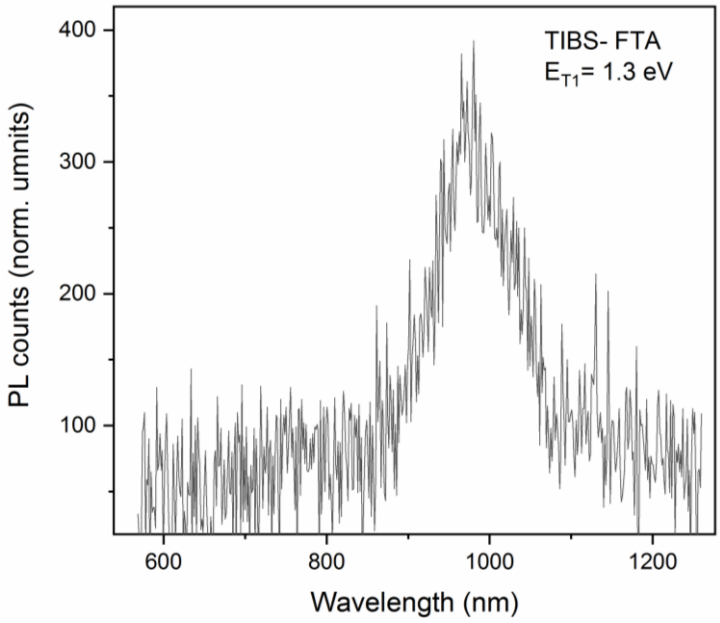

Figure 7.2- Sensitised T_1 spectrum of TIBS-FTA films with PdTPTBP.
The film dropcast from a solution mixture of PdTPTBP (10% by weight) and TIBS-FTA (3% by weight) was excited at 658nm.

7.3.2 Triplet Sensitization in Solution-State

To validate this T_1 energy of ~1.3 eV from steady-state phosphorescence by a parallel experiment, we sensitised solutions of TIBS-FTA by a fullerene-based sensitizer (n-methylfulleropyrrolidine) with E_{T_1} ~1.4 eV and a Pd-based sensitizer (PdPc, Palladium(II) octabutoxy-phthalocyanine) with E_{T_1} ~1.24 eV. The pump-probe dynamics of solutions with the sensitizers were measured to see the emergence of 'brightened' TIBS-FTA triplet population. Figure 7.4 shows the pump-probe dynamics of TIBS-FTA solution sensitised with PdPc, where we see the initially formed PdPc spectral features living beyond 1μs. If PdPc triplets were to be injected into TIBS-FTA, we expect to see quenching of the signal from the former and a corresponding growth of triplet signal from TIBS-FTA. However, we do not see any quenching of the initial PdPc signal, and we conclude that triplet transfer to TIBS-FTA was not successful. This proves that E_{T_1} of PdPc is lower than that of TIBS-FTA, impeding triplet transfer to the latter.

The same experiment was performed with the fullerene- based sensitizer with E_{T_1} lower than that expected of TIBS-FTA obtained through phosphorescence measurements. The pump- probe dynamics of this experiment is shown in Figure 7.5, where we see the initial fullerene signal decaying to form two sharp peaks at 650 nm, 800 nm and ~900 nm by 100 ns or so, which are markers of triplets in TIBS-FTA. This confirms that E_{T_1} of TIBS-FTA lie lower than that of the fullerene- based sensitizer (~1.4 eV). Figure 7.3 shows the sensitised spectra at 500ns with both sensitizers for comparison.

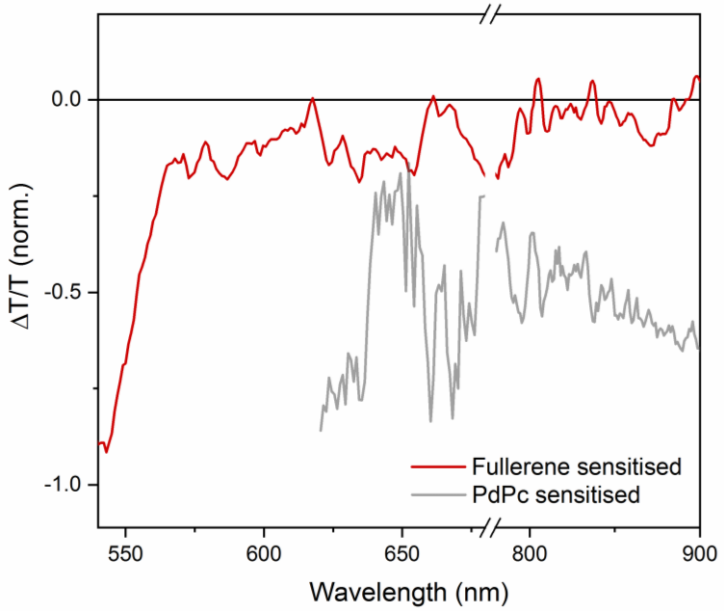

Figure 7.3- Pump-probe spectra at a time delay of 500 ns in sensitised TIBS-FTA solutions with fullerene and PdPc. The fullerene-sensitised (red) spectrum shows triplet formation from initial species while PdPc-sensitised spectrum shows long-lived single species that does not form free triplets.

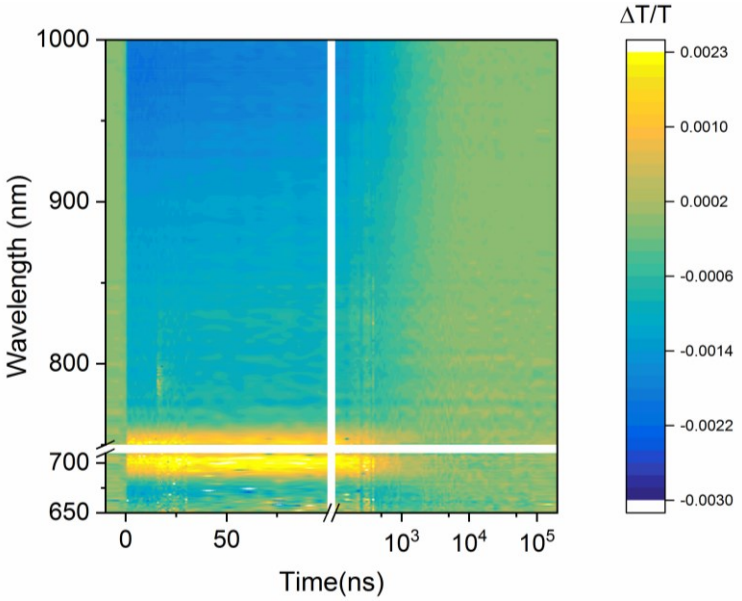

Figure 7.4- PdPc sensitised TIBS-FTA pump-probe ns dynamics. PdPc excited at 680 nm produces triplets that decay by 1 µs. No secondary forming species or evidence for triplet transfer to TIBS-FTA is observed.

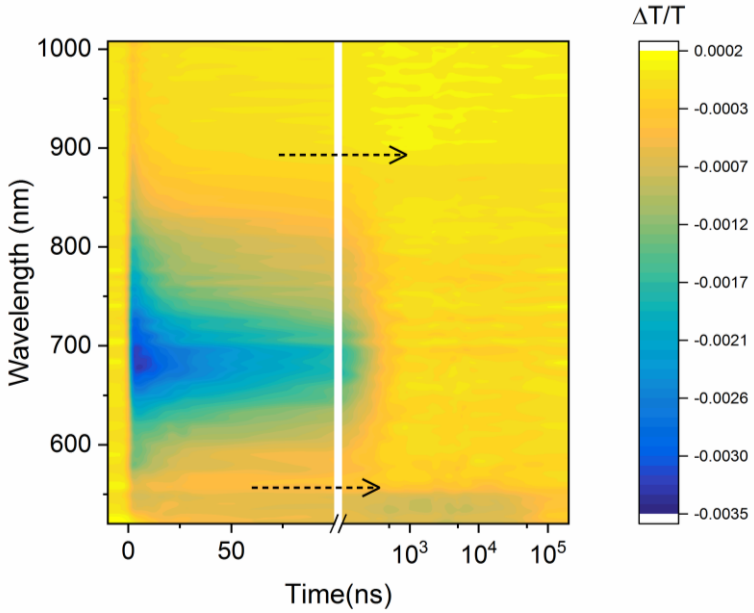

Figure 7.5- Fullerene sensitised TIBS-FTA pump-probe ns dynamics. Exciting the sensitizer at 355 nm forms an initial, distinct PIA of the fullerene that decays by 100 ns to sharp peaks at 650, 800 nm and ~900 nm, which are triplet bands of TIBS-FTA. This indicates triplet transfer from the sensitizer to the films.

7.3.3 Theoretical Prediction of Triplet Energy Using *TD*- DFT

For the molecule of interest, the electronic structure was described by density functional theory (DFT). To access the energies of the corresponding transitions, we employed the closed- shell formulation of the time-dependent DFT under the Tamm-Dancoff approximation at the optimized ground state geometry of a single molecule in the gas phase. The DFT calculations were performed using B3LYP functional and def2-SV(P) basis set, as implemented in TURBOMOLE 6.5[45]. Calculations were carried out by our collaborators. The experimental value of E_{T_1}, 1.3 eV agrees with theoretical calculations for the triplet 1.3 eV.

7.4 Evidence for Singlet Fission

Direct and indirect evidence for SF in TIBS-FTA films has been discussed in detail in chapter 6, based on results from techniques such as TRES, ESR and pump- probe spectroscopy, and are summarised as follows.

7.4.1 Identifying TT states and SF-generated Triplets

The presence of a secondary emissive species that we identified as TT emission was discussed as a consequence of a Herzberg- Teller type of mechanism in the excited state. The concern with the TT state being emissive is whether this is a population that bypasses the SF route and instead relaxes to S_0 state, reducing the T_1 yield of the system. Comparing the signal strength of S_1 and TT emissions from the tr-PL data, the fraction of TT states that undergo radiative recombination is very minor, shown in Figure 7.6. In addition to this, the photoluminescence quantum efficiency (PLQE) of less than 5 % measured for TIBS-FTA thin films indicates a major non-radiative pathway for excited singlet states, which is suggestive of SF.

Another piece of direct evidence for SF is provided by electron spin resonance (ESR) spectroscopy. In Figure 7.7 we present the ESR spectrum borrowed from chapter 6. The emergence *AEEAAE* pattern in TIBS-FTA film is consistent with the polarization pattern expected in SF- generated triplets as explained in detail in section 6.4.2, Chapter 6.

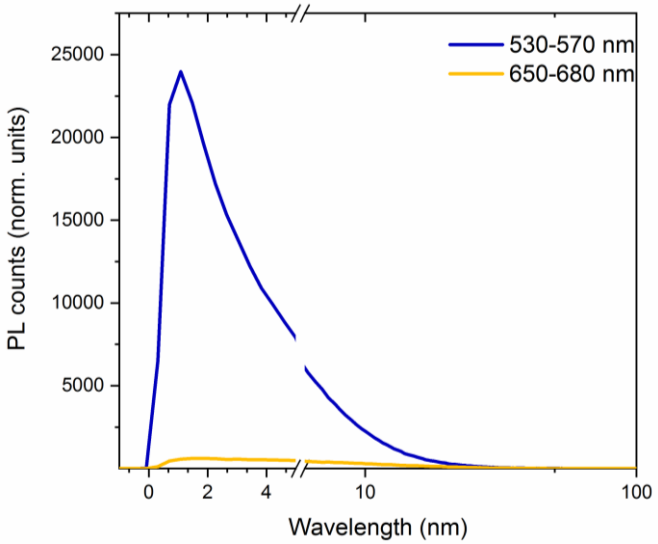

Figure 7.6- Kinetics of S_1 and TT kinetics in TIBS-FTA films excited at 470 nm. S_1 kinetics is given by the peak at 550 nm which decays with a time constant of <5ns and TT kinetics given by the low- energy feature at 670 nm which gives a rise time of 2 ns and decays with a lifetime beyond 10 ns. The very low relative kinetic maximum of TT with respect to S_1 indicates the very small fraction of TT states being emissive, beyond 2 ns.

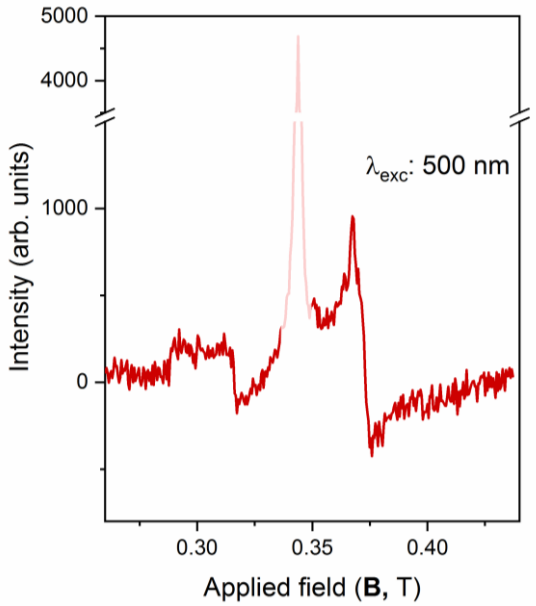

Figure 7.7- ESR spectrum of TIBS-FTA film excited at 500 nm with SF T_1 signature. The distinct AEEAAE spin polarisation pattern suggests the formation of triplet excitons mediated by SF.

7.4.2 Identifying Triplets by Pump-Probe Spectroscopy

Triplet sensitization measurements in solutions of TIBS-FTA are done using a fullerene based sensitizer as discussed in section 7.3.2 and the data is shown in Figure 7.5. As E_{T_1} of the sensitizer (1.4 eV) is higher than that of TIBS-FTA (~1.3 eV), T_1 injection to the latter occurs by *Dexter transfer* in solution state. Figure 7.8 shows the fullerene- sensitised T_1 pump-probe spectrum of TIBS-FTA in solution overlaid on the pump- probe spectrum at a delay of 10 ns in a TIBS-FTA film, when excited at 480 nm. The common peaks at 800 nm and ~910 nm confirm that SF-generated triplets are present at the long delay of 10 ns in thin films. This spectrum serves as the basis T_1 spectrum used in this study for spectral and kinetic deconvolution of pump- probe data at earlier fs-ps timescales discussed in later sections.

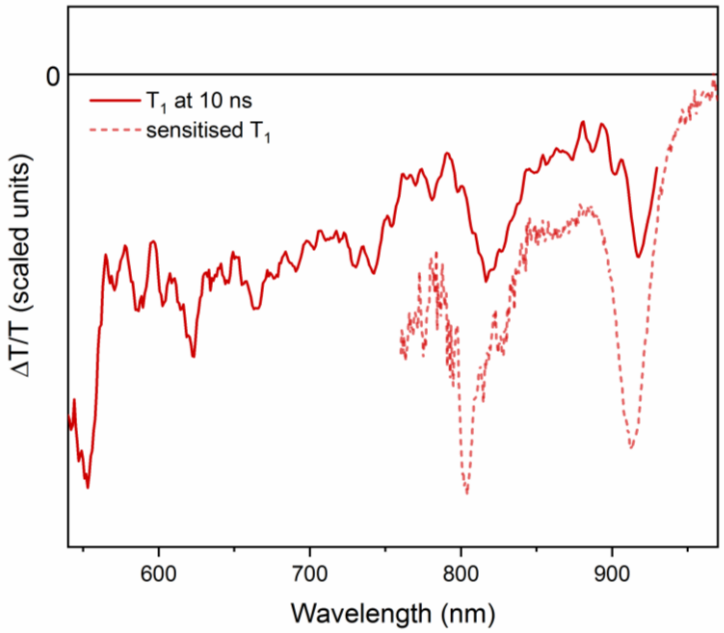

Figure 7.8- Pump- probe T_1 spectra of TIBS-FTA film at 10 ns and solution- sensitised T_1 spectrum with fullerene sensitizer. The major triplets peaks in the films match those in the sensitized spectrum at 800 nm and 910 nm. The line plot is used as the reference for T_1 state, for spectral and kinetic deconvolution in this study.

7.5 Thermally Activated Endothermic Singlet Fission

Several studies on endothermic SF systems such as tetracene and its derivatives highlight the temperature-dependent behaviour of processes involved in SF[55,95,197]. Now we come to the major focus of this chapter, to explore the temperature-controlled behaviour in films of TIBS-FTA. Further, we extend it to our analysis based on the entropic drive for endothermic SF.

Temperature dependent pump- probe spectroscopy measurements from 298 K to 10 K are performed on thin films of TIBS-FTA excited at 480 nm with a narrowband ~200 fs long pulse. The two-dimensional plot of $\Delta T/T$, wavelength and time delays are shown in Figure 7.9. From the data at 298 K we observe that at times less than 10 ps, films show spectral signatures of S_1 mixed with an intermediate state that rises within 100 fs. We assign the early-rising state that mixes with S_1, to the TT state. The TT state dominates the spectra at intermediary timescales (>100 ps) beyond which they break up to form free triplets ($2T_1$).

Extending these remarks to lower temperatures we find some major changes in spectral evolution of excited states, listed below.

(i) The photoexcited S_1 decays into intermediate TT states at all temperatures. This implies that TT formation is not thermally activated and is discussed in detail later in this section.

(ii) TT formation kinetics are expected to be as fast as < 200 fs and thus we do not see the ultrafast rise of the TT states. However, at temperatures lower than 100 K, we notice a rise of TT population in the picosecond time regime.

(iii) TT populations at temperature higher than 150 K face a decline at longer timescales which implies the breaking up of TT states to form free triplets, complementing $2T_1$ rise times.

(iv) TT states decouple to form free triplets ($2T_1$) as fast as 50 ps at 298 K, while at 100 K occurring in nanoseconds. We also notice the absence of

$2T_1$ formation at 50 K and 10 K, where TT states live beyond the experimental time window (2 ns).

(v) $2T_1$ formation and the breaking up of TT states are therefore concluded to be thermally activated. We analyse this process by following an Arrhenius type model in the following section.

Temperature dependent pump- probe data show a multitude of spectral and kinetic components (as briefly discussed for 298 K) which have been deconvoluted by means of DAS analysis. The SVD-based method of DAS pulls out S_1, TT and $2T_1$ signatures where applicable, at temperatures between 298 K and 10 K. An instance of this is shown in Figure 7.10 with the DAS components extracted from pump- probe data at 298 K, in the left panel. The $2T_1$ DAS spectrum here matches that of the sensitized T_1 spectrum as well as the 10 ns time delay spectrum shown in Figure 7.8.

Spectral features unique to each state from the DAS components with respective kinetic constants are compared to the raw kinetics. The method of comparing the raw data with DAS analysis helps us to identify *pure* kinetics of S_1 and T_1 states in the raw data. The corresponding kinetics thus identified by are shown in the right panel. The process of DAS analysis and comparison to raw data helps us isolate kinetics of distinct states. This method is repeated on datasets recorded at all temperatures and we discuss numerical fitting of thus obtained kinetics in the following section. We notice that late-TT and early $2T_1$ kinetics differ greatly with temperature.

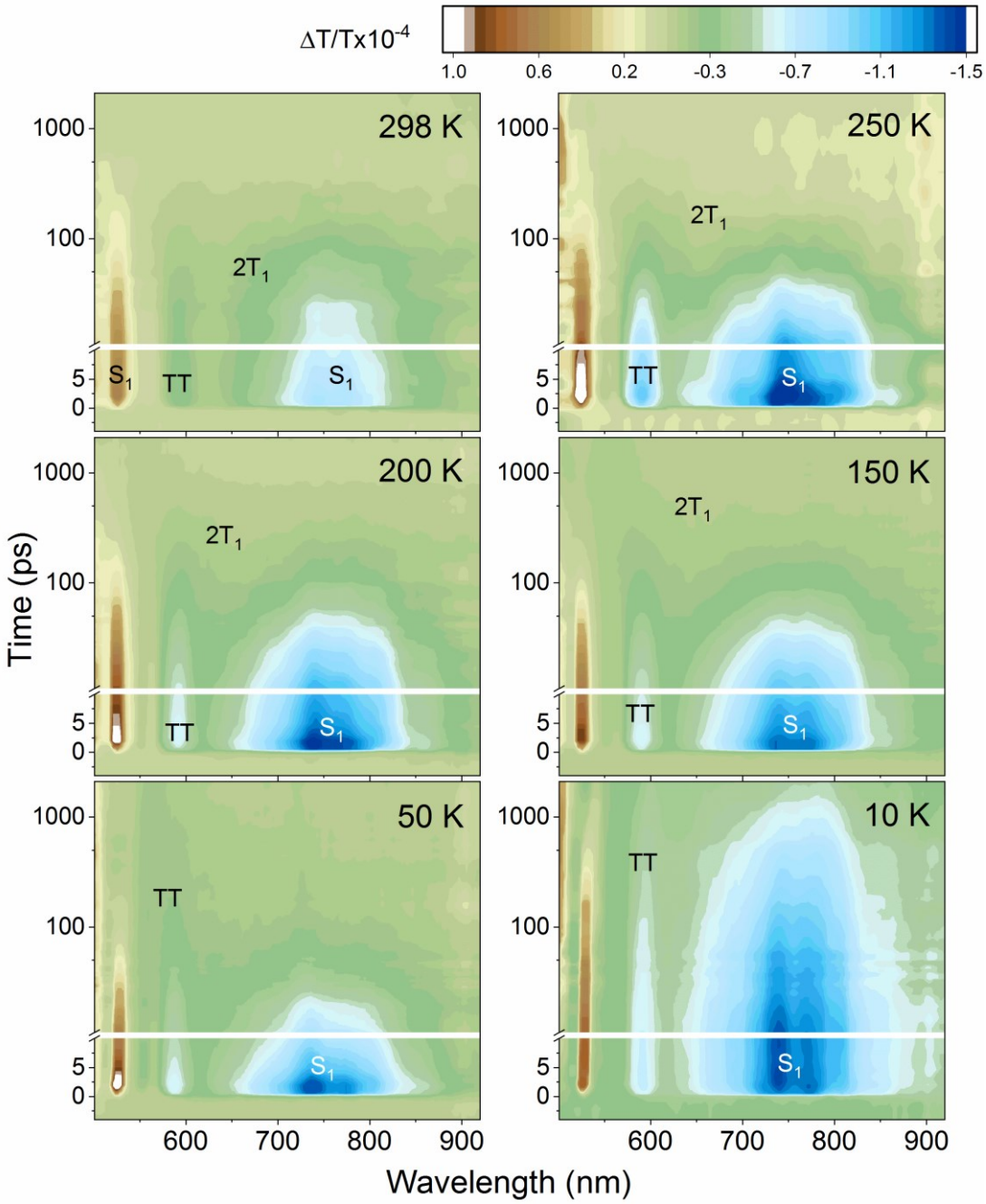

Figure 7.9- Temperature dependent pump- probe ps-ns dynamics of TIBS-FTA films excited at 480 nm from 298 K to 10 K. The spectra are shown for time delays from 100 fs to 1.8 ns. TT decays faster at higher temperatures to form free triplets. The activation energy for triplet formation is estimated to be 60 meV by methods described in the following section.

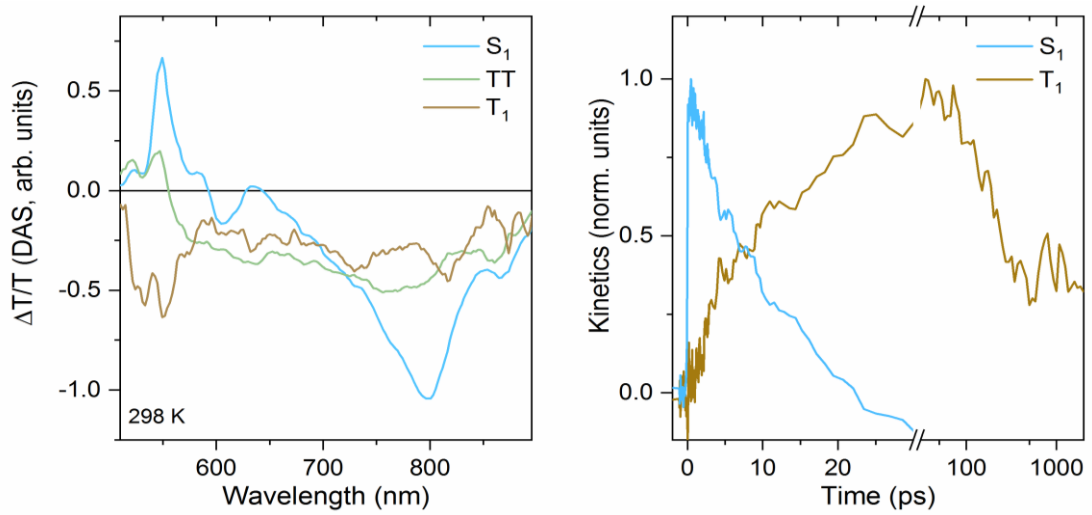

Figure 7.10- Decay Associated Spectral components by SVD method from pump- probe data recorded at 298 K. The three spectrally distinct DAS components S_1, TT and $2T_1$ are shown in the left panel. S_1 and $2T_1$ dynamics are shown in the right panel. Adapted from Chapter 6. S_1 kinetics becoming negative beyond 20 ps is indicative of a complementary growth in the TT population that eats into the former, as they have many overlapping spectral features. This results in a sharp climb in TT kinetics, shown in Figure 7.13.

7.5.1 Numerical Fitting of Temperature-Dependent Singlet Fission Kinetics

Triplet ($2T_1$) kinetics obtained by the method of comparison described above are fit to a bi-exponential curve with growth and decay time constants, given by 7.1. An example of a kinetic fitting with physical parameters including t_g, the growth rate of $2T_1$ states, t_d, the decay rate of the $2T_1$ states and the point of inflection, x_c, is shown in Figure 7.11. In this example, $2T_1$ states form by 13 ps (t_g), peaks in population by 45 ps (x_c) and decays with a fast time constant of 143 ps (t_d).

$$y = \begin{cases} y_0 + A_d + A_g\left(e^{\frac{-x_c}{t_g}} - e^{\frac{-x}{t_g}}\right) & x \le x_c \\ y_0 + A_d\, e^{\frac{-(x-x_c)}{t_d}} & x > x_c \end{cases} \qquad 7.1$$

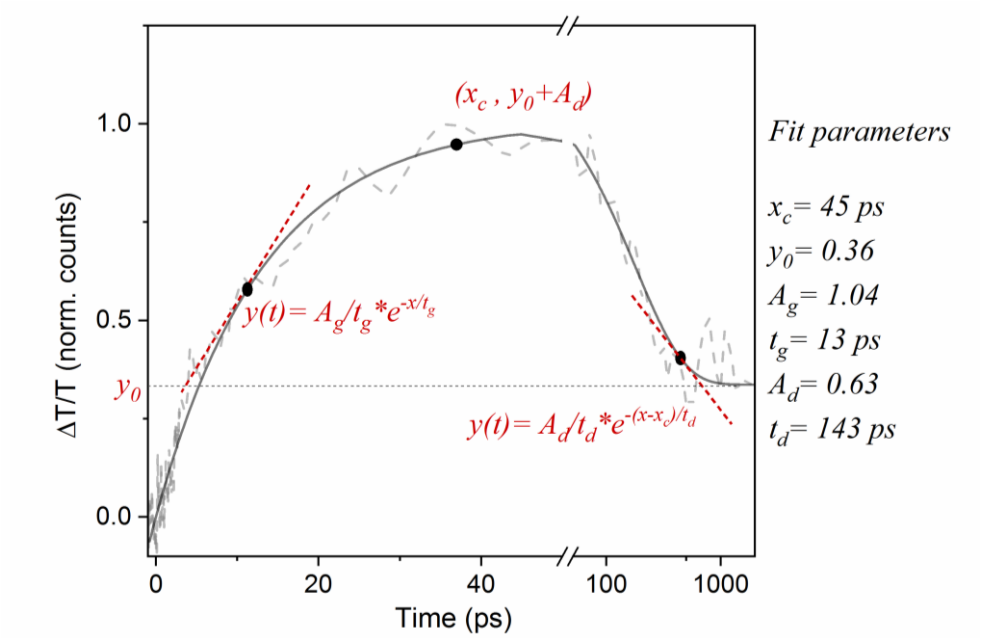

Figure 7.11- Fitting $2T_1$ kinetics with the bi- exponential growth- decay with relevant fit parameters. Dotted line shows the $2T_1$ formation dynamics recorded at 298 K by pump- probe experiment. The growth (t_g) and decay time (t_d) of the two exponentials and the population peak (x_c) are the parameters used for fitting and they vary with the strength and kinetics of excited-state populations involved.

This method of kinetic-fitting performed on data recorded between 298K and 50K are shown in Figure 7.12. We see that the x_c values (or the $2T_1$ population maximum) shifts to longer times as temperature decreases, eventually going beyond the experimental time window of 1.8 ns at 100 K and 50 K. As seen from the raw data in Figure 7.9 alongside the kinetic fitting below, the formation and decay rates of $2T_1$ states change drastically with temperature.

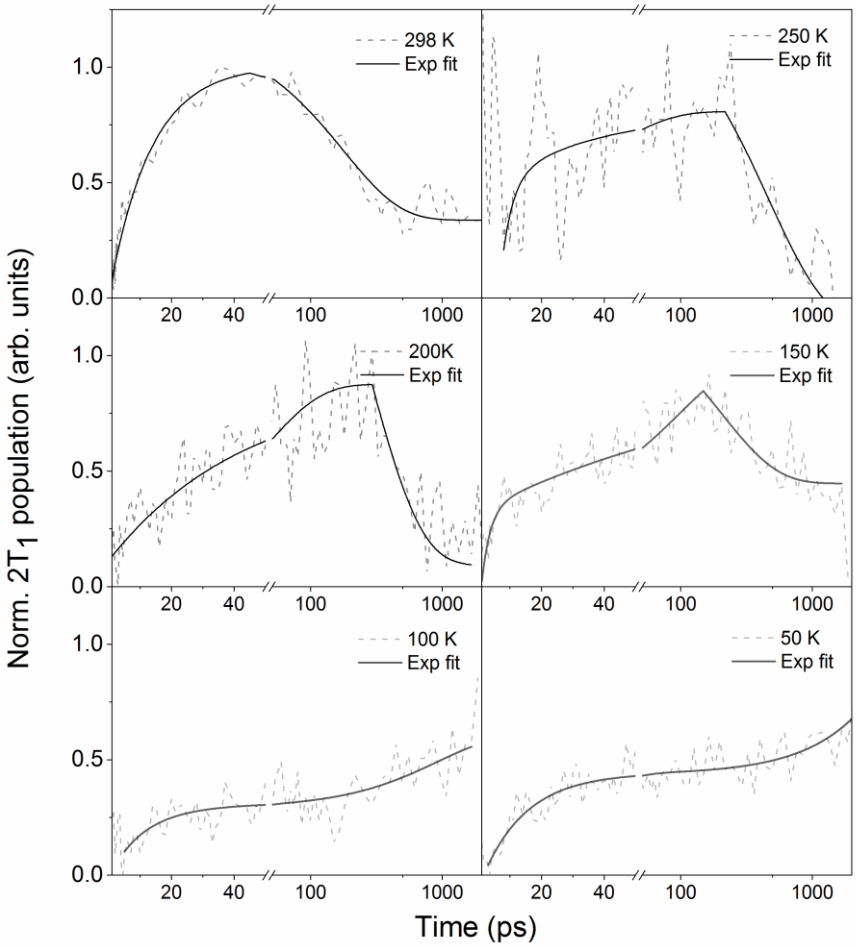

Figure 7.12- Temperature- dependent pump- probe $2T_1$ dynamics fit to a bi- exponential. Formation of $2T_1$ slows down at lower temperatures, befitting an Arrhenius model with thermal activation.

Following the fitting method for triplet populations generated by SF, we extract TT kinetics from respective pump- probe data and fit them using 7.1. The results of kinetic fitting for TT states as a function of temperature are consolidated in Figure 7.13. While the formation kinetics of TT state is expected to occur under 200 fs, we do not necessarily see its rise given the experimental time resolution of ~200 fs. However, as temperatures fall below 100 K, TT states rise within 1- 2 ps, hinting at a very weak thermal activation in TT formation. The decay kinetics of TT states largely depends on their breaking up into $2T_1$ states and thus, any effect of temperature on TT decay dynamics shall be read together with the

formation of $2T_1$. Rate constants obtained from the kinetic fitting are given in *Table 7.1*.

Table 7.1- Kinetic constants of TT and $2T_1$ formation as a function of temperature.

	298K	250K	200K	150K	100K	50K	10K
TT rise	< 200 fs	< 200 fs	< 200 fs	300 fs	450 fs	560 fs	710 fs
$2T_1$ rise	13ps	33ps	43ps	107ps	2ns	>2ns	>2ns

From the kinetic modelling of TT and $2T_1$ populations above we have established a strong temperature dependence in the breaking up of TT to form $2T_1$, however the formation of TT states itself is not thermally driven to a large extent. However, when temperatures go below 100 K, we see a very mild thermal activation which could be attributed to change in morphology of the films at low temperatures or the absence of enough thermal energy in the bath to favour the transition of S_1 to the TT state.

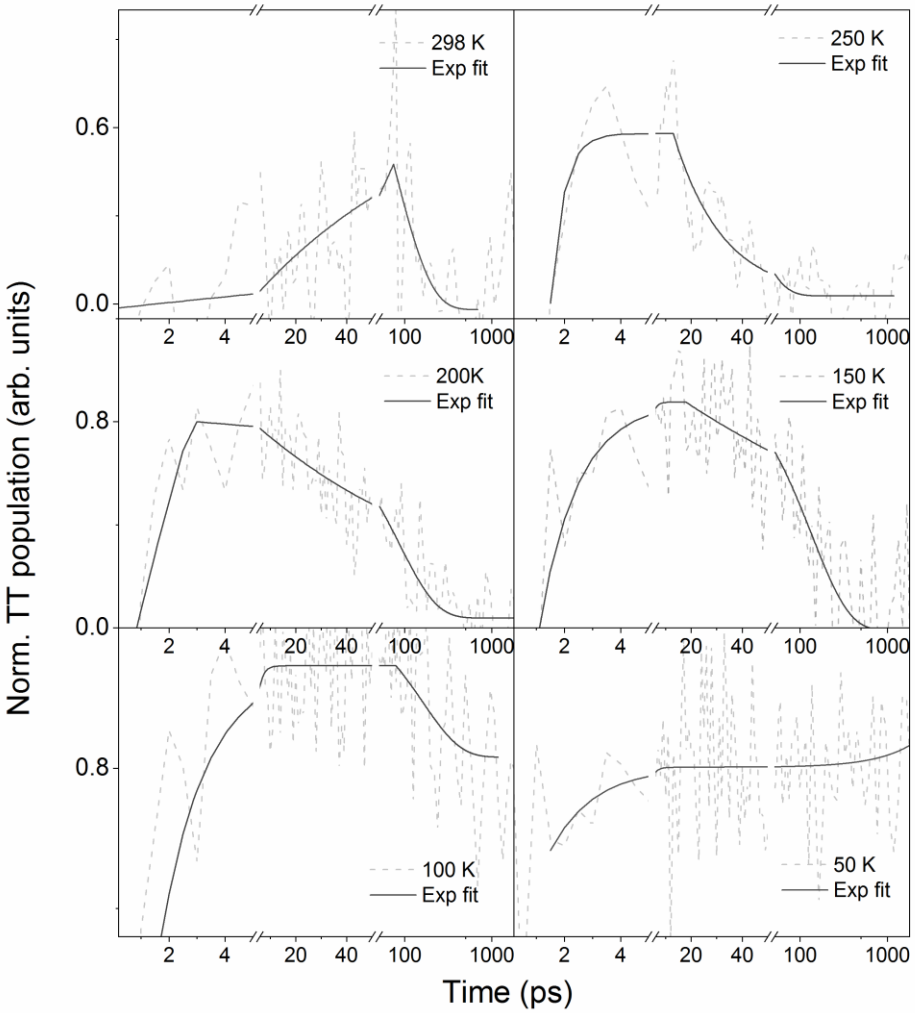

Figure 7.13- Fitting pump- probe kinetics of TT states at 298-50 K with a bi-exponential. TT decay slows down with lowering temperature and lives beyond 2 ns below 100 K. TT rises by 1-2 ps below 100 K as well, indicating a very weak, negligible thermal activation

7.5.2 The Arrhenius Model and Activation Energy

The temperature dependent nature of chemical reactions invoke the concept of equilibrium of various reactant/product states. Often transition state theory is used in conjunction to explain the thermal activation of equilibrium reactions[198]. Within the premises of transition state theory, we design an Arrhenius-type model[199] to describe the temperature-dependence observed in SF, as follows.

$$k(t) = A_0 \, e^{\frac{-E_a}{k_B T}} \qquad 7.2$$

k(t): Rate of the reaction
A_0*:* Attempt frequency at t, or initial rate of the reaction at t=0 before product formation
E_a*:* Activation energy for product formation
T: Temperature in Kelvin
k_B*:* Boltzmann constant

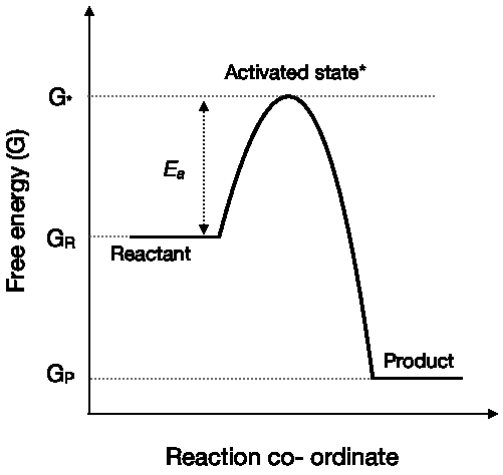

Transition state theory proposes the presence of a hypothetical activated state whose energy is higher than that of the reactant and product states, occurring along the reaction co-ordinate, after the initial reactants but before the products can form. Thus, all conversions from the reactant to the product state must go through this higher energy activated state, which can chemically be a hybrid reactant- product state. The Arrhenius equation given above in 7.2 correlates the temperature dependence of the reaction rate to the activation energy, E_a. The activation energy is the energy required by the reactants to overcome the activated state and form products.

Kinetics of formation of TT and $2T_1$ shown in Figure 7.12 and Figure 7.13 are fit to the Arrhenius-type model given by 7.2. The results of this fitting in linear form following, $ln\ k_{T1} = ln\ A_0 - E_a/k_B T$, are shown in Figure 7.14. The slope of the plot thus gives the activation energy, $E_a = 60$ meV for $2T_1$ formation (red) and $E_a = 2$ meV for TT formation (black, inset). Note that this activation energy for $2T_1$ formation is via a higher energy, activated state and E_a is much lower than the endothermicity of the system at 300 meV. This forms basis for the entropy model we are trying to build for endothermic SF systems in this chapter. Also note that the linear fits have been confined to temperatures above 100 K as triplet formation is impeded at lower temperatures. The break of slopes in this region

for both $2T_1$ and TT formation is similar what has been observed in several triplet forming systems before, and is attributed to hopping within low-energy domains.

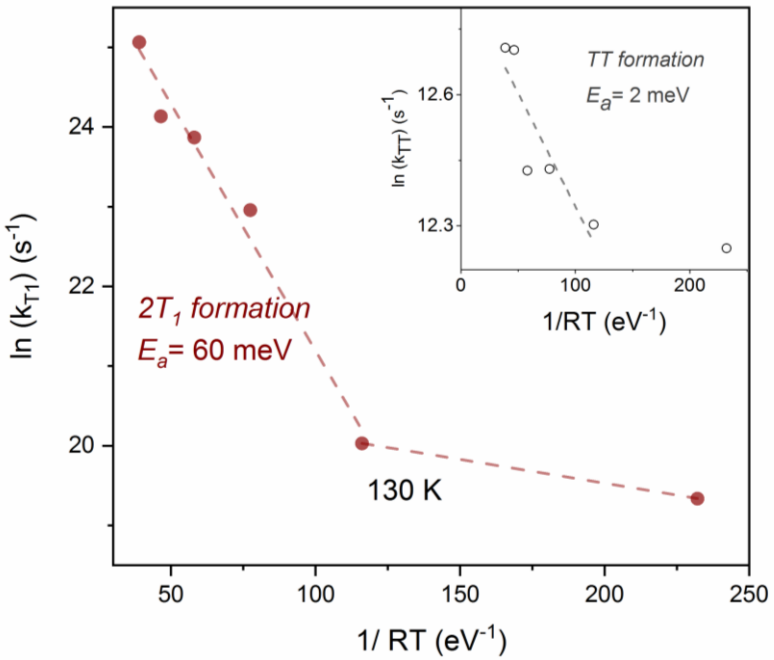

Figure 7.14- Arrhenius plot for $2T_1$ formation in films of TIBS-FTA. A thermal activation energy of 60 meV is predicted for $2T_1$ formation while the inset shows a 2 meV activation for TT formation rendering the latter a negligibly thermally activated process.

From a mechanistic point of view, the ultrafast formation of the TT state from the S_1 state holds a strong position in the process of SF[95]. However, we observe that in TIBS-FTA this process is negligibly thermally activated. SF has been recently defined as, not just the formation of free triplets ($2T_1$) but also the formation of correlated triplet pair states (TT). Nevertheless, from a statistical mechanical perspective what matters for the drive of a reaction depends on the reactant and product states alone, i.e. for SF, S_1 and $2T_1$ states. The free energy difference influenced by the entropic drive of the system from S1 to $2T_1$ is thus the most critical parameter to entertain SF in an endothermic system. Having said that, we do not neglect the entropic drive in the first step of fission, S_1 to TT, or the entropic contribution from the breaking up of the TT state to facilitate the first hop of a free triplet at the end of the reaction.

We note that previous experiments done on other endothermic systems such as tetracene and TIPS-Tc have reported activation energies for triplet formation in the range of 55-70 meV[95,138,139], which are also much lower than the E_{STT} for these systems, >200 meV. With the mechanistic and energy basis that we have sculpted so far in this chapter, we now move on to the entropic model for endothermic SF system of TIBS-FTA.

7.6 Endothermic Singlet Fission and the Entropic Model

We build our two- state model as follows. The initially photo- excited singlet, S_1 (1st state), goes through an activated state, which mediates the breaking up of correlated TT states, and forms free triplets, $2T_1$ (2nd state). We incorporate aspects such as singlet delocalization and triplet diffusion in this model, explained shortly. Before addressing the energetics of the states, we first look at what entropy means in an ensemble of molecules capable of doing SF.

7.6.1 Counting the Number of Microstates

Entropy is defined as the degree of disorder in a system. The physical interpretation of entropy of a system is given by the number of equiprobable states or microscopic configurations accessible by a molecule in the entire ensemble, within the thermal fluctuations that the ensemble experience. These states in the ith configuration are known as the microstates of the system, denoted by Ω_i, whose spatial and temporal evolution are guided within the constraints of physical laws in the system. The entropy of the i^{th} state, S_i, is given by the *Boltzmann equation*[200] as,

$$S_i = k_B \ln \Omega_i \qquad 7.3$$

In an ensemble of endothermic, intermolecular SF molecules in solid-state, there are predominantly three states with a distinct number of microstates each: S_1, TT and $2T_1$ states. The number of microstates for each of these states is restricted by the crystal structure or molecular packing in a system. The initially photo-excited S_1 occupies a certain number of microstates defined by the delocalization of the exciton (typically 1-2 molecules), making the entropy of S_1 microstates negligibly small. S_1 then gives way for the intermediate TT states formed in an ultrafast (<100 fs) and perhaps coherent fashion like in TIPS- Tc reported elsewhere. The electronic coupling between S_1 and TT, $||\gamma||^2$, is influenced by the crystal structure and solid- state ordering of molecules in the thin films and may be attributed to the ultrafast forming TT states, which could be a key factor in guiding the reaction in forward direction. It is therefore important to understand the role entropy plays in going from S_1 to TT for a conclusive understanding of what is to follow: the breaking up of TT to form free triplets. Counting these various microscopic configurations i.e. the number of microstates for various excited states such as TT and $2T_1$ is demonstrated below.

The solid- state packing of TIBS-FTA molecules can be seen in the crystal structure shown in Figure 7.15. The crystal structure is viewed in the *ab* plane as SF has the largest probability of occurring in the *ab* plane based on theoretical and experimental considerations[102,173,201,202]. In the *ab* plane, the molecules arrange themselves in a hexagonal lattice, spaced 8 Å apart, and the number of molecules (N) in each molecular shell (n) is estimated by mathematical induction, also represented in Figure 7.15 (middle and right panels).

Hexagonal lattices are defined by the i^{th} shell containing $6i$ number of molecules.

N in the 1st shell= 1

N in the 2nd shell= 6+1

N in the 3rd shell= 12+6+1

.

.

Thus, N in the n^{th} shell= $3n^2+3n+1$

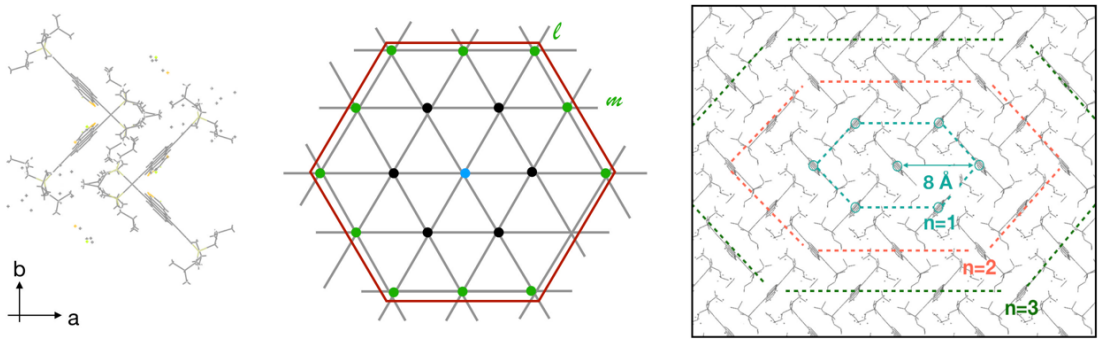

Figure 7.15- Crystal structure and solid- state molecular ordering of TIBS-FTA molecules in the ab plane. The left- most panel shows the unit cell arrangement in the ab plane, the middle panel shows the schematic of hexagonal packing with a molecule on every dot (coloured to distinguish shells) and the rightmost panel shows the schematic overlaid on the actual crystal structure in solid- state with shells highlighted.

The number of TT configurations in the n^{th} shell is given by the number of adjacent molecules within n shells. The number of ways for pairing up one molecule to the nearest neighbor or the number of shared edges is 6 i.e. for every blue dot, there are 6 black ones to connect to. However, this is counted twice (when we translate the blue dot horizontally by one site in either direction, we are recounting 6 edges again). For every red hexagon, there are two different types of apices: 6 *l*'s with 3 edges and the rest, (n-6) *m*'s with 2 edges. Hence the number of edges outside the red hexagon is, 3n + 2(n-6) = 12n + 6, counting both *l* and *m* apices. Now, the total number of edges or pairs is, (6N + 12n + 6)/2 (divided by 2 due to recounting), giving a total number of pairs of $9n^2+15n+6$. This is the number of configurations of pairing up neighboring molecules without repetition which makes it the number of TT microstates, Ω_{TT}.

$$\Omega_{TT} = 9n^2 + 15n + 6$$

7.4

Now, we begin counting the number of microstates for free triplets or $2T_1$ that are formed by the breaking up of TT states. The n^{th} shell contains N_d molecules that the triplets can diffuse into, given by $3n^2 + 3n + 1$. Thus, the number of ways two sites are occupied by 2 triplets is given by N_d number of ways in site 1 and (N_d-1) number of ways in site 2. For every TT state, 2 triplets are formed, and we incorporate that by dividing the number of ways by 2, and we also divide by 2 to incorporate two distinguishable spin configurations.

$$\Omega_{2T_1} = \frac{N_d(N_d\text{-}1)}{2}\,2 = (3n^2 + 3n + 1)(3n^2 + 3n) \qquad 7.5$$

The number of $2T_1$ microstates, Ω_{2T_1}, is defined by the number of molecular sites accessible for triplets to hop and diffuse (defined by *n* for N_d), which vary with temperature. We shall discuss the physical relevance of N_d in the following section. Note that while Ω_{2T_1} depends quadratically on the number of molecules within diffusion/hopping limits, Ω_{TT} depends linearly on the number of accessible sites in the nth shell defined by TT dynamics. This implies that if the TT states are weakly correlated (unlike strongly correlated quintet states) leading to hopping or migration, this will contribute to increasing the effective diffusion lengths of $2T_1$ states, thereby increasing Ω_{2T_1}, contributing to a higher entropic drive.

7.6.2 Defining the Energy Landscape

In this section we congregate the energetic understanding that we have so far developed in TIBS-FTA and tie them together with entropic factors to define the free energy (G) parameters for different states involved in SF. The energies are defined as follows.

(i) Endothermicity of the system, $E_{STT,}$ or the difference in internal energies of the initial and final states is given by E_{S_1} - $2E_{T_1}$.
(E_{S_1} = 2.3 eV and $E_{2T1} \sim$ 1.3 eV, E_{STT} = 300 meV)

(ii) The activation energy, E_a, to form $2T_1$ states, experimentally measured at 60meV.

(iii) Gibb's free energy of states define the thermodynamic feasibility of a reaction. Free energy of S_1 is denoted by G_{S1} and that of $2T_1$ is G_{2T_1}.
$G_{S_1} = E_{S_1} - TS_{S_1} = E_{S_1}$, as $S_{S_1} \sim 0$
$G_{2T_1} = E_{2T_1} - TS_{2T_1}$

The overall change in free energy in SF is given by,

$$\Delta G_{2T_1} = G_{2T_1} - G_{S_1} = 2E_{T_1} - TS_{2T_1} - E_{S_1}$$

Thus, the change in Gibb's free energy for the whole process of SF is dependent on the extent of endothermicity (E_{STT}) as well as the entropy due to $2T_1$ microstates, given by,

$$\Delta G_{2T_1} = -E_{STT} - TS_{2T_1} \qquad 7.6$$

7.6.3 Limiting Parameters for Endothermic Singlet Fission

For SF to proceed spontaneously at any temperature T, ΔG must become negative, leading to $-E_{STT} - TS_{2T_1} < 0$. In the limiting case at equilibrium ($\Delta G = 0$), $-TS_{2T_1}$ becomes close in energy to E_{STT}. As the system pushes away from the equilibrium, the higher TS_{2T_1} gets, the more negative ΔG becomes, leading to $2T_1$ formation. Thus, if Ω_{2T1} is high enough to make ΔG negative, SF proceeds in the forward direction resulting in the formation of free triplets. We define this quantity, the energetic drive due to entropy, TS_{2T_1} as $\mathcal{F}E_a$. This has been done simply because any energy may be re-written as a factor multiplied by another energy, mathematically. In the limiting case when $-E_{STT} - TS_{2T_1} < 0$, the value of $\mathcal{F}$ will be given by,

$$\mathcal{F} > -\frac{E_{STT}}{E_a} = 5$$

Thus, the limiting value for $\mathcal{F}$ is ~5. The use of $\mathcal{F}$ is only to help us draw a comparison between the free energy change and activation for triplet formation, discussed more in section 7.6.5. Now, we find the minimum value of S_{2T_1} to drive SF combining 7.5 and 7.6.

At T= 298 K to enforce the condition $-E_{STT} - TS_{2T_1} < 0$,

$$S_{2T_1} < \frac{0.3}{298} < 0.001006\text{eV K}^{-1}$$

Now, $S_{2T_1} = k_B \ln [(3n^2 + 3n + 1)(3n^2 + 3n)]$, which satisfies the above condition for the minimum values of S_{2T_1} only when $n > 11$. This means that $2T_1$ states need to diffuse to a minimum of 11 shells, a distance of ~ 8nm (given by the crystal structure) so that SF proceeds. This being a physically reasonable distance for triplet hopping, SF proceeds with high efficiency (165% triplet yield) at 298K, as seen in chapter 6. We extend this analysis to explain physical consequences as a function of temperature, in section 7.6.5.

7.6.4 Kinetic Modelling and Entropy

We now discuss the role of entropy in the kinetics of $2T_1$ formation. For this, we define the kinetic model via an activated state by transition- state theory discussed in section 7.5.2. The rate of formation of the product species p, k_p, is dependent on a few key parameters: the difference in free energies of the p^{th} and $(p\text{-}1)^{th}$ species, $\Delta G_{p\text{-}(p\text{-}1)}$, temperature of the system and the extent of the reaction determined by the position of the activated state (p^*) between $(p\text{-}1)^{th}$ and p^{th} states. If the formation of the p^{th} state is thermally activated, an additional term that involves this activation energy (E_a) may also be included in determining the rate k_p. Empirically, this may be represented by,

$$\text{rate of formation of } p^{th} \text{ state, } k_p = A_0\, e^{(-\theta\beta\Delta G_{p\text{-}(p\text{-}1)})}$$

where θ sets the extent of the reaction (we assume this to be 0.5 for simplicity), $\beta=1/k_BT$ and A_0 is the pre- exponential factor that changes with temperature. In the case of thermally activated formation of the p^{th} state, A_0 becomes $e^{(-\beta Ea)}$. $\Delta G_{p\text{-}(p\text{-}1)}$ is given by, $\Delta E_{p\text{-}(p\text{-}1)}$- $T\Delta S_{p\text{-}(p\text{-}1)}$ where E denotes internal energy and S denotes entropy of the respective states. In SF where S_1 decays to an activated intermediate TT state that break- up to form $2T_1$ states, S_1 is the $(p\text{-}1)^{th}$ state, TT is the p^{*th} state and $2T_1$ is the p^{th} state, shown in Figure 7.17.

Thus, the rate of formation of $2T_1$ is written as,

$$k_{2T_1} = e^{(-\beta E_a)} e^{(-\theta\beta\Delta G_{2T_1\text{-}S_1})} \qquad 7.8$$

where $\Delta G_{2T_1\text{-}S_1} = -E_{STT} - T\Delta S_{2T_1\text{-}S_1}$

$= -E_{STT} - TS_{2T_1}$, as $S_{S1} \sim 0$.

In the limiting case discussed in page 184 of entropy driving SF forward with a negative ΔG_{2T_1} , we defined $-E_{STT}$ as $\mathcal{F}E_a$. Thus 7.8 becomes,

$$k_{2T_1} = e^{(-\beta E_a)} e^{(-\theta\beta(\mathcal{F}E_a - TS_{2T_1}))} \qquad 7.9$$

The empirical rate equation is used to fit the experimental timeconstants obtained from pump-probe experiments shown in Figure 7.14 and Table 7.1 for $2T_1$ state. The constants used while fitting are T, E_a, θ and an estimated minimum value of S_{2T_1}. The unknown here, while fitting the experimental rates to the empirical equation, is the entropic driving energy given by $\mathcal{F}E_a$ or simply, the factor $\mathcal{F}$. We have already estimated the value of $\mathcal{F} \sim 5$ from the limiting case in terms of ΔG in the previous section. Now we tend to the kinetic model based on our empirical assumptions to optimise for $\mathcal{F}$, for comparison. The fitted rate constants for different values of the unknown, $\mathcal{F}$, are shown in an Arrhenius plot below, in Figure 7.16. The solid lines show k_{2T1} as a function of temperature for different values of $\mathcal{F}$. The experimental rates of formation of $2T_1$ states (orange discs) align

with the solid line at $\mathcal{F} = 4.85$, very close to the non- kinetic estimate of $\mathcal{F} \sim 5$ obtained from energetics. When $\mathcal{F}$ is higher, the thermal activation of empirically predicted rates is steeper, indicating an activation barrier greater than that of E_a= 60 meV of TIBS-FTA. When $\mathcal{F}$ is smaller (=2), the rate of $2T_1$ formation will decrease as temperature increases, which is contrary to what is expected of a thermally activated process. The right balance of $\mathcal{F}$ is thus crucially set by the endothermicity of a system as well as its E_a to form free triplets. Also note that from fitting kinetics in the above fashion, the optimal $\mathcal{F}$ value sets the minimum energy of entropic drive (TS_{2T_1}, set as $\mathcal{F}E_a$) at ~290 meV which is used to overcome the internal energy barrier or endothermicity of 300 meV in TIBS-FTA, for SF to occur.

The so far seemingly arbitrary value of $\mathcal{F}$ gives us a measure of the entropic contribution for SF with respect to its activation energy. This is significant from a historical perspective of entropic contribution in many fundamental physical phenomena discussed later.

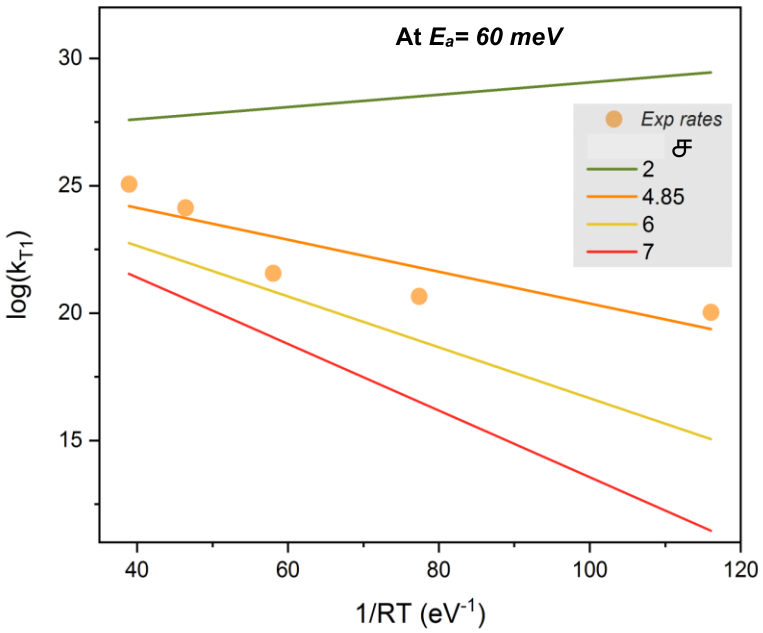

Figure 7.16- Fitting of experimental rate of triplet formation by empirical rate equation. Rates are predicted for various values of ℱ their trend with respect to temperature in the x- axis is compared to that of experimental rates. Rates for ℱ= 4.85 complement the experimental rates the closest.

7.6.5 Activated State, Entropy (ℱ) and Triplet Diffusion

An estimate of the entropic drive the system experiences when going from S_1 to $2T_1$ via an activated state can be made by means of: (i) free energy parameters limited by the endothermicity of the system and (ii) kinetic modelling that depends on the activation barrier as well as the free energy change. The nature of this activated state is rather important to understand as it is the rate limiting step in SF with high energetic expense as seen from the free energy diagram in Figure 7.17.

Recent reports of endothermic SF systems suggest ultrafast formation of TT states are a result of vibronic coupling with S_1 and the likelihood of a conical intersection influencing vibrational dynamics at these timescales[95,203,204]. Decoupling of the TT states to form free triplets or $2T_1$ states involves overcoming the binding energy of the TT state. Spin-exchange interactions (J) on the order

~4 meV were reported for quintet states at low temperatures (10 K) from ESR studies on TIPS-Tc films recently[112,205], which suggests that tightly bound TT states or quintets lie very close to S_1 in energy. However, from the pump-probe data discussed in this work it is not possible to distinguish between strongly and weakly coupled TT states. What we observe instead is an activation barrier of 60 meV for $2T_1$ formation, from the break-up of TT states. Recent experimental studies identify spectrally distinct TT states with various strength of coupling[206]. They postulated that the TT wavefunction delocalised over two molecules are initially strongly coupled, and gradually move further apart spatially, calling them the (T..T) state before complete decoupling to form T_1+T_1 (herein referred to as $2T_1$). Physically speaking, this first step of energetic migration of TT to (T..T) would be the most energy consuming process as it involves overcoming the TT binding energy before forming T_1+T_1. The (T..T) state may be perceived as the result of the very first hop the localised T_1 wavefunction would take at this stage and could be the *silent* activated state that we associate E_a to.

Interestingly, there is still a lack of understanding on the relative contribution from binding energy of TT state and activation energy for the formation of $2T_1$ in endothermic SF. Some reports have loosely estimated this dependence to be, the binding energy equaling twice the activation energy[20,95], however this has not been experimentally verified. The estimation stems from the theoretical observation made by *Durrant et al.*[196], in calculating the role of entropy of electron-hole separation in donor-acceptor (D-A) systems such as polymer- PCBM interfaces. The major finding from that study was that the coulombic energy of the electron-hole pair equals the entropic contribution due to free charges upon separation at the D-A interface, and the combination of both contributes to the negative change in free energy of the process. However, in the absence of sufficient experimental support one may not extrapolate it to SF, resulting in an underestimated entropic drive. In the case of TIBS-FTA however, we have distinctly calculated entropy changes in processes involved in SF, with a (T..T) state forming with an activation of 60 meV while the entropic drive is $\mathcal{F}$~5 times higher than the activation energy. Thus, $\mathcal{F}$ is introduced in this work as the

relative importance of entropic drive with respect to the process of activation in endothermic SF systems.

7.6.6 Triplet Diffusion and Endothermicity

From pump-probe dynamics discussed in section 7.5 we see that SF becomes less favourable below 130 K, where free triplets are formed at much longer timescales of tens of nanoseconds as opposed to 100-500 ps at higher temperatures. The activation for triplet formation in TIBS-FTA is consistent with other reports[95,138,139] on temperature-dependent triplet formation in endothermic SF systems. The > 100 K activation also explains the ns- μs long triplet signal we observed from the ESR data recorded at 70 K from a small population, as we expect the triplet yield to be very low. In our model we fit energetic and kinetic parameters to find not only the energetic drive given by $\mathcal{F}$, but also the minimum value for Ω_{2T_1} at temperatures between 298-10 K. For instance, we note that the triplets must diffuse to at least 11 shells before pushing SF to occur spontaneously. We extend this analysis to other temperatures in this section. The minimum n-values that correspond to the minimum number of microstates for $2T_1$ states required for SF to proceed are shown in Figure 7.19 as a function of temperature. The major findings are listed below.

(i) As temperature decreases, the minimum required S_{2T_1} for SF to proceed becomes larger, i.e. the minimum number of microstates for triplets, or the minimum number of shells that triplets shall diffuse into (n_{TI}), will increase.

(ii) The entropic drive is thus limited by accessible triplet diffusion lengths observed, before recombination. With lowering the temperature, triplets in the system therefore must diffuse to distances longer than before. While the required diffusion length is 8 nm at 298 K, it jumps to 100 nm at 200 K, and becomes 3-4 μm at 100 K. While diffusion distances under 100 nm is physically acceptable, longer distances increases the chances of triplet recombination, impeding SF.

(iii) Hence, below a certain critical temperature SF will become unfavourable from the above discussed entropic and kinetic considerations. From pump-probe experiments we see that triplet formation ceases below 150 K (~130 K from Arrhenius plot), and between 100-150 K from our entropic calculations.

(iv) Triplet yield is thus expected to decrease with temperature as well.

Our model predicts the minimum triplet diffusion length that favour SF and it is a distance of 8 nm at 298 K in TIBS-FTA, while this has been estimated as 2 nm for tetracene at 298 K. The difference in minimum diffusible lengths for triplets in TIBS-FTA and Tc stems from the endothermicity of the respective SF systems, as the minimum entropic drive is related to E_{STT} by 7.6. While E_{STT} of TIBS-FTA is -300 meV, which of tetracene is much lower at -180 meV. Thus, the tetracene triplets may diffuse much smaller distances when compared to TIBS-FTA and still facilitate fission.

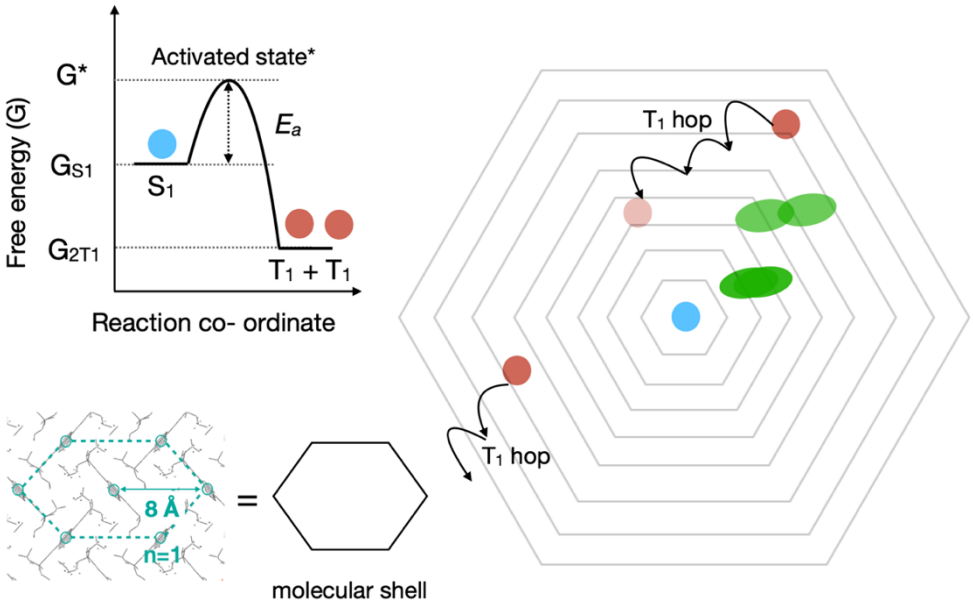

Figure 7.17- Energy diagram and $2T_1$ hopping in TIBS-FTA at 298 K. The S_1 delocalised over 1-2 molecules, TT states forming on neighbouring molecules and free triplets formed at n>11 are shown in the schematic representation of the solid-state structure. The energy diagram associated with SF involving an activated state (T..T) is shown as a function of reaction co- ordinate. The size of the circles is representative of the respective states' delocalization.

We now try to extend our model to two hypothetical SF systems with endothermicity above and below that of TIBS-FTA, but with the same activation barrier for free triplet formation of 60 meV. The systems have endothermicities of 200 meV (A, similar to TIPS- Tc[113]), 300 meV (B, TIBS-FTA) and 500 meV (C, close to anthracene[47]). The other important assumption that we make is that the conservation of hexagonal lattice packing in the *ab* plane among all these systems. Now, the packing density or the distance between the nearest neighbours might be different as long as the packing arrangement is fixed. From 7.6, we can calculate the limiting case of what minimum values of S_{2T_1} the system has a negative ΔG. Further, extending the results to 7.4 and 7.5, we can calculate the minimum value of n_{T1} that satisfies the thermodynamic feasibility of SF as a function of temperature.

The results of n_{TI} values as a function of temperature and endothermicity are shown in Figure 7.18. As endothermicity increases, the number of shells free triplets access at a certain temperature (n_{TI}) increases. The increase in n_{TI} occurs as the change in entropy should be high enough to compensate for the increased endothermicity of the system. For instance, at 300 K while the minimum number of shells, n_{TI}, corresponds to 3 for A (200 meV) and 11 for B (300 meV), for C (500 meV) this will be ~100 shells. Depending on the crystal packing of the molecules for the system, these distances could be large, especially for 100 shells in the case of C (if the spacing between neighbouring atoms is 8-10 Å, then 100 shells equals a distance of 80-100 nm). Hence, while SF occurs without much fuss for the cases of A (TIPS-Tc like) and B (TIBS-FTA like) systems, system C may not undergo thermodynamically and energetically feasible SF. The reason being that for C, it will be difficult to generate a large enough change in entropy going from TT to $2T_1$, as fewer triplets will have the chance to diffuse the required long distances of 80-100 nm, before recombining. We validate this by the poor SF observed in anthracene crystals, which lie close to >500 meV.

Figure 7.19 shows the change in entropy and free energy for triplet hopping from the 11th shell for TIBS-FTA at 298 K. While the entropy of $2T_1$ states increases with the number of shells they can move across, we can find that for every subsequent triplet hop to the next shell, the change in entropy decreases as shown in the figure. The change in entropy (and free energy) plateaus beyond a certain number of hops which leads to thermodynamic equilibrium, translating to sites across molecular shells becoming equally probable for triplet diffusion. Overall, we have developed a reasonable understanding about how accessible triplet diffusion lengths are correlated to the entropic drive of a system. The required entropic drive of the system is dependent on how endothermic it is, however if too endothermic, the required diffusion distances may not be accessible for triplets before recombination. This brings us to two major factors from a design perspective for efficient endothermic SF systems: endothermicity and triplet diffusion lengths. For efficient SF we conclude that one needs to hit the balance

between endothermicity and triplet diffusion lengths that satisfy thermodynamic and kinetic conditions.

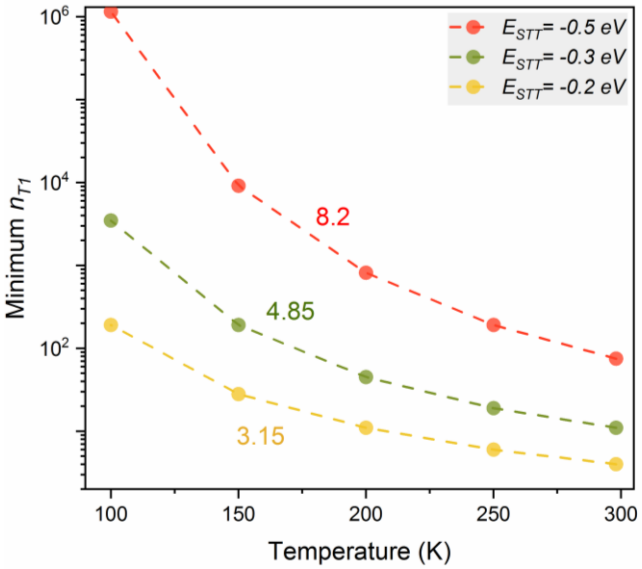

Figure 7.18- Influence of endothermicity on minimum number of shells accessible for triplets. From free energy considerations, the minimum number of shells triplets may diffuse to (n_{T1}) in largely influenced by endothermicity of a system. As endothermicity increases, minimum n_{T1} increases, which means that now the triplets have to access larger distances for SF to be thermodynamically feasible.

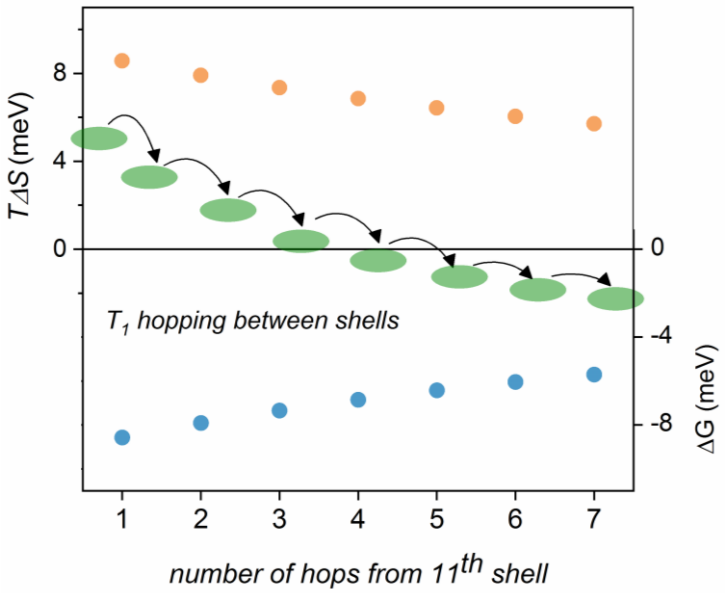

Figure 7.19- Triplet hopping from the 11th shell and change in entropy and free energy associated with every subsequent hop at 298 K. Triplet hopping from the 11th shell, one shell at a time, results in gradual plateauing of change in entropy and free energy as molecular sites becomes degenerate.

7.7 Conclusions and Outlook

In this final and rather crucial chapter, we shed new light on the vital part that endothermicity plays in designing an efficient SF system. We chose an efficient SF molecule, TIBS-FTA, as a model system and tried to connect changes in thermodynamic quantities such as internal energy (or enthalpy), entropy and Gibb's free energy for microscopic configurations of various excited state species. TIBS-FTA shows a triplet yield of ~165% and a triplet energy of 1.3 eV, making it endothermic by 300 meV. In films of TIBS-FTA triplets form within 50 ps at 298 K and as temperature decreases, triplets forms at longer timescales. We explored the temperature dependent nature of TT formation and free triplet formation in films of TIBS-FTA and found that while TT formation is not thermally activated, the breaking up of TT to form free triplets has an activation barrier of 60 meV. The large difference between endothermicity and the activation

barrier in the system probed us to question what was driving efficient SF in TIBS-FTA, despite the large triplet energy. In the past, several studies loosely estimate the driving energy due to entropy to be twice the activation energy, however, this has not been experimentally verified. We intended to find a tangible solution to this.

To answer what drives endothermic SF from a thermodynamics perspective, we explicitly calculate the change in entropy during different steps of SF, by getting down to the fundamentals of how different types of excitons (S_1, TT and $2T_1$) are formed and how they are delocalised or migrate spatially as a function of temperature. We put together several pieces of spectroscopic and structural data and build the microscopic picture for SF in TIBS-FTA. This led us to calculate the minimum number of microstates for free triplets ($2T_1$), which is correlated to the minimum distance $2T_1$ states should be able to access before recombination. A two- state model is developed in this study involving S_1 and $2T_1$ states, to rationalize the highly efficient endothermic SF in TIBS-FTA from a structural and free energy perspective. We find that structural factors that define S_1-TT coupling and triplet diffusion lengths, as well as electronic factors that define the endothermicity are crucial to the thermodynamic feasibility of SF in a system.

In this study we find that it is imperative to balance endothermicity of a system and designing molecular structures with appropriate solid- state geometries with accessible triple diffusion lengths. As we study a highly endothermic SF system, TIBS-FTA (300 meV), compared to tetracene and its derivatives (180-200 meV) in this chapter the entropic drive we estimate in TIBS-FTA is much higher than that in tetracene reported elsewhere. The details of this inquiry led to establishing the pivotal role of entropy in the efficacy of an endothermic SF system through this study. Further, we find that molecular packing and triplet diffusion distances impact the extent of entropic drive for SF. While triplet formation is efficient at temperatures above 200 K, what allows for efficient SF at temperatures lower than that are denser packing of molecules in geometries that favour SF with fast triplet- triplet hopping that allows more accessible microstates for $2T_1$ states. Thus, it is decisive to combine electronic structure, molecular design,

intermolecular coupling and long triplet lifetimes to engineer materials with highly efficient endothermic SF for photovoltaic applications.

Chapter 8

Conclusions and Future Work

This whole world is a story. I've read every page except the last one. I need to find out how it ends. I want to know what this all means.

-The Man in Black, Westworld

This dissertation began with an emphasis on building a story- a story on endothermic singlet fission. Over several chapters with varied experimental strategies and material designs, we hope to have built on to our understanding of endothermic SF. While we delved into a fundamental understanding of the phenomenon of SF in this dissertation, we have tried to impart some elements of clarity towards tuning molecular design for SF to suit PV device applications. We briefly summarize the important conclusions from individual chapters here

We introduced well established instrumentation in Chapter 3, that majorly rely on two modes of processes: spin-based and non-spin-based, when used complementarily, helped bring forth an all-encompassing understanding of excited-state processes this dissertation deals with. These techniques give rise to datasets that have populations with overlapping spectral and kinetic components. Numerical methods based on Singular Value Decomposition (SVD) and Decay Associated Spectra (DAS) were introduced to deconvolute and identify major spectral and kinetic components in such datasets.

The first experimental chapter on exploring endothermic SF dynamics as a function of morphology, Chapter 4, dealt with nanoparticles of a well-characterized SF material, TIPS-Tetracene. The preparation of NPs, their spectral and structural characterization are described in this chapter. The NPs

have a crystalline core and an amorphous exterior, characterised by electron microscopy and diffraction techniques. SF in TIPS-Tc NPs occur with initially photo-excited S_1 states and coherently forming TT states under 200 fs. When the NPs are excited at the *band-edge*, TT states break apart to form free triplets in the nanosecond timescales. However, we observed an interesting phenomenon when the NPs are excited above this energy. We observed that higher excitation energies favour the formation of spectrally and kinetically distinct TT states that can become emissive through a Herzberg-Teller type mechanism in nanoseconds. We also observed that yield of TT and T_1 formation varied with excitation energy. The implication of this result is interpreted as the TT state wavepacket initially relaxing away from the Frank-Condon point that controls the choice of SF pathway, with distinct intermediates within the TT manifold formed in this process. We term this phenomenon as *photo-engineering* of TT formation pathways in SF, in this chapter. Based on spectral comparisons with a published report on SF dynamics on TIPS-Tc films, our results also hint at morphology-driven TT migration in TIPS-Tc NPs. Upon photo-excitation, S_1 states form in the crystalline core of the NP where TT forms coherently as well. Formation of free triplets are likely to occur at the amorphous exterior of the NP, after a detailed spectral and kinetic comparison to the published film data. Therefore, this is an indication of TT states migrating from the crystalline-core to the amorphous-exterior of the NPs, where then breaking apart to form free triplets. These results on photo-engineering the fate of excited states in SF and morphology-driven migration of excited states carry crucial implications when employing similar materials for PV applications.

Chapter 5 explores the morphology dependence of SF on TIPS-TC NPs, taking a step further from the previous chapter. Here, we stabilize and assemble thermodynamically stable nano-configurations of NPs using SDS micelles. Micelle-mediated assembly of NPs resulted in highly crystalline NPs of TIPS-Tc that exhibit the most efficient and rapid SF amongst all reported morphologies of TIPS-Tc thus far. Photo-excited S_1 states are initially formed, followed by rapid TT formation under 200 fs which break apart three times quicker than bare

NPs or films of TIPS-Tc discussed in Chapter 4. We concluded that the micellar-driven crystallisation of NPs helped in the formation of a *decisive SF geometry* or local ordering of molecules that allows excited states to access vibrational modes allowing for rapid T_1 formation via SF. Therefore, we experimentally established the crucial nature of accessing vibrational modes that results in efficient SF, as a result of molecules achieving their decisive SF geometry in solid-state.

In Chapter 6, we introduce a new class of materials, thienoanthracenes, with higher HOMO-LUMO gap, T_1 energies and photo-stability compared to other well-characterized acenes for endothermic SF. The four thienoanthracenes introduced in this chapter vary not so widely in terms of molecular structure, but with very distinguishable crystal structures. Excited-state processes were characterized using pump-probe, fluorescence and ESR spectroscopic techniques to look for SF. Molecular packing densities and endothermicities varied greatly amongst these molecules, which reflected in their SF dynamics as well. We observed efficient SF with high molecular packing density and low endothermicity, while drawing correlations between SF dynamics, molecular packing and endothermicity. In this chapter, we establish the limit of endothermicity in thienoanthracenes that allows for SF, and observed that SF rates decreased with lower packing densities as well. Therefore, we have built a new set of four photo-stable molecules, with comprehensive spectral and energetic information and criteria for efficient SF. This could serve as a basis of future SF studies, especially for PV applications.

In the final chapter, we attempted to answer the long standing question of what drives SF in endothermic systems despite the enthalpic uphill nature of it. Chapter 7 used a thienoanthracene characterised in the previous chapter, TIBS-FTA, as the model system for studying the thermodynamic feasibility of endothermic SF. Following the second law of thermodynamics, the enthalpic deficit in endothermic systems must be overcome by entropic change, for spontaneous SF. Thus, we developed a model based on entropic considerations by counting the number of accessible microstates for S_1 and T_1 excited states,

from crystal structure parameters. By extending thermodynamic and kinetic conditions with experimentally determined temperature-dependent triplet formation in TIBS-FTA, we arrived at key conclusions to what factors dictate endothermic SF. We extend our results based on this model to predict that the change in entropy due to SF is heavily influenced by the number of molecular shells that are accessible to triplets by diffusion. At high temperatures and low endothermicity, triplets can access the minimum number of shells that satisfy the thermodynamic limit of SF. However, at lower temperatures, increased intermolecular distances in solid-state and higher endothermicity, the minimum shells that triplets are expected to diffuse to becomes non-physical (>1 μm). Therefore, we established links between endothermicity, crystal structure parameters and triplet diffusion lengths accessible in the solid-state as key factors that influence SF.

The theme that emerges from this dissertation, as the title suggests, is how morphological and energetic factors influence endothermic singlet fission in acene molecules. While the initial chapters shape our understanding on how morphology influences SF in an endothermic model system of TIPS-Tc NPs, the latter chapters discuss the importance of solid-state molecular packing as well as energetic parameters. We tie the major concepts gathered from these chapters and formulate a statistical mechanics perspective of SF to expand on the relevance of thermodynamic feasibility of SF and physical factors driving it. The effects of morphology and energetic drive in endothermic SF developed in this thesis is thus hoped to be extremely relevant for designing materials for potential practical PV devices. Extending these results to device applications can thus be extremely important to showcase their significance. Further theoretical and experimental formulations to investigate processes such as photo-engineering of excited states and morphology driven migrations of excited states will be helpful to add value to our results. Experimental measurements of triplet diffusion lengths as a function of temperature and comparison with predictions by our entropic model is another important direction to be taken as well.

References

(1) Swenberg, C. E.; Geacintov, N. E. *Exciton Interactions in Organic Solids*; 1973; Vol. 18.

(2) Barford, W. *Electronic and Optical Properties of Conjugated Polymers*; 2005.

(3) Köhler, A.; Bässler, H. *Electronic processes in organic semiconductors: An introduction*; 2015.

(4) Frenkel, J. *Phys. Rev.* **1931**, *37* (1), 17.

(5) Wannier, G. H. *Phys. Rev.* **1937**, *52* (3), 191.

(6) Riede, M.; Mueller, T.; Tress, W.; Schueppel, R.; Leo, K. *Nanotechnology* **2008**, *19* (42), 424001.

(7) Köhler, A.; Bässler, H. *Mater. Sci. Eng. R Reports* **2009**, *66* (4–6), 71.

(8) Köhler, A.; Dos Santos, D. A.; Beljonne, D.; Shuai, Z.; Brédas, J. L.; Holmes, A. B.; Kraus, A.; Müllen, K.; Friend, R. H. *Nature* **1998**, *392* (6679), 903.

(9) Gregg, B. A.; Hanna, M. C. *J. Appl. Phys.* **2003**, *93* (6), 3605.

(10) Smith, M. B.; Michl, J. *Chem. Rev.* **2010**, *110* (11), 6891.

(11) Köhler, A.; Beljonne, D. *Adv. Funct. Mater.* **2004**, *14* (1), 11.

(12) Zheng, Y.; Batsanov, A. S.; Jankus, V.; Dias, F. B.; Bryce, M. R.; Monkman, A. P. *J. Org. Chem.* **2011**, *76* (20), 8300.

(13) Merrifield, R. E. *Pure Appl. Chem.* **2008**, *27*, 481.

(14) Merrifield, R. E. *Acc. Chem. Res.* **1968**, *1*, 130.

(15) Johnson, R. C.; Merrifield, R. E. *Phys. Rev. B* **1970**, *1*, 896.

(16) Dirac, P. A. M. *Proc. R. Soc. A Math. Phys. Eng. Sci.* **1927**, *114* (767), 243.

(17) Temple, G.; Dirac, P. A. M. *Math. Gaz.* **1930**.

(18) Brédas, J. L.; Beljonne, D.; Coropceanu, V.; Cornil, J. *Chem. Rev.* **2004**,

104 (11), 4971.

(19) Clark, J. Intermolecular Interactions in πConjugated Molecules : Optical Probes of Chain Conformation, 2007.

(20) William, M.; Wilson, B. Ultrafast Triplet Generation in Organic Semiconductors, 2012.

(21) Pabst, M.; Köhn, A. *J. Chem. Phys.* **2008**, *129* (21), 214101.

(22) Zimmerman, P. M.; Bell, F.; Casanova, D.; Head-Gordon, M. *J. Am. Chem. Soc.* **2011**, *133* (49), 19944.

(23) Willock, D. J. *Molecular Symmetry*; 2009.

(24) Nijegorodov, N.; Ramachandran, V.; Winkoun, D. P. *Spectrochim. Acta - Part A Mol. Biomol. Spectrosc.* **1997**, *53* (11), 1813.

(25) Spano, F. C. *Annu. Rev. Phys. Chem.* **2006**, *57*, 217.

(26) Lakowicz, J. R. *Principles of fluorescence spectroscopy*; 2006.

(27) Lim, S. H.; Bjorklund, T. G.; Spano, F. C.; Bardeen, C. J. *Phys. Rev. Lett.* **2004**, *92*, 107402.

(28) Burdett, J. J.; Gosztola, D.; Bardeen, C. J. *J. Chem. Phys.* **2011**, *135* (21), 54505.

(29) Spano, F. C. *Acc. Chem. Res.* **2010**, *43* (3), 429.

(30) Beljonne, D.; Shuai, Z.; Pourtois, G.; Bredas, J. L. *J. Phys. Chem. A* **2001**, *105* (15), 3899.

(31) King, S. M.; Matheson, R.; Dias, F. B.; Monkman, A. P. *J. Phys. Chem. B* **2008**, *112* (27), 8010.

(32) Fonseca, S. M.; Pina, J.; Arnaut, L. G.; De Melo, J. S.; Burrows, H. D.; Chattopadhyay, N.; Alcácer, L.; Charas, A.; Morgado, J.; Monkman, A. P.; Asawapirom, U.; Scherf, U.; Edge, R.; Navaratnam, S. *J. Phys. Chem. B* **2006**, *110* (16), 8278.

(33) Byrne, H. J.; Maser, W. K.; Kaiser, M.; Akselrod, L.; Anders, J.; Rühle, W. W.; Zhou, X. Q.; Thomsen, C.; Werner, A. T.; Mittelbach, A.; Roth, S. *J.*

Mater. Process. Tech. **1995**, *54* (1–4), 149.

(34) Arbogast, J. W.; Darmanyan, A. P.; Foote, C. S.; Diederich, F. N.; Whetten, R. L.; Rubin, Y.; Alvarez, M. M.; Anz, S. J. *J. Phys. Chem.* **1991**, *95* (1), 11.

(35) Schueppel, R.; Uhrich, C.; Pfeiffer, M.; Leo, K.; Brier, E.; Reinold, E.; Baeuerle, P. *ChemPhysChem* **2007**, *8* (10), 1497.

(36) Bixon, M.; Jortner, J. *J. Chem. Phys.* **1968**, *48* (2), 715.

(37) Gadermaier, C.; Cerullo, G.; Manzoni, C.; Scherf, U.; List, E. J. W.; Lanzani, G. *Chem. Phys. Lett.* **2004**, *384* (4–6), 251.

(38) Robinson, G. W.; Frosch, R. P. *J. Chem. Phys.* **1963**, *38* (5), 1187.

(39) Janssen, R. A. J.; Smilowitz, L.; Sariciftci, N. S.; Moses, D. *J. Chem. Phys.* **1994**, *101* (3), 1787.

(40) Pope, M.; Swenberg, C. E. *Electronic Processes in Organic Crystals and Polymers*; 1999.

(41) Förster, T. *Ann. Phys.* **1948**, *437* (1–2), 55.

(42) Dexter, D. L. *J. Chem. Phys.* **1953**, *21* (5), 836.

(43) Scholes, G. D. *Annu. Rev. Phys. Chem.* **2003**, *54*, 57.

(44) Förster, T. *Ann. Phys.* **1948**, *437* (1), 55.

(45) Laquai, F.; Park, Y.-S. S.; Kim, J.-J. J.; Basché, T. *Macromol. Rapid Commun.* **2009**, *30 VN-r* (14), 1203.

(46) Dexter, D. L. *J. Lumin.* **1979**, *18–19*, 779.

(47) Singh, S.; Jones, W. J.; Siebrand, W.; Stoicheff, B. P.; Schneider, W. G. *J. Chem. Phys.* **1965**, *42* (1), 330.

(48) Klein, G.; Voltz, R.; Schott, M. *Chem. Phys. Lett.* **1973**, *19* (3), 391.

(49) Klein, G.; Voltz, R.; Schott, M. *Chem. Phys. Lett.* **1972**, *16* (2), 340.

(50) Bhattacharyya, K.; Datta, A. *J. Phys. Chem. C* **2017**, *121* (3), 1412.

(51) Von Burg, K.; Zschokke-Gränacher, I. *J. Chem. Phys.* **1979**, *70*, 3807.

(52) Swenberg, C. E.; van Metter, R.; Ratner, M. *Chem. Phys. Lett.* **1972**, *16* (3), 482.

(53) Swenberg, C. E.; Stacy, W. T. *Chem. Phys. Lett.* **1968**, *2*, 327.

(54) Tayebjee, M. J. Y.; Clady, R. G. C. R.; Schmidt, T. W. *Phys. Chem. Chem. Phys.* **2013**, *15* (35), 14797.

(55) Wilson, M. W. B.; Rao, A.; Johnson, K.; Ge, S.; Pietro, R.; Clark, J.; Friend, R. H. *J. Am. Chem. Soc.* **2013**, *135*, 16680.

(56) Groff, R. P.; Avakian, P.; Merrifield, R. E. *Phys. Rev. B* **1970**, *2* (1), 815.

(57) Arias, D. H.; Ryerson, J. L.; Cook, J. D.; Damrauer, N. H.; Johnson, J. C. *Chem. Sci.* **2016**, *7*, 1185.

(58) Burdett, J. J.; Bardeen, C. J. *Acc. Chem. Res.* **2013**, *46*, 1312.

(59) Kim, H. Y.; Bjorklund, T. G.; Lim, S.-H.; Bardeen, C. J. *Langmuir* **2003**, *19*, 3941.

(60) Merrifield, R. E.; Avakian, P.; Groff, R. P. *Chem. Phys. Lett.* **1969**, *3* (6), 386.

(61) Faltermeier, D.; Gompf, B.; Dressel, M.; Tripathi, A. K.; Pflaum, J. *Phys. Rev. B* **2006**, *74*, 125416.

(62) Rao, A.; Wilson, M. W. B.; Albert-Seifried, S.; Di Pietro, R.; Friend, R. H. *Phys. Rev. B - Condens. Matter Mater. Phys.* **2011**, *84* (19).

(63) Wilson, M. W. B.; Rao, A.; Clark, J.; Kumar, R. S. S.; Brida, D.; Cerullo, G.; Friend, R. H. *J. Am. Chem. Soc.* **2011**, *133* (31), 11830.

(64) Geacintov, N. E.; Burgos, J.; Pope, M.; Strom, C. *Chem. Phys. Lett.* **1971**, *11* (4), 504.

(65) Meyenburg, I.; Breuer, T.; Karthäuser, A.; Chatterjee, S.; Witte, G.; Heimbrodt, W. *Phys. Chem. Chem. Phys.* **2016**, *18*, 3825.

(66) Berkelbach, T. C.; Hybertsen, M. S.; Reichman, D. R. *J. Chem. Phys.* **2013**, *138*, 114102.

(67) Tabachnyk, M.; Ehrler, B.; Gélinas, S.; Böhm, M. L.; Walker, B. J.; Musselman, K. P.; Greenham, N. C.; Friend, R. H.; Rao, A. *Nat. Mater.* **2014**, *13* (11), 1033.

(68) Geacintov, N.; Pope, M.; Vogel, F. *Phys. Rev. Lett.* **1969**, *22* (12), 593.

(69) Pope, M.; Geacintov, N. E.; Vogel, F. *Mol. Cryst.* **1969**, *6* (1), 83.

(70) Merrifield, R. E. *J. Chem. Phys.* **1968**, *27* (3), 481.

(71) Hanna, M. C. & Nozik, A. J. *J. Appl. Phys.* **2006**, *100*, 074510.

(72) Xia, J.; Sanders, S. N.; Cheng, W.; Low, J. Z.; Liu, J.; Campos, L. M.; Sun, T. *Adv. Mater.* **2017**, *29* (1601652).

(73) Shockley, W.; Queisser, H. J. *J. Appl. Phys.* **1961**, *32*, 510.

(74) Lee, J.; Jadhav, P.; Reusswig, P. D.; Yost, S. R.; Thompson, N. J.; Congreve, D. N.; Hontz, E.; Voorhis, T. V. A. N.; Baldo, M. A. *Acc. Chem. Res.* **2013**, *46* (6), 1300.

(75) Rao, A.; Friend, R. H. *Nat. Rev. Mater.* **2017**, *2* (17063), 1.

(76) Ehrler, B.; Wilson, M. W. B.; Rao, A.; Friend, R. H.; Greenham, N. C. *Nano Lett.* **2012**, *12*, 1053.

(77) Congreve, D. N.; Lee, J.; Thompson, N. J.; Hontz, E.; Yost, S. R.; Reusswig, P. D.; Bahlke, M. E.; Reineke, S.; Van Voorhis, T.; Baldo, M. A. *Science (80-.).* **2013**, *340*, 334.

(78) Jadhav, P. J.; Mohanty, A.; Sussman, J.; Lee, J.; Baldo, M. A. *Nano Lett.* **2011**, *11* (4), 1495.

(79) Davis, N. J. L. K.; Allardice, J. R.; Xiao, J.; Petty, A. J.; Greenham, N. C.; Anthony, J. E.; Rao, A. *J. Phys. Chem. Lett.* **2018**, *9* (6), 1454.

(80) Jadhav, P. J.; Brown, P. R.; Thompson, N.; Wunsch, B.; Mohanty, A.; Yost, S. R.; Hontz, E.; Van Voorhis, T.; Bawendi, M. G.; Bulović, V.; Baldo, M. A. *Adv. Mater.* **2012**, *24*, 6169.

(81) Futscher, M. H.; Rao, A.; Ehrler, B. *ACS Energy Lett.* **2018**, *3* (10), 2587.

(82) Einzinger, M.; Wu, T.; Kompalla, J. F.; Smith, H. L.; Perkinson, C. F.;

Nienhaus, L.; Wieghold, S.; Congreve, D. N.; Kahn, A.; Bawendi, M. G.; Baldo, M. A. *Nature* **2019**, *571*, 90.

(83) Smith, M. B.; Michl, J. *Annu. Rev. Phys. Chem.* **2013**, *64*, 361.

(84) Zimmerman, P. M.; Musgrave, C. B.; Head-Gordon, M. *Acc. Chem. Res.* **2013**, *46* (6), 1339.

(85) Chan, W. L.; Berkelbach, T. C.; Provorse, M. R.; Monahan, N. R.; Tritsch, J. R.; Hybertsen, M. S.; Reichman, D. R.; Gao, J.; Zhu, X. Y. *Acc. Chem. Res.* **2013**, *46*, 1321.

(86) Wai-Lun Chan, Manuel Ligges, Askat Jailaubekov, Loren Kaake, Luis Miaja-Avila, X. Y. Z. *Science (80-.).* **2011**, *334* (6062), 1541.

(87) Chan, W.-L.; Ligges, M.; Zhu, X.-Y. *Nat. Chem.* **2012**, *4* (10), 840.

(88) Greyson, E. C.; Stepp, B. R.; Chen, X. D.; Schwerin, A. F.; Paci, I.; Smith, M. B.; Akdag, A.; Johnson, J. C.; Nozik, A. J.; Michl, J. *J. Phys. Chem. B* **2010**, *114*, 14223.

(89) Havenith, R. W. A.; De Gier, H. D.; Broer, R. *Mol. Phys.* **2012**, *10*, 2445.

(90) Berkelbach, T. C.; Hybertsen, M. S.; Reichman, D. R. *J. Chem. Phys.* **2013**, *138* (11), 114103.

(91) Berkelbach, T. C.; Hybertsen, M. S.; Reichman, D. R. *J. Chem. Phys. J. Chem. Phys. J. Chem. Phys. J. Chem. Phys.* **2013**, *114102* (May 2014).

(92) Yost, S. R.; Lee, J.; Wilson, M. W. B.; Wu, T.; McMahon, D. P.; Parkhurst, R. R.; Thompson, N. J.; Congreve, D. N.; Rao, A.; Johnson, K.; Sfeir, M. Y.; Bawendi, M. G.; Swager, T. M.; Friend, R. H.; Baldo, M. A.; Van Voorhis, T. *Nat. Chem.* **2014**, *6* (6), 492.

(93) Zimmerman, P. M.; Zhang, Z.; Musgrave, C. B. *Nat. Chem.* **2010**, *2* (8), 648.

(94) Alguire, E. C.; Subotnik, J. E.; Damrauer, N. H. *J. Phys. Chem. A* **2015**, *119* (2), 299.

(95) Stern, H. L.; Cheminal, A.; Yost, S. R.; Broch, K.; Bayliss, S. L.; Chen, K.; Tabachnyk, M.; Thorley, K.; Greenham, N.; Hodgkiss, J. M.; Anthony, J.;

Head-Gordon, M.; Musser, A. J.; Rao, A.; Friend, R. H. *Nat Chem* **2017**, *9*, 1205.

(96) Kolomeisky, A. B.; Feng, X.; Krylov, A. I. *J. Phys. Chem. C* **2014**, *118*, 5188–5195.

(97) Eaton, S. W.; Shoer, L. E.; Karlen, S. D.; Dyar, S. M.; Margulies, E. A.; Veldkamp, B. S.; Ramanan, C.; Hartzler, D. A.; Savikhin, S.; Marks, T. J.; Wasielewski, M. R. *J. Am. Chem. Soc.* **2013**.

(98) Le, A. K.; Bender, J. A.; Arias, D. H.; Cotton, D. E.; Johnson, J. C.; Roberts, S. T. *J. Am. Chem. Soc.* **2018**, *140* (2), 814.

(99) Van Stokkum I.H.M., Van Oort B., Van Mourik F., Gobets B., V. A. H. *Biophysical Techniques in Photosynthesis. Advances in Photosynthesis and Respiration*; 2008.

(100) Thampi, A.; Stern, H. L.; Cheminal, A.; Tayebjee, M. J. Y.; Petty, A. J.; Anthony, J. E.; Rao, A. *J. Am. Chem. Soc.* **2018**, *140* (13), 4613.

(101) Wilson, M. W. B.; Rao, A.; Ehrler, B.; Friend, R. H. *Acc. Chem. Res.* **2013**, *46*, 1330.

(102) Wan, Y.; Guo, Z.; Zhu, T.; Yan, S.; Johnson, J.; Huang, L. *Nat. Chem.* **2015**, *7* (10), 785.

(103) Roberts, S. T.; McAnally, R. E.; Mastron, J. N.; Webber, D. H.; Whited, M. T.; Brutchey, R. L.; Thompson, M. E.; Bradforth, S. E. *J. Am. Chem. Soc.* **2012**, *134*, 6388.

(104) Akdag, A.; Havlas, Z.; Michl, J. *J. Am. Chem. Soc.* **2012**, *134*, 14624.

(105) Wen, J.; Havlas, Z.; Michl, J. *J. Am. Chem. Soc.* **2015**, *137* (1), 165.

(106) Musser, A. J.; Maiuri, M.; Brida, D.; Cerullo, G.; Friend, R. H.; Clark, J. *J. Am. Chem. Soc.* **2015**, *137*, 5130.

(107) Wang, C.; Schlamadinger, D. E.; Desai, V.; Tauber, M. J. *ChemPhysChem* **2011**, *12*, 2891.

(108) Klenina, I.; Makhneva, Z.; Moskalenko, A.; Gudkov, N. D.; Bolshakov, M.; Pavlova, E.; Proskuryakov. *Biochemistry* **2014**, *79*, 235.

(109) Stern, H. L.; Cheminal, A.; Yost, S. R.; Broch, K.; Sam, L.; Chen, K.; Tabachnyk, M.; Thorley, K.; Greenham, N.; Anthony, J.; Head-gordon, M.; Musser, A. J.; Rao, A. *https://arxiv.org/abs/1704.01695* **2017**.

(110) Burdett, J. J.; Muller, A. M.; Gosztola, D.; Bardeen, C. J. *J. Chem. Phys.* **2010**, *133* (14).

(111) Burdett, J. J.; Bardeen, C. J. *J. Am. Chem. Soc.* **2012**, *134*, 8597.

(112) Weiss, L. R. L. R.; Bayliss, S. L. S. L.; Kraffert, F.; Thorley, K. J. K. J.; Anthony, J. E. J. E.; Bittl, R.; Friend, R. H. R. H.; Rao, A.; Greenham, N. C. N. C.; Behrends, J. *Nat. Phys.* **2017**, *13*, 176.

(113) Stern, H. L.; Musser, A. J.; Gelinas, S.; Parkinson, P.; Herz, L. M.; Bruzek, M. J.; Anthony, J.; Friend, R. H.; Walker, B. J. *Proc. Natl. Acad. Sci. U. S. A.* **2015**, *112*, 7656.

(114) Pensack, R. D.; Tilley, A. J.; Parkin, S. R.; Lee, T. S.; Payne, M. M.; Gao, D.; Jahnke, A. A.; Oblinsky, D. G.; Li, P.-F.; Anthony, J. E.; Seferos, D. S.; Scholes, G. D. *J. Am. Chem. Soc.* **2015**, *137*, 6790.

(115) Mastron, J. N.; Roberts, S. T.; McAnally, R. E.; Thompson, M. E.; Bradforth, S. E. *J. Phys. Chem. B* **2013**, *117*, 15519.

(116) Tayebjee, M. J. Y.; Schwarz, K. N.; MacQueen, R. W.; Dvořák, M.; Lam, A. W. C.; Ghiggino, K. P.; McCamey, D. R.; Schmidt, T. W.; Conibeer, G. J. *J. Phys. Chem. C* **2016**, *120*, 157.

(117) Kasai, H.; Oikawa, H.; Okada, S.; Nakanishi, H. *Bull. Chem. Soc. Jpn.* **1998**, *71*, 2597.

(118) Faltermeier, D.; Gompf, B.; Dressel, M.; Tripathi, A.; Pflaum, J. *Phys. Rev. B* **2006**, *74*, 125416.

(119) Kahlweit, M. *Adv. Colloid Interface Sci.* **1975**, *5* (1), 1.

(120) Liu, Y.; Kathan, K.; Saad, W.; Prud'homme, R. K. *Phys. Rev. Lett.* **2007**, *98* (3), 036102.

(121) Avram, L.; Cohen, Y. *Chem. Soc. Rev.* **2015**, *44*, 586.

(122) Keresztes, I.; Williard, P. G. *J. Am. Chem. Soc.* **2000**, *122* (41), 10228.

(123) Odom, S. A.; Parkin, S. R.; Anthony, J. E. *Org. Lett.* **2003**, *5*, 4245.

(124) Clark, J.; Silva, C.; Friend, R. H.; Spano, F. C. *Phys. Rev. Lett.* **2007**, *98*, 206406.

(125) Gong, J. R.; Wan, L. J.; Lei, S. Bin; Bai, C. L.; Zhang, X. H.; Lee, S. T. *J. Phys. Chem. B* **2005**, *109* (5), 1675.

(126) Koti, A. S. R.; Krishna, M. M. G.; Periasamy, N. *J. Phys. Chem. A* **2001**, *105* (10), 1767.

(127) IUPAC. In *IUPAC Compendium of Chemical Terminology*; 2008.

(128) Sharp, T. E.; Rosenstock, H. M. *J. Chem. Phys.* **1964**, *41*, 3453.

(129) Small, G. J. *J. Chem. Phys.* **1971**, *54*, 3300.

(130) Lukman, S.; Richter, J. M.; Yang, L.; Hu, P.; Wu, J.; Greenham, N. C.; Musser, A. J. *J. Am. Chem. Soc.* **2017**, *139* (50), 18376.

(131) Musser, A. J.; Clark, J. *Annu. Rev. Phys. Chem.* **2019**, *70*, 323.

(132) Ehrler, B.; Wilson, M. W. B.; Rao, A.; Friend, R. H.; Greenham, N. C. *Nano Lett.* **2012**, *12*, 1053.

(133) Thompson, N. J.; Wilson, M. W. B.; Congreve, D. N.; Brown, P. R.; Scherer, J. M.; Bischof, T. S.; Wu, M.; Geva, N.; Welborn, M.; Voorhis, T. Van; Bulović, V.; Bawendi, M. G.; Baldo, M. A. *Nat. Mater.* **2014**, *13*, 1039.

(134) Huang, Z.; Tang, M. L. *J. Am. Chem. Soc.* **2017**, *139*, 9412.

(135) Mongin, C.; Garakyaraghi, S.; Razgoniaeva, N.; Zamkov, M.; Castellano, F. N. *Science (80-.).* **2016**, *351*, 369.

(136) Caira, M. R. In *Design of Organic Solids. Topics in Current Chemistry*; 1998; p vol 198. Springer, Berlin, Heidelberg.

(137) Christopher, G.; S., D. G.; M., M. J.; R., K. E.; Youngmin, L.; Adam, R.; M., P. M.; Nichole, W.; E., A. J.; Ismaila, D.; D., G. E.; B., A. J. *Adv. Funct. Mater.* **2017**, *27*, 1703929.

(138) Piland, G. B.; Bardeen, C. J. *J. Phys. Chem. Lett.* **2015**, *6*, 1841.

(139) Thorsmølle, V. K.; Averitt, R. D.; Demsar, J.; Smith, D. L.; Tretiak, S.; Martin, R. L.; Chi, X.; Crone, B. K.; Ramirez, A. P.; Taylor, A. J. *Phys. Rev. Lett.* **2009**, *102*, 17401.

(140) Dillon, R. J.; Piland, G. B.; Bardeen, C. J. *J. Am. Chem. Soc.* **2013**, *135*, 17278.

(141) Eaton, S. W.; Miller, S. A.; Margulies, E. A.; Shoer, L. E.; Schaller, R. D.; Wasielewski, M. R. *J. Phys. Chem. A* **2015**, *119* (18), 4151.

(142) Jurchescu, O. D.; Mourey, D. A.; Subramanian, S.; Parkin, S. R.; Vogel, B. M.; Anthony, J. E.; Jackson, T. N.; Gundlach, D. J. *Phys. Rev. B* **2009**, *80*, 085201.

(143) Bernstein, J. *J. Phys. D. Appl. Phys.* **1993**, *26* (8B), 66.

(144) An, B. K.; Kwon, S. K.; Jung, S. D.; Park, S. Y. *J. Am. Chem. Soc.* **2002**, *124* (48), 14410.

(145) Li, K.; Liu, B. *Chem. Soc. Rev.* **2014**, *43* (18), 6570.

(146) Zhang, X.; Wang, S.; Xu, L.; Feng, L.; Ji, Y.; Tao, L.; Li, S.; Wei, Y. *Nanoscale* **2012**, *4*, 5581.

(147) Yang, J.; Choi, J.; Bang, D.; Kim, E.; Lim, E. K.; Park, H.; Suh, J. S.; Lee, K.; Yoo, K. H.; Kim, E. K.; Huh, Y. M.; Haam, S. *Angew. Chemie - Int. Ed.* **2011**, *50* (2), 441.

(148) Wu, L.; Luderer, M.; Yang, X.; Swain, C.; Zhang, H.; Nelson, K.; Stacy, A. J.; Shen, B.; Lanza, G. M.; Pan, D. *Theranostics* **2013**, *3* (9), 677.

(149) Hua, F.; Erogbogbo, F.; Swihart, M. T.; Ruckenstein, E. *Langmuir* **2006**, *22* (9), 4363.

(150) Vijaya Sarathy, K.; Kulkarni, G. U.; Rao, C. N. R. *Chem. Commun.* **1997**, No. 6, 537.

(151) Lu, J.; Ma, S.; Sun, J.; Xia, C.; Liu, C.; Wang, Z.; Zhao, X.; Gao, F.; Gong, Q.; Song, B.; Shuai, X.; Ai, H.; Gu, Z. *Biomaterials* **2009**, *30* (15), 2919.

(152) Eastoe, J.; Hollamby, M. J.; Hudson, L. *Adv. Colloid Interface Sci.* **2006**, *128–130*, 5.

(153) Wasan, D.; Nikolov, A. *Curr. Opin. Colloid Interface Sci.* **2008**, *13* (3), 128.

(154) Uskokovic, V.; Drofenik, M. *Surf. Rev. Lett.* **2005**, *12* (2), 239.

(155) Stuart, M. C. A.; Boekema, E. J. *Biochim. Biophys. Acta - Biomembr.* **2007**, *1768* (11), 2681.

(156) Everett, D. H. In *Basic Principles of Colloid Science, The Royal Society of Chemistry, Cambridge, UK.*; 1988.

(157) Pedersen, J. S. *J. Appl. Crystallogr.* **2000**, *33*, 637.

(158) Chien, M. P.; Rush, A. M.; Thompson, M. P.; Gianneschi, N. C. *Angew. Chemie - Int. Ed.* **2010**, *49* (30), 5076.

(159) Spatz, J. P.; Sheiko, S.; Möller, M. *Macromolecules* **1996**, *29* (9), 3220.

(160) Cabane, B. *J. Phys. Fr.* **1981**, *42* (6), 847.

(161) Mukerjee, P.; Mysels, K. J. *Critical micelle concentrations of aqueous surfactant systems*; 1971.

(162) Cui, X.; Mao, S.; Liu, M.; Yuan, H.; Du, Y. *Langmuir* **2008**, *24* (19), 10771.

(163) Sahu, P. K.; Kulkarni, B. D.; Khomane, R. B.; Pardhy, S. A.; Phalgune, U. D.; Rajmohanan, P.; Pasricha, R. *Chem. Commun.* **2003**, 1876.

(164) Yang, L.; Wang, N.; Wang, X.; Chen, H. *Micro & Nano Lett.* **2013**, *8*, 94.

(165) Yu, D.; Huang, F.; Xu, H. *Anal. Methods* **2012**, *4*, 47.

(166) Dover, C. B.; Gallaher, J. K.; Frazer, L.; Tapping, P. C.; Petty, A. J.; Crossley, M. J.; Anthony, J. E.; Kee, T. W.; Schmidt, T. W. *Nat. Chem.* **2018**, *10*, 305.

(167) Vaubel, G.; Baessler, H. *Mol. Cryst. Liq. Cryst.* **1970**, *12* (1), 47.

(168) Jen, A. K. Y.; Rao, V. P.; Wong, K. Y.; Drost, K. J. *J. Chem. Soc. Chem. Commun.* **1993**, 90.

(169) Doddi, G.; Illuminati, G.; Mencarelli, P.; Stegel, F. *J. Org. Chem.* **1976**, *41* (17), 2824.

(170) Lukman, S.; Chen, K.; Hodgkiss, J. M.; Turban, D. H. P.; Hine, N. D. M.; Dong, S.; Wu, J.; Greenham, N. C.; Musser, A. J. *Nat. Commun.* **2016**, *7*, 13622.

(171) Sutton, C.; Tummala, N. R.; Beljonne, D.; Brédas, J. L. *Chem. Mater.* **2017**, *29* (7), 2777.

(172) Casanova, D. *Chem. Rev.* **2018**, *118*, 7164–7207.

(173) Xie, X.; Ma, H. *ChemistryOpen* **2016**, *5* (3), 201.

(174) Lunt, R. R.; Giebink, N. C.; Belak, A. A.; Benziger, J. B.; Forrest, S. R. *J. Appl. Phys.* **2009**, *105* (5).

(175) Najafov, H.; Lee, B.; Zhou, Q.; Feldman, L. C.; Podzorov, V. *Nat. Mater.* **2010**, *9*, 938.

(176) Ren, T. B.; Xu, W.; Zhang, W.; Zhang, X. X.; Wang, Z. Y.; Xiang, Z.; Yuan, L.; Zhang, X. B. *J. Am. Chem. Soc.* **2018**, *140* (24), 7716.

(177) Rogers, J. E.; Nguyen, K. A.; Hufnagle, D. C.; McLean, D. G.; Su, W.; Gossett, K. M.; Burke, A. R.; Vinogradov, S. A.; Pachter, R.; Fleitz, P. A. *J. Phys. Chem. A* **2003**, *107* (51), 11331.

(178) Tayebjee, M. J. Y.; Sanders, S. N.; Kumarasamy, E.; Campos, L. M.; Sfeir, M. Y.; McCamey, D. R. *Nat. Phys.* **2017**, *13*, 182.

(179) Piland, G. B.; Burdett, J. J.; Kurunthu, D.; Bardeen, C. J. *J. Phys. Chem. C* **2013**, *117*, 1224.

(180) Austin, R. H.; Baker, G. L.; Etemad, S.; Thompson, R. *J. Chem. Phys.* **1989**, *90* (11), 6642.

(181) Basel, B. S.; Zirzlmeier, J.; Hetzer, C.; Phelan, B. T.; Krzyaniak, M. D.; Reddy, S. R.; Coto, P. B.; Horwitz, N. E.; Young, R. M.; White, F. J.; Hampel, F.; Clark, T.; Thoss, M.; Tykwinski, R. R.; Wasielewski, M. R.; Guldi, D. M. *Nat. Commun.* **2017**, *8*, 15171.

(182) Kraffert, F.; Steyrleuthner, R.; Albrecht, S.; Neher, D.; Scharber, M. C.; Bittl, R.; Behrends, J. *J. Phys. Chem. C* **2014**, *118* (49), 28482.

(183) Budil, D. E.; Thurnauer, M. C. *Biochim. Biophys. Acta - Bioenerg.* **1991**,

1057 (1), 1.

(184) Bardeen, C. J. *Annu. Rev. Phys. Chem.* **2013**, *65*, 127.

(185) Johnson, J. C.; Nozik, A. J.; Michl, J. *J. Am. Chem. Soc.* **2010**, *132* (46), 16302.

(186) Marder, S. R.; Torruellas, W. E.; Blanchard-Desce, M.; Ricci, V.; Stegeman, G. I.; Gilmour, S.; Brédas, J. L.; Li, J.; Bublitz, G. U.; Boxer, S. G. *Science (80-.).* **1997**, *276* (5316), 1233.

(187) Sturala, J.; Etherington, M. K.; Bismillah, A. N.; Higginbotham, H. F.; Trewby, W.; Aguilar, J. A.; Bromley, E. H. C.; Avestro, A. J.; Monkman, A. P.; McGonigal, P. R. *J. Am. Chem. Soc.* **2017**, *139* (49), 17882.

(188) Fulton, R. L.; Gouterman, M. *J. Chem. Phys.* **1964**, *421*, 2280.

(189) F H Todd. *Nature* **1958**, *181*, 456.

(190) Crespo-Hernández, C. E.; Cohen, B.; Kohler, B. *Nature* **2005**, *436*, 1141.

(191) Scholes, G. D.; Rumbles, G. *Nat. Mater.* **2006**, *5*, 683.

(192) Ghosh, R.; Mondal, J. A.; Palit, D. K. *J. Phys. Chem. B* **2010**, *114* (37), 12129.

(193) Walker, B. J.; Musser, A. J.; Beljonne, D.; Friend, R. H. *Nat. Chem.* **2013**, *5*, 1019.

(194) Smith, M. B.; Michl, J. *Annu. Rev. Phys. Chem.* **2013**, *64*, 361.

(195) Tayebjee, M. J. Y.; Gray-Weale, A. A.; Schmidt, T. W. *J. Phys. Chem. Lett.* **2012**, *3*, 2749.

(196) Clarke, T. M.; Durrant, J. R. *Chem. Rev.* **2009**, *110*, 6736.

(197) Li, J.; Chen, Z.; Zhang, Q.; Xiong, Z.; Zhang, Y. *Org. Electron.* **2015**, *26*, 213.

(198) Laidler, K. J.; King, M. C. *J. Phys. Chem.* **1983**, *87* (15), 2657.

(199) Lindemann, F. A.; Svante Arrhenius; Langmuir, I.; Dhar, N. R.; Perrin, J.; Lewis, W. C. M. *Transactions of the Faraday Society*. 1922,.

(200) Ludwig Boltzmann. *Vorlesungen u ber Gastheorie*; 1896.

(201) Ern, V. *Phys. Rev. Lett.* **1969**, *22* (8), 343.

(202) Akselrod, G. M.; Deotare, P. B.; Thompson, N. J.; Lee, J.; Tisdale, W. A.; Baldo, M. A.; Menon, V. M.; Bulović, V. *Nat. Commun.* **2014**, *16* (5), 3646.

(203) Bakulin, A. A.; Morgan, S. E.; Kehoe, T. B.; Wilson, M. W. B.; Chin, A. W.; Zigmantas, D.; Egorova, D.; Rao, A. *Nat. Chem.* **2016**, *8*, 16.

(204) Musser, A. J.; Liebel, M.; Schnedermann, C.; Wende, T.; Kehoe, T. B.; Rao, A.; Kukura, P. *Nat. Phys.* **2015**, *11*, 352.

(205) Bayliss, S. L.; Weiss, L. R.; Mitioglu, A.; Galkowski, K.; Yang, Z.; Yunusova, K.; Surrente, A.; Thorley, K. J.; Behrends, J.; Bittl, R.; Anthony, J. E.; Rao, A.; Friend, R. H.; Plochocka, P.; Christianen, P. C. M.; Greenham, N. C.; Chepelianskii, A. D. *Proc. Natl. Acad. Sci.* **2018**, *115* (20), 5077.

(206) Scholes, G. D. *J. Phys. Chem. A* **2015**, *119* (51), 12699.

List of Publications

(1) Thampi, A., Stern, H.L., Cheminal, A., Tayebjee, M.J.Y., Petty, A.J., Anthony, J.E., and Rao, A. (2018). Elucidation of Excitation Energy Dependent Correlated Triplet Pair Formation Pathways in an Endothermic Singlet Fission System. *J. Am. Chem. Soc.* 140, 4613–4622.

(2) Thampi, A., Holland, E., Weiss, L., Pershin, A., Taffet, E., Alvertis, A.M., Gu, Q., Myers, W., Beljonne, D., Greenham, N., Anthony, J. E. and A.Rao (2019). Entropic Drive and Triplet Diffusion Dictate Efficiency in Endothermic Singlet Fission, *under review*.

(3) Thampi et al., manuscript on Structural Influence on Singlet Fission Dynamics in Thienoanthracenes, *in preparation*.

(4) Thampi et al., manuscript on Modifying Singlet Fission Dynamics by Micelle-driven Surface Modification, *in preparation*.

Appendix A

Computational Screening of Molecules

The initial screening was based on thienoanthracene molecule, which stability was expected to improve with introducing functional groups. Considering experimental fusibility of their synthesis, we designed in silico 16 chemical derivatives of thienoanthracene, shown in Figure A 1. The screening was performed with a robust ADC(2) electronic structure method using def2-TZVP basis set, resulting in energies close to the complete basis set limit. To facilitate the process, we opted for comparing the singlet and triplet excitation energies at the relaxed S_1 geometry obtained by TD(A)-DFT calculations with B3LYP functional in vacuum. The results are summarized inTable A 1. For the compound **1** we observed large endothermic energy difference of -0.56eV that likely hinders the singlet fission process. At the same time, double substitution in the central ring of anthracene substantially reduces the triplet energy, as evident for compounds **7**, **16**, and **17**. Other positions are less relevant for the efficiency of SF. For clarity, we would like to mention that molecule 16 and 17 are the closest to the fluorinated and non-fluorinated thienoanthracenes discussed in Chapter 6 and Chapter 7.

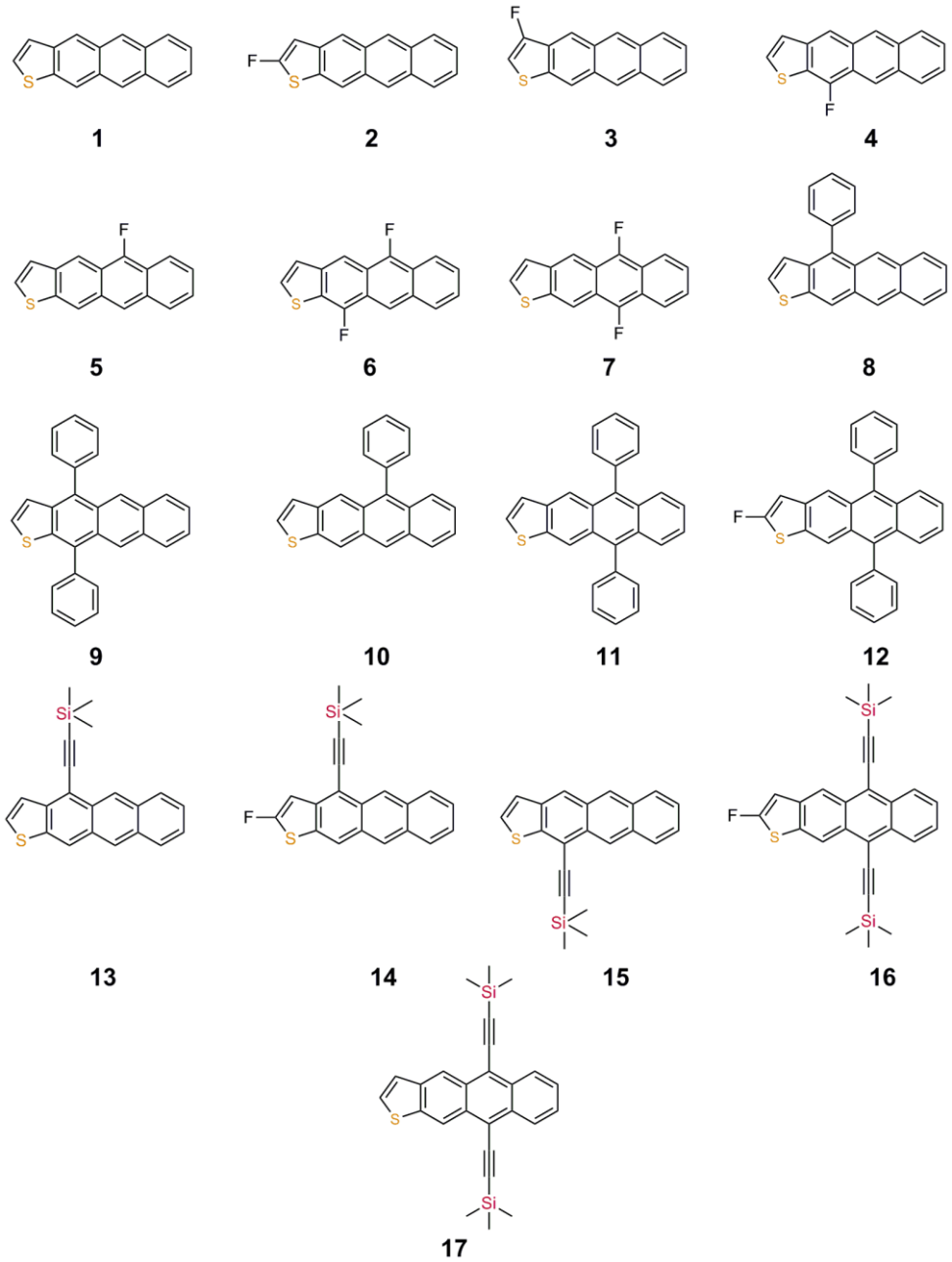

Figure A 1-Chemical structures of compounds selected for the computational screening.

Table A 1-Singlet and triplet excitation energies (in eV) for the compounds from Figure A 1 obtained at ADC(2) level using relaxed S_1 geometry from TD(A)-DFT calculations.

	S_1	T_1	S_1-2T_1
1	2.82	1.69	-0.56
2	2.92	1.75	-0.58
3	2.78	1.67	-0.56
4	2.79	1.67	-0.55
5	2.75	1.63	-0.51
6	2.75	1.63	-0.51
7	2.66	1.56	-0.46
8	2.71	1.65	-0.59
9	2.62	1.62	-0.62
10	2.73	1.65	-0.57
11	2.65	1.62	-0.59
12	2.73	1.68	-0.63
13	2.64	1.58	-0.52
14	2.73	1.65	-0.57
15	2.73	1.62	-0.51
16	2.54	1.45	-0.36
17	2.45	1.40	-0.35

Furthermore, for selected compounds **16** and **17**, we refined the excitation energies by considering structural relaxations at ADC(2) level as well as polarization effect by the environment via polarizable continuum model (PCM). The resulting transitions together with the corresponding TD(A) results are given in Table A 2. Here, we observe that TDA-DFT does not fully capture the relaxation process in the excited state as evident by comparing with the energies at the relaxed ADC(2) geometries. Moreover, strong reorganizations in the triplet states favours the singlet fission process reducing the endothermic energy difference to -0.09eV

for compound **16**. Nevertheless, we anticipate that those relaxations might be partially suppressed in crystal as further confirmed by the experimental measurements. Moreover, once considering the triplet energy at the relaxed S_1 geometry from ADC(2) calculations, the energy difference approaches the experimental value for **16**. At the same, the polarization of the environment shows minor impact on the excitation energies.

Table A 2-Singlet and triplet excitation energies (in eV) for the compounds 16 and 17 from Figure A 1 obtained at the specified levels of theory including structural relaxation. Here, "vertical" stands for the excitation energies at the ground state geometry, while "relaxed" is for the energies at the geometries optimized for the respective states.

		vertical		**relaxed**		**Relaxed + PCM ($\varepsilon = 4$)**		**relaxed S_1**
		S_1	T_1	S_1	T_1	S_1	T_1	T_1
17	ADC(2)	2.63	1.65	2.26	1.17	2.23	1.16	1.25
	TD	2.34	1.13	2.10	0.65			
	TDA	2.55	1.38	2.40	1.00			
16	ADC(2)	2.7	1.75	2.33	1.21	2.31	1.21	1.32
	TD	2.38	1.16	2.16	0.70			
	TDA	2.6	1.43	2.46	1.04			
	exp	**2.58**				**2.25**	**1.3**	